OPTICAL CONTROL OF EXCITON QUBITS IN SEMICONDUCTOR QUANTUM DOTS USING PULSE SHAPING TECHNIQUES

by

Reuble Mathew

Submitted in partial fulfillment of the
requirements for the degree of
Doctor of Philosophy

at

Dalhousie University
Halifax, Nova Scotia
August 2015

Table of Contents

List of Tables

List of Figures

Abstract

Semiconductor quantum dots have been featured in a number of proposals for quantum computing because of the advantages afforded by confinement on the nanoscale, such as well separated, discrete energy levels and ease of optical manipulation. In addition, they can leverage established semiconductor fabrication techniques and, like the quantum dots used in this work, can be designed to match the telecommunication band, improving the scalability and potential integration of the platform into existing technologies. This thesis work applied optical pulse engineering to manipulate exciton qubits in self-assembled InAs quantum dots.

Optimal quantum control theory was used to design pulse shapes that implement high fidelity single-qubit and two-qubit operations, with constraints on the numerical optimization that ensure that the pulses can be accurately implemented using a commercial $4f$ pulse shaper. In the case of single-qubit operations, the results showed that two uncoupled qubits can be manipulated in parallel using a single phase-shaped laser pulse, provided their optoelectronic properties are sufficiently different. It was demonstrated that targeted differences in inversion and phase between the qubits can be achieved on an ultrafast timescale with high fidelity. In the case of two-qubit operations, the controlled-rotation gate was optimized using amplitude-only and phase-only pulse shaping schemes. The shaped pulses for both schemes were shown to produce higher fidelity operations.

The ability to implement robust state inversion on short timescales is particularly useful for technologies such as ultrafast optical switches, single-photon sources, and entangled-photon sources. This work has demonstrated state inversion in a single InAs quantum dot via adiabatic rapid passage using linearly chirped laser pulses. The achieved gate times were an order of magnitude shorter than previous demonstrations. Theoretical predictions of the dependence of the inversion efficiency of the exciton on the sign of the pulse chirp were also verified experimentally, allowing for the identification of phonon-mediated dephasing as the dominant source of decoherence.

List of Abbreviations and Symbols Used

2DEG two-dimensional electron gas

AlGaAs aluminum gallium arsenide

ARP adiabatic rapid passage

BBO β barium borate

C-NOT controlled-NOT

C-ROT controlled-rotation

CCD charge-coupled device

CW continuous-wave

DCM dichroic mirror

DD dynamical decoupling

FCC face-centered cubic

FROG frequency-resolved optical gating

FWHM full-width at half maximum

GaAs gallium arsenide

IFQD interface fluctuation quantum dot

In indium

InAs indium arsenide

IR infrared

LA longitudinal acoustic

MBE molecular beam epitaxy

MIIPS multiphoton intrapulse interference phase scan

OBE optical Bloch equation

OPO optical parametric oscillator

OQC optimal quantum control

PL photoluminescence

PLE photoluminescence excitation

QD quantum dot

QEC quantum error correction

RWA rotating wave approximation

SAQD self-assembled quantum dot

SFG sum-frequency generation

SHG second-harmonic generation

SI International System of Units

SK Stranski-Krastanov

SLM spatial light modulator

SPIDER spectral phase interferometry for direct electric field reconstruction

TL transform limited

Acknowledgements

First and foremost, I would like to thank my supervisor, Kimberley Hall, for her guidance and for generously placing her confidence in me. Her unassailable optimism in the face of challenging experiments is inspiring.

I extend my gratitude to Michael Flatté and Craig Pryor at the University of Iowa for sharing their expertise on electronic structure calculations. Thanks also to Dennis Deppe at the University of Central Florida for providing the quantum dot samples.

I am deeply indebted to the troupe of Team Ultrafast for what seems like a lifetime of friendship, jokes, and japes. Where else could birthday presents run the gamut from the nautical to the ornithological? Over the years, the membership has included personalities such as Mat Britton, Amy Chapman, Tristan de Boer, Eric Dilcher, Jonathan Franklin (honorary member), Angela Gamouras, Luke Hacquebard, Mohanad Khairy, Sam March, Ajan Ramachandran, Drew Riley, Hong Yi Shi Yang, Colin Sonnichsen, Dan Webber, and Murat Yildirim. Their contributions toward the refinement of this thesis and the retention of my sanity are appreciated in equal measure.

Hats off to the support staff in Physics department. Thanks to Kevin Borgel and John Noddin in the machine shop for fashioning mission-critical parts for the experiments. Thanks to Andy George for advice regarding vacuum systems and Jim Chisholm for deciphering "PC Load Letter" errors. Thanks to multiple generations of office staff, including, Jennifer Currie, Krista Cullymore, Barbara Gauvin, Sarah Hayes-Brown, Heather Ann Jennex, Anne Murphy, Valerie O'Neill, and Tanya Timmins for helping with administrative matters and their concern for student welfare. Thanks to Joe, Karen, and Steve for keeping the Dunn building operational.

Thanks most of all to my family. To my brother, Reuben, for his advice and encouragement, my sister-in-law, Kyra, for her kindness and support, and my niece, Sophia, for being her wonderful self. Thanks also to my parents, John and Sophiamma, for their lifelong care and love.

Chapter 1

Introduction

Previous decades have borne witness to vast improvements in information processing speeds, memory capacity, and display resolution, driven in part by the exponential increase in density of transistors, memory elements, and pixels in electronic devices. However, this paradigm for technological progress will be challenged as device elements approach the size of single atoms or molecules, a regime in which quantum mechanics governs device function. A computer that makes direct use of quantum mechanical phenomena would operate on completely different principles. Such a computer would not be intended to supplant classical computers, but rather, the great promise of quantum computers is that they may be able to outperform their classical counterparts for certain important computational tasks such as integer factorization and searching of databases.

The fundamental building block of a quantum computer, and the quantum analogue of the classical bit, is the quantum bit (or qubit) consisting of two quantum mechanical states $|0\rangle$ and $|1\rangle$ (see Fig. 1.1(a)). It differs from the binary classical bit in that the qubit can exist in a coherent superposition of the two states. In general, a system of n qubits can exist in a superposition of 2^n states. It is this ability to be in multiple states at the same time that allows for parallel processing on a massive scale. The single-qubit superposition state can be written as $|\Psi\rangle = C_0 |0\rangle + C_1 |1\rangle$, where C_0 and C_1 are complex probability amplitudes. The state is a pseudospin that can be represented geometrically on the so-called *Bloch sphere* by writing the state as $|\Psi\rangle = \cos(\theta/2)|0\rangle + \sin(\theta/2)e^{-i\phi}|1\rangle$, where the azimuthal angle ϕ represents the relative phase between the basis states and the polar angle θ determines the relative occupation (see Fig. 1.1(b)). A further distinction between classical and quantum bits is that two distinct qubits can be entangled to generate strong correlations between them, such that the measurement of the state of one qubit dictates the state of the entangled partner. Quantum computing in the gate model is carried out by

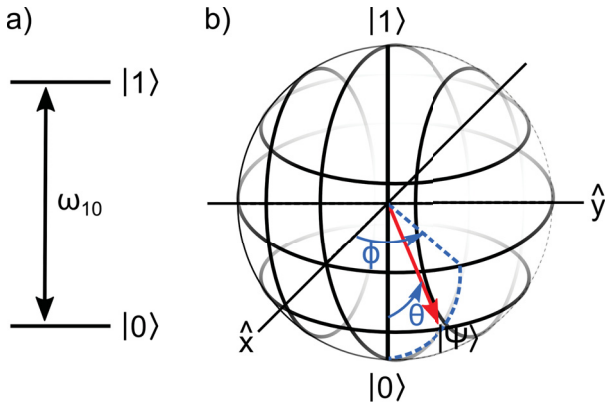

Figure 1.1: (a) Two-level system comprising the qubit with states $|0\rangle$ and $|1\rangle$. (b) Representation of the qubit on the Bloch sphere. The vector that represents the state $|\Psi\rangle$ is a unit vector that lies on the surface of the sphere and is defined by the azimuthal angle ϕ and the polar angle θ. The south and north poles denote the pure states $|0\rangle$ and $|1\rangle$, respectively, while every other point represents a superposition state.

manipulating the wave function of the system of qubits as prescribed by a given algorithm, using a series of single-qubit gates that modify the state of one qubit, and two-qubit gates that entangle the qubits. The problem is encoded such that measurement of the state of the qubits at the end of the algorithm provides the solution.

Algorithms that exploit the principles of superposition and entanglement have already been developed for tasks such as integer factorization (developed by Shor [1]) and fast searching of databases (developed by Grover [2]). Another application that is currently under research is the use of a quantum computer to debug software [3]. Perhaps the most promising application of quantum computing, envisioned by Richard Feynman, is the simulation of multi-particle quantum systems [4]. The challenge is to discover efficient, scalable multiple-qubit systems upon which to implement these algorithms.

The discussions thus far have focused on the gate model of quantum computing, where qubits are manipulated by a sequence of universal gates to implement a quantum algorithm. Other approaches such as adiabatic quantum computation, complex instruction set computing, and measurement-based quantum computation operate on different principles. In adiabatic quantum computing, the solution to the problem is designed such that it is the ground state of a set of interacting qubits.

The qubits are then annealed from a simple fiducial state to the desired final state by adjusting the Hamiltonian adiabatically. This technique is employed by the company D-Wave Systems, that uses superconducting qubit based quantum processors to solve optimization problems [5]. In complex instruction set quantum computing, several universal gates are replaced with a single shaped gate. It has been shown that this approach can significantly reduce the number of steps required to carry out a quantum algorithm compared to the gate model. Furthermore, by transferring the complexity of the algorithm to the optical control pulse, for which arbitrary control is already experimentally accessible, this approach may accelerate the development of multiqubit gates using existing qubit systems [6]. For example, this approach has been used together with control pulses engineered via femtosecond pulse shaping to implement a multiple input AND gate involving 6 qubits encoded in the coupled rovibrational eigenstates of a lithium molecule [7]. Lastly, in measurement-based quantum computing, one prepares a 2D lattice of spins in a specific entangled quantum state and then performs a sequence of single-qubit measurements to perform the computation [8].

The physical requirements for the development of a successful quantum computation platform depend on the computational approach adopted. For instance within the gate model, the demands imposed on any viable physical implementation of a quantum computer were enumerated by DiVinenzo in Ref. [9]. The first requirement is that the system be built on a scalable architecture of qubits with well characterized physical properties. Additionally, it must be possible to initialize and read out the state of a given qubit. It is also critical that the required gate manipulations be performed within the decoherence time of the qubit. This translates into twin efforts to minimize the influence of the decoherence by isolating the qubit from its environment while simultaneously pursuing faster manipulation schemes. Lastly, a universal set of quantum gates, such as the combination of single-qubit and the two-qubit controlled-NOT (C-NOT) gates, into which any quantum algorithm can be decomposed, must be developed for the platform. The requirements on the other computational approaches are not as well known, but clearly there will still be a need for well-characterized, coupled qubits and precise control of the resulting physical system.

There are a number of qubit candidates under active development that may enable the development of useful quantum computing platforms, including those based atomic/molecular systems and others based on solid state approaches. Platforms based on solid state qubits have the advantage that they can leverage existing fabrication techniques. This will prove to be beneficial when the platforms have to be scaled up to a large number of qubits and integrated with classical computing technologies. Qubit platforms under development include nitrogen-vacancy centers in diamond [10], ion traps [11], superconducting loops [12], dopants in silicon [13], and semiconductor quantum dots (QDs) [14]. The nitrogen-vacancy center in diamond is a point defect consisting of a substitutional nitrogen atom and an adjacent lattice vacancy. An electron spin trapped in the vacancy serves as the qubit and can be manipulated using laser light in the presence of an external magnetic field. (See Ref. [10] for a recent review of the field.) In the ion trap platform, the spin state of an ion, electrically levitated in a vacuum, is used as the qubit. Adjacent ions are coupled through mutual electric repulsion and the spin state of individual ions can also be manipulated using laser light. (See Ref. [11] for a recent review of the field.) Superconducting circuits employ superconducting loops interrupted by Josephson junctions. The quantized charge, phase, or flux of Cooper pairs across the junction can serve as the qubit. Magnetic biases are used to control the state of the qubit and they are coupled to each other through mutual inductance or capacitance. (See Ref. [12] for a recent review of the field.) For silicon dopant based qubits, the spin state of either the donor's nucleus or its outermost electron may be used as a qubit. Single-electron transistors can be used to read out the quantum state. (See Ref. [13] for a recent review.) The stages of development toward a fault-tolerant quantum computer, focusing on the gate model of quantum computing, and the progress that scientists have made using these qubit platforms are discussed in Appendix A. This thesis aims to further the semiconductor QD based platform where confined charge or spin states can be used as qubits.

1.1 Semiconductor Quantum Dots

1.1.1 Bulk Semiconductor Properties

The electronic properties of a semiconductor quantum dot can be understood by first considering the nature of the electron states in their bulk constituents. The regular arrangement of atoms in a semiconductor crystal creates a periodic potential for the electron. The resulting wave functions are Bloch waves, $\Psi_{\nu,\mathbf{k}}(\mathbf{r}) = e^{-i\mathbf{k}\cdot\mathbf{r}}u_{\nu,\mathbf{k}}(\mathbf{r})$, corresponding to the product of a plane wave with wave vector $\mathbf{k}$ and a function $u_{\nu,\mathbf{k}}(\mathbf{r})$ that has the periodicity of the lattice. In a semiconductor at $0\,\mathrm{K}$, the fully occupied bands are called valence bands and the unoccupied bands are called conduction bands. The energy separation between the top valence band and the lowest conduction band is called the band gap energy (E_g). (See Fig. 1.2(a).) The material is transparent to light with frequencies below E_g, but for optical excitation above this energy, an electron can be promoted from the valence band to the conduction band, leaving a hole (absence of electron) in the valence band. The value of E_g is determined by the elements that form the crystal. For instance, indium arsenide (InAs) and gallium arsenide (GaAs) have band gaps of $0.35\,\mathrm{eV}$ and $1.42\,\mathrm{eV}$, respectively, at $300\,\mathrm{K}$.

1.1.2 Quantum Confinement

To realize a quantum dot within a semiconductor, one must introduce a spatially varying potential that localizes electrons and holes to a region of space that is comparable to the de Broglie wavelength (typically $20\,\mathrm{nm}$ or less). The spatially varying potential creates a physical manifestation of the particle-in-a-box problem of elementary quantum mechanics. The lowest energy states for electrons and holes in such a structure corresponding to "standing waves" and the associated energy states are discrete levels. A series of confined levels exist for each band ν of the corresponding bulk crystal. A schematic band structure of a semiconductor quantum dot is shown in Fig. 1.2(b), where the z-dependence of the bulk band edges of the valence band and the conduction band are shown together with the discrete confined valence and conduction states.

There are a variety of ways to realize a spatially-varying potential, resulting

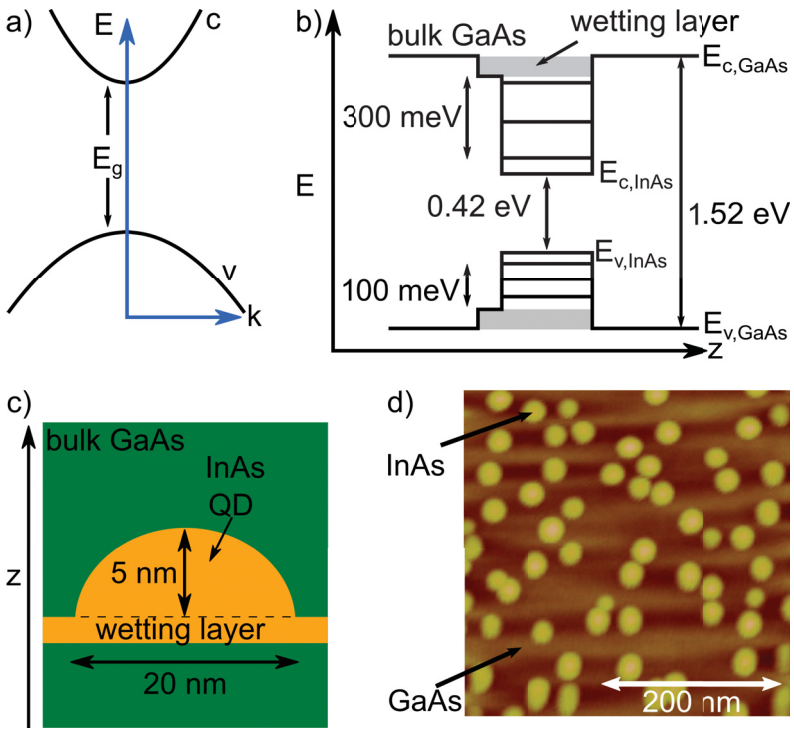

Figure 1.2: (a) Schematic of the band structure of a typical direct band gap semiconductor such as GaAs or InAs. The bands indicate allowed energies at a particular wave vector $\mathbf{k}$ for the electron. At $0\,\mathrm{K}$, the valence band (v) states are occupied and the conduction band (c) is empty. Optical excitation with a photon of energy greater than the band gap energy E_g, will excite an electron from the valence band to the conduction band. (b) Schematic band structure diagram of an InAs/GaAs self-assembled QD, showing the band edges as a function of position as well as the confined valence and conduction levels. The z-direction is the growth direction of the semiconductor heterostructure. The WL indicated by the grey band consists of a continuum of delocalized states. (c) Schematic diagram of an InAs QD embedded in a GaAs matrix. The wetting layer is a graded layer of InGaAs that can support states localized to a two-dimensional layer perpendicular to the $\hat{z}$ direction, in the plane of the QDs. Typical dimensions for the QD are shown. (d) Atomic force microscope image of the InAs quantum dots prior to capping with GaAs. Image courtesy of Dennis Deppe.

in different types of semiconductor quantum dots. For instance, lateral QDs are created by using patterned electrical gates to create a potential well in a two-dimensional electron gas (2DEG). The 2DEG is a thin conducting layer of semiconductor (typically GaAs) where carriers are free to move in two dimensions but confined in the third. A region of lower potential is formed in the 2DEG by applying a voltage to electrical gates arranged in a triangle. This leads to discrete electron

energy states that can be optically and electrically manipulated. Colloidal QDs are nanocrystals synthesized from solution, by nucleation of the required chemical compounds. For such quantum dots, the potential well is created by the interface between the semiconductor and the outside vacuum. Quantum dots can also be grown using epitaxial techniques that provide sub-monolayer control over the growth process. The first type of epitaxial QD is called an interface fluctuation quantum dot (IFQD). It is formed by growing a partial monolayer of one type of semiconductor on a substrate of another type of semiconductor, after which more of the substrate material is deposited on top. This results in the formation of monolayer high islands. The difference in the energy of the band extrema in the two different semiconductors (typically GaAs and aluminum gallium arsenide (AlGaAs)), called band offsets, creates potential steps that confine the carriers in the lower band gap region, corresponding to the localized islands. A related type of QD to IFQDs are self-assembled quantum dots (SAQDs). These are grown using the Stranski-Krastanov growth mode, which makes use of the difference in lattice constant between the two different semiconductor materials, resulting in a strain-driven self-assembly process. In this case, one semiconductor material is deposited using molecular beam epitaxy onto a substrate material. For example, in the case of InAs QDs embedded in a GaAs matrix, indium and arsenide atoms are sublimated through an ultra-high vacuum and deposited on a heated, spinning GaAs substrate (also epitaxially grown). Due to the 7% lattice mismatch between InAs and GaAs, it forms a strained monolayer of InAs. Beyond a critical thickness it becomes energetically favourable for the strained layer to nucleate into nanoscale islands (see Fig. 1.2(c) and Fig. 1.2(d)). The islands sit on an InAs wetting layer and have lateral dimensions on the order of $20\,\mathrm{nm}$ and heights on the order of $5\,\mathrm{nm}$. The band offsets between the InAs islands and the surrounding GaAs creates the potential used for quantum confinement.

Lateral QDs have a relatively large spatial extent ($\sim 100\,\mathrm{nm}$). As a result, the energy level spacing is only about $2\,\mathrm{meV}$. To realize optically-controlled quantum bits using the confined energy states, a larger level spacing is desirable. All three of the other quantum dot types (colloidal QDs, IFQDs, and SAQDs) have much larger energy spacing (~ 10's of meV or larger), which makes them good candidates

for optical control. Colloidal QDs offer ease of synthesis, however the existence of dangling bonds at the surface and other surface states can lead to rapid non-radiative recombination of the electron and hole following optical excitation. As a result, the decoherence time is relatively short in such QDs.

IFQDs and SAQDs have exceptionally good optical properties because the potential well is created by the interfaces between semiconductors. In this case, high quality interfaces lead to low rates of non-radiative recombination and thus longer coherence times in comparison to colloidal QDs. IFQDs are characterized by a fairly large dipole moment ($\sim 100\,\mathrm{Debye}$), and have radiative transitions between the confined hole and electron levels in the near-infrared, compatible with high-efficiency silicon optical detectors. As a result, these QDs have been important for early demonstrations of coherent control [15, 16, 17, 18, 19, 20]. The random spatial and size distribution of IFQDs make them unlikely to be used in scalable quantum computing applications. In contrast, SAQDs can be engineered by varying the growth conditions to tailor the ground state transition energy and the degree of inhomogeneity [21]. In addition, advances in nano-template growth techniques now allow for site-selected quantum dots with more control over the QD properties [22]. Laser annealing has been used to further tune the electronic properties [23, 24]. SAQDs have a lower dipole moment than IFQDs ($\sim 5\times$ lower), making optical experiments on them more challenging. Nevertheless, due to all of the above advantages, they have been the focus of the majority of recent coherent control experiments on semiconductor QDs. In this thesis work, the experiments and theoretical calculations all focus on InAs/GaAs SAQDs.

1.1.3 Optical Properties of SAQDs

The band offsets between the valence and conduction bands of InAs and GaAs provide a 3D confining potential well for carriers trapped in the QD, with a 100–$300\,\mathrm{meV}$ potential well for the electrons and 30–$100\,\mathrm{meV}$ potential well for the holes [25]. The strong confinement results in a set of discrete atomic-like states with optical transitions between the valence and conduction states characterized by electric dipole moments $\sim 20\,\mathrm{Debye}$. SAQDs may be grown under conditions that yield

optical transitions between the valence and conduction states that match telecom-relevant wavelengths ($1.3\,\mu\mathrm{m}$ and $1.55\,\mu\mathrm{m}$, representing the minimum dispersion and absorption wavelengths, respectively, for optical fibers). This makes them compatible with existing photonic and telecommunication infrastructure, a feature that would greatly simplify the ultimate integration of a quantum device using SAQDs with classical technologies. These properties greatly facilitate optical control and therefore SAQDs lend themselves to a number of optoelectronic applications such as single-photon sources [26], cellular imaging [27], QD lasers [28, 29], entangled-photon sources [30], solar cells [31], and all-optical switches [32]. Their large moments also allow for manipulation using ultrafast optical pulses.

For SAQDs, the random nature of the self-assembly process results in stochastic variations in the QD size, composition and concomitant optoelectronic properties. As discussed above, there has been considerable progress in the development of growth techniques to tailor the properties of the resulting QD distribution. To provide a perspective on such variations, the typical spread of ground state transition energies for our QD samples is $\sim 20\,\mathrm{meV}$, corresponding to a $1\,\%$ variation in QD size. The advantages of SAQDs are accompanied by the challenges associated with learning to control fragile quantum states in a solid state environment, where qubits can lose coherence due to interactions with defects, coupling to phonons, and many body effects. Schemes designed to mitigate these effects have been developed [33, 34, 35, 36, 37] and will be critical to storage and processing of quantum information in these systems.

To describe the response of an InAs/GaAs SAQD to laser excitation, the nature of the confined quantum states of the relevant valence and conduction bands must be taken into account. For a III-V semiconductor like InAs or GaAs, the optical properties are governed by the top three valence bands and the lowest conduction band. These bands are derived from the bonding and antibonding states of the GaAs molecule. The three valence bands are referred to as the heavy-hole, light-hole, and spin-orbit split-off bands (see Fig. 1.3(a)). The extrema of the heavy-hole and light-hole bands are degenerate in the bulk semiconductor. The edge of the spin-orbit split-off band occurs at lower energies due to the spin-orbit interaction. The names “heavy-hole” and “light-hole” refer to the differing curvature of these bands,

which determines a different effective mass for carriers in each band. Quantum confinement in the quantum dot leads to the discretization of each of the three valence bands and the conduction band into associated confined levels. The strain present in the quantum dot as a result of the self-assembly process, together with the larger effective mass of the heavy-hole band in comparison to the light-hole band, has the consequence that the confined heavy-hole states are the highest in energy of all of the valence states in the QD. As a result, the lowest-energy optical transitions in the quantum dot are between the heavy-hole and conduction states, such that we can restrict our attention to the heavy-hole and conduction levels only. (More details regarding the influence of other valence levels will be discussed in Ch. 2.)

The optical selection rules of an SAQD are dictated by the optical selection rules of the associated bulk crystal, which are in turn determined by the orbital and spin angular momenta of the band states. The three valence bands are characterized by an orbital angular momentum $l = 1$, while the conduction band has an orbital angular momentum of $l = 0$. The spin state of the carrier in one of these bands is determined by the total angular momentum, including both orbital angular momentum and spin. For the conduction band, the total angular momentum is $j = 1/2$, and there are two spin projections with $m_j = \pm 1/2$. For the heavy-hole band, the total angular momentum is $j = 3/2$, and the corresponding "spin" states have $m_j = \pm 3/2$. The optical selection rules involving the heavy-hole and conduction levels in the quantum dots are depicted schematically in Fig. 1.3(b). The dipole matrix elements for these transitions are circularly-polarized. As a result, circularly-polarized light excites carriers (both electrons and holes) with a single spin projection.

1.2 Realizing Qubits in SAQDs

States confined in the potential well of an SAQD can be used to create a qubit. Consider an electron (with spin angular momentum $m_j = 1/2$) that is optically excited to the conduction band using a circularly-polarized σ_- photon, creating a hole in the heavy hole valence band (with angular momentum $m_j = -3/2$). (Note: The spin projections in Fig. 1.3(b) indicate electron states. The corresponding hole

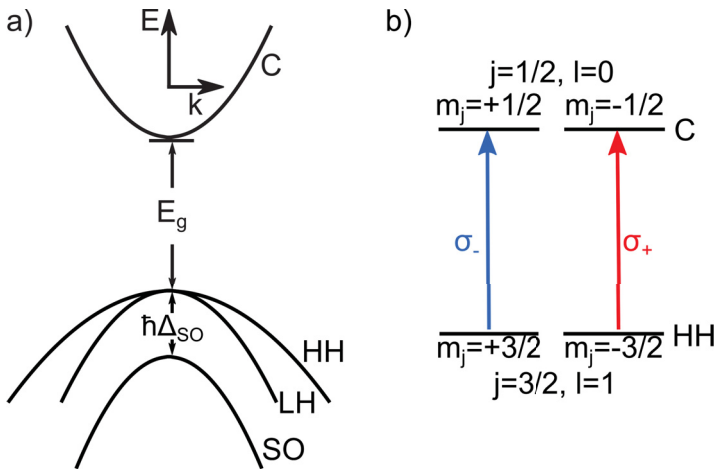

Figure 1.3: (a) Schematic of the band structure for GaAs in the vicinity of the band gap, with C band, HH band, LH band, and SO band. E_g is the band gap energy and $\hbar\Delta_{\mathrm{SO}}$ is the split-off energy. (b) Optical selection rules for zone-center transitions between the heavy-hole band and the conduction band. The angular momentum of the states and the polarizations of the transitions (right- or left- circularly polarized, denoted by $\sigma_{\pm}$) are indicated.

spin projections are opposite of the electron spin that was removed from he valence level.) Confinement and Coulomb interactions results in the creation of a bound two-particle state of the electron and hole called the exciton. The absence or presence of this exciton state can be used to form a qubit. A qubit can also be realized using the absence or presence of an exciton with opposite spin (composed of an electron with $m_j = -1/2$ and a hole with $m_j = 3/2$). Alternatively, in the presence of a static magnetic field $\mathbf{B} = B_0\hat{z}$ it is possible to use the projection of a carrier spin as the qubit (*e.g.* $m_j = \pm 1/2$ if the carrier is a conduction band electron or $m_j = \pm 3/2$ if the carrier is a hole in the heavy hole band).

Theoretical proposals to encode qubits in SAQDs that can be manipulated by light include charge-based qubits based on the absence or presence of an exciton [38, 39, 40], spin-based qubits that use the spin states of single carriers (electron or hole) split by a magnetic field [41, 42, 43, 44, 45], and hybrid approaches that use exciton qubits for computation and spin qubits for information storage [46]. This thesis work concerns the optical control of exciton qubits. A description of this type of qubit is introduced in the next section. To provide a complete perspective of the use of SAQDs in quantum computing, spin-based qubits are also described in the subsequent section.

Exciton Transitions in Neutral QDs

The optoelectronic properties of an SAQD are determined by the constituent atoms, as described above, as well as the symmetry of the QD. QDs with different symmetry (*e.g.* round or elongated in the plane of the QD layer) may be achieved by varying the growth conditions. The energy level diagram for optically-allowed exciton transitions in a cylindrically symmetric, lens-shaped QD is shown in Fig. 1.4(a). The crystal ground state (*i.e.* no excitons) is indicated by the state $|00\rangle$. The two degenerate, orthogonally spin-polarized exciton states $|\uparrow\Downarrow\rangle$ and $|\downarrow\Uparrow\rangle$ are composed of a conduction band electron with spin-angular momentum $m_j = \pm 1/2$ (indicated as $\uparrow$ and $\downarrow$), and a heavy hole with angular momentum $m_j = \pm 3/2$ (indicated as $\Uparrow$ and $\Downarrow$). As discussed above, corresponding optical transitions exist associated with the light-hole band, however, due to strain and quantum confinement, the lowest confined hole levels have heavy-hole character. Therefore, we will restrict our attention to the heavy-hole to conduction transitions. The single exciton states of each spin species ($\uparrow\Downarrow$ and $\downarrow\Uparrow$) are optically coupled to the bound biexciton state $|\uparrow\Downarrow\downarrow\Uparrow\rangle$ and the energy required to create the second exciton is reduced by the binding energy of the biexciton, $\hbar\Delta$. This allows for the transitions to be selectively addressed using pulse energy and polarization to distinguish between them, and therefore either ground state to exciton transition can be used as a qubit.

InAs QDs grown on the (001) surface of GaAs under the most typical growth conditions have been observed to have a truncated pyramidal structure that is *asymmetric*, with their long and short axes aligned along the $[110]$ and $[1\bar{1}0]$ directions in the plane of the quantum dots, respectively [47]. The broken symmetry results in eigenstates that are symmetric and antisymmetric combinations of the spin polarized exciton states: $|01\rangle = (|\uparrow\Downarrow\rangle - |\downarrow\Uparrow\rangle)/\sqrt{2}$ and $|10\rangle = (|\uparrow\Downarrow\rangle + |\downarrow\Uparrow\rangle)/\sqrt{2}$. The electron-hole exchange interaction lifts the degeneracy of the exciton states with a fine structure splitting of $\hbar\delta \approx 100\,\mu\mathrm{eV}$ [25]. The resulting optical selection rules are shown in Fig. 1.4(b). The orthogonal exciton eigenstates are coupled by light that is polarized linearly, along each of the long (x) and short (y) axes of the QD. For asymmetric dots, the crystal ground state and one of the exciton states can be used as a qubit. Due to the coupling to the biexciton states, such a qubit scheme requires a narrow bandwidth pulse to enable selective excitation of each species of

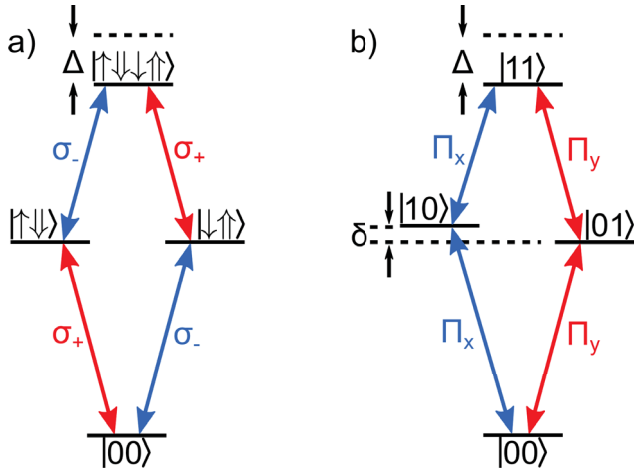

Figure 1.4: Energy level diagram and optical selection rules for excitons confined to: (a) spherically symmetric QDs, and (b) elongated (asymmetric) QDs. For symmetric QDs, the exciton states ($|\uparrow\Downarrow\rangle$, $|\downarrow\Uparrow\rangle$) are degenerate and the transitions are coupled by circularly polarized light ($\sigma_{\pm}$). The binding energy of the biexciton state ($|\uparrow\Downarrow\downarrow\Uparrow\rangle$) is $\hbar\Delta$. For elongated QDs, the transitions are linearly polarized ($\Pi_{x,y}$) and the exciton states are symmetric and antisymmetric superpositions of $|\uparrow\Downarrow\rangle$ and $|\downarrow\Uparrow\rangle$, denoted by $|10\rangle$ and $|01\rangle$, respectively.

exciton. Selective excitation may also be achieved using pulse shaping techniques, as discussed in one of the topics of this thesis work.

QDs that possess cylindrical symmetry are of interest for the generation of entangled photon pairs [30] while QDs with broken symmetry can find application as single photon sources [48]. Either level scheme can be used to realize a controlled-rotation (C-ROT) gate using two qubits in the same QD [39, 38].

Spin-based Qubits in Charged QDs

The spin states of a single carrier (electron or hole) confined to a QD can also be used as a qubit. They can be implemented using charged QDs which contain one excess electron or hole due to doping and/or the application of a bias using a gate. A magnetic field is applied to generate a Zeeman splitting between the spin eigenstates of the built-in electron or hole. For optical control there are two geometries of interest: (i) the Faraday geometry, where the external magnetic field is parallel to the growth and optical axis (z), and (ii) the Voigt geometry, where the magnetic field is applied in plane (x), perpendicular to the growth and optical axis. The energy level diagram for the case of a negatively-charged QD in the Faraday

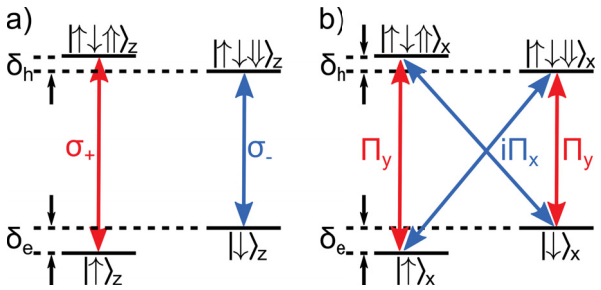

Figure 1.5: Energy level diagram and optical selection rules for spin states in (a) the Faraday geometry, and (b) the Voigt geometry for a QD charged with an electron. In the Faraday geometry, the external magnetic field is parallel to the growth direction (labelled z), resulting in circularly polarized transitions ($\sigma_{\pm}$) between the electron spin states ($|\uparrow\rangle_z$, $|\downarrow\rangle_z$) and the trion states ($|\uparrow\downarrow\Uparrow\rangle_z$, $|\uparrow\downarrow\Downarrow\rangle_z$). The states are split by the Zeeman energy $\hbar\delta_{\mathrm{e,h}}$. In the Voigt geometry, the magnetic field is perpendicular to the growth direction ($\mathbf{B} = B_0\hat{x}$) and the spin states are aligned with the x axis. The electron spin states ($|\uparrow\rangle_x$, $|\downarrow\rangle_x$) are coupled by linearly polarized light ($\Pi_{x,y}$), forming a double Λ system.

and Voigt geometries are shown in Fig. 1.5(a) and (b), respectively. Corresponding diagrams exist for positively charged QDs, but for illustrative purposes we will focus on negatively charged QDs here. The external magnetic field, B_{ext}, generates a Zeeman splitting $\hbar\delta_{\mathrm{e,h}} = \mu_B g_{\mathrm{e,h}} B_{\mathrm{ext}}$ of the electron (hole) states, where μ_B is the Bohr magneton and g_{e} (g_{h}) is the Landé g-factor. In both the Faraday and Voigt geometries, optical control of the spin state of the individual carrier is realized by using the optical transition from the single carrier state to a trion state. A trion is a charged exciton, composed of an electron-hole pair and an additional carrier (hole or electron). In the Faraday geometry, each spin state is optically coupled to a trion state by circularly polarized selection rules, whereas in the Voigt geometry, the spin states are coupled by linearly polarized light to each other via a trion state, forming two Λ systems. The methods used for spin initialization and for coherent control differ for the two geometries, as described in Sec. 1.4.3.

1.3 Experimental Characterization and Optical Control Techniques

1.3.1 Characterization of QD Optical Transitions

Prior to use in coherent control experiments, the QDs of interest must be characterized to determine the electronic structure of the relevant confined states. The

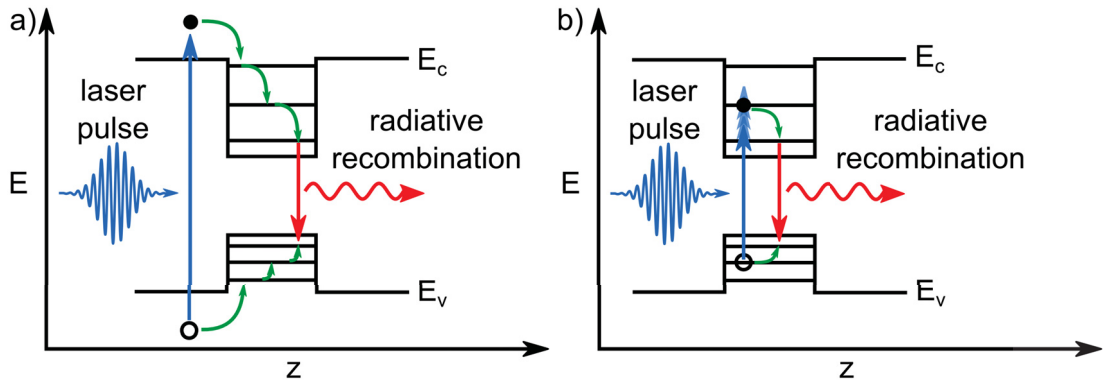

Figure 1.6: Excitation scheme for (a) PL spectroscopy, and (b) PLE spectroscopy. The horizontal axis denotes the growth direction and the vertical axis indicates increasing energy. For PL spectroscopy, the laser pulse excites carriers in the surrounding matrix material, some of which are captured by the QD. When electrons and holes recombine, the emitted PL identifies the transition. In the case of PLE spectroscopy, the excitation wavelength is scanned across an excited state transition while monitoring the PL emitted from the ground state transition. If the excited state decays into the ground state, a peak in the PL will be observed when the excitation laser is resonant with the excited state.

transition energies can be determined using photoluminescence (PL) spectroscopy, as depicted in Fig. 1.6(a). The excitation source, which can be pulsed or continuous-wave, is tuned above the band gap of the semiconductor material surrounding the QD (also referred to as the barrier material), exciting carriers that subsequently relax into the discrete states of the QDs. The PL emitted from the recombination of electron hole pairs is spectrally resolved to identify the transitions of interest.

The transition energy of excited states that decay to a ground state can be identified using photoluminescence excitation (PLE) spectroscopy (see Fig. 1.6(b)), where the frequency of the excitation laser is swept through the resonance of the excited state while measuring the PL intensity emitted from the ground state. The laser wavelength corresponding to the maximum in ground state PL intensity identifies the excited state transition.

1.3.2 Methods of Quantum State Readout

A number of experimental techniques have been developed to monitor the occupation of the exciton state and demonstrate coherent control.

The approach taken in this work is to measure the incoherent photon emitted

from the *s*-shell exciton, following optical control of the *p*-shell exciton [49, 50, 51, 52]. This approach has also been used most extensively in the literature due to its relative simplicity. The associated excitation geometry is shown in Fig. 1.7(a). Photoexcited excitons in the *p*-shell decay non-radiatively into the *s*-shell [25]. The PL intensity from the subsequent radiative decay of the *s*-shell exciton provides a measure of occupation of the *p*-shell at the end of the laser pulse. The advantage of this technique is that the energy difference between the excited and ground state exciton, which is approximately $85\,\mathrm{meV}$ in our samples, allows for strong suppression of scattered laser light using a wavelength filter and monochromator. This simplification of the quantum state *readout* supports the primary focus of this work, namely the development of advanced optical quantum *control* techniques.

Other groups have used photocurrent measurements to measure the *s*-shell exciton occupation [53, 54]. The scheme used for photocurrent readout is depicted in Fig. 1.7(b). The quantum dots are embedded in a photodiode structure with a tunable voltage bias that controls the charge state of the QD and the tunnelling rate of the photoexcited carriers. An optically excited exciton in the QD is dissociated by the bias voltage and the constituent electron and hole tunnel into opposite contacts, resulting in a current. The total current measured for a given excitation pulse provides a measure of the occupation of the exciton state at the end of the excitation pulse. This method is highly efficient since there are few sources of loss for the detected current. Disadvantages of this method include a background signal that is proportional to the incident optical power and an inability to discriminate between carriers that tunnel from different states. This method of quantum state readout also has the important disadvantage that the exciton measurement by dissociation is destructive and therefore lowers the coherence time of the qubit being manipulated.

In resonance fluorescence, the laser pulse is resonant with the *s*-shell exciton from which photon emission is detected after radiative decay. The corresponding geometry for quantum state readout is shown in Fig. 1.7(c). The challenge is to measure the single photon emitted from the QD in the presence of the intense scattered laser light at the same wavelength. A number of methods have been developed in recent years to aid in discrimination between the PL emitted from

the QD and the incident pump light. These include detection at an orthogonal polarization to the excitation source, and using a laser beam that is incident on the sample at a large angle such that a spatial filter can be used [55]. Recent techniques have also used excitation on the edge of the semiconductor wafer in which the QD layer is contained in a vertical planar microcavity. In this case the PL is detected normal to the surface [56].

For quantum dot ensembles the most widely used method for detecting the exciton occupation or spin is time-resolved pump-probe spectroscopy. A schematic showing this detection scheme is provided in Fig. 1.7(d). An intense pump pulse is used to excite the exciton, and the subsequent temporal dynamics of the exciton state can be monitored by measuring the optical properties of a weak probe pulse as a function of the delay between the pair of pulses. The change in intensity of the transmitted probe pulse provides information about the exciton occupation in the QD, while the change in probe polarization can be used to infer the exciton spin polarization. For measurements in QD ensembles, the small change in the optical properties of the probe pulse caused by excitons in each QD is easy to detect and so this approach has been used extensively [57, 58, 59, 60, 61]. For single QDs, this technique is quite challenging due to the low optical signals involved. This technique was used by Stievater *et al.* to demonstrate Rabi rotations in the *s*-shell of a single GaAs IFQD [15]. In this measurement, the large optical dipole moment of the IFQD studied aided in the observation of the change in transmission caused by the exciton occupation. The extension of this technique to SAQDs that have a smaller optical dipole moment is a challenging proposition. It was nevertheless recently achieved using a phase-sensitive homodyne detection technique [62].

1.4 Coherent Control of Qubits in SAQDs

This section provides an overview of methods of coherent control of fundamental quantum states in semiconductor quantum dots, including a summary of past experimental demonstrations. This thesis work is focused on the optical control of excitons, however, approaches for controlling spin-based qubits are also summarized to give a broader view of the field of quantum control in QDs. The physical processes that cause dephasing of each type of qubit are also highlighted.

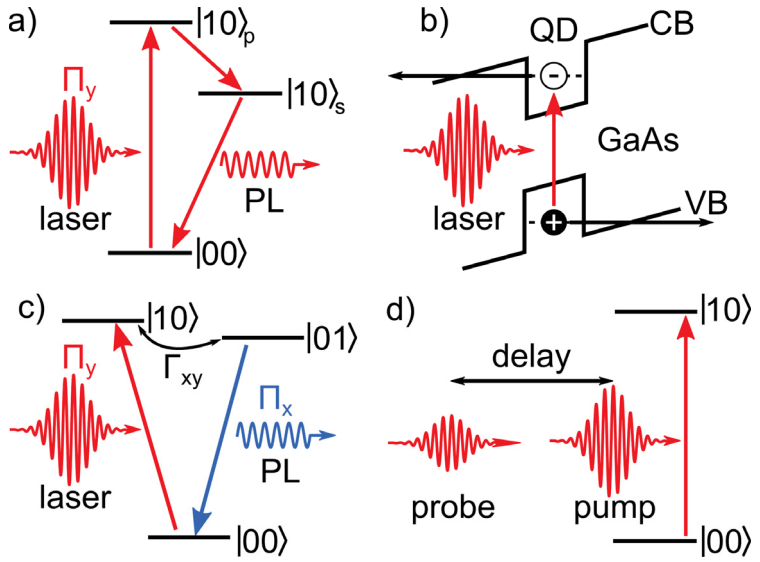

Figure 1.7: Exciton detection schemes: (a) *p*-shell excitation and *s*-shell detection. The excited state decays non-radiatively into the *s*-shell exciton state. The PL from subsequent radiative recombination is detected. (b) Band structure of the sample under a bias voltage for photocurrent detection. The exciton is optically excited in the s-shell. The sloping bands cause exciton ionization and result in the carriers tunnelling out of the QD, producing a current that can be measured. (c) In resonance fluorescence measurements, the excitation and detection both occur on the s-shell transition. One approach to suppressing the scattered pump light is to excite and detect on the orthogonally polarized transitions. In this case, a polarizer may be used to suppress the pump light. Spin-flip scattering at a rate Γ_{xy} populates the orthogonal exciton state that decays radiatively. (d) For pump-probe measurements, the probe measures the pump-induced change in the probe pulse optical characteristics (intensity, polarization) as a function of the delay between the pump and probe pulses.

1.4.1 Exciton Qubit Control

Rabi Rotations

The dynamics of a qubit under the influence of a strong driving field can be described in terms of the motion of the Bloch vector, $\mathbf{U}$, defined as $\mathbf{U} = (u, v, w) = (2\,\mathrm{Re}\{C_0 C_1^*\},\ -2\,\mathrm{Im}\{C_0 C_1^*\}, |C_1|^2 - |C_0|^2)$ on the Bloch sphere (see Fig. 1.1(b)). Lines of longitude are lines of constant phase difference between states $|0\rangle$ and $|1\rangle$, *i.e.*, a fixed value of ϕ. The lines of latitude mark lines of constant inversion ($|\sin(\theta)|^2 - |\cos(\theta)|^2$), determined by the difference in occupation of states $|1\rangle$ and $|0\rangle$. Under the influence of an optical control field, $\mathbf{U}$ rotates about a torque vector

defined by the driving field with components $\mathbf{\Lambda} = (-\mathrm{Re}\{\Omega_R\}, -\mathrm{Im}\{\Omega_R\}, \Delta)$, where $\Delta = \omega_{10} - \omega_l$ is the detuning of the laser field from the transition, $\Omega_R = \mu E_0(t')/\hbar$ is the Rabi frequency, μ is the dipole moment of the transition and $E_0(t)$ is the electric field strength of the light field. Therefore, the qubit can be manipulated by applying a laser field to rotate the Bloch vector to a desired final state. The dynamics of the Bloch vector, *i.e.* the rotation axis and speed of rotation, will depend on the instantaneous phase, amplitude, and detuning of the electric field. For example, laser light that is resonant with the $|0\rangle$ to $|1\rangle$ transition will rotate the Bloch vector about a fixed axis on the equatorial plane of the sphere. The angle through which the Bloch vector rotates is given by integral of the field amplitude, $\Theta(t) = \int_{-\infty}^{t} \mathrm{d}t'\, \Omega_R(t') = (\mu/\hbar) \int_{-\infty}^{t} \mathrm{d}t'\, E_0(t')$, and is called the *pulse area*. The resulting oscillations in the occupation of state $|1\rangle$ are called Rabi oscillations and the probability of being in the upper state is given by $|C_1|^2 = \sin^2[\Theta(t)/2]$.

Rabi oscillations were measured by Flagg *et al.* using a CW laser tuned to the exciton transition of a QD confined to a microcavity [63]. The exciton occupation was measured indirectly through the second-order correlation ($g^2(\tau)$) of the emitted photons (see Fig. 1.8(a)). The $g^2(\tau)$ intensity is proportional to the occupation of the exciton state at time τ after a photon has been emitted from the QD, which initializes the qubit in the crystal ground state. They found that the spacing of the peaks as a function of τ scaled proportionally with $\sqrt{P_{\mathrm{avg}}}$, as predicted by theory. A fit to the data is used to extract a relaxation time of $227\,\mathrm{ps}$ and a dephasing time of $132\,\mathrm{ps}$ for the qubit.

For pulsed laser sources, the total angle of rotation at the end of the pulse is $\Theta(\infty)$. There have been a number of demonstrations of pulsed Rabi rotations in recent years [15, 64, 53, 65, 19, 66, 67, 68, 69]. Figure 1.8(b) shows measurements of Rabi rotations of the exciton occupation as a function of the pulse area. The measurements were carried out by Ramsay *et al.* using the photocurrent detection technique [69]. Data taken at different temperatures, which are offset for clarity, show the effect of phonon-mediated dephasing. The red curves are fits to data using a theory that models excitation-induced dephasing associated with coupling to longitudinal acoustic (LA) phonons.

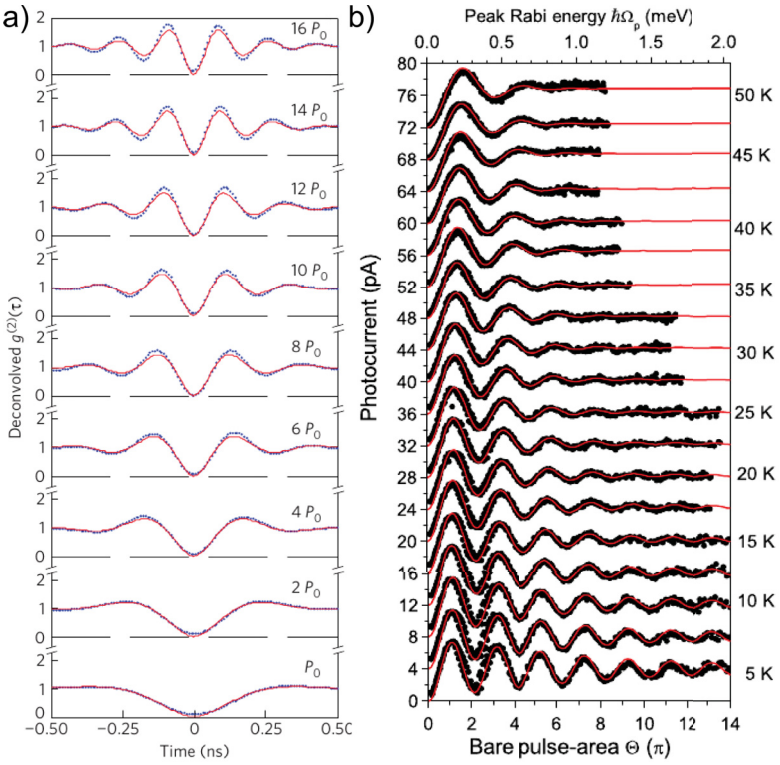

Figure 1.8: (a) Second order correlation, $g^2(\tau)$, of photons emitted from an SAQD driven by a CW laser field, for increasing laser power in multiples of P_0. The $g^2(\tau)$ intensity is proportional to the exciton occupation at time τ after the emission of a photon from the QD, which initializes the qubit in the $|00\rangle$ state. The lines are a fit to theory that provides a measure of the relaxation time $T_1 = 227\,\mathrm{ps}$ and a dephasing time of $T_2 = 132\,\mathrm{ps}$. Adapted with permission from Ref. [63]. Copyrighted 2009 by Macmillan Publishers Ltd: Nature Physics. (b) Photocurrent measurements of Rabi rotations of an exciton as a function of the pulse area. The red lines are a fit to theory that includes an intensity-dependent dephasing mechanism that is mediated by LA phonons. The curves for increasing temperature are offset for clarity. Adapted with permission from Ref. [69]. Copyrighted 2010 by the American Physical Society.

Multi-Axis Control of the Bloch Vector

Consecutive rotations about two different axes gives complete control of a qubit, providing the ability to target any desired final state. Typically, this is carried out using two pulses, resonant with the desired transition and separated by time τ using a path-stabilized Michelson interferometer that maintains a fixed relative phase between the pulses. If the first pulse rotates the Bloch vector about the $\hat{\mathbf{x}}$ direction, the second pulse, with a phase difference $\phi = \omega_l \tau$ will rotate the vector about the

$\cos(\phi)\hat{\mathbf{x}} + \sin(\phi)\hat{\mathbf{y}}$ direction. Such experiments are referred to as Ramsay interference measurements and can also be used to perform quantum-state tomography to determine the three components of the Bloch vector.

Multi-axis qubit control has been demonstrated in single QDs by a number of groups [49, 52, 70, 71, 72]. Figure 1.9(a) shows the results of Ramsay interference measurements for a *p*-shell exciton in a GaAs IFQD measured by Bonadeo *et al.* [49]. The exciton occupation is measured via the s-shell photoluminescence signal, which is detected as a function of the phase difference (ϕ), and the excited state occupation ($|C_1|^2$). The occupation oscillates as $|C_1|^2 = [1 + \cos(\phi)\exp(-\tau/T_2)]/2$, where T_2 is the transverse dephasing time of the qubit. By measuring the decay of the Ramsay interference fringe contrast as a function of τ, one can determine the dephasing time of the exciton in the QD. For example, a fit to the data in Fig. 1.9(a) gives a T_2 time of $40\,\mathrm{ps}$ for the *p*-shell exciton.

Wu *et al.* performed quantum state tomography on an exciton qubit in a GaAs IFQD, using differential transmission measurements to measure the occupation of $|1\rangle$ [20] (see Fig. 1.9(b)). They used a $\pi/2$ pulse to generate an equal superposition of the crystal ground state and an exciton state. A second delayed $\pi/2$ pulse was used to project the state onto the z axis and read out the u and v components of the Bloch vector.

Two-axis control can also be achieved using a resonant pulse that rotates the qubit about the x-axis, and a detuned laser pulse that rotates the Bloch vector about the z-axis via the ac- or optical-Stark effect [17]. Provided the detuning is much larger than the Rabi frequency, the change in occupation induced by the second pulse will be weak. Unold *et al.* [17] used differential reflectivity measurements in a GaAs IFQD to measure phase shifts up to π radians generated by the ac-Stark effect.

Quantum State Inversion Using Adiabatic Rapid Passage

The ability to implement a π gate with high efficiency is of importance for technologies such as ultrafast optical switches, and robust single- and entangled-photon sources. It is also of importance for dynamical decoupling schemes that mitigate

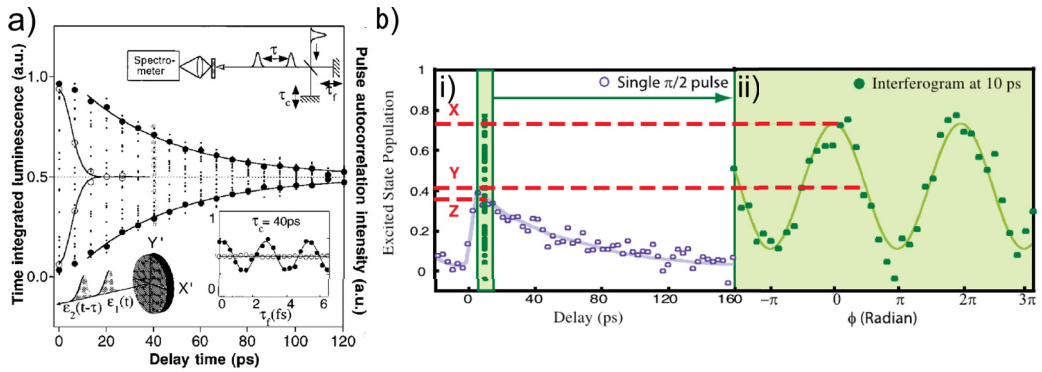

Figure 1.9: (a) Ramsay interference data obtained using excitation of a *p*-shell exciton in a GaAs IFQD by two phase-locked pulses. The black dots indicate the magnitude of the PL intensity as a function of delay τ between the pulses. The black curves are a fit to the maxima and minima of the interferogram, used to extract the dephasing time of the qubit. The top inset shows a schematic of the Michelson interferometer that generates the phase-locked pulses. The bottom left inset shows the pulse polarizations and delay. The bottom right inset shows an expanded view of the interferogram at a coarse delay of $40\,\mathrm{ps}$. Adapted with permission from Ref. [49]. Copyrighted 1998 by the American Association for the Advancement of Science. (b) Quantum state tomography on an exciton qubit in a GaAs IFQD. Plot (i) shows results of differential transmission measurements of the exciton occupation as a function of delay between the $\pi/2$ pump pulse and the weak probe pulse. Plot (ii) shows the interferogram taken at a pump-probe delay of $10\,\mathrm{ps}$ while changing the fine delay between the two phase-locked pump $\pi/2$ pulses. The horizontal lines are the projections on the z axis that allows for a read-out of the x and y components of the Bloch vector. Adapted with permission from Ref. [20]. Copyrighted 2006 by the American Physical Society.

dephasing of the exciton associated with coupling to the phonon bath. In these dynamical decoupling schemes, the exciton is subjected to rapid pairs of π pulses. An optical method of achieving a π gate is adiabatic rapid passage (ARP), which uses a frequency swept laser pulse to invert the qubit. In contrast to the control schemes discussed in the preceding subsections, for ARP the optical torque vector (and thus the axis about which the Bloch vector rotates) changes as a function of time as the relative magnitudes of the detuning and bare Rabi frequency change. It also differs in that the system remains in one of the instantaneous eigenstates as a function of time and evolves through an anticrossing. ARP has recently been demonstrated for an exciton qubit in a single InGaAs SAQD by two different groups [73, 74]. The experimental apparatus and photocurrent measurement results from Ref. [74] are

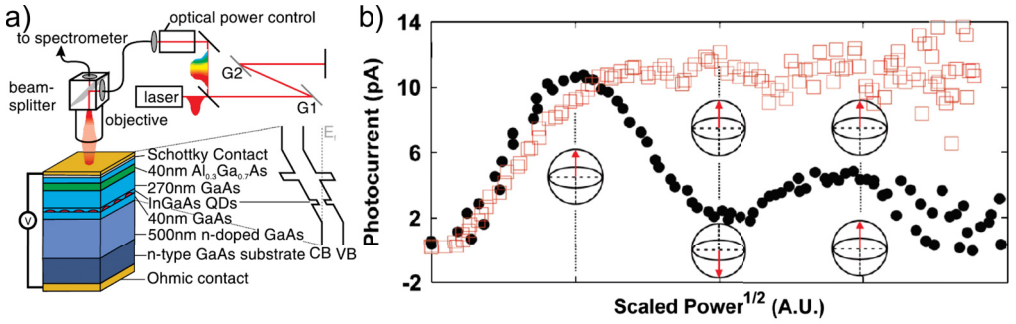

Figure 1.10: Demonstration of adiabatic rapid passage. (a) Schematic of experimental apparatus. The laser pulses are chirped using a grating pair and focused onto the QD that is embedded in a Schottky diode structure. The band diagram for the structure under bias is shown on the right. The photocurrent provides a measure of the exciton occupation. (b) Photocurrent measurements as a function of $\sqrt{P_{\rm avg}}$ ($\propto \Theta$) for a transform-limited pulse (black dots) and a chirped laser pulse (red squares). The orientation of the Bloch vector is indicated for a transform-limited and chirped laser pulse. Adapted with permission from Ref. [74]. Copyrighted 2011 by the American Physical Society.

shown in Fig. 1.10. The authors Wu *et al.* used a grating pair to chirp the laser pulse, *i.e.* introduce a time-dependent instantaneous frequency, and measured the exciton occupation for Rabi rotations and ARP as a function of pulse area using the photocurrent technique [74]. The signature of ARP is the insensitivity of the exciton occupation to pulse area beyond a threshold value. This insensitivity implies that the exciton inversion via ARP is robust to variations in laser power.

The evolution of the quantum state during ARP can also be described in the so-called *dressed states picture*, where the dynamics are expressed in terms of the instantaneous eigenstates of the system (QD + light), $|\Psi_+; N\rangle$ and $|\Psi_-; N\rangle$, that are split in energy by $\hbar|\mathbf{\Lambda}|$ as shown in Fig. 1.11(a). Observation of these Rabi split states in the frequency domain can be used to demonstrate strong-field coupling and the ability to control the exciton qubit. Figure 1.11(b) and (c) show two methods used to detect these states. For observation of the Autler-Townes doublet, a strong pump field creates the dressed states while a probe pulse monitors the absorption due to transitions from a witness state. In the case of the Mollow triplet, the transitions of interest are between dressed state manifolds that differ by one photon. The frequency of the probe pulse is swept to measure the absorption of the four transitions of interest: two that occur at ω_l and two that occur at $\omega_l \pm \Lambda$.

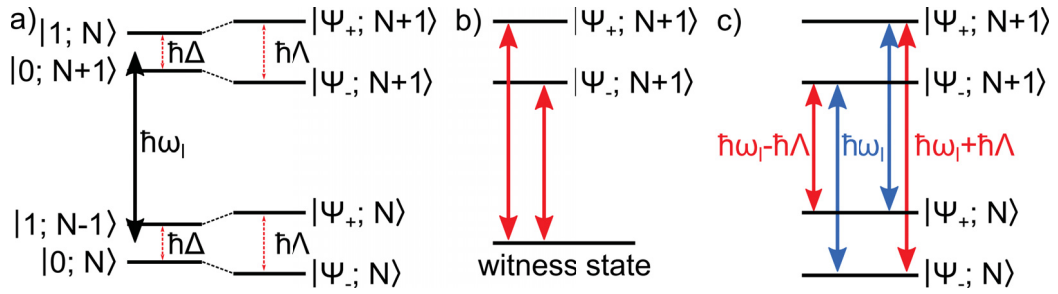

Figure 1.11: Rabi-split dressed states: (a) The dressed states with N photons, $|\Psi_{\pm}, N\rangle$, are split by $\hbar\Lambda$ where the effective Rabi frequency $\Lambda = \sqrt{\Omega_R^2 + \Delta^2}$, which is determined by the bare Rabi frequency, Ω_R, and the detuning of the pulse from the transition, Δ. Manifolds with different numbers of photons are split by ω_l. (b) Observed transitions for the Autler-Townes doublet are due to transitions from a witness state to the Rabi-split states. (c) Observed transitions for the Mollow triplet are due to transitions between the four states of manifolds that differ by one photon. Two of the transitions have the same energy, ω_l, so the absorption spectrum will have a peak ratio of $1:2:1$.

The Autler-Townes doublet and Mollow triplet have been observed for excitons confined to SAQDs [50, 75, 76, 77, 78, 79, 80]. The Autler-Townes doublet was first observed for the *p*-shell exciton [50]. It has since been demonstrated by: (i) pumping and probing the orthogonal exciton states [75], and (ii) pumping the exciton to biexciton transition while probing the ground state to exciton transition [76, 77, 78, 79]. The Mollow triplet was first observed in differential transmission measurements of an exciton in an InAs SAQD [75] but has since been observed in resonance fluorescence measurements in a InAs SAQD [80]. Figure 1.12(a) and (b) shows results of experimental measurements of the Autler-Townes doublet and Mollow triplet observed by Xu *et al.* [75]. In both measurements, the splitting between the states is observed to be proportional to $\sqrt{P_{\text{avg}}}$, as predicted by theory.

Conditional Operations

In addition to single-qubit operations, a universal circuit model quantum computer also requires pair-wise two-qubit logic operations such as C-ROT gates or C-NOT gates. Entangling operations can be demonstrated in the four-level system shown in Fig. 1.4(b) using the two orthogonally polarized excitons [38]. The C-ROT logic gate applies a π gate with a phase shift of π radians to the second qubit if and only

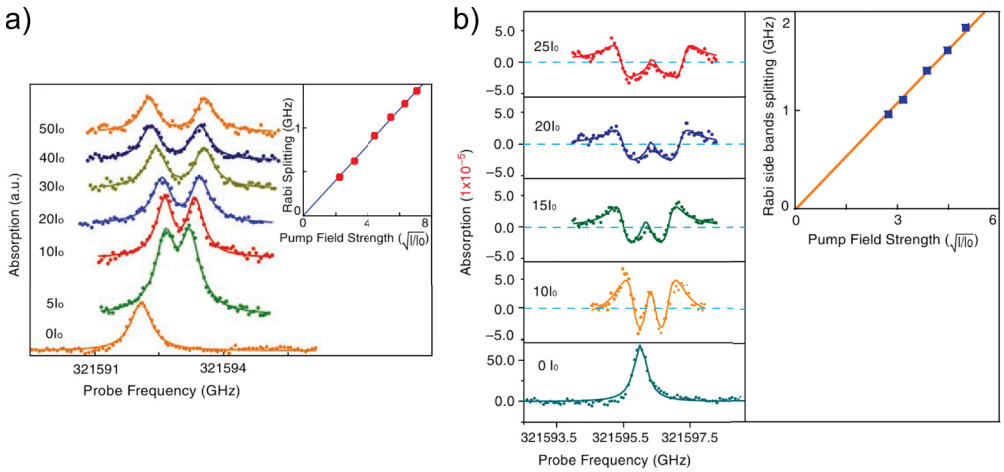

Figure 1.12: Observation of Rabi-split state in the frequency domain. A strong pump pulse creates the dressed states while a weak probe monitors the absorption of the transitions. (a) The Autler-Townes doublet observed on an exciton transition while probing the orthogonally-polarized exciton transition that shares the common ground state $|00\rangle$. (b) Mollow triplet observed for transitions between dressed state manifolds. The inset shows that the state splitting increases linearly with field strength. Adapted with permission from Ref. [75]. Copyrighted 2007 by the American Association for the Advancement of Science.

if the first qubit is in the $|1\rangle$ state. This operation was first demonstrated by Li *et al.* in a GaAs IFQD [16] using differential transmission methods and later in an InAs SAQD by Boyle *et al.* using the photocurrent measurement technique [81]. Figure 1.13(a) and (b) show the logic operation of the C-ROT gate and experimental results from Ref. [81], respectively. Pre-pulses (with a pulse area of π rad) were used to prepare the four pure qubit states and a spectrally narrow, Π_x polarized pulse was used to carry out the logic operation.

Other two-qubit demonstrations include Rabi oscillations between the crystal ground state and the biexciton state using a two-photon transition [82]. Biexcitons can be created sequentially by first exciting one of the exciton transitions, *e.g.*, $|00\rangle$-$|01\rangle$, followed by excitation of the exciton to biexciton $|01\rangle$-$|11\rangle$ transition. In contrast, the two-photon transition demonstrated in Ref. [82] creates two excitons simultaneously with a laser pulse with half the energy of the ground state to biexciton transition, *i.e.*, $\omega_l = \omega_{00-01} - \Delta/2$. The results in Fig. 1.14(a) and (b) show Rabi oscillations for the exciton and biexciton, highlighting the slower increase of biexciton population and a lower period of Rabi oscillation of the biexciton in comparison

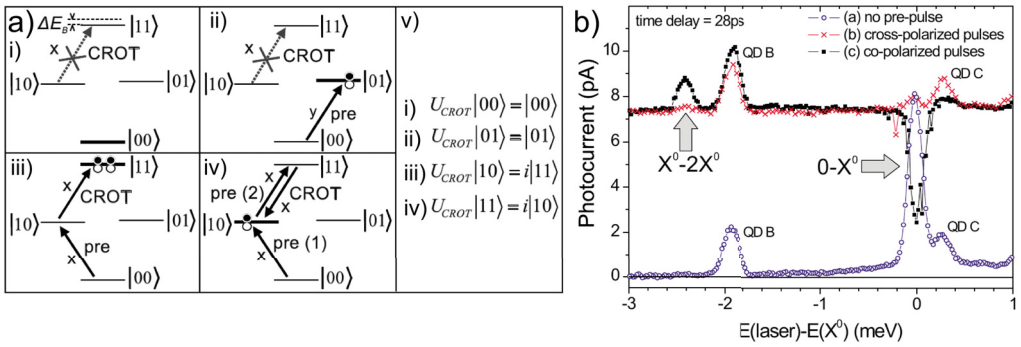

Figure 1.13: (a) Conditional logical for the C-ROT gate in the four-level exciton-biexciton system performed by an operational x-polarized laser pulse. (i) $|00\rangle$ is decoupled from the pulse due to the difference in energy. (ii) A pre-pulse initializes the system in the $|10\rangle$ state but is decoupled from the operational pulse due to the polarization. (iii) A pre-pulse initializes the system in the $|10\rangle$ state that is driven to the $|11\rangle$ state by the operational pulse. (iv) Two sequential pre-pulses are used to initialize the system in the $|11\rangle$ state that is driven to the $|10\rangle$ state by the operational pulse. (v) Action of the C-ROT operator on the four states. (b) Photocurrent spectrum as a function of the laser detuning for no pre-pulse (blue dots), cross-polarized pre-pulse (red x) and co-polarized pre-pulse (black squares). When the pulse is tuned to the $X^0 - 2X^0$ transition, photocurrent is only observed if a pre-pulse populates the X^0 state. In the absence of a pre-pulse or for a cross-polarized pre-pulse, there is no change to the system. (QD B and QD C are adjacent QDs not used in the demonstration.) Adapted with permission from Ref. [81]. Copyrighted 2008 by the American Physical Society.

to the Rabi oscillation of the exciton.

While the exciton-biexciton four-level system can be used to demonstrate two-qubit logic operations, a scalable architecture will require coupling between multiple, spatially distinct, uncoupled quantum dots. Proposals for extending C-ROT operations to excitons in different QDs have been presented [83, 84, 85] but have not yet been demonstrated experimentally. Coupling between qubits to enable conditional operations can be achieved via dipole-dipole interactions in the presence of a static electric field [83], through exchange of photons through a microcavity [42, 85], or through Coulomb interactions of closely spaced quantum dots [84].

1.4.2 Dephasing Times of Excitons

The number of gate operations that can be implemented on a qubit is fundamentally limited by the coherence time of the qubit. The coherence time of an exciton

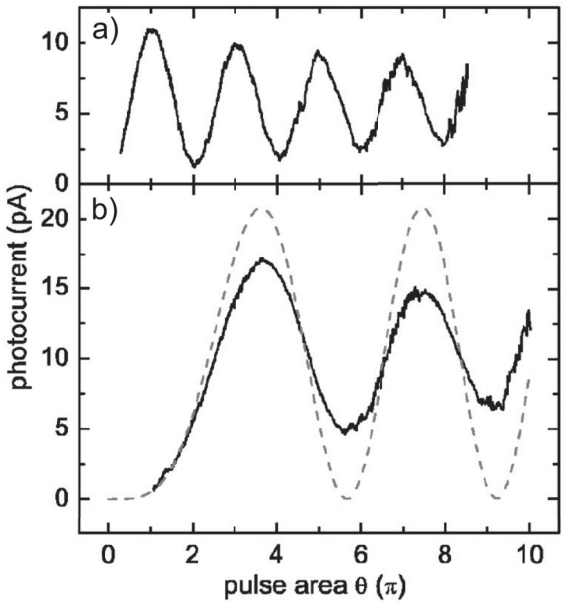

Figure 1.14: (a) Exciton Rabi oscillations measured in an InAs SAQD, using the photocurrent method of quantum state readout for the exciton, as a function of pulse area, and (b) two-photon Rabi oscillations in the same QD between the ground state and the biexciton state measured as a function of pulse area. The dashed line shows a theoretical curve for the two-photon process without taking into account any excitation-induced dephasing. Adapted with permission from Ref. [82]. Copyrighted 2006 by the American Physical Society.

at low temperatures is limited by the radiative lifetime of the electron-hole pair, with QD size-dependent dephasing times measured to be between 400 and $1000\,\mathrm{ps}$ [86, 87, 88]. Since laser pulses with shorter durations are readily available, the quality of the quantum control process on an exciton in a QD can be very high (*i.e.* the associated optical gate can be made to have a high fidelity) through the use of an ultrashort laser pulse for quantum state control. However, as the data in Fig. 1.8(b) indicates, the Rabi oscillations are also damped by a source of dephasing that depends on the driving field intensity (at a fixed pulse width). Such an intensity-dependent process is referred to as *excitation-induced dephasing*. There are two potential sources of intensity-dependent damping, including: (i) interactions with carriers in the wetting layer that are generated by crossed transitions [64], and (ii) interactions with longitudinal acoustic phonons [89, 90]. Recent experiments have confirmed the dominance of phonon-mediated dephasing for the *p*-shell and *s*-shell exciton [91, 54, 69]. The influence of such an excitation-induced

dephasing process on the quantum control of excitons may be minimized by using dynamical decoupling techniques [92, 46, 35]. Such techniques are effective provided that the time between π pulse is short compared to the correlation time associated with the phonons.

1.4.3 Spin Qubit Control

Qubit Control in Gate-Patterned QDs

The first proposal for QD-confined spin qubits envisioned their implementation in lateral QDs, where the electrostatic potential applied via patterned gates controls the strength of coupling between adjacent qubits [41]. The qubits were manipulated using electron spin resonance to drive Rabi oscillations via rf fields in the Faraday geometry. Single qubit operations including initialization, coherent control, and measurement [93, 94, 95, 96], and multiple-qubit operations have also been demonstrated [97, 98]. However, because the electrostatic potentials can only capture a single type of carrier, they do not permit optical control or conversion of spins to *flying qubits* (photons).

Optical Control Schemes for Spins in QDs

Spin qubits can be realized in charged SAQDs where the optically allowed transition to the trion state allows for state manipulation using optical pulses (see Fig. 1.5). Spin initialization in the Voigt geometry can be achieved using a vertically-polarized CW laser field that excites the trion state, which subsequently decays with equal probability into the spin-up and spin-down single carrier spin states. Continued pumping will shelve the spin state in the $|\uparrow\rangle_x$ state, where it is decoupled from the laser field (see Fig. 1.15(a)). In the Faraday geometry, one can use the same approach but it relies on small imperfections in the selection rules, which is a result of a spin-flip transition to the $|\uparrow\rangle_z$ state. Time-resolved detection schemes for single spins include Kerr and Faraday rotation, for which the change in polarization state of a linearly polarized probe pulse is measured. This change is caused by the difference in phase shift for the $\sigma_\pm$ components of the pulse and the polarization rotation

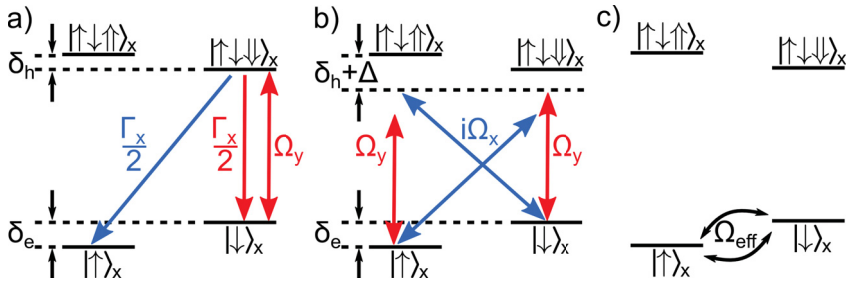

Figure 1.15: (a) Spin initialization and measurement in the Voigt geometry is carried out by continuously pumping one of the electron to trion transitions with a narrow CW laser. For initialization, the trion state will decay at a rate $\Gamma_x/2$ into the oppositely polarized spin state with 50% probability, where it will be decoupled from the laser pulse. For measurement of the state after manipulation, the steady state photon count indicates whether the system was in $|\downarrow\rangle_x$. (b) A broadband circularly polarized pulse, detuned from the trion transition by Δ, will couple the spin states via a stimulated Raman transition. (c) The coupling scheme in (b) decouples the trion states from the dynamics and allows for Rabi oscillations between the spin states at an effective Rabi frequency $\Omega_{\text{eff}} = |\Omega_{\text{H}}\Omega_{\text{V}}|/\Delta$.

can be measured using a polarizing beam splitter and balanced photodetectors. Alternatively, a steady state measurement of the spin state can be made by continuing to pump the system with the CW laser to create the trion state. The count rate of the emitted photons when the trion relaxes will then provide a measure of whether the system was in a spin-up or spin-down single carrier spin state prior to excitation.

In the Voigt geometry (see Fig. 1.5(b) and (c)), a circularly-polarized, detuned, broadband pulse can be used to couple the $|\uparrow\rangle_x$ and $|\downarrow\rangle_x$ states via a stimulated Raman transition. The circular polarization ensures that the probability amplitudes from the two Λ transitions add constructively, while the large detuning (Δ) prevents occupation of the trion states. The laser pulse can be used to generate rotations of the qubit about an axis in the x-y plane at an effective Rabi frequency ($\Omega_{\text{eff}} = |\Omega_{\text{H}}\Omega_{\text{V}}|/\Delta$). In conjunction with the Larmor precession about the z axis, this provides complete control over the qubit.

This approach to coherent control of spin qubits has been demonstrated by several groups [99, 100, 101, 102]. Figure 1.16(a) and (b) present experimental demonstrations of coherent control of the electron spin by Press *et al.* in Ref. [99]. Figure 1.16(a) shows Rabi oscillations of the electron spin state occupation as a

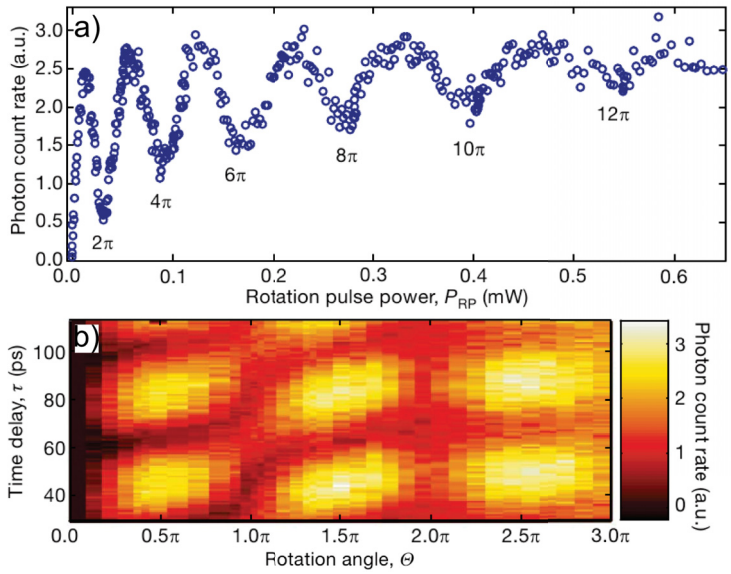

Figure 1.16: (a) Rabi oscillations of electron spin states measured in an InAs SAQD, where the quantum state readout of the electron spin state was achieved by measuring the photon count rate on the associated trion transition for increasing pulse area. The variation of the power required for successive rotations of the Bloch vector associated with the spin qubit varies due a breakdown of the two-level model when the occupation of the trion state become non-negligible. (b) Ramsay interference measurements using two pulses. The plot is a colour map of the photon count from the trion transition as a function of the pulse area Θ and the delay time between the pulse pair. Adapted with permission from Ref. [99]. Copyrighted 2008 by Macmillan Publishers Ltd: Nature Letters.

function of pulse area, while Fig. 1.16(b) shows a contour plot of the spin state occupation as a function of the pulse area and the delay between two pulses used for optical control. Similar demonstrations have been made for control of hole spins in SAQDs [103, 104, 105].

Multi-qubit operations have also been realized involving spin-based qubits in charged QDs. These include exchange-coupled spin qubits controlled using a tunnel barrier between vertically stacked QDs [106] and an all-optical controlled-phase gate for electrons [106] and holes [107].

1.4.4 Dephasing of Spin Qubits in SAQDs

The primary dephasing mechanism for electron spin qubits in a semiconductor QD results from the contact hyperfine interaction with the fluctuating Overhauser field

of the nuclear spins, which in turn produces variations in the Zeeman splitting. Methods of mitigating dephasing via this process include: (i) polarizing the nuclear spins to reduce random fluctuations in the Overhauser field, and (ii) using a hole spin for which the *p*-shell nature of the wave function reduces overlap with the nucleus. In the first case, the distribution of the nuclear spin bath can be narrowed by pumping with circularly polarized light to generate a dynamic nuclear polarization, with demonstrations of up to $60\,\%$ net polarization [108]. In these systems, pure dephasing for electrons in SAQDs is on the order of $3\,\mu\mathrm{s}$ [109] while spin-relaxation times are on the order of $20\,\mathrm{ms}$ [58]. In the case of hole spins, the reduced overlap with the nucleus does reduce the hyperfine interaction, however it does not compensate for mixing between the light-hole and heavy-hole states, which increases dephasing. The decoherence time for a single hole spin in a QD has been measured to be $1.1\,\mu\mathrm{s}$ [110] and spin-relaxation times of $0.5\,\mu\mathrm{s}$ [103] have been measured.

1.5 Scope of the Thesis

In this section, the work carried out for this doctoral dissertation is placed in the context of past optical quantum control experiments in semiconductor QDs. A broad perspective of this context is provided in Sec. 1.5.1 followed by a more detailed discussion appropriate for each of the three topics covered in this thesis in Sec. 1.5.2-1.5.4. This is followed by a summary of the accomplishments within this thesis work in Sec. 1.5.5.

1.5.1 Thesis in Context of Existing Work

The previous sections highlighted experimental demonstrations of single- and two-qubit control in SAQDs. These demonstrations have, with the exception of ARP, used transform limited (TL) pulses, *i.e.* pulses with constant phase. The use of TL pulses to control the qubit restricts the dynamics to sequential rotations about fixed axes that lie in the equatorial plane of the Bloch sphere [49, 52, 70, 71, 20, 72, 111]. In addition, the control pulses have thus far been restricted to optical pulses with a duration of several picoseconds or longer so as to avoid unintended dynamics in nearby optical transitions. However, with the use of subpicosecond control pulses

and pulse shaping [112], this restriction may be alleviated since the laser pulse may be designed, taking into account the final state for all optical transitions simultaneously coupled by the laser pulse. The central idea is to manipulate the phase and amplitude of the control Hamiltonian, by shaping the phase and amplitude of the excitation laser pulse to achieve a desired final state of the exciton or spin of the quantum state in the QD at the end of the laser pulse. This form of control can also be used to replace multiple single-qubit and two-qubit quantum gates with a single transformation of a multi-qubit system by a shaped laser pulse, as in the case of complex instruction set quantum computing [6].

The science of controlling the evolution to bring a quantum system to a desired final state is called optimal quantum control (OQC) [113, 114]. This approach is now routinely used in the control of a variety of physical processes. It is particularly useful for intractable system Hamiltonians, where powerful adaptive feedback algorithms are employed, for example, to target specific pathways in chemical reactions [115, 116], detect molecular species while suppressing a background signal [117], and for the generation of high harmonics [118, 119]. OQC has also been employed to achieve high fidelity quantum gates for applications in quantum information processing in different qubit platforms. It has been used to optimize single- and multiple-qubit [120, 121, 122] gates in ion trap qubits, multiple-qubit gates in superconducting qubits [123], spin entanglement gates in nitrogen vacancies [124], and multiple-input AND gates in molecular qubits [7]. The work presented in this thesis aims to further the use of OQC and pulse shaping for exciton qubits confined to SAQDs.

1.5.2 Studies of Parallel Quantum Control in Multiple QDs

This thesis builds upon the recent experimental demonstrations of π and 2π parallel gates in uncoupled semiconductor QDs using a single laser pulse [125]. In that work, the controlling laser pulse was numerically optimized using OQC and then implemented experimentally in InAs SAQDs using control of the p-shell transition and detection of the s-shell PL [125]. Shaping enabled the achievement of differing occupations of the excitons in two different QDs (one ending in $|1\rangle$ and the other in $|0\rangle$) with high fidelity despite differing dipole moments and transition energies

in each QD. In this thesis work, I have shown using theoretical simulations that, in addition to population transfer to the poles of the Bloch sphere as was carried out in Ref. [125], OQC can also be used to target desired final states with arbitrary (prescribed) occupations and relative phases, provided the QDs have sufficiently different optoelectronic properties. The findings of this study suggest that more than 10 QDs may be controlled using a single laser pulse with a sufficiently complex phase functional, limited only be the energy resolution of the pulse shaping system. Quantum gates designed in such a manner could either be implemented directly in experiments, or improve the speed of convergence of experimentally optimized evolutionary algorithms by providing seeding candidates. The advances in ultrafast control of multiple qubit systems using a single shaped pulse (instead of several phase-locked pulses) should promote scalability in QD systems by reducing the laser resources and experimental infrastructure required to manipulate qubits.

This work has been submitted to Physical Review B, and the submitted manuscript is presented in Ch. 4.

1.5.3 Numerical Optimization of C-ROT Gate Using Femtosecond Pulse Shaping Techniques

In addition to single-qubit operations, I have also demonstrated that OQC can be used to numerically optimize the two-qubit C-ROT gate involving two excitons in a single QD. Having recently been demonstrated experimentally [16, 81], the C-ROT gate provides a useful test case that illustrates the effectiveness of pulse shaping as an approach to optimizing the fidelity and speed of elementary quantum control process involving semiconductor QD states. In recent theoretical work by Chen *et al.* [39], the C-ROT gate was numerically optimized using two phase-locked pulses. The associated proposed experimental scheme in the theoretical work by Chen *et al.* requires the use of stabilized delay lines and independent control over the bandwidth of the individual pulses. This proposed implementation is further complicated by the use of two separately optimized, synchronous laser sources as well as a stabilized Michelson interferometer. The approach taken in this thesis work differs in that it uses a single laser pulse, optimized using optimal quantum control and general pulse shaping techniques, to implement the gate. The goal of my project

was to develop general amplitude- and phase-shaping protocols that could be easily implemented with a single mode-locked femtosecond oscillator and a standard commercially available pulse shaping system. I designed numerically optimized pulses to implement the C-ROT gate in the four-level exciton-biexciton system of Fig. 1.4(b). The optoelectronic properties of the confined states were determined using strain-dependent $\mathbf{k}\cdot\mathbf{p}$ theory for realistic physical parameters of a SAQD. The theoretical results show that amplitude- and phase-shaping schemes provide considerable improvements in fidelity over TL pulses with similar gate times. The addition of dephasing to the theoretical model was found to have a minimal effect on the gate fidelity, reflecting the benefits of subpicosecond gate times. The results presented in this thesis work lay the groundwork for the implementation of pulse shaping in other quantum control processes, including two-photon Rabi rotations of biexcitons [126] and schemes for dynamical decoupling [92, 46, 35].

This work was published in Physical Review B (R. Mathew et al., Phys. Rev. B 84, 205322 (2011)). The associated manuscript is reproduced with permission in Ch. 5.

1.5.4 Robust State Inversion in a Single QD Using ARP

I have also employed femtosecond pulse shaping to: (i) experimentally demonstrate robust state inversion in SAQDs via ARP using chirped (frequency-swept) laser pulses with a subpicosecond time duration; and (ii) to gain insight into the role of phonons in dephasing of excitons in QDs through measurement of the dependence of the exciton inversion efficiency on the sign of the laser pulse chirp. Both of these goals were achieved using much shorter control pulses than in past demonstrations of ARP ($\sim$20 fold).

Fast and robust state inversion is of technological importance because it finds application in efficient single- and entangled-photon sources [48, 127], all-optical switches [128, 129] and quantum gates [130, 131, 132, 133, 134]. Building on demonstrations in atomic systems [135, 136], ARP was recently demonstrated in SAQDs [73, 74], representing a ground-breaking achievement, however, the control pulses were of duration 15–$40\,\mathrm{ps}$. In this thesis work, I used wide bandwidth control pulses to demonstrate ARP in a single QD experimentally using a subpicosecond

gate time. This achievement of a ~ 20 fold reduction in gate time is useful for quantum computing applications because it permits more optical operations within the decoherence time of the exciton. The demonstration of fast, high fidelity π gates will also be critical to future demonstrations of dynamical decoupling schemes that are designed to isolate the qubit from its environment [33, 34, 35, 36, 37], since a rapid succession of ultrashort π pulses are required for such schemes.

The role of phonons in dephasing of excitons in quantum dots has been the focus of considerable theoretical and experimental research in recent years [25, 69, 89, 137, 138, 139, 140, 141, 130, 142, 143, 144, 145, 129, 146]. The efficiency of inversion via ARP has been predicted to depend on the sign of the pulse chirp at low temperature due to the differing rates of phonon absorption and emission [139, 140, 138]. This theoretical prediction indicates that experimental demonstration of ARP with both signs of chirp would provide important new insight into the role of phonons in dephasing for exciton qubits. However, prior to this thesis work the demonstrations of ARP used only negative pulse chirp. Using femtosecond pulse shaping techniques I have observed, for the first time, the predicted difference in inversion efficiency for positively- and negatively-chirped pulses. The result has confirmed the dominance of phonon-mediated dephasing in SAQDs and demonstrated that these effects can be mitigated by the correct choice of the sign of the pulse chirp at low temperatures. In this work, I also showed through theoretical simulations of the quantum state dynamics incorporating excitation induced dephasing via LA phonons that phonon-mediated dephasing in the regime of strong (and rapidly-varying) Rabi energies persists for negative pulse chirp, suggesting that multiphoton emission and non-Markvoian effects play an important role.

This work was published in Physical Review B (R. Mathew et al., Phys. Rev. B 90, 035316 (2014)). The associated manuscript is reproduced with permission in Ch. 6.

1.5.5 Summary of Thesis Work

To summarize the contributions made in this thesis, I have used numerical pulse shaping and optimal quantum control to demonstrate that a single laser pulse can

be used to manipulate multiple uncoupled exciton qubits that are confined to different quantum dots. The results showed that it is possible to specify the phase and occupation of the different qubits, provided that the quantum dots could be distinguished by either their transition energy or dipole moment. The same approach was also used in theoretical simulations to demonstrate the C-ROT gate for two excitons confined to a single quantum dot, with realistic optoelectronic parameters that were obtained using $\mathbf{k}\cdot\mathbf{p}$ theory. The use of shaped pulses in this case improved the fidelity of the operation, compared to unshaped pulses with a similar pulse width. In both applications, the use of a single shaped pulse to control multiple qubits, in place of multiple phase-locked pulses, should promote scalability in QD systems. In the third project, I experimentally demonstrated adiabatic rapid passage for an exciton confined to an InGaAs QD, using pulses that are over an order of magnitude shorter than previous experimental demonstrations of this method of control in single QDs. Control over the sign of the pulse chirp also allowed for the observation of the theoretically predicted difference in inversion efficiency for positively- and negatively-chirped control pulses, and the concomitant identification of phonon-mediated dephasing as the dominant source of decoherence. Faster ARP gates will be of benefit to single- and entangled-photon technologies, and for future demonstrations of dynamical decoupling techniques in QD systems.

1.6 Structure of the Thesis

The outline of the thesis is as follows: Chapter 2 begins with a review of the theory of the optical control of exciton qubits in SAQDs, including pulse shaping approaches to the optimization of gate fidelity. Chapter 3 describes the experimental apparatus and methods used in this thesis work. Building upon recent experimental work [125], Chapter 4 presents the use of OQC to theoretically optimize simultaneous high fidelity single-qubit quantum gates in uncoupled QDs. This manuscript has been submitted to Physical Review B. Chapter 5 presents the results of OQC applied to the theoretical optimization of the C-ROT two-qubit gate in the exciton-biexciton system. This work was published in Physical Review B. Chapter 6 presents the use of ultrafast ARP to implement high fidelity π gates and includes both experimental

results and theoretical simulation incorporating LA phonon-mediated excitation-induced dephasing. The results were published in Physical Review B. Conclusions and future outlook are presented in Chapter 7.

Chapter 2

Background and Theory

Self assembled quantum dots are nanometer-sized semiconductor structures with abrupt material discontinuities. Confinement of charge carriers in these structures creates a discrete spectrum of energy states akin to an atom. However, in contrast to atoms, the spatial extent of the wave functions extends over tens of atoms, providing a dipole moment that is an order of magnitude larger. This enhanced light-matter interaction facilitates optical control of the quantum states using ultrafast optical pulses. The electronic and optical properties of the QDs can be tuned via their size and composition, both of which can be controlled through the growth process. The combination of atom-like spectra and tunability makes SAQDs useful for fundamental studies of light-matter interactions in a solid state environment. As a scalable architecture that can leverage existing semiconductor fabrication technologies, interact with photons, and operate at telecommunication wavelengths, QDs could also be used to implement qubits in a quantum computing platform. This chapter provides the theoretical background necessary to understand optical state manipulation in semiconductor SAQDs. Section 2.1 describes the fabrication technique used to create SAQDs. Section 2.2 discusses the electronic and optical properties of the bulk constituents. The effects of confinement on the optoelectronic properties are discussed in Sec. 2.3. Sec. 2.4 describes the use of strain-dependent $\mathbf{k}\cdot\mathbf{p}$ theory to calculate the energies and wave functions of the confined eigenstates. Sec. 2.5 provides an overview of coherent control techniques using ultrafast optical pulses, and Sec. 2.6 describes the theory of optimal quantum control of qubits using pulse shaping techniques.

2.1 Fabrication and Samples

The QD samples studied in this work were grown using molecular beam epitaxy (MBE), a growth technique used to fabricate high quality, single crystals. In MBE,

the constituent elements of the crystal are heated to their sublimation point, whereupon the evaporated atoms travel through an ultra-high vacuum and condense on a substrate. The long mean-free paths resulting from the ultra-high vacuum environment allows for submonolayer control of the deposition rates. SAQDs are formed by a growth process called Stranski-Krastanov (SK) growth as depicted in Fig. 2.1, where a lattice mismatch between the substrate and the deposited film makes it energetically favourable for the strained film to nucleate, forming nanoscale islands. For example, when an InAs film is deposited on a GaAs substrate, the strain induced by the $7\,\%$ lattice mismatch is relieved after a critical thickness (typically a few monolayers) by the nucleation of nanoscale islands with base dimensions on the order of 20–$40\,\mathrm{nm}$ and heights on the order of 5–$10\,\mathrm{nm}$. (The lattice constants for GaAs and InAs are $0.565325\,\mathrm{nm}$ and $0.60583\,\mathrm{nm}$, respectively, resulting in a compressive strain when a few monolayers of InAs is deposited onto a GaAs substrate.) SK growth is an inherently stochastic process, resulting in a distribution of the QD physical properties (dimensions, composition, and residual strain) and a concomitant distribution of its electronic and optical properties (transition energies and optical dipole moments). Cross-sectional scanning-tunnelling microscopy measurements of the structures have found that the InAs/GaAs nanostructures tend to form truncated pyramids with a graded stoichiometric composition that is indium rich in the center and gallium rich at the outer edges [47]. Capping the InAs QDs with GaAs serves to terminate the chemical bonds on the surface, which would otherwise provide an effective pathway for non-radiative carrier relaxation. The two-dimensional, graded, InGaAs layer that surrounds the dot is called the wetting layer, and can support delocalized states confined to two dimensions.

2.2 Electronic Structure and Optical Properties of III-V Semiconductors

The quantum dots studied in this work are composed of two direct band gap III-V semiconductors, namely GaAs and InAs, that possess a face-centered cubic (FCC) zinc-blende crystal structure (see Fig. 2.2(a)). The first Brillouin zone for this lattice and the high symmetry points and lines are shown in Fig. 2.2(b).

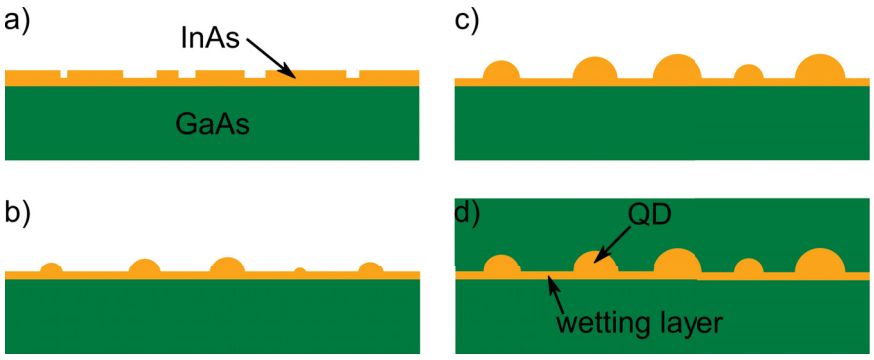

Figure 2.1: Stranski-Krastanov growth mode: (a) A few strained monolayers of InAs are deposited on a GaAs substrate. (b) After a critical thickness the strain is relieved by the formation of nanometer-sized islands on a thin layer of InGaAs called the wetting layer. (c) The quantum dots grow as more InAs is deposited, and (d) are capped with GaAs.

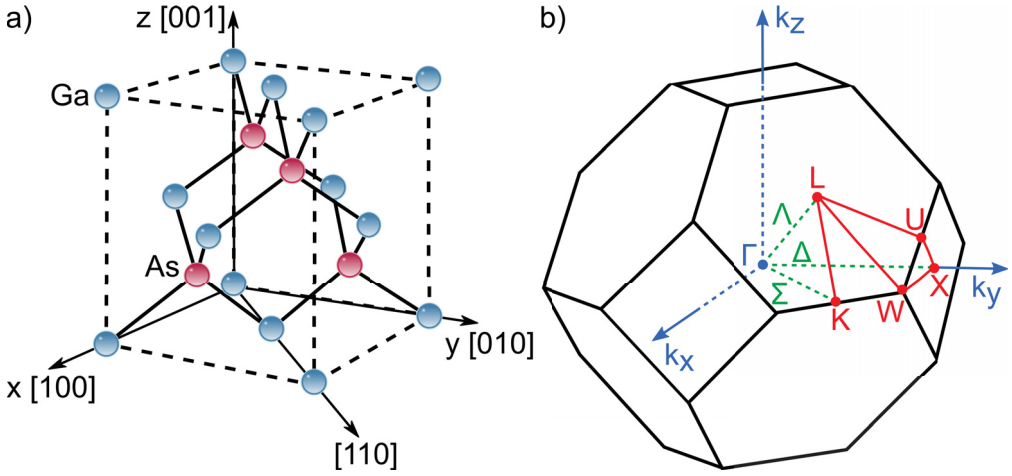

Figure 2.2: (a) FCC lattice structure for GaAs. The positions of the atoms (blue for Ga and maroon for As), the covalent bonds (black solid lines), and crystal directions are indicated. (b) The corresponding first Brillouin zone in reciprocal space. Γ denotes $\vec{k} = 0$ at the zone center. Other high symmetry points are indicated by Roman letters and the symmetry lines are indicated by Greek letters.

In a perfect semiconductor crystal, the potential $V(\mathbf{r})$ experienced by every electron in a band is identical and the Hamiltonian is given by,

$$\left[\frac{p^2}{2m_0} + V(\mathbf{r})\right]\psi_{\nu,\mathbf{k}}(\mathbf{r}) = E_{\nu,\mathbf{k}}\psi_{\nu,\mathbf{k}}(\mathbf{r}), \tag{2.1}$$

where m_0 is the rest mass of the electron, $\psi_{\nu,\mathbf{k}}(\mathbf{r})$ is the wave function, and $E_{\nu,\mathbf{k}}$ is the energy of an electron in an eigenstate denoted by the band ν and wave vector $\mathbf{k}$. The potential describes the ion cores and therefore exhibits the periodicity of the

lattice *i.e.*, $V(\mathbf{r}) = V(\mathbf{r} + \mathbf{R})$, where $\mathbf{R}$ is a lattice vector of the crystal. Therefore, the solutions to the Schrödinger equation take the form of Bloch functions,

$$\psi_{\nu,\mathbf{k}}(\mathbf{r}) = e^{i\mathbf{k}\cdot\mathbf{r}} u_{\nu,\mathbf{k}}(\mathbf{r}), \tag{2.2}$$

that are the product of a plane wave with wave vector $\mathbf{k}$, modulated by the cell function $u_{\nu,\mathbf{k}}(\mathbf{r})$, that also exhibits the periodicity of the lattice. The cell function represents the atomic part of the wave function and is different for each band. For example, in GaAs and InAs, the highest three valence bands, namely the HH, LH and SO bands, originate from bonding *p*-type orbitals while the lowest C band originates from an anti-bonding *s*-type orbital. A schematic of the band structure of GaAs near the Γ point is shown in Fig. 2.3(a) where each line denotes allowed energies and wave vectors for a single band. The valence and conduction bands are separated by a band gap, E_g, that results from Bragg scattering of the electron with the crystal lattice when its de Broglie wavelength is equal to twice the lattice spacing. In GaAs, the band gap at a temperature of $300\,\mathrm{K}$ is $1.42\,\mathrm{eV}$. InAs, on the other hand, has a smaller band gap of $0.35\,\mathrm{eV}$ at the same temperature. It is this difference in band gap energy, along with the band offsets for the conduction and valence bands, that allows for the confinement of carriers in InAs/GaAs QDs.

2.2.1 Band Edge States and $\mathbf{k}\cdot\mathbf{p}$ Theory

The nature of the states near the band gap has important implications for the electronic and optical properties of any semiconductor. InAs and GaAs exhibit direct band gaps, *i.e.*, the minimum of the conduction band occurs at the same wave vector as the maximum of the valence band (the Γ point at $\mathbf{k} = \mathbf{0}$), making it an excellent choice for optoelectronic devices that benefit from the enhanced coupling with light. $\mathbf{k}\cdot\mathbf{p}$ theory is a semi-empirical method for obtaining highly accurate solutions for the states and the energy dispersion near the band extrema. In this approach, the electron and hole states near the band edge are expanded in the complete basis of the zone-center cell functions $\{u_{\nu,0}(\mathbf{r})\}$ using perturbation theory. The Schrödinger equation for the cell function, is given by,

$$\left[\frac{p^2}{2m_0} + \frac{\hbar^2 k^2}{2m_0} + \frac{\hbar}{m_0}\mathbf{k}\cdot\mathbf{p} + V(\mathbf{r})\right] u_{\nu,\mathbf{k}}(\mathbf{r}) = E_{\nu,\mathbf{k}} u_{\nu,\mathbf{k}}(\mathbf{r}). \tag{2.3}$$

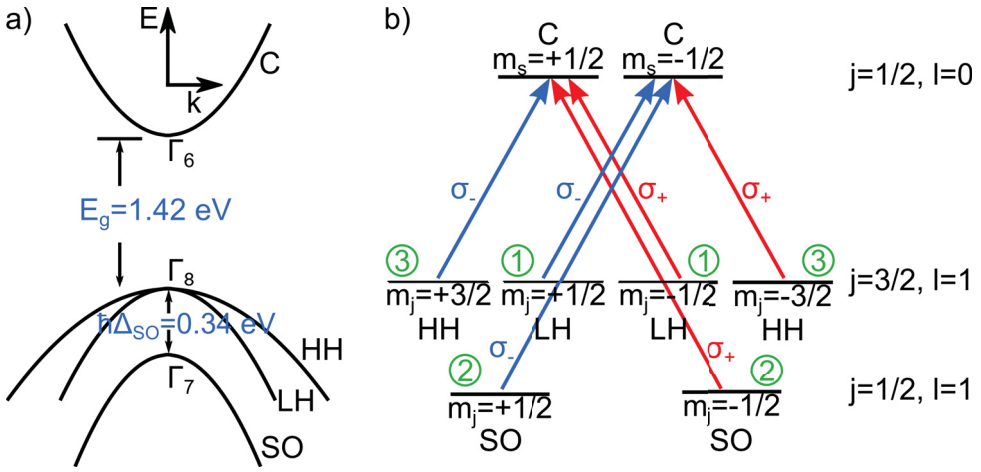

Figure 2.3: (a) Schematic of the band structure for GaAs in the vicinity of the band gap, with C band, HH band, LH band, and SO band. The band gap E_{g} and the split-off energy $\hbar\Delta_{\mathrm{SO}}$ at a temperature of $300\,\mathrm{K}$ are indicated. (b) Optical selection rules for zone-center transitions between the valence bands and the conduction band. The polarizations of the transitions are right- or left- circularly polarized ($\sigma_{\pm}$). The relative intensities, as determined by the Clebsch-Gordan coefficients, are indicated in circles.

For a non-degenerate band such as the lowest conduction band, the cell functions, to second order in perturbation theory, are given by,

$$u_{\nu,\mathbf{k}}(\mathbf{r}) = u_{\nu,\mathbf{0}}(\mathbf{r}) + \frac{\hbar}{m_0}\sum_{\nu'\neq\nu}\frac{\left|\langle\nu,\mathbf{0}|\,\mathbf{k}\cdot\mathbf{p}\,|\nu',\mathbf{0}\rangle\right|^2}{E_{\nu,\mathbf{0}}-E_{\nu',\mathbf{0}}}u_{\nu',\mathbf{0}}(\mathbf{r}). \tag{2.4}$$

For states away from $k=0$, the second term results in mixing of zone-center cell functions from other bands. The energy eigenvalues are given by,

$$E_{\nu,\mathbf{k}} = E_{\nu,\mathbf{0}} + \frac{\hbar^2k^2}{2m_0} + \frac{\hbar^2}{m_0^2}\sum_{\nu'\neq\nu}\frac{\left|\langle\nu,\mathbf{0}|\,\mathbf{k}\cdot\mathbf{p}\,|\nu',\mathbf{0}\rangle\right|^2}{E_{\nu,\mathbf{0}}-E_{\nu',\mathbf{0}}}. \tag{2.5}$$

Near the band extrema, the carriers move as if they were free particles with an effective mass m_ν^*, that encapsulates the interaction of the carriers with the lattice. This is called the *effective mass approximation* and the energies for the conduction and valence bands are given by,

$$\begin{aligned} E_{\mathrm{c},\mathbf{k}} &= E_g + \frac{\hbar^2k^2}{2m_c^*}, \\ E_{\mathrm{v},\mathbf{k}} &= -\frac{\hbar^2k^2}{2m_v^*}. \end{aligned} \tag{2.6}$$

Comparison with Eqn. 2.5 shows that electrons in the conduction band have an effective mass

$$\frac{1}{m_c^*} = \frac{1}{m_0} + \frac{2}{m^2 k^2} \sum_{\nu' \neq \nu} \frac{|\langle \nu, \mathbf{0}| \, \mathbf{k}\cdot\mathbf{p} \, |\nu', \mathbf{0}\rangle|^2}{E_{\nu,\mathbf{0}} - E_{\nu',\mathbf{0}}}. \tag{2.7}$$

In GaAs, conduction band electrons have an effective mass of $m_c^* = 0.063 m_0$ while holes in the valence band have an effective mass $m_v^* = 0.51 m_0$. To calculate the energies and wave functions for the degenerate valence bands, one must either use non-degenerate perturbation theory or approaches such as the Kane model where the Hamiltonian, which includes the spin-orbit interaction, is diagonalized in the finite basis consisting of the conduction band and the three highest valence bands. The approximation that the other bands can be ignored is assumed to be valid as their contribution decreases with increasing energy separation.

2.2.2 Angular Momentum and Optical Selection Rules

The discussion thus far has ignored the angular momentum of the states which dictates the optical selection rules. For each Bloch state, there are two allowed angular momentum projections, leading to two "spin" subbands for each band. The total angular momentum for an eigenstate of the crystal Hamiltonian is dictated by the total angular momentum of the cell functions that form the basis. As previously mentioned, the zone-center cell function for the conduction band has *s*-type symmetry, with orbital angular momentum quantum number $l = 0$, while the valence band has *p*-type symmetry, with an orbital angular momentum of $l = 1$.

Away from the Γ point, the mixing of the states implies that valence bands are not pure angular momentum states. The matrix elements of the dipole operator between states $|\nu, \mathbf{k}\rangle$ and $|\nu', \mathbf{k}'\rangle$ are given by,

$$\begin{aligned} d_{\nu,\nu',\mathbf{k},\mathbf{k}'} &= \langle \nu', \mathbf{k}'| \, (-e\mathbf{r}) \, |\nu, \mathbf{k}\rangle \, , \\ &= \frac{-i\hbar e}{m(E_{\nu,\mathbf{k}} - E_{\nu',\mathbf{k}'})} \langle \nu', \mathbf{k}'| \, \mathbf{p} \, |\nu, \mathbf{k}\rangle \, . \end{aligned} \tag{2.8}$$

For optical transitions, $\mathbf{k} \approx \mathbf{k}'$ because the photon has negligible momentum relative to the carriers, so that near the band edge the optical properties of the material are determined by the matrix elements of $\mathbf{p}$ between the zone-center cell functions,

given by,

$$d_{\nu,\nu',\mathbf{0},\mathbf{0}} = \frac{-i\hbar e}{m(E_{\nu,\mathbf{0}} - E_{\nu',\mathbf{0}})}\mathbf{p}_{\nu,\nu',\mathbf{0},\mathbf{0}}. \tag{2.9}$$

The resulting optical selection rules for transitions between the valence and conduction bands are illustrated in Fig. 2.3(b). The transitions are coupled to circularly polarized light ($\sigma_{\pm}$), as dictated by the angular momentum projections of the states and the relative intensities of transitions (indicated by the numbers in circles) are determined by the Clebsch-Gordon coefficients .

2.3 Effects of Confinement on Electronic and Optical Properties

The confinement of carriers to dimensions smaller than its de Broglie wavelength has profound consequences for the electronic and optical properties of the material. The SAQDs used in this work are droplets of InAs embedded in a GaAs matrix. Three-dimensional confinement of electrons and holes to dimensions smaller than its Bohr radius ($\sim 12\,\mathrm{nm}$ for electrons in GaAs) results in a discrete spectra, with energy level spacings greater than the average thermal energy $k_B T/2$, even up to room temperature. Figure 1.2(b) and (c) shows a simplified band structure diagram and schematic of an InAs/GaAs QD. Quantum dots are nanostructures containing on the order of 10^4 atoms with material discontinuities, so an accurate calculation of the energy levels and wave functions typically requires the use of computationally intensive methods such as eight-band, strain-dependent $\mathbf{k}\cdot\mathbf{p}$ theory with realistic models for the QD shape, size and composition. However, a qualitative understanding of the confined states can be developed using a series of approximations that reduce the complexity of the system, allowing for analytical solutions.

2.3.1 Envelope Functions

The first approximation is that the quantum dot, despite its reduced dimensions, can still be treated as a bulk sample insomuch as the potential experienced by electrons in a given band is still identical. The confined single-particle states can then be expressed in terms of the Bloch functions of Eqn. 2.2, such that,

$$\Psi_{\mathrm{sp}} = \sum_k C_{\nu,\mathbf{k}} e^{i\mathbf{k}\cdot\mathbf{r}} u_{\nu,\mathbf{k}}(\mathbf{r}). \tag{2.10}$$

This is known as the *envelope function approximation* and is valid when the dot dimensions are much larger than the lattice constant. It is also assumed that the cell functions have a weak $\mathbf{k}$ dependence such that Eqn. 2.10 can be expressed as,

$$\begin{aligned}\Psi_{\rm sp} &= u_{\nu,\mathbf{0}}(\mathbf{r}) \sum_k C_{\nu,\mathbf{k}} e^{i\mathbf{k}\cdot\mathbf{r}} \\ &= u_{\nu,\mathbf{0}}(\mathbf{r}) f_{\rm sp}(\mathbf{r}),\end{aligned} \tag{2.11}$$

where $f_{\rm sp}(\mathbf{r}) \equiv \sum_k C_{\nu,\mathbf{k}} e^{i\mathbf{k}\cdot\mathbf{r}}$ is the single particle *envelope function*. In the effective mass approximation, the envelope functions can be obtained by solving

$$\left[\frac{p^2}{2m^*} + V_{\rm eff}(\mathbf{r})\right] f_{\rm sp}(\mathbf{r}) = E f_{\rm sp}(\mathbf{r}), \tag{2.12}$$

where $V_{\rm eff}(\mathbf{r})$ is the effective potential seen by the carrier, and E is the energy of the state. The QDs in question are typically flattened lens- or pyramid-shaped structures with vertical dimensions that are smaller than the in-plane lateral dimensions. They have also been found to exhibit approximately equidistant energy spacings between excited states. Therefore, an appropriate choice for the confinement potential $V_{\rm eff}(\mathbf{r})$ is an infinite square well in the $\hat{\mathbf{z}}$ growth direction and a harmonic potential in the lateral plane of the dot, such that in cylindrical coordinates,

$$V_{\rm eff}(\mathbf{r}) = \begin{cases} \frac{1}{2}m^*\omega_0^2(x^2+y^2); & -L/2 \le z \le L/2 \\ \infty & \text{otherwise,} \end{cases}$$

where L is the height of the QD and $\hbar\omega_0$ is the energy spacing between harmonic oscillator states. The solution to Eqn. 2.12 is given by,

$$f_{\rm sp}(\mathbf{r}) = A H_{n_x}(x) H_{n_y}(y) \exp\left[\frac{-(x^2+y^2)}{2k^2}\right] \cos\left(\frac{\pi z}{L}\right), \tag{2.13}$$

where A is a normalization constant, H_n are the Hermite polynomials, and $k \equiv \sqrt{m^*\omega_0/\hbar}$. The corresponding energy levels are,

$$\begin{aligned}E_{n_x,n_y,n_z} &= E_{\text{in plane}} + E_z \\ &= \hbar\omega_0\left(n_x + n_y + 1\right) + \frac{\hbar^2 n_z^2}{8m^*L^2}.\end{aligned} \tag{2.14}$$

Due to strong vertical confinement, only the ground state excitation ($n_z = 1$) along the z-direction is found in the quantum dot. The wave functions are labelled using the nomenclature of atomic physics such that angular momentum eigenstates $l = 0$, ±1, ±2,... are labelled as s, p, d,..., respectively.

2.3.2 Optical Transitions

Excitation of QDs with laser pulses can create a bound exciton (electron-hole pair). In the *strong confinement approximation*, it is assumed that the contribution to the exciton binding energy resulting from the Coulomb interaction between the electron and hole, which scales as $1/L$, can be ignored when compared with the contribution from the confinement energy, which scales as $1/L^2$. This is valid for small dots where the quadratic term due to confinement dominates. This assumption implies that the two-particle state can be written as the product of the single-particle states. It is further assumed that the strain breaks the degeneracy between the heavy-hole and light-hole states to the extent that mixing between the two can be ignored, and the hole state can be written in terms of the zone center cell function $|u_{\rm h}\rangle \equiv |u_{\rm HH,\mathbf{0}}\rangle$, associated with the heavy hole. Written in Dirac notation, we have,

$$\begin{aligned} |\Psi_{eh}\rangle &= |\Psi_e\rangle\,|\Psi_h\rangle\,, \\ &= |u_{\rm h}\rangle\,|f_{\rm h}\rangle\,|u_{\rm e}\rangle\,|f_{\rm e}\rangle\,, \end{aligned} \tag{2.15}$$

where $|u_{\rm e}\rangle = |u_{\rm C,\mathbf{0}}\rangle$. In the two-particle picture, the probability for an optical transition is given by,

$$P = |\,\langle\Psi_{\rm eh}|\,\hat{\boldsymbol{\epsilon}}\cdot\mathbf{p}\,|0\rangle\,|^2, \tag{2.16}$$

where $\hat{\boldsymbol{\epsilon}}$ is the polarization vector of the light field and $|0\rangle$ is the crystal ground state, also called the vacuum state. In the single particle picture, this is equivalent to,

$$P = |\,\langle\Psi_{\rm e}|\,\hat{\boldsymbol{\epsilon}}\cdot\mathbf{p}\,|\Psi_{\rm h}\rangle\,|^2. \tag{2.17}$$

It is assumed that since the envelope functions vary slowly on the scale of a unit cell, the momentum operator only acts on the cell functions, giving,

$$\begin{aligned} P &= |\,\langle u_{\rm e}|\,\hat{\boldsymbol{\epsilon}}\cdot\mathbf{p}\,|u_{\rm h}\rangle\,|^2|\,\langle f_{\rm e}|f_v\rangle\,|^2, \\ &= \hat{\boldsymbol{\epsilon}}\cdot(\hat{\mathbf{x}}\pm i\hat{\mathbf{y}})\mu_{\rm eh}|\,\langle f_{\rm e}|f_v\rangle\,|^2, \end{aligned} \tag{2.18}$$

where $\mu_{\rm eh}$ is the dipole moment. As indicated in Fig. 2.3(b), transitions between the heavy-hole valence band and the conduction band are circularly polarized. However, for dots that do not possess rotational symmetry, the exchange interaction induces mixing of the angular momentum eigenstates, altering the selection rules as outlined in the following section.

2.3.3 Multi-Particle Interaction

Due to the strong spatial localization, the contribution of the direct Coulomb interaction to the binding energy is typically around $10\,\mathrm{meV}$ [147]. The exchange Coulomb interaction between the electron and hole is typically two orders of magnitude smaller and leads to the fine structure splitting of the exciton states. The Hamiltonian describing electron-hole exchange for an electron with spin S_e and a hole with spin J_h is given by [148],

$$H_\mathrm{exch} = -\sum_{i=x,y,z} \left(a_i \mathbf{J}_{\mathrm{h},i} \cdot \mathbf{S}_{\mathrm{e},i} + b_i \mathbf{J}^3_{\mathrm{h},i} \cdot \mathbf{S}_{\mathrm{e},i} \right). \tag{2.19}$$

The four exciton states can be labelled by the total angular momentum projections $M = S_{\mathrm{e},z} + J_{\mathrm{h},z}$. For an exciton formed by a conduction electron ($S_\mathrm{e} = 1/2$, $S_{\mathrm{e},z} = \pm 1/2$) and a valence heavy hole ($J_\mathrm{h} = 3/2$, $J_{\mathrm{h},z} = \pm 3/2$), the total angular momentum projection is either $M = |2|$ or $M = |1|$. The $|M| = 2$ states cannot couple to light that carries a spin-angular momentum of $\hbar$ and are therefore called "dark excitons", whereas the $|M| = 1$ states are optically active and called "bright excitons". The exchange interaction can be written in the exciton basis $\{|-1\rangle, |+1\rangle, |-2\rangle, |+2\rangle\}$ as

$$H_\mathrm{exch} = \frac{1}{2} \begin{pmatrix} +\delta_0 & \delta_1 & 0 & 0 \\ \delta_1 & +\delta_0 & 0 & 0 \\ 0 & 0 & -\delta_0 & \delta_2 \\ 0 & 0 & \delta_2 & -\delta_0 \end{pmatrix} \tag{2.20}$$

where $\delta_0 = -3/4(a_z + 9b_z/4)$, $\delta_1 = 3/8(b_x - b_y)$, and $\delta_2 = 3/8(b_x + b_y)$. The constants a_z, b_x, b_y, and b_z are material parameters The Hamiltonian is block diagonal in this basis, which means that there is no mixing between the bright and dark excitons but the interaction introduces a splitting between them of $2\hbar\delta_0$. For rotationally symmetric dots (D_{2d} symmetry), $b_x = b_y$, resulting in degenerate bright states and circularly-polarized selection rules (see Fig. 2.4(a)). (The splitting between the dark states, $\hbar\delta_2$, persists despite symmetry due to the exchange interaction.) However, for elliptical dots with broken symmetry, angular momentum is no longer a good quantum number and the eigenstates are symmetric and antisymmetric combinations of the two $|M| = 1$ states and split from each other by $\hbar\delta_1$ (which is on the order of $100\,\mu\mathrm{eV}$). The resulting eigenstates, are labelled $|10\rangle = (|+1\rangle - |-1\rangle)/\sqrt{2}$

and $|01\rangle = (|+1\rangle + |-1\rangle)/\sqrt{2}$ and couple to linearly-polarized light (Π_x, Π_y) aligned along the major and minor axes of the quantum dot (see Fig. 2.4(b)).

It is also possible to optically excite a biexciton in a QD. The energy of the exciton to biexciton transition will differ from that of ground state to exciton transition by the binding energy of the biexciton, $\hbar\Delta$, which can be positive (binding) or negative (anti-binding) and are typically on the order of a few meV [149].

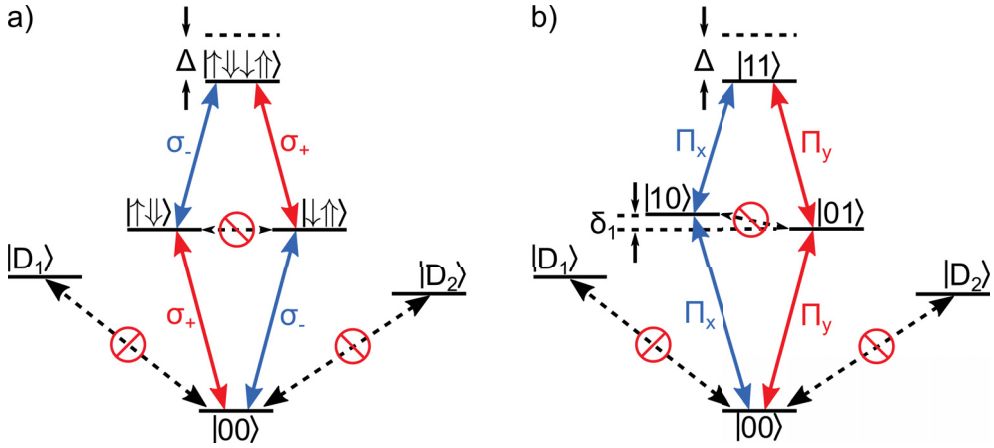

Figure 2.4: Energy level diagram and optical selection rules for excitons confined to: (a) spherically symmetric QDs, and (b) asymmetric QDs. For symmetric QDs, the bright exciton states ($|\uparrow\Downarrow\rangle$, $|\downarrow\Uparrow\rangle$) are degenerate and coupled to the ground state ($|00\rangle$) and biexciton state ($|\uparrow\Downarrow\downarrow\Uparrow\rangle$) by circularly polarized light ($\sigma_\pm$). The exciton states are not optically coupled to each other but transitions can occur due to spin-flip scattering. The dark states ($|D_{1,2}\rangle$) are split by the exchange interaction and are not optically coupled to other transitions. However, recent experiments have shown that they can be generated via a metastable biexciton state and coherently controlled [150]. For asymmetric QDs the exciton states ($|01\rangle$, $|10\rangle$) are symmetric and antisymmetric superpositions of the symmetric bright exciton states. The exchange interaction introduces a splitting $\hbar\delta_1$ between them.

Short optical pulses, resonant with the exciton transition, but with a bandwidth that is comparable to, or larger than Δ, can result in the excitation of the biexciton and lead to a breakdown of the two-level model. It has been shown that the occupation of the biexciton can be suppressed by using circularly polarized light [151]. For example, for excitation with σ_+ light, the state at $t = 0$ is given by,

$$|\psi(t=0)\rangle = \frac{1}{\sqrt{2}}\left(|10\rangle + i\,|01\rangle\right). \tag{2.21}$$

For small times relative to the inverse fine structure splitting in frequency, the exciton is in the $|\uparrow\Downarrow\rangle$ state and the σ_+-polarized pulse cannot excite the biexciton state

due to the Pauli exclusion principle. In effect, the small splitting energy relative to the transition frequency $\hbar\omega_{10}$, transforms the selection rules into that of a symmetric quantum dot for short times. For longer times relative to the inverse fine structure splitting in frequency, the state evolves into an admixture of $|\uparrow\Downarrow\rangle$ and $|\downarrow\Uparrow\rangle$, allowing for the creation of a biexciton.

$$\begin{aligned} |\psi(t)\rangle &= \frac{e^{-i\omega_{10}t}}{\sqrt{2}}\left(e^{-i\delta t/2}\,|10\rangle + ie^{+i\delta t/2}\,|01\rangle\right) \\ &= e^{-i\omega_{10}t}\left[\cos\left(\delta t/2\right)|\uparrow\Downarrow\rangle + i\sin\left(\delta t/2\right)|\downarrow\Uparrow\rangle\right]. \end{aligned} \tag{2.22}$$

In addition to excitation via the exciton states, the biexciton can also be generated using a two-photon absorption from the ground state $|00\rangle$ using light with frequency $\omega_{00-10} - \Delta/2$, *i.e.*, half the frequency of the direct transition.

2.4 Eight-Band, Strain-Dependent $\mathbf{k}\cdot\mathbf{p}$ Theory

While the approximations invoked in Sec. 2.3 provide a qualitative picture of the optoelectronic properties of a QD, more accurate calculations of the confined states are typically carried out using $\mathbf{k}\cdot\mathbf{p}$ theory, including the contribution from multiple bands and the effects of the residual strain field [152, 153, 154]. The first project in this thesis (see Chap. 5) used eight-band, strain-dependent $\mathbf{k}\cdot\mathbf{p}$ theory to explore the tunability of the biexciton binding energy in an InAs/GaAs QD. The $\mathbf{k}\cdot\mathbf{p}$ computer code used in this work was developed by Craig Pryor and Michael Flatté at the University of Iowa. The computational method and implementation are described in detail in Ref. [153] and Ref. [154].

The procedure for calculating the energies and wave functions using this method is as follows. First, a realistic QD geometry and composition is defined on a discrete three-dimensional grid. Next, the elastic energy of the system, given by,

$$\begin{aligned} E_{\text{elast}} = \frac{1}{2}\int &[C_{xxxx}(\epsilon_{xx}^2 + \epsilon_{yy}^2 + \epsilon_{zz}^2) + C_{xxxx}(\epsilon_{xx}\epsilon_{yy} + \epsilon_{xx}\epsilon_{zz} + \epsilon_{yy}\epsilon_{zz}) \\ &+ 2C_{xyxy}(\epsilon_{xy}^2 + \epsilon_{xz}^2 + \epsilon_{yz}^2)]\,d^3x, \end{aligned} \tag{2.23}$$

is minimized as a function of the displacement of the atoms, which provides an estimate of the residual strain field. The constants C_{ijkl} are elastic constants of the material and ϵ_{ij} is the strain tensor. In addition to mixing, the strain field

also induces a polarization $\mathbf{P}$, which creates an electrostatic potential $V_p(\mathbf{r})$. The potential can be calculated using Poisson's equation, which is given by,

$$\boldsymbol{\nabla} \cdot \mathbf{P} = \boldsymbol{\nabla}[\epsilon_S(\mathbf{r})\boldsymbol{\nabla} V_p(\mathbf{r})], \tag{2.24}$$

where $\epsilon_S(\mathbf{r})$ is the static dielectric constant. The total Hamiltonian to be diagonalized is given by,

$$H_{\text{tot}} = H_0(\mathbf{r}) + H_s(\mathbf{r}) - eV_p(\mathbf{r}), \tag{2.25}$$

where $H_0(\mathbf{r})$ is the $\mathbf{k}\cdot\mathbf{p}$ Hamiltonian, and $H_s(\mathbf{r})$ is the strain Hamiltonian. The form of the Hamiltonian in the eight-band basis of the doubly-degenerate conduction, heavy hole, light hole and split-off bands, is given in Ref. [154]. The single-particle electron and hole wave functions, $\{\varphi_e(\mathbf{r}_e),\ \varphi_h(\mathbf{r}_h)\}$, and energies $\{E_{h0},\ E_{e0}\}$ are determined in the envelope approximation, by solving the Schrödinger equation on the discrete grid using finite-difference methods to estimate derivatives.

The properties of multi-particle states are calculated using the Hartree method, which assumes that the state can be written as a product of single-particle states. The wave functions and energies are found using a self-consistent iterative approach that solves the Schrödinger equation for the electron or hole in the potential created by the other particle. This provides an estimate of the direct Coulomb interaction between the particles. For example, in this approximation, the exciton wave function can be written as $\psi(\mathbf{r}) = \varphi_{\text{e}}(\mathbf{r}_{\text{e}})\varphi_{\text{h}}(\mathbf{r}_{\text{h}})$ and the potentials are found by solving Poisson's equation, given by,

$$\begin{aligned} 4\pi e|\varphi_{\text{e}}(\mathbf{r})|^2 &= \boldsymbol{\nabla}[\epsilon_S(\mathbf{r})\boldsymbol{\nabla} V_{\text{h}}(\mathbf{r})], \\ -4\pi \text{e}|\varphi_{\text{h}}(\mathbf{r})|^2 &= \boldsymbol{\nabla}[\epsilon_S(\mathbf{r})\boldsymbol{\nabla} V_{\text{e}}(\mathbf{r})], \end{aligned} \tag{2.26}$$

where V_e and V_h are the potential experienced by the electron and hole, respectively. The energy and wave function of each particle in the potential of the other is determined by solving the Schrödinger equation,

$$\begin{aligned} \{H_{\text{tot}} + eV_{\text{h}}(\mathbf{r}_h)\}\varphi_{\text{h}}(\mathbf{r}_h) &= E_h\varphi(\mathbf{r}_{\text{h}}), \\ \{H_{\text{tot}} - eV_{\text{e}}(\mathbf{r}_{\text{e}})\}\varphi_{\text{e}}(\mathbf{r}_{\text{e}}) &= E_e\varphi(\mathbf{r}_h). \end{aligned} \tag{2.27}$$

Equations 2.26 and 2.27 are solved iteratively until convergence of the energies to an acceptable threshold. The binding energy of the exciton is given by,

$$E_{\text{exc,bind}} = [E_{\text{h0}} + E_{\text{e0}} - E_{\text{h}} - E_{\text{e}}]/2, \tag{2.28}$$

where the factor of $1/2$ avoids double counting of the Coulomb interaction.

2.5 Coherent Control Using Ultrafast Optical Pulses

The work presented in this thesis considers the coherent excitation of a two-level system, consisting of the vacuum crystal ground state and the confined exciton state, labelled here as $|0\rangle$ and $|1\rangle$, respectively. This section presents a derivation of the so-called optical Bloch equations (OBEs) —the equations of motion that govern the laser-qubit interaction, based on the approach taken in Ref. [155]. We also examine the role of dephasing, paying particular attention to excitation-induced dephasing that results from the field-intensity dependent coupling of the qubit to phonons in its solid state environment.

2.5.1 Optical Bloch Equations

An arbitrary superposition of the two-level system is written as,

$$|\psi(t)\rangle = C_0(t)\,|0\rangle + C_1(t)\,|1\rangle\,, \tag{2.29}$$

with complex probability amplitudes C_0 and C_1. The Hamiltonian for optical excitation of this two-level system is given by,

$$H_{\rm sys} = H_0 + H_{\rm int}, \tag{2.30}$$

where H_0 is the Hamiltonian describing the electronic structure of the unperturbed multi-particle states, and $H_{\rm int}$ represents the interaction of the states with laser light. In the $\{|0\rangle\,, |1\rangle\}$ basis, the unperturbed Hamiltonian is,

$$H_0 = \frac{\hbar\omega_{10}}{2}\sigma_z, \tag{2.31}$$

where $\hbar\omega_{10} = \hbar(\omega_1 - \omega_0)$ is the transition energy between states $|0\rangle$ and state $|1\rangle$, and σ_i are the Pauli matrices. The interaction Hamiltonian for the electric dipole transition is given by,

$$H_{\rm int} = -\mathbf{d}\cdot\mathbf{E}(t), \tag{2.32}$$

where $\mathbf{d} = -e\mathbf{r}$, is the optical dipole moment operator. $\mathbf{E}(t)$ is the electric field of the optical pulse, given by,

$$\mathbf{E}(t) = \frac{1}{2}\left\{\hat{\epsilon}E_0(t)e^{-i[\omega_l t+\phi(t)]} + \text{c.c.}\right\}. \tag{2.33}$$

where $\hat{\boldsymbol{\epsilon}}$ is the polarization unit vector, $E_0(t)$ is the field envelope, ω_l is the center frequency of the laser, and $\phi(t)$ is the phase. Note that the electric field has been expressed in the *electric dipole approximation*, which neglects the spatial variation of the field strength across the dot. The matrix elements of the dipole operator are: $\langle i|\,\mathbf{d}\,|i\rangle = 0$ and $\langle i|\,\mathbf{d}\,|j\rangle = \mathbf{d}_{ij} = \mathbf{d}_{ji}^*$. For a linearly polarized transition, the dipole element can be written as a real quantity $\mathbf{d} \equiv \mathbf{d}_{ij} = \mathbf{d}_{ji}$ [155]. The interaction Hamiltonian can then be expressed in terms of the Pauli spin matrices as

$$H_{\text{int}} = -\mathbf{d} \cdot \mathbf{E}(t)\sigma_x. \tag{2.34}$$

The total Hamiltonian is then given by

$$H = \frac{1}{2}\hbar\omega_{10}\sigma_z - \mathbf{d} \cdot \mathbf{E}(t)\sigma_x. \tag{2.35}$$

The Heisenberg equations of motion for the three Pauli matrices are then given by,

$$\begin{aligned}
\dot{\sigma}_x &= -\omega_{10}\sigma_y, \\
\dot{\sigma}_y &= \omega_{10}\sigma_x + \left(\frac{2}{\hbar}\right)\mathbf{d} \cdot \mathbf{E}(t)\sigma_z, \\
\dot{\sigma}_z &= -\left(\frac{2}{\hbar}\right)\mathbf{d} \cdot \mathbf{E}(t)\sigma_y.
\end{aligned} \tag{2.36}$$

The equations of motion can be written in terms of the expectation value of the Pauli operators $s_i = \langle\sigma_i\rangle$, such that,

$$\begin{aligned}
\dot{s}_x &= -\omega_{10}s_y, \\
\dot{s}_y &= -\omega_{10}s_x + \kappa E(t)s_z, \\
\dot{s}_z &= -\kappa E(t)s_y,
\end{aligned} \tag{2.37}$$

where $\kappa \equiv 2\mathbf{d} \cdot \hat{\boldsymbol{\epsilon}}/\hbar$. (Note that this definition assumes that $\mathbf{E}(t)$ is linearly polarized such that $\hat{\boldsymbol{\epsilon}} = \hat{\boldsymbol{\epsilon}}^*$.) Equations 2.37 describe the precession of the pseudospin vector $\mathbf{S} = (s_x, s_y, s_z)$, also called the Bloch vector, around a torque vector $\boldsymbol{\Lambda}^F(t) = (-\kappa E(t), 0, \omega_{10})$, such that

$$\dot{\mathbf{S}}(t) = \boldsymbol{\Lambda}^F(t) \times \mathbf{S}(t). \tag{2.38}$$

The components of $\mathbf{S}$ can be expressed in terms of the probability amplitudes C_0 and C_1, as

$$\begin{aligned}
s_x(t) &= 2\,\text{Re}\{C_0(t)C_1(t)\}, \\
s_y(t) &= -2\,\text{Im}\{C_0(t)C_1(t)\}, \\
s_z(t) &= |C_1(t)|^2 - |C_0(t)|^2.
\end{aligned} \tag{2.39}$$

The component s_x (s_y) are proportional to the real (imaginary) parts of the dipole moment while s_z is the population inversion of the two-level system. If the state of the system remains normalized for all time, then the components of $\mathbf{S}$ satisfy $s_x^2(t) + s_y^2(t) + s_z^2(t) = 1$.

The precession of $\mathbf{S}$ around $\mathbf{\Lambda}$ can be visualized on the Bloch sphere, a geometric representation of the two-level system, shown in Fig. 2.5. The Bloch vector lies on the surface of the sphere, which uniquely identifies any possible state of the two-level system. As described in Sec. 1.4.1, lines of longitude mark lines of constant phase between the two basis states, while lines of latitude mark a constant relative amplitude. The south and north pole mark the states $|0\rangle$ or $|1\rangle$, respectively, while the equator indicates an equal superposition of the states $|\psi\rangle = (|0\rangle + e^{i\phi}|1\rangle)/\sqrt{2}$.

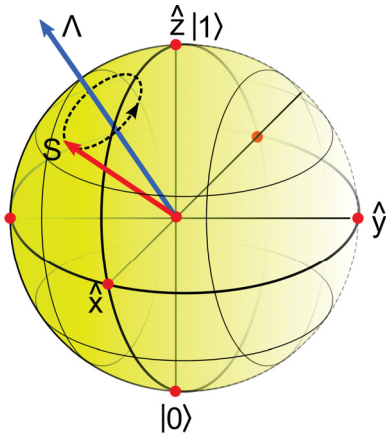

Figure 2.5: Precession of the Bloch vector $\mathbf{S}$ around the torque vector $\mathbf{\Lambda}$ depicted on the Bloch sphere. Control over the light field provides control over the direction and speed of rotation.

Note that the vectors $\mathbf{S}$ and $\mathbf{\Lambda}^F(t)$ are rapidly varying quantities. The vector $\mathbf{S}$ rotates around $\mathbf{\Lambda}^F(t)$ at a frequency $|\mathbf{\Lambda}^F(t)| = \sqrt{[\kappa E(t)]^2 + \omega_{10}^2}$, while $\mathbf{\Lambda}^F(t)$ varies rapidly because $\kappa E(t)$ oscillates at the laser frequency, which is typically close to resonance with the transition frequency ω_{10}. These fast variations can be removed, providing a more intuitive picture of the system dynamics, by moving to a coordinate frame that rotates in the counter clockwise direction at the instantaneous laser frequency $\omega_{\text{inst}} \equiv \omega_l + \dot{\phi}(t)$ about the $\hat{\mathbf{z}}$ direction. The transformation is carried out by writing $\mathbf{\Lambda}^F(t)$ in terms of three vectors,

$$\mathbf{\Lambda}^F(t) = \mathbf{\Lambda}^+(t) + \mathbf{\Lambda}^-(t) + \mathbf{\Lambda}^0(t), \tag{2.40}$$

where

$$\begin{aligned}\mathbf{\Lambda}_+ &= [-\kappa E_0(t)\cos(\omega_{\text{inst}}t), -\kappa E_0(t)\sin(\omega_{\text{inst}}t), 0],\\ \mathbf{\Lambda}_- &= [-\kappa E_0(t)\cos(\omega_{\text{inst}}t), +\kappa E_0(t)\sin(\omega_{\text{inst}}t), 0],\\ \mathbf{\Lambda}_0 &= [0, 0, \omega_{10}],\end{aligned} \tag{2.41}$$

The vector $\mathbf{\Lambda}_+$ rotates counter clockwise about $\hat{\mathbf{z}}$, while $\mathbf{\Lambda}_-$ rotates clockwise about $\hat{\mathbf{z}}$. In a reference frame that is rotating counter clockwise at frequency ω_{inst}, $\mathbf{\Lambda}_+$ is stationary and $\mathbf{\Lambda}_-$ rotates clockwise at a frequency $2\omega_{\text{inst}}$. In this rotating reference, the response of $\mathbf{S}$ to the fast variations associated with $\mathbf{\Lambda}_-$ is negligible, allowing us to ignore the resulting dynamics. The change to a rotating basis and the removal of the non-resonant dynamics associated with $\mathbf{\Lambda}_-$ is called the rotating wave approximation (RWA). The Bloch vector $\mathbf{U}$ in the RWA can be expressed in terms of $\mathbf{S}$ as,

$$\begin{bmatrix} u \\ v \\ w \end{bmatrix} = \begin{bmatrix} \cos\omega_{\text{inst}}t & \sin\omega_{\text{inst}}t & 0 \\ -\sin\omega_{\text{inst}}t & \cos\omega_{\text{inst}}t & 0 \\ 0 & 0 & 1 \end{bmatrix} \begin{bmatrix} s_1 \\ s_2 \\ s_3 \end{bmatrix}. \tag{2.42}$$

The equations of motion for $\mathbf{U}$ is given by

$$\dot{\mathbf{U}} = \mathbf{\Lambda} \times \mathbf{U}, \tag{2.43}$$

where the torque vector $\mathbf{\Lambda}$, called the *effective Rabi frequency*, is defined as

$$\mathbf{\Lambda} \equiv (-\Omega, 0, \Delta). \tag{2.44}$$

$\Omega(t) \equiv \kappa E_0(t)$ is the bare Rabi frequency and $\Delta(t) \equiv \omega_{10} - \omega_{\text{inst}}(t)$ is the instantaneous detuning of the laser from the transition. Expressing $\dot{\mathbf{U}}$ in terms of its vector components, we have

$$\begin{aligned}\dot{u} &= -\Delta v,\\ \dot{v} &= \Delta u + \Omega w,\\ \dot{w} &= -\Omega v.\end{aligned} \tag{2.45}$$

These equations are the OBEs that describe the dynamics of a two-level system with the electric field of a laser pulse. Sec. 2.5.4 describes how these equations are modified in the presence of dephasing that results from a coupling of the qubit to its solid-state environment.

2.5.2 Rabi Oscillations

In the case of resonant excitation with a CW laser beam ($\phi(t) = 0$, $\Delta = 0$), the Bloch vector rotates about $\mathbf{\Lambda}$, which points in the $-\hat{\mathbf{x}}$ direction, at the bare Rabi frequency $\Omega(t)$ (see Fig. 2.6(a)). The angle Θ swept out by the Bloch vector is called the *pulse area* and is given by,

$$\Theta(t) = \int_{-\infty}^{t} \mathrm{d}t'\, \Omega(t') = \frac{\mu}{\hbar} \int_{-\infty}^{t} \mathrm{d}t'\, E_0(t'). \tag{2.46}$$

For a pulsed source, the total angle of rotation is $\Theta(\infty)$. For example, if a qubit is in the ground state, *i.e.*, $\mathbf{U} = (0, 0, -1)$, then a pulse with an area $\Theta = \pi$ radians will invert the two-level system. As a function of Θ, the inversion is given by,

$$w = 2\sin^2(\Theta/2) - 1. \tag{2.47}$$

The periodic inversions of the two-level system as a function of pulse area, plotted in Fig. 2.6(b), are called *Rabi oscillations*.

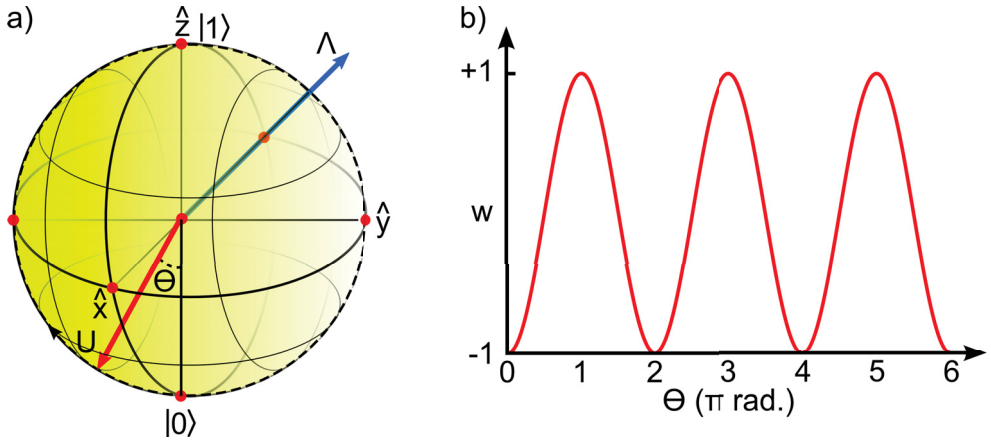

Figure 2.6: Rabi rotations: (a) Rotation of the Bloch vector $\mathbf{U}$ around $\mathbf{\Lambda}$ by an angle Θ, and (b) inversion, w, as a function of pulse area.

2.5.3 Adiabatic Rapid Passage

As described above, a resonant, transform-limited pulse with a pulse area of π radians can be used to invert a two-level system. However, this method is sensitive to fluctuations in experimental parameters such as the optical dipole, laser power, and laser detuning. Moreover, such a pulse would be unable to invert a

inhomogeneously-broadened ensemble of QDs with high efficiency because of the spread of transition energies and optical dipole moments. A more robust method of state inversion that has a reduced sensitivity to these variations, is adiabatic rapid passage. This approach differs from the Rabi method in that the detuning is non-zero. Rather, the detuning changes as a function of time as the pulse is swept through resonance, resulting in a rotation of the torque vector, $\mathbf{\Lambda}$, about the $\hat{\mathbf{y}}$ axis, as shown in Fig. 2.7(a). Provided the process is carried out adiabatically, the Bloch vector will be "dragged" along, while precessing around $\mathbf{\Lambda}$. The inversion is robust because at the end of the pulse, $\mathbf{\Lambda}$ points in the $\hat{\mathbf{z}}$ direction. One method of

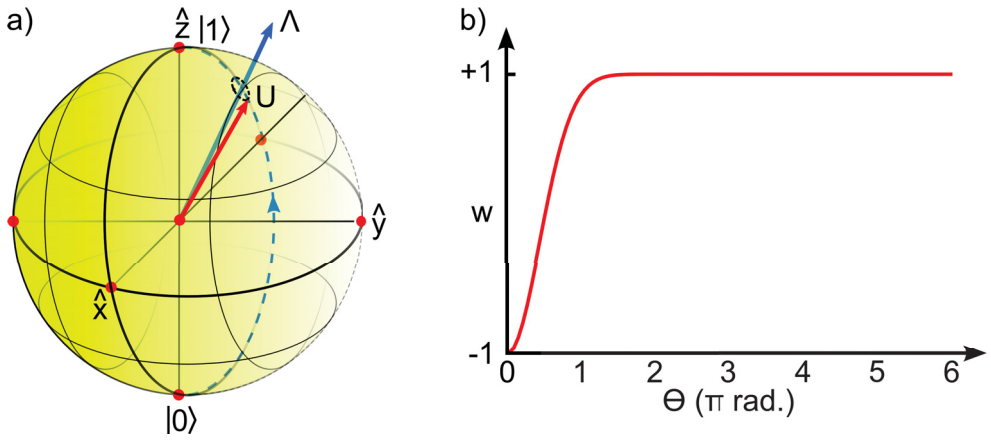

Figure 2.7: State inversion using adiabatic rapid passage: (a) Dynamics of $\mathbf{U}$ and $\mathbf{\Lambda}$, and (b) inversion, w, as a function of pulse area.

achieving ARP is to use a linearly chirped pulse, for which the electric field is given by,

$$\mathbf{E}(t) = \frac{1}{2}\left\{\hat{\boldsymbol{\epsilon}} E_0(t) e^{-i[\omega_l t + \alpha t^2]} + \text{c.c.}\right\}. \tag{2.48}$$

where α is the temporal chirp rate. For such a pulse, the detuning of the pulse is time dependent and is given by,

$$\begin{aligned} \Delta(t) &= \omega_{10} - \omega_{\text{inst}}(t), \\ &= \omega_{10} - (\omega_l + 2\alpha t), \\ &= -2\alpha t, \end{aligned} \tag{2.49}$$

where it was assumed that the center frequency of the laser is resonant with the transition, *i.e.*, $\omega_l = \omega_{10}$. The effective Rabi frequency in this case is

$$\mathbf{\Lambda}(t) = (-\Omega(t), 0, -2\alpha t). \tag{2.50}$$

Consider excitation of a two-level system with a Gaussian pulse, with field strength,

$$E_0(t) = E_0 \exp\left(-2\ln 2t^2/\tau^2\right), \tag{2.51}$$

for which the torque vector undergoes a rotation about the $\hat{\mathbf{y}}$ axis. At early times the torque vector will point in the $-\hat{\mathbf{z}}$ direction because the field strength is negligible and the detuning is large and negative. At $t = 0$, the field strength is at its maximum value and the detuning is zero such that the torque vector points in the $-\hat{\mathbf{x}}$ direction. At late times, the field strength is once again negligible but the detuning is large and positive such that the torque vector points in the $+\hat{\mathbf{z}}$ direction (see Fig. 2.7(a)). If the Bloch vector follows the torque vector by precessing around it, the inversion can be very efficient above a critical pulse area because the Bloch vector will also point in the $+\hat{\mathbf{z}}$ direction. A signature of ARP and robust state inversion is the insensitivity to pulse area above a certain threshold (see Fig. 2.7(b)). The requirements for adiabaticity can be expressed mathematically as [156]:

$$\begin{aligned} \frac{\dot{\Omega}}{\Lambda} &\ll 1, \\ \frac{\dot{\Delta}}{\Lambda} &\ll 1. \end{aligned} \tag{2.52}$$

A more intuitive description of the system dynamics during ARP can be obtained in the so-called *dressed states picture*. In this approach, one solves the James-Cummings Hamiltonian, based on a fully quantum mechanical model [157], to find the time dependent eigenstates and eigenvalues of the coupled quantum dot-light field system. In the RWA, the Hamiltonian is given by,

$$\hat{H} = \frac{1}{2}\hbar\omega_0\hat{\sigma}_z + \hbar\omega a^\dagger a + \hbar\lambda(\sigma_+ a + \sigma_- a^\dagger), \tag{2.53}$$

where $\hat{a}^\dagger$ and $\hat{a}$ are the creation and annihilation operators of the light field, respectively. The operators $\sigma_+ = |1\rangle\langle 0|$ and $\sigma_- = |0\rangle\langle 1|$ are the atomic transition operators and λ is a measure of the atom-light coupling strength. The Hamiltonian only couples the so-called bare states $|0; N\rangle$ and $|1; N-1\rangle$, where $|N\rangle$ is the number state of the light field with N photons. Diagonalizing the Hamiltonian provides the energy eigenvalues, given by,

$$E_\pm(t) = \pm\frac{\hbar}{2}\left[\Omega^2(t) + \Delta^2(t)\right]^{1/2}. \tag{2.54}$$

This shows that the time-dependent splitting between the eigenstates is determined by the magnitude of the effective Rabi frequency, given by $\Lambda(t)$ (see Eqn. 2.44). The instantaneous eigenstates, also called the *dressed states*, can be expressed in terms of the bare states, and are given by,

$$\begin{aligned} |\psi_+; N\rangle &= \cos(\Phi)e^{i\phi/2}\,|0; N\rangle + \sin(\Phi)e^{-i\phi/2}\,|1; N-1\rangle\,, \\ |\psi_-; N\rangle &= -\sin(\Phi)e^{-i\phi/2}\,|0; N\rangle + \cos(\Phi)e^{i\phi/2}\,|1; N-1\rangle\,, \end{aligned} \tag{2.55}$$

where $\tan(2\Phi) \equiv \Omega(t)/\Delta(t)$, and $\phi(t)$ is the phase of the electric field as defined in Eqn. 2.33. During ARP, the Hamiltonian (Eqn. 2.53) is evolved adiabatically such that the system remains in one of the instantaneous eigenstates $|\psi_+; N\rangle$ or $|\psi_-; N\rangle$ for all time. In contrast, for resonant excitation with a TL pulse, the system is in a superposition of $|\psi_+; N\rangle$ and $|\psi_-; N\rangle$. Figure 2.8(a) and (b) show the evolution of the dressed state splitting for a resonant transform-limited pulse and a positively chirped pulse, respectively.

In addition to providing robust inversion, ARP can also serve as a probe of the strength of phonon-mediated dephasing in a system. This is because the sign of the chirp parameter α dictates whether the system traverses the lower or upper adiabatic branch. For positively-chirped pulses, the system traverses the lower adiabatic branch, for which diabatic transitions to the upper branch via phonon absorption are suppressed at low temperatures. For negatively-chirped pulses on the other hand, the system traverses the upper adiabatic branch, for which diabatic transitions via phonon emission can occur in the vicinity of the anti-crossing. Therefore the coupling to phonons will manifest itself as a difference in inversion efficiency as a function of pulse area for positively- and negatively-chirped pulses [138, 139, 140]. Other dephasing mechanisms, such as those stemming from interactions with carriers trapped in the wetting layer depend on the field intensity and pulse bandwidth [158], but would not exhibit a dependence of the sign of the pulse chirp. Chapter 6 presents the results from an experimental demonstration of ARP using subpicosecond optical pulses. The results also demonstrate for the first time, the chirp-sign dependence of ARP, confirming the dominance of phonon-mediated dephasing for exciton qubits confined to SAQD.

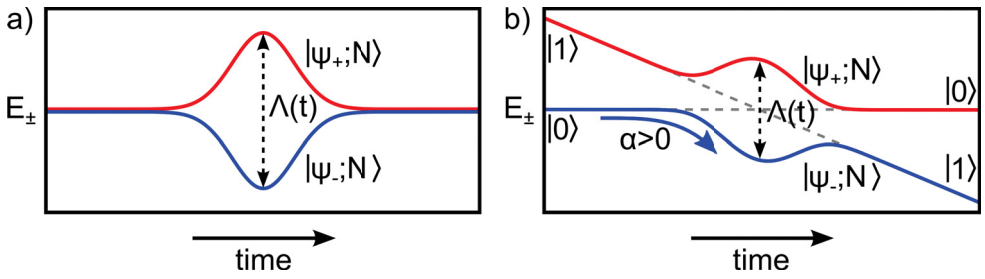

Figure 2.8: Splitting of the dressed states for (a) a TL, resonant laser pulse, and (b) a positively chirped pulse ($\alpha > 0$). For the TL pulse, the system is in a superposition of $|\psi_{\pm}; N\rangle$, whereas for the positively chirped pulse the system traverses the lower adiabatic branch, remaining in the state $|\psi_{-}; N\rangle$ for all time.

2.5.4 Effects of Decoherence

A qubit can lose coherence due to interactions with its environment, placing a fundamental limit on the number of operations that can be performed before the information is lost. In the low excitation regime, these effects can be modelled using phenomenological decay constants, $\gamma_1 = 1/T_1$ and $\gamma_2 = 1/T_2$, that describe the rates of radiative recombination and dephasing due to elastic scattering, respectively. The modified OBEs in this regime are given by,

$$\begin{aligned} \dot{u} &= -\Delta v - \gamma_2 u, \\ \dot{v} &= \Delta u + \Omega w - \gamma_2 v, \\ \dot{w} &= -\Omega v - \gamma_1 (w + 1), \end{aligned} \tag{2.56}$$

resulting in an exponential decay of the coherence of the qubit. At low temperatures, it has been shown that the coherence time is limited only by the radiative lifetime of the exciton, *i.e.* $T_2 = 2T_1$. In SAQDs, four-wave mixing experiments have been used to measure T_2 times between $400\,\mathrm{ps}$ and $1\,\mathrm{ns}$, with a strong dependence on confinement energy [86, 87, 88].

In the strong excitation regime, recent experiments [54, 69, 137] have uncovered an excitation-induced dephasing mechanism that leads to a pulse-intensity dependent damping of Rabi oscillations, beyond that predicted by the homogeneous broadening of the exciton transition. It has been attributed to the coupling of the qubit to its solid-state environment via phonons [90, 54, 130]. During manipulation of the qubit, the pulse drives the charge configuration in the quantum dot at the Rabi frequency, which results in an enhanced coupling to LA phonons at the

same frequency via the deformation potential. The total Hamiltonian, including the bath and interaction terms, is given by,

$$H = H_{\text{sys}} + \sum_q \hbar\omega_q \hat{b}_q^\dagger \hat{b}_q + \sum_q \hbar(g_q \hat{b}_q^\dagger + g_q^* \hat{b}_q) \left|1\right\rangle \left\langle 1\right|, \tag{2.57}$$

where g_q is the exciton-phonon coupling strength and $\hat{b}_q$ ($\hat{b}_q^\dagger$) are annihilation (creation) operators for phonons with momentum q and frequency ω_q. Equations of motion that do not require tracking of the full evolution of the environment can be derived under the Born-Markov approximation, which assumes that: (i) the environment is a large system that is unaffected by coupling to the exciton, and (ii) the correlation times of the phonons is much shorter than the time scales associated with the exciton dynamics. At this level of approximation, the model can only account for single-phonon processes. For more details regarding the model, see Ref. [90] and Ref. [137].

The spectral density of the interaction between LA phonons and an exciton depends on the electron-phonon coupling form factor, which for identical Gaussian electron and hole wave functions, is given by,

$$J(\omega) = \alpha\omega^3 e^{-(\omega/\omega_c)^2}, \tag{2.58}$$

where α is a coupling constant, and ω_c is a cut-off frequency that depends on the spatial extent of the wave functions. The bath correlation function, $\tilde{K}(t)$, can be expressed in terms of $J(\omega)$ as,

$$\tilde{K}(t) = \int_0^\infty \mathrm{d}\omega\, J(\omega) \coth\left(\frac{\hbar\omega}{2k_B T}\right) \cos(\omega t), \tag{2.59}$$

where k_B is the Boltzmann constant and T is the temperature. The OBEs can be expressed in terms of $J(\omega)$ and $K(\omega) = \int_0^\infty \mathrm{d}t\, \tilde{K}(t) e^{i\omega t}$ as,

$$\begin{aligned}
\dot{u} &= \Delta v - \left(\frac{\Delta\Omega}{\Lambda^2}\right) \mathrm{Re}[K(\Lambda)] w - \frac{\pi\Omega J(\Lambda)}{2\Lambda} - \left(\frac{\Omega}{\Lambda}\right)^2 \mathrm{Re}[K(\Lambda)] u, \\
\dot{v} &= -\Delta u + \Omega\left(1 + \frac{\mathrm{Im}[K(\Lambda)]}{\Lambda}\right) w - \left(\frac{\Omega}{\Lambda}\right)^2 \mathrm{Re}[K(\Lambda)] v, \\
\dot{w} &= -\Omega v,
\end{aligned} \tag{2.60}$$

where the functions are evaluated at the time-dependent Rabi frequency Λ. These equations show that the qubit suffers an intensity-dependent dephasing rate that

arises from the real part of $K(\omega)$ and a renormalization of the rotation frequency of the Bloch vector that results from the imaginary part of $K(\omega)$. Figure 2.9(a) and (b) show the spectral dependence of the real and imaginary part of $K(\omega)$, for different temperatures for a realistic coupling parameter ($\alpha = 0.025\,\mathrm{ps}^2$) and cut-off frequency ($\hbar\omega_c = 1.3\,\mathrm{meV}$).

Note that this model for the exciton-phonon interaction predicts a decoupling from the bath, provided the Rabi energy of the pulse exceeds the peak of the correlation spectrum. However, the results from Ch. 6 suggest that for larger Rabi frequencies, multi-phonon processes and non-Markovian effects, not included in the model, may increase coupling to the phonon bath. The findings suggest that simply increasing the Rabi frequency may not suffice for decoherence mitigation in these systems.

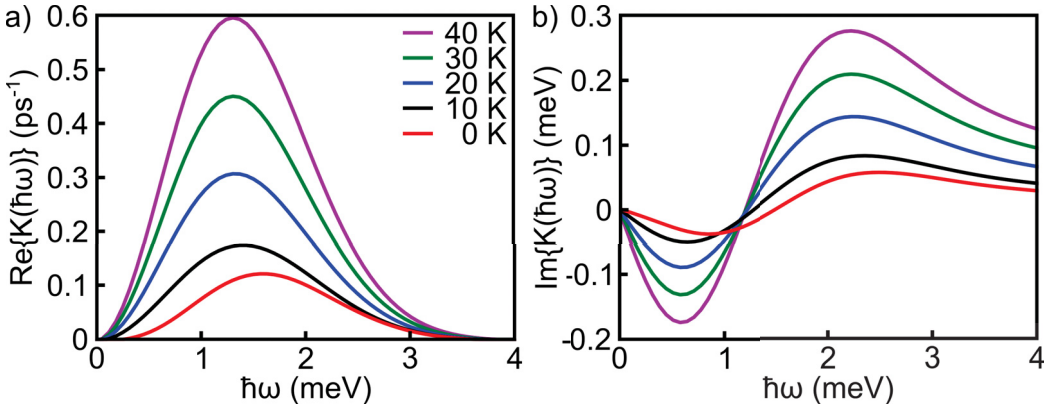

Figure 2.9: Spectral dependence of (a) the real, and (b) imaginary part of the bath correlation function a coupling constant $\alpha = 0.025\,\mathrm{ps}^2$ and a cut-off frequency $\hbar\omega_c = 1.3\,\mathrm{meV}$. $\mathrm{Re}[K(\hbar\omega)]$ is responsible for dephasing and $\mathrm{Im}[K(\hbar\omega)]$ results in a renormalization of the bare Rabi frequency. The strength of these effects are observed to increase with increasing temperature.

Decoherence is one of the great challenges faced by quantum computation systems and finding strategies to reduce or control decoherence in the system is of critical importance. Interactions with the phonon bath can be understood to transiently alter the resonance frequency of the qubit, resulting in an accumulated phase error. A promising approach towards limiting decoherence is dynamical decoupling, the quantum equivalent of a classical noise filter. It employs a series of optical pulses with a pulse area of π radians to periodically flip the qubit, changing the

sign of the accumulated phase error [33, 35, 46, 92]. Provided the pulse spacing is shorter than the correlation time of the phonon bath, the total phase error can be greatly reduced. Compared to traditional quantum error correction techniques DD is seen to be modest on resources [159], requiring only a few decoupling pulses to significantly improve the coherence time. Hodgson *et al.* [46] showed that the decoherence can be dramatically reduced if sufficiently rapid DD pulses ($< 500\,\mathrm{fs}$) are employed. The predictions of Hodgson *et al.* could pave way for a scalable computing system with greatly reduced phase errors. However, current optical control experiments have been limited to optical pulses longer than $5\,\mathrm{ps}$, precluding the demonstration of dynamical decoupling in these systems. The implementation of fast, high fidelity π pulses via ARP, as described in Ch. 6, should prove to be important for this effort.

2.6 Optimal Quantum Control Using Shaped Optical Pulses

The interaction of the exciton qubit with a TL laser pulse will rotate the qubit about a fixed axis in the equatorial plane. Complete control of the qubit can be achieved using two phase-locked TL pulses, designed to rotate the Bloch vector to an arbitrary point on the Bloch sphere. Alternatively, the evolution and final state of the two-level system can be engineered by manipulating the amplitude and phase of the optical pulse. In this work, we use a $4f$ pulse shaper, with a programmable, 128-pixel spatial light modulator (SLM) at the Fourier plane, to provide a more versatile form of control of the pulse properties and the concomitant system dynamics. A detailed description of the experimental apparatus and related constraints is provided in Sec. 3.4.

The $4f$ pulse shaper can be modelled as a linear filter [112]. In this case, the action of the filter on the input pulse can be described in the time domain as the convolution product,

$$E_{\mathrm{out}}(t) = R(t) \otimes E_{\mathrm{in}}(t), \tag{2.61}$$

where E_{in} (E_{out}) is the electric field of the input (output) pulse, and $R(t)$ is the impulse response of the filter. However, for femtosecond pulses, it is difficult to design optical elements that can apply the filter in the time domain. Instead, the

pulse is shaped in the frequency domain such that,

$$\tilde{E}_{\text{out}}(\omega) = M(\omega)\tilde{E}_{\text{in}}(\omega), \tag{2.62}$$

where $\tilde{E}_{\text{in}}$ ($\tilde{E}_{\text{out}}$) is the complex spectrum of the of the input (output) pulse, and $M(\omega)$ is the transfer or mask function of the filter. As described in Sec. 3.4, the mask is comprised of a horizontal polarizer, followed by two liquid-crystal SLMs, and then another horizontal polarizer. The effect of the horizontal polarizers and voltage-controlled liquid-crystal pixels can be described using the Jones matrix formalism. The input beam $\mathbf{E}_{\text{in}} = E_x\hat{\mathbf{x}} + E_y\hat{\mathbf{y}}$ can be written as,

$$\mathbf{E}_{\text{in}} = \begin{bmatrix} E_x \\ E_y \end{bmatrix}. \tag{2.63}$$

The mask function M modulates the input beam to produce the shaped output, $\mathbf{E}_{\text{out}}$. For a single pass through the SLM, the Jones matrix for the mask is given by

$$M = H \cdot L_{\text{PR}}(\phi_2, \theta_2) \cdot L_{\text{PR}}(\phi_1, \theta_1) \cdot H, \tag{2.64}$$

where,

$$H = \begin{pmatrix} 1 & 0 \\ 0 & 0 \end{pmatrix}, \tag{2.65}$$

is the Jones matrix for a horizontal polarizer, and

$$L_{\text{PR}}(\phi, \theta) = \begin{pmatrix} e^{i\phi/2}\cos\theta^2 & e^{i\phi/2}\cos\theta^2 \\ e^{i\phi/2}\cos\theta^2 & e^{i\phi/2}\cos\theta^2 \end{pmatrix}, \tag{2.66}$$

is the Jones matrix for a phase retarder with its optical axis at an angle θ, measured from the positive $\hat{\mathbf{x}}$ axis, that imparts a phase retardance of ϕ radians. If the optical axis of the first and second liquid-crystal array are at $+\pi/4$ and $-\pi/4$, respectively, then the mask function is given by,

$$M(\phi_1, \phi_2) = e^{i(\phi_1+\phi_2)/2} \begin{bmatrix} \cos\left(\frac{\phi_1-\phi_2}{2}\right) \\ 0 \end{bmatrix}. \tag{2.67}$$

Therefore, the output beam is given by,

$$\mathbf{E}_{\text{out}} = \hat{\mathbf{x}}E_x \cos\left[\frac{\phi_1(\omega) - \phi_2(\omega)}{2}\right] \exp\left[i\frac{\phi_1(\omega) + \phi_2(\omega)}{2}\right], \tag{2.68}$$

showing that the pulse shaper provides independent control of the amplitude and phase of the frequency components. Therefore, the mask function can be written as,

$$M(\omega) = A_M(\omega) \exp\left[i\Phi_M(\omega)\right], \tag{2.69}$$

where $A_M(\omega) \equiv \cos\left\{[\phi_1(\omega) - \phi_2(\omega)]/2\right\}$ is the amplitude mask and $\Phi_M(\omega) \equiv [\phi_1(\omega) + \phi_2(\omega)]/2$ is the phase mask.

Changes to either the amplitude or phase mask will shape the driving field and therefore alter the qubit dynamics via the interaction Hamiltonian. As previously mentioned, the science of manipulating the Hamiltonian to drive the system to a desired final state is called optimal quantum control. Consider a quantum gate with a desired target state defined by a density matrix ρ_{I}. If the pulse drives the system to a final state with density maxtrix ρ_{P}, then the fidelity of the operation can be defined as [16],

$$F = \mathrm{Tr}[\rho_p \rho_I]. \tag{2.70}$$

An optimization algorithm that manipulates the pulse shape via the mask function, $M(\omega)$, can use the fidelity as the objective function that is to be maximized. The frequency dependence of the mask can be parametrized using any convenient function. For example, the optimization routine used in Ch. 5 used a phase mask defined by a cosine function, given by,

$$\Phi_M(\omega) = \alpha \cos\left[\gamma(\omega - \omega_{10}) - \delta\right]. \tag{2.71}$$

The parameters α, γ, δ and the pulse area Θ were optimized, subject to constraints that restricted them to experimentally accessible values. The fidelity is now a function of these four variables, such that,

$$F = f(\alpha, \gamma, \delta, \Theta). \tag{2.72}$$

For a given initial vector $\mathbf{q}_i = (\alpha_i, \gamma_i, \delta_i, \Theta_i)$, the optimization algorithm will drive the parameters to local optima in fidelity $F_{\mathrm{opt}} = f(\alpha_{\mathrm{opt}}, \gamma_{\mathrm{opt}}, \delta_{\mathrm{opt}}, \Theta_{\mathrm{opt}})$. The optimization routine is repeated for more initial vectors, distributed using a Sobol' sequence, to provide sufficient coverage of the four-dimensional constrained parameter space. The local optima with the highest fidelity is then used to define the optimal pulse shape.

Pulse shaping is used to achieve quantum control in the three projects described in this work. In Ch. 4, optimal quantum control theory is used to design pulses that can implement simultaneous high fidelity gates in two uncoupled QDs using a single laser pulse. The work presented in Ch. 5, applies optimal quantum control to implement a C-ROT gate in the exciton-biexciton four-level system. In Ch. 6, phase-only shaping is used to create chirped laser pulses for ARP.

Chapter 3

Experimental Methods

This chapter presents the experimental techniques used to demonstrate ARP as presented in Ch. 6. Section 3.1 begins with a description of the QD sample structure, a discussion of the ensemble photoluminescence spectrum, and the technique used to isolate single QDs from the ensemble. Sec. 3.2 describes how PL and PLE spectroscopy are used to elucidate the electronic structure of QDs. The apparatus used to implement optical quantum control and read out the quantum state is presented in Sec. 3.3. Sec. 3.4 discusses the function of the pulse shaper and the associated experimental constraints. Sec. 3.5 describes the techniques used to characterize the pulse, including the use of multiphoton intrapulse interference phase scan (MIIPS) to compensate for phase distortions, the knife-edge technique to measure the focused spot-size of the laser, and intensity autocorrelations to determine the temporal pulse width.

3.1 InAs/GaAs Quantum Dot Sample

The quantum dot sample studied in this work (labelled UCF-628, piece $\#7$) was grown using epitaxial techniques by Dennis Deppe at the University of Central Florida. As described in Sec. 2.1(b), the structural and optical properties of QDs, grown using the Stranski-Krastanov growth mode, depend on the growth conditions that are employed. Figure 3.1 shows a schematic of the sample structure. The sample is grown on an n-doped GaAs substrate with AlGaAs diffusion barriers. The InAs QDs are embedded in a GaAs matrix. Figure 1.2(d) shows an AFM image prior to capping with GaAs, taken by Dennis Deppe, for a sample grown under similar conditions to UFC-628. The QDs were measured to have an average height of $5\,\mathrm{nm}$ and a lateral width between $15\,\mathrm{nm}$ to $25\,\mathrm{nm}$. The growth conditions were tailored to produce a reduced areal density of QDs with s-shell transition wavelengths around $1.3\,\mu\mathrm{m}$ at low sample temperature. Growing the samples at reduced temperature

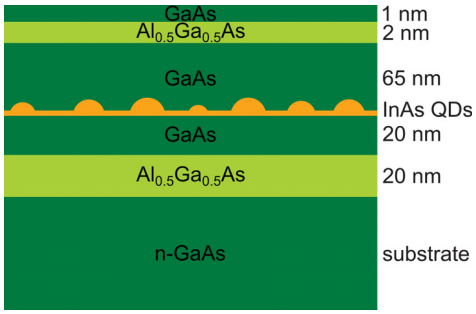

Figure 3.1: Schematic of the quantum dot structure used in this work. The $\mathrm{Al_{0.5}Ga_{0.5}As}$ layers, with a higher band gap energy than GaAs ($1.998\,\mathrm{eV}$ versus $1.424\,\mathrm{eV}$ at $300\,\mathrm{K}$), serves to trap photoexcited carriers within the GaAs layer that surrounds the QD.

helped to eliminate intermixing of indium (In) and Ga, resulting in an indium-rich core (almost pure InAs). The confinement energy was then shifted to lower values by covering the QDs with $\mathrm{In_{0.2}Ga_{0.8}As}$. The areal density was controlled by slowing down the growth rate.

The spectral dependence of the ensemble PL intensity from UCF-628, measured using PL spectroscopy at a sample temperature of $10\,\mathrm{K}$, is shown in Fig. 3.2(a). (See Fig. 1.6(a) for a description of the experimental technique.) The PL spectrum shows three distinct peaks and a shoulder on one of the peaks. PLE spectroscopy helped identify them to be the result of a bimodal size distribution of QDs. Emission from the high-energy and low-energy subsets are indicated by red and blue dashed vertical lines, respectively. The high-energy subset has a *p*-shell emission peak at $1152\,\mathrm{nm}$ and a *s*-shell emission peak at $1220\,\mathrm{nm}$, with an energy separation of $60\,\mathrm{meV}$. The low-energy subset has a *p*-shell emission peak at $1190\,\mathrm{nm}$ and an *s*-shell emission peak at $1294\,\mathrm{nm}$, with an energy separation of $84\,\mathrm{meV}$. The large energy separation between the *p*- and *s*-shells allows for effective suppression of scattered laser light during coherent control experiments performed on the *p*-shell, where the quantum state is read out via emission from the *s*-shell.

The large areal densities of QDs can make single-dot spectroscopy a challenging proposition. For this reason, we elected to use the low-energy subset of QDs that had an areal density of $1\,\mu\mathrm{m}^{-2}$ (compared to $10\,\mu\mathrm{m}^{-2}$ for the high-energy subset). Even a diffraction-limited laser spot size ($\sim 2\,\mu\mathrm{m}$) would excite 10–15 QDs in the low energy subset and 100–150 QDs in the high energy subset. The isolation of

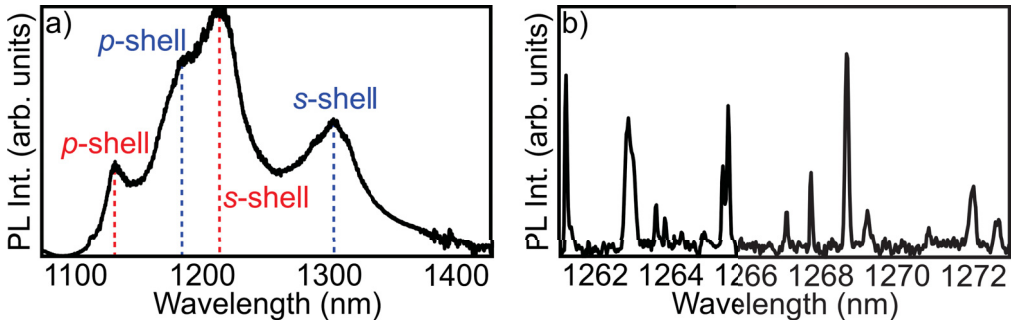

Figure 3.2: (a) Spectrally-resolved ensemble PL from UFC-628-7. The sample has a bimodal distribution of QDs sizes, resulting in a pair of *s*-shell and *p*-shell transitions, marked by the pairs of blue and red vertical lines. (b) Spectrally-resolved micro-PL collected through the $0.4\,\mu\mathrm{m}$ aperture S-15 on mask 12.

single QDs from the ensemble therefore requires the use of a spatial filter, which is created by depositing an apertured metal mask on the sample. (Fabrication of the mask was carried out by CMC Microsystems using electron-beam lithography.) Figure 3.3 shows the pattern of apertures on the mask and a photograph of the sample within the cryostat. Each of the numbered masks (1–25) have apertures of a fixed radius as labelled on the schematic. The apertures are labelled by the mask number and an alphanumeric label that denotes the row and column. Figure 3.2(b) shows the spectrally resolved PL from the $0.4\,\mu\mathrm{m}$ aperture S-15 on mask 12.

3.2 Photoluminescence and Photoluminescence Excitation Spectroscopy

Photoluminescence and photoluminescence excitation spectroscopy are two techniques used to measure the electronic structure of quantum dots. The optical excitation scheme for each technique is illustrated in Fig. 1.6. PL spectroscopy provides a means of identifying the allowed transitions within the quantum dots. In this technique, the wavelength of the laser source is tuned above the bandgap of GaAs to create electron-hole pairs in the GaAs matrix surrounding the quantum dot. The excited carriers relax via phonon emission and carrier-carrier scattering before recombining radiatively in one of the discrete transitions in a quantum dot. The emitted light, or photoluminescence, is spectrally resolved using a spectrometer. With the aid of a spatial filter, PL spectroscopy can be used to identify the transition energies of confined states in single quantum dots. On the other hand, when the

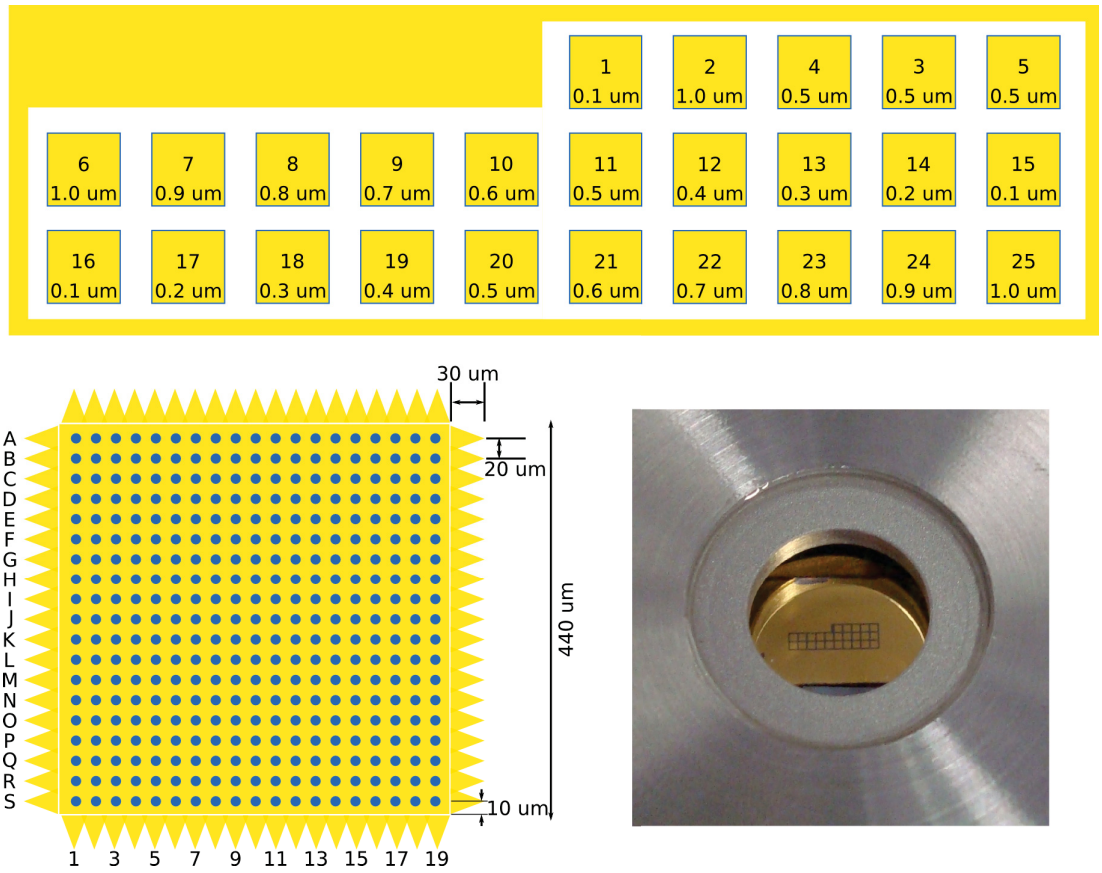

Figure 3.3: (a) Schematic of the apertured gold mask. The mask is divided into 25 sub-masks, each with an array of apertures of a defined radius (indicated below the mask number). (b) Detail of a sub-mask with alphanumeric labelling scheme used for aperture identification. Also shown are the "teeth" at the edges of the mask that are used for ease of alignment. The dimensions of the mask features are indicated. (c) Photograph of sample viewed through the ultra-thin window of the cryostat.

laser beam is used to excite an ensemble of QDs, it provides a means for identifying the average separation between the ground and excited states and a measure of the inhomogeneous broadening that results from variations in the QD size and composition. Figure 3.2 shows spectrally resolved ensemble PL from the quantum dot sample used in this work.

PLE spectroscopy provides a means of identifying the excited state transitions of a QD. For this technique, the photoluminescence from the ground state is measured as a function of the wavelength of the laser as it is scanned across the transition of an excited state. For example, in this work, PLE spectroscopy was used to measure the transition energy of the *p*-shell exciton by measuring the PL intensity at

the *s*-shell exciton transition. The *p*-shell state decays non-radiatively, via phonon emission, into the *s*-shell exciton so the time-averaged PL from the *s*-shell provides a measure of the occupation of the excited state.

3.3 Single-Dot Spectroscopy

The coherent control experiments on single quantum dots were carried out using the control apparatus shown in Fig. 3.4. The laser source is a $76\,\mathrm{MHz}$ infrared (IR) optical parametric oscillator (OPO) generating pulses with a TL pulse width of $120\,\mathrm{fs}$, that are resonant with the ground state to *p*-shell exciton transition in the quantum dot of interest ($\lambda_0 \cong 1160\,\mathrm{nm}$). The pulses pass through a $4f$ pulse shaper with a 128-pixel SLM in the Fourier plane (MIIPS Box 128 from Biophotonic Solutions). (See Sec. 3.4 for more details regarding the pulse shaper.) A dichroic mirror (DCM) is used to reflect the laser pulses into the vertical arm of the apparatus. The pulses are focused onto the sample, which is held at $10\,\mathrm{K}$ in a continuous flow cryostat (ST-500 from Janis Research Company), using a high numerical aperture microscope objective ($100\times$ Plan Apo, long working distance, near-infrared, high resolution, infinity-corrected objective with 0.7 numerical aperture from Mitutoyo). The sample is mounted on a 3D nano-positioner (ANP101 stages with ANC300 controller from Attocube Systems AG) allowing the aperture containing the quantum dot of interest to be positioned in the laser focus. The photoluminescence emitted from the *s*-shell exciton, after non-radiative decay from the *p*-shell, is collected using the same microscope objective. The PL transmitted by the DCM is coupled into a $0.75\,\mathrm{m}$ focal length spectrometer (from Princeton Instruments) where it is detected using a 1024-pixel liquid nitrogen cooled InGaAs charge-coupled device (CCD) array detector (Symphony II IGA from Horiba Jobin Yvon). A long-pass filter placed in the PL path further reduces the scattered pump light entering the spectrometer.

For the experiments described in Ch. 6, the pulse shaper is used to apply the desired spectral chirp to the pulse. ARP is demonstrated by measuring the PL intensity as a function of the average pulse power ($\sqrt{P_{\mathrm{avg}}} \propto \Theta$) incident on the sample which can be controlled using a variable neutral-density filter.

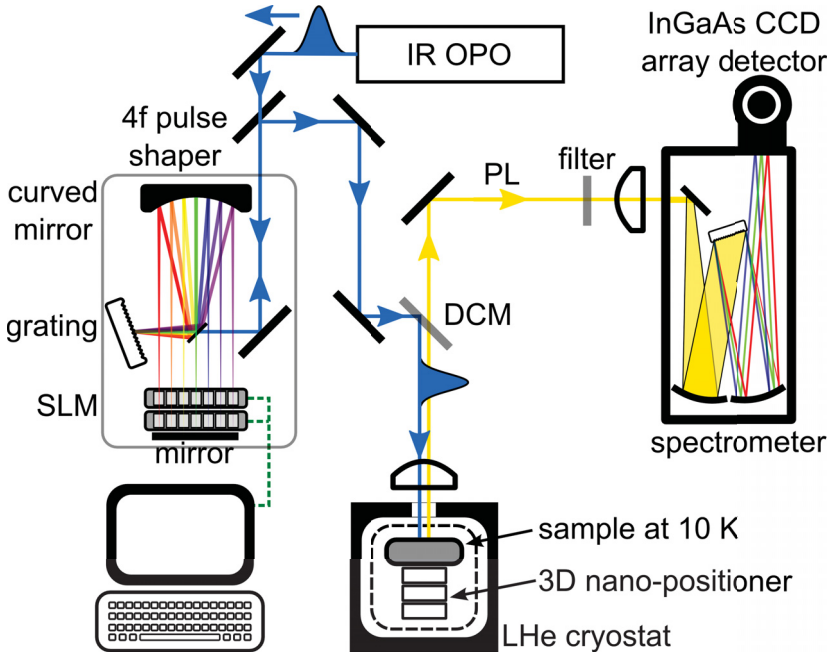

Figure 3.4: Experimental setup used for quantum control experiments. The pulse train from the IR OPO laser source goes through a $4f$ pulse shaper with a dual-mask SLM where they are shaped. The shaped pulses are reflected by a DCM and focused onto the sample using a high-resolution microscope objective lens. The sample is held in a cryostat at $10\,\mathrm{K}$ on a 3D nano-positioning stage. The emitted PL is filtered to remove scattered laser light, and spectrally resolved using a spectrometer and detected by an InGaAs CCD detector.

3.4 Femtosecond Pulse Shaping

The amplitude and phase of the optical pulses used to control the exciton qubit were tailored using a femtosecond $4f$ optical pulse shaper, with a liquid-crystal SLM in the Fourier plane (see Fig. 3.5(a)). The input pulses are spectrally dispersed by the grating and focused by the curved mirror. The focused light passes through the SLM and is reflected back by a planar mirror, such that it follows the same path as the input beam but in reverse, with a slight vertical offset used to pick off the output.

Figure 3.5(b) shows a schematic of the SLM, which consists of four optical elements, namely, two horizontal polarizers and two 128-pixel liquid crystal arrays with orthogonally-oriented fast axes. The incoming light passes through the first horizontal polarizer, through the liquid-crystal SLMs, and through a second horizontal polarizer. The mirror reflects the beam back through the four optical elements to double the modulation induced by the SLM. The index of refraction of the

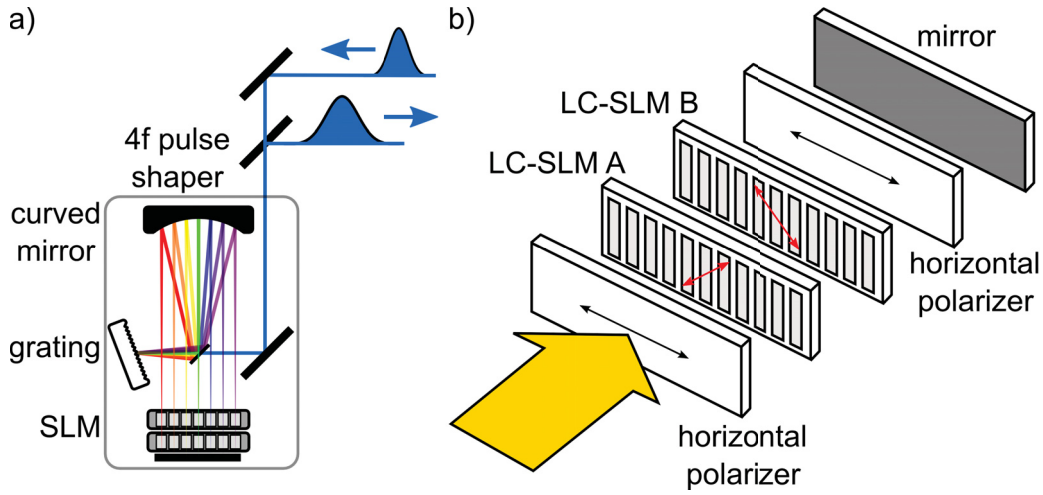

Figure 3.5: (a) Schematic of the $4f$ pulse shaper. The shaper consists of a grating that spectrally disperses the pulse. The spatially separated frequency components are focused onto the Fourier plane by a curved mirror with a focal length of $50\,\mathrm{cm}$. The dual-mask SLM in the Fourier plane is used to shape the pulse. A planar mirror behind the SLM reflects the beam with a slight vertical offset such that it can be picked off at the output of the pulse shaper. (b) Schematic of the dual-mask SLM with planar mirror at one end. Each SLM has 128 liquid-crystal pixels with a pixel pitch of $100\,\mu\mathrm{m}$ and inter-pixel gap of $2\,\mu\mathrm{m}$. The optical axis of each liquid-crystal array is at $\pm 45^\circ$ with respect to the horizontal (indicated by red, double-arrowed lines).

nematic liquid crystals can be controlled using electrodes. The change in the optical phase produced by a given pixel on one of the SLMs is

$$\phi(\omega, V) = \frac{\omega \Delta n(\omega, V) l}{c}, \tag{3.1}$$

where c is the speed of light, l is the thickness of the crystal, and Δn is the change in index of refraction that depends on the frequency ω and the applied voltage V. As described in Sec. 2.6, the mask function for each pixel can be expressed in terms of the phase retardance ϕ_1 and ϕ_2, imparted by the SLMs, and is given by,

$$\begin{aligned} M(\omega) &= \cos\left[\frac{\phi_1(\omega) - \phi_2(\omega)}{2}\right] \exp\left[i\frac{\phi_1(\omega) + \phi_2(\omega)}{2}\right], \\ &= A_M(\omega) \exp\left[i\Phi_M(\omega)\right]. \end{aligned} \tag{3.2}$$

The mask function provides independent control over the amplitude and phase of the pulse spectrum, providing a versatile method for controlling the qubit dynamics.

3.4.1 Experimental Constraints on Pulse Shaping

The previous section described the dual-mask spatial light modulator as an ideal linear filter with infinite resolution, however, the finite spot-size of the frequency components in the Fourier plane of the shaper restricts the resolution of the shaping system and also results in the coupling of space and time. The full-width at half maximum (FWHM) spot size of the spectral components at the SLM can be expressed as,

$$w_0 = \frac{\cos\theta_{\mathrm{i}}}{\cos\theta_{\mathrm{d}}}\left(\frac{f\lambda}{\pi w_{\mathrm{in}}}\right), \tag{3.3}$$

where θ_{i} is the incident angle of light on the grating, θ_{d} is the diffracted angle, f is the focal length of the curved mirror, λ is the wavelength, and w_{in} is the FWHM spot size of the input beam. The spectral field amplitude after the mask is given by,

$$\tilde{E}_{\mathrm{out}} \sim \tilde{E}_{\mathrm{in}} e^{-(x-\alpha\omega)^2/w_0^2} P(x), \tag{3.4}$$

where x is the spatial coordinate in the Fourier plane, $P(x)$ is the physical masking function, and $\alpha = x/\omega$ is the spatial dispersion given by,

$$\alpha = \frac{\lambda^2 f}{2\pi c d \cos\left(\theta_{\mathrm{d}}\right)}. \tag{3.5}$$

Equation 3.4 is a non-separable function of the spatial coordinate and frequency. This mask alters the spatial profile of the spectral components, leading to different amounts of diffraction for different spectral components, and an output pulse that has non-zero amplitudes in the higher order Hermite-Gaussian modes. Assuming that a spatial filter can be used to isolate the fundamental Hermite-Gaussian mode, the mask function can be written as follows:

$$M(\omega) = \left(\frac{2}{\pi w_0^2}\right)^{1/2} \int \mathrm{d}x\, P(x) e^{-2(x-\alpha\omega)^2/w_0^2}. \tag{3.6}$$

The convolution of the physical mask with the Gaussian intensity profile of the spectral components has the effect of limiting the frequency resolution of the shaper to $\delta\omega \approx (\ln 2)^{1/2} w_0/\alpha$. In the time domain, this translates into a maximum temporal window, T, within which the impulse response of the filter can be accurately implemented. The time window is specified by,

$$T = \frac{4\ln 2}{\delta w} = \frac{4\alpha(\ln 2)^{1/2}}{w_0} = \frac{2(\ln 2)^{1/2} w_{\mathrm{in}} \lambda_0}{cd\cos\theta_i}. \tag{3.7}$$

The lower bound for the temporal window is set by the time-bandwidth product, and is given by $\delta t = 0.44/(\Delta f)$ where Δf is the pulse bandwidth. The ratio of these limits defines a parameter $\eta = T/(\delta t)$ called the complexity, that describes the maximum number of spectral or temporal features that can be implemented. η can be expressed in terms of the grating parameters as,

$$\eta = \frac{\Delta\lambda}{\lambda}\frac{\pi}{(\ln 2)^{1/2}}\frac{w_{\mathrm{in}}}{d\cos\theta_{\mathrm{in}}}. \tag{3.8}$$

The plane ruled reflectance grating used in the pulse shaper has a blaze wavelength of $1.2\,\mu\mathrm{m}$, a blaze angle of $22\,^\circ$, and a groove period of $d = 1/600\,\mathrm{mm}$. It is used in the Littrow configuration as depicted in Fig. 3.5(a) such that $\theta_{\mathrm{in}} = \theta_{\mathrm{d}} = 22\,^\circ$. The pulse has a center wavelength of $\lambda_0 = 1160\,\mathrm{nm}$, a bandwidth of $\Delta\lambda = 18\,\mathrm{nm}$, and an input beam size of $w_{\mathrm{in}} = 3.5\,\mathrm{mm}$. An estimate of the limitations placed on the shaper system are presented in Tab 3.1 and show that the experiments are conducted well within the limits of the shaping system. The longest pulse generated for the ARP measurements presented in Ch. 6 is $\sim$3 ps. Equations 3.7 and 3.8 show that the input beam can be expanded to increase the temporal window T and complexity η because of the reduced spot-size in the Fourier plane.

Table 3.1: Experimental constraints imposed on the pulse shaping system as a result of the finite spot size at the Fourier plane. (See text for details.)

Parameter	**Value**
Spot size (w_0)	$61.5\,\mu\mathrm{m}$
Spatial dispersion (α)	$23.1\,\mathrm{cm}\cdot\mathrm{fs/rad}$
Frequency resolution ($\hbar\delta\omega$)	$0.145\,\mathrm{meV}$
Temporal window (T)	$12.5\,\mathrm{ps}$
Complexity (η)	114

3.5 Pulse Characterization

The optical control of qubits requires precise knowledge of the pulse characteristics, that in turn dictate the form of the interaction Hamiltonian. Characterization includes measurements of the pulse spectrum intensity and phase, the pulse width via the temporal intensity profile, and the focused beam waist at the sample. This section describes the methods used to measure these properties.

3.5.1 Dispersion Compensation Using MIIPS

It is of critical importance to the success of the quantum control experiments that the optimal phase mask be applied to a dispersion-compensated pulse, *i.e.* to a pulse $E_{\text{in}}(t)$ that is transform-limited with $\phi(t) = 0$ in Eqn. 2.33. However, propagation of the pulses through optical elements in the experimental apparatus introduces phase distortions that would frustrate any attempt to engineer the Bloch vector dynamics via control of the optical torque vector. We measure and compensate for dispersion using a phase-retrieval technique called multiphoton intrapulse interference phase scan. In contrast to two-beam techniques such as frequency-resolved optical gating (FROG) [160] and spectral phase interferometry for direct electric field reconstruction (SPIDER) [161], MIIPS [162] uses only a single pulse train and can be implemented at an equivalent focus to the sample. It uses the phase-dependence of the intensity of the second-harmonic generation (SHG) spectrum to infer the unknown spectral phase, $\phi(\omega)$, in the beam that must be compensated for to obtain a TL pulse. The experimental apparatus used in this technique is shown in Fig. 3.6. The laser beam passes through the $4f$ pulse shaper where a reference phase function $f(\omega)$ is added to the pulse. The shaped laser beam is focused onto a non-linear β barium borate (BBO) crystal to generate second harmonic light that is focused into an optical fiber connected to a spectrometer. The SHG spectrum provides feedback to the algorithm that determines the unknown phase, $\phi(\omega)$.

The intensity of the SHG signal can be expressed in terms of the spectral field strength $E(\omega)$ and phase $\varphi(\omega) = \phi(\omega) + f(\omega)$ of the fundamental as [163],

$$I(2\omega) \propto \left| \int |E(\omega+\Omega)||E(\omega-\Omega)| \exp\left\{i[\varphi(\omega+\Omega)+\varphi(\omega-\Omega)]\right\} d\Omega \right|^2 . \qquad (3.9)$$

The intensity at 2ω will be at a maximum when $\varphi(\omega+\Omega)+\varphi(\omega-\Omega) = 0$. A Taylor expansion of $\varphi(\omega+\Omega)+\varphi(\omega-\Omega)$ gives,

$$\varphi(\omega+\Omega)+\varphi(\omega-\Omega) = 2\varphi(\omega) + \Omega^2\varphi^{(2)}(\omega) + \ldots + \frac{2}{(2n!)}\Omega^{2n}\varphi^{(2n)} + \ldots , \qquad (3.10)$$

where $\varphi^{(n)}(\omega) = d^n\varphi(\omega)/d\omega^n$. Second-order phase distortions will be compensated by the reference function when $f^{(2)}(\omega) = -\phi^{(2)}(\omega)$. In experiments, a sinusoidal reference function is chosen, such that,

$$f(\omega) = \alpha \sin(\gamma\omega - \delta). \qquad (3.11)$$

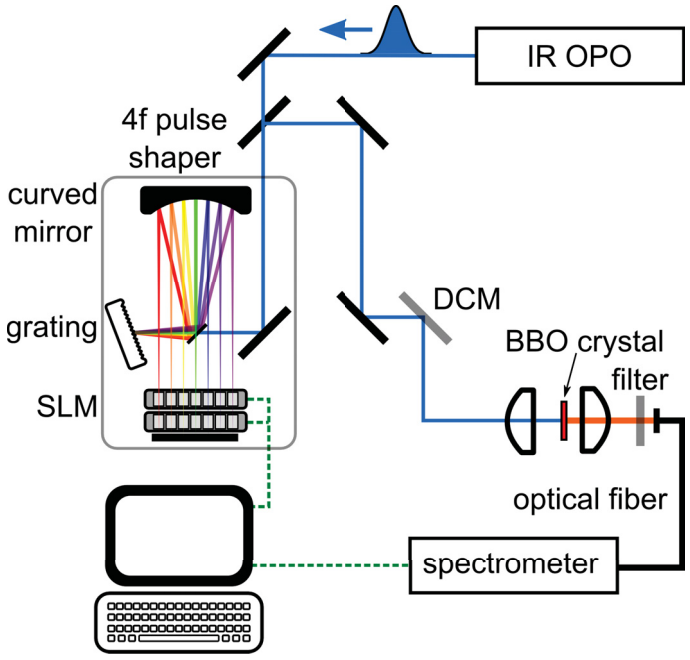

Figure 3.6: Experimental setup for MIIPS phase retrieval. The shaped pulses are focused into a non-linear BBO crystal and the SHG light is focused into an optical fiber coupled to a spectrometer. The spectral intensity data is used by the MIIPS computer algorithm to determine the phase distortions.

The phase factor δ is varied between between 0 and 4π radians. In this manner, $f^{(2)}(\omega)$ is swept between $\pm\alpha\gamma^2$. Typical values for the parameters of the reference function are: $\alpha = 1.5\pi$ and $\gamma = \tau_0$, where τ_0 is the pulse width of the TL pulse. The linear chirp is compensated when $f^{(2)}(\omega)$ cancels the phase distortions, such that,

$$\phi^{(2)}(\omega) = -f^{(2)}(\omega) = -\alpha\gamma^2 \sin\left[\gamma\omega - \delta_{\max}(\omega)\right]. \tag{3.12}$$

Figure 3.7 shows the so-called MIIPS trace: a plot of the SHG intensity as a function of the SHG wavelength, λ_{SHG}, and the phase parameter, δ, for (a) a chirped pulse and (b) a TL pulse.

The MIIPS trace also acts as a quick diagnostic tool, providing qualitative information about phase distortions in the pulse. For example, a TL pulse is characterized by parallel lines spaced π radians apart, because for $\phi^{(2)}(\omega) = 0$, the SHG intensity has a maximum at $\delta_{\max} = \gamma\omega \pm \pi/2$. The presence of second-order phase distortions manifests itself as irregular spacing between the lines of $\delta_{\max}$, while third-order distortions change the slope. Once the unknown phase, $\phi(\omega)$, is determined by double integration of $\phi^{(2)}(\omega)$, a compensation mask function equal to

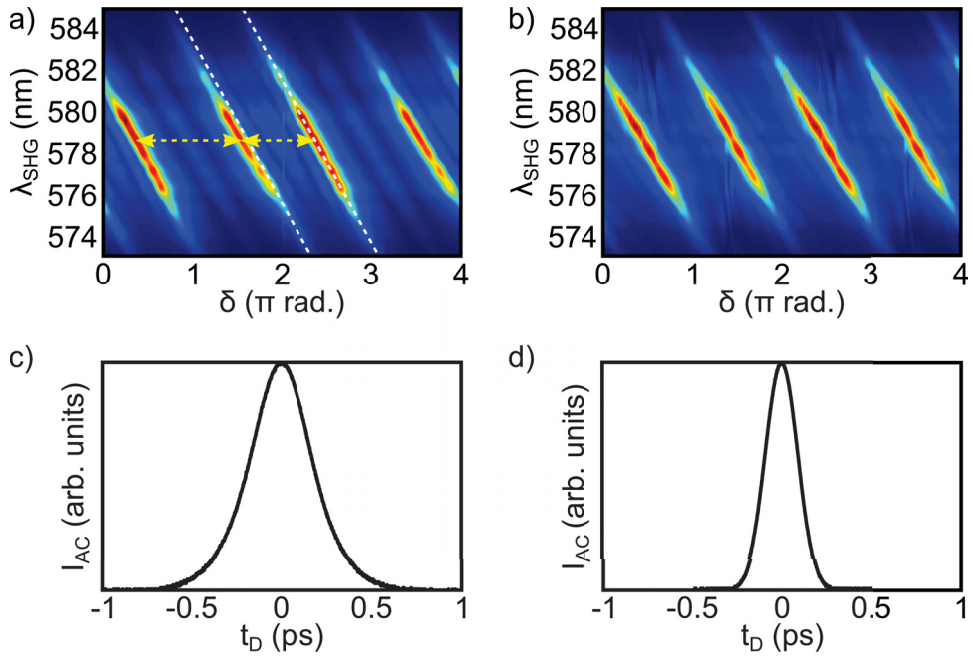

Figure 3.7: Characterization of phase distortions. (a), (b) MIIPS trace for (a) a laser pulse with phase distortions, and (b) a dispersion-compensated pulse. The plots show the SHG intensity as a function of the phase δ of the sinusoidal reference function, $f(\omega)$, and the second-harmonic wavelength. Unequal spacing between the diagonal lines of high intensity indicate the presence of linear chirp, while variations in their slope indicates the presence of third-order phase distortions. (c), (d) Intensity autocorrelations for (c) the uncompensated and (d) compensated pulses, with pulse widths of $257\,\mathrm{fs}$ and $137\,\mathrm{fs}$, respectively. The plots show the SHG intensity as a function of the delay between the pulse pair.

$-\phi(\omega)$ is added to the pulse. Higher order phase errors are removed by an iterative process that measures $\delta_{\max}(\omega)$ and retrieves higher-order phase errors. After six iterations, the pulse width is typically restored to within $0.2\,\%$ of the TL value, *i.e.*, $\tau/\tau_{\mathrm{TL}} \leq 1.002$. Figure 3.7(c) and (d) show measured autocorrelation intensity for a chirped laser pulse and dispersion-compensated pulse, with pulse widths of $257\,\mathrm{fs}$ and $137\,\mathrm{fs}$, respectively. (See Sec. 3.5.3 for a description of the autocorrelation measurement technique.)

3.5.2 Measurement of the Laser Spot Size

The average laser power, $P_{\rm avg}$, required for a Θ radian Rabi rotation, is given by [164],

$$P_{\rm avg} = \left(\frac{1.76}{\tau_0}\right)\left(\frac{\hbar\Theta}{\mu\pi}\right)^2 (\pi w^2)(c\epsilon_0 n)\nu_{\rm rep}, \tag{3.13}$$

where τ_0 is TL pulse width for a sech^2 pulse, μ is the dipole moment, w is the $1/e^2$ radius of the focused laser beam, n is the index of refraction of GaAs, and $\nu_{\rm rep}$ is the repetition rate of the laser. (All parameters are in International System of Units (SI) units.) An effective method of reaching larger pulse areas, for a given average power, is to minimize the laser spot size (w). In our experiment, w was determined using a knife-edge measurement where the laser beam was scanned across the edge of the deposited gold mask and onto the GaAs sample surface. The reflected laser intensity was measured with an InGaAs photodiode using an optical chopper and lock-in techniques. If the laser spot is assumed to have a Gaussian intensity profile and the metal-to-semiconductor transition is modelled as a step function at $x = x_0$, the reflected intensity can be fit to the convolution of the two functions, such that,

$$I(x) = I_0 + \frac{\Delta I}{2}\mathrm{erfc}\left[\sqrt{2}\left(\frac{x_0 - x}{w}\right)\right], \tag{3.14}$$

where $\mathrm{erfc}(x)$ is the complementary error function, and ΔI is the difference in reflected intensity between the metallic and semiconductor surfaces. The QD sample sits on a nano-positioning stage that can be moved by applying a voltage. To carry out the spot-size measurement, one must first determine the step size of the stage which varies with temperature and applied voltage. The calibration was carried out by scanning across a row of alignment "teeth" (see Fig. 3.3 on the gold masks which has a period of $20\,\mu\mathrm{m}$. Figure 3.8(a) shows the periodic variations in the reflected laser intensity as a function of the number of steps taken on the stage. The step size was determined to be $178\,\mathrm{nm}$ (at room temperature with an applied voltage of $30\,\mathrm{V}$). The reflected laser intensity for the spot size measurement is shown in Fig. 3.8(b) as circles. A fit to Eqn. 3.14 (blue curve) gives a spot size $w = 1.7\,\mu\mathrm{m}$.

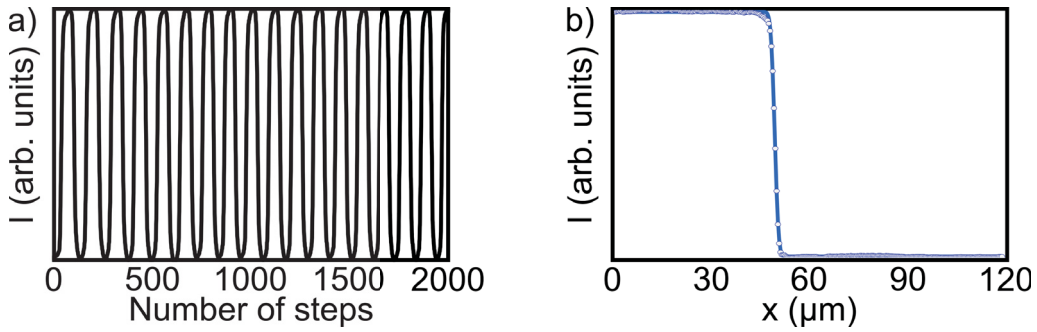

Figure 3.8: (a) Attocube step size calibration curve showing reflected laser intensity as a function of steps. (b) Reflected laser intensity (circles) as a function of the Attocube stage position and a fit to the data (curve) using Eqn. 3.14.

3.5.3 Measuring Pulse Width

The experiments carried out in Ch. 6 examined the effects of increasing linear spectral chirp on the transition to the ARP regime. An increase in chirp increases the TL pulse width to, $\tau_p = \tau_0[1 + (4\ln 2\phi'')^2/\tau_0^4]^{1/2}$ for a Gaussian pulse. The TL and chirped pulse widths were measured using non-collinear autocorrelation. In this technique, a beam splitter is used to create a copy of the pulse that travels down a variable delay line consisting of a retroreflector mounted on a linear stage (see Fig. 3.9(a)). The beams, propagating with wavevectors $\mathbf{k_1}$ and $\mathbf{k_2}$, are focused onto the same spot on a non-linear BBO crystal to induce sum-frequency generation (SFG). Photons with energy $\hbar\omega_1$ and $\hbar\omega_2$ are annihilated and a single photon with energy $\hbar(\omega_1 + \omega_2)$ and wavevector $\mathbf{k_1} + \mathbf{k_2}$ is created. The intensity of the SFG signal is measured as a function of the time delay between the pulses using a silicon photodetector and lock-in techniques. If the two pulse trains are identical, the measured intensity is an autocorrelation of the field intensity of the beam, given by,

$$I_{\mathrm{AC}}(\tau) \propto \int_{-\infty}^{\infty} dt\, I(t)I(t-\tau) \tag{3.15}$$

The FWHM of the autocorrelation signal, $\tau_{\mathrm{FWHM,AC}}$, is proportional to that of the optical pulse, with a deconvolution factor that is determined by the pulse shape. For example, the FWHM pulse width of a Gaussian pulse is $\tau_{\mathrm{FWHM}} = 0.707\tau_{\mathrm{FWHM,AC}}$ [165]. Figure 3.7(c) and (d) show examples of measured autocorrelation signals for a chirped laser pulse and dispersion-compensated pulse, respectively.

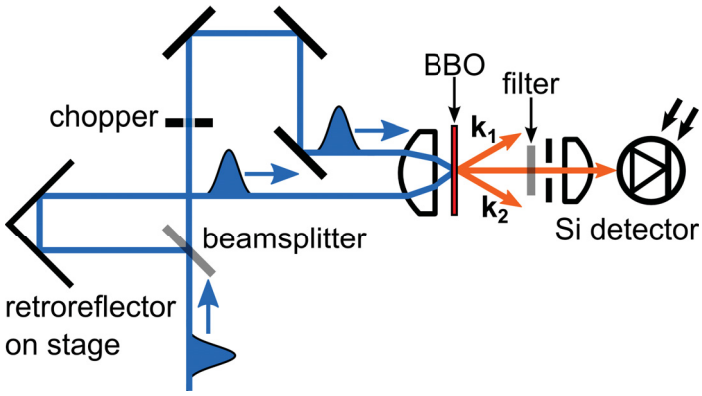

Figure 3.9: Autocorrelation technique: the pulse is mixed with a copy in a nonlinear BBO crystal. The SFG light emitted in the $\mathbf{k_1} + \mathbf{k_2}$ direction is measured by a silicon detector using lock-in techniques as a function of the inter-pulse delay.

Chapter 4

Simultaneous SU(2) Rotations on Multiple Quantum Dot Exciton Qubits Using a Single Shaped Pulse

Authors: Reuble Mathew[1], Hong Yi Shi Yang[1], and Kimberley C. Hall[1]

[1]Department of Physics and Atmospheric Science, Dalhousie University, Halifax, Nova Scotia B3H4R2, Canada

Submitted to Physical Review B on 25 June 2015. Reuble Mathew developed the pulse shaping computer code and used it to carry out the theoretical simulations and the data analysis. Hong Yi Shi Yang ran simulations to explore the parameter space. Kimberley C. Hall and Reuble Mathew conceived the direction for research. Kimberley C. Hall and Reuble Mathew wrote the manuscript with input from all authors.

4.1 Abstract

Recent experimental demonstration of a parallel (π, 2π) single qubit rotation on excitons in two distant quantum dots [Nano Lett. 13, 4666 (2013)] is extended in numerical simulations to the design of pulses for more general quantum state control, demonstrating the feasibility of full SU(2) rotations of each exciton qubit. Our results show that simultaneous high-fidelity quantum control is achievable within the experimentally-accessible parameter space for commercial Fourier-domain pulse shaping systems. The identification of a threshold of distinguishability for the two quantum dots (QDs) for achieving high-fidelity parallel rotations, corresponding to a difference in transition energies of $\sim 0.25\,\mathrm{meV}$, points to the possibility of controlling more than 10 QDs with a single shaped optical pulse.

4.2 Introduction

Optimal quantum control (OQC) describes the science of controlling the evolution of quantum systems to transfer an initial state to a desired final state [113, 114]. (For a recent review, see Ref. [166].) In quantum systems controlled by laser fields, one can use sophisticated pulse-shaping techniques coupled with closed-loop evolutionary algorithms to manipulate the interaction Hamiltonian that governs the dynamics. Adaptive algorithms are particularly effective for the optimization of imprecisely characterized systems [167, 123] or for those with a numerically intractable system Hamiltonian. They have, for example, been used to control chemical reaction pathways [115, 116], to detect molecular species [117], and to generate high harmonics [118, 119]. In the field of quantum information science, OQC may be applied to the optimization of quantum gate fidelity and/or operating speed. This approach has been applied in recent experiments involving multiple-qubit gates in trapped ion systems [122] and superconducting qubits [123], as well as spin entanglement in nitrogen vacancies [124]. OQC could also aid in the development of complex instruction set approaches to quantum computing, wherein multiple single- and two-qubit gates are replaced with a single system transformation, reducing the time required to carry out the computation while exploiting the relative ease of control pulse engineering [6]. Progress along these lines has been realized in molecular qubit systems with the demonstration of a multiple-input AND gate [7]. The achievement of such goals in scalable solid state systems is particularly attractive due to the advantages of such platforms in terms of future integration with classical technologies.

Among the solid state systems being explored for quantum-enabled device development, semiconductor quantum dots offer a number of advantages. A QD-based device architecture would leverage existing semiconductor and photonic fabrication infrastructure with the possibility of optically-mediated quantum state control and readout at telecommunication wavelengths, facilitating integration with existing hardware. The implementation of short laser pulses for rapid manipulation of QD excitations paves the way toward fast quantum gates and potential THz operation rates. Demonstrations of fundamental quantum control processes involving charge and spin states in QDs have included single-qubit rotations of excitons

[15, 53, 50, 52, 57], biexcitons [168, 82], and single carrier spins [99, 104], quantum state tomography [49, 52, 70, 71, 20, 72, 111], manipulation of exciton spin superpositions [169, 170], the establishment of entanglement between excitons [16, 81, 171], and the use of an optical microcavity for selective control of QDs within an ensemble [172]. These studies illustrate the ease of coherent optical control of quantum states within semiconductor QDs; however, the exclusive use of control pulses with constant phase severely limits the scope and flexibility of the quantum control process.

The extension of the above optical control experiments to tailored quantum state control via OQC in QDs has been explored in recent years [173, 125, 174]. A reduction in the control pulse duration for a C-ROT gate involving two exciton qubits confined to a single QD [16, 38] to the subpicosecond regime was demonstrated in numerical applications of OQC [174, 173], where pulse shaping ensured the achievement of high-fidelity conditional dynamics despite the large pulse bandwidth. General pulse shape engineering has also been applied experimentally in the implementation of simultaneous π and 2π single qubit rotations in two uncoupled QDs using a single laser pulse [125]. These proof-of-principle experiments demonstrated the feasibility of parallel quantum computing enabled by the stochastic variations in optoelectronic properties that result from the quantum dot self-assembly process. In this work, we numerically explore the ability to achieve independent SU(2) control of excitons in a pair of quantum dots using a single shaped pulse. Our calculations show that high fidelity parallel qubit rotations can be found for an arbitrary choice of state inversions and phases of the two exciton qubits provided the pair of QDs utilized have sufficiently different optoelectronic properties: A difference in *either* the dipole moment ($\sim 2\,\mathrm{Debye}$) *or* transition energy ($>0.25\,\mathrm{meV}$) is sufficient, commensurate with typical variations in self-assembled quantum dot ensembles [54, 175, 176, 57, 21]. These findings demonstrate the feasibility of parallel quantum state control in systems of more than 10 quantum dots using conventional laser and pulse shaping systems. The simultaneous manipulation of multiple qubits using a single shaped laser pulse would help reduce the required laser resources for qubit control and promote scalability of these systems for quantum information processing.

4.3 Optimal Quantum Control: Numerical Methods

We model each QD as a two-level system, defined by states $|0\rangle$ and $|1\rangle$ that are separated in energy by $\hbar\omega_{10}$. The qubits possess an optical dipole moment $\boldsymbol{\mu}_{10} = \langle 1|\,\boldsymbol{\mu}\,|0\rangle$, which allows for manipulation using an ultrafast laser pulse with an electric field given by

$$\mathbf{E}(t) = \frac{1}{2}\hat{\boldsymbol{\epsilon}} E_0(t)\left\{e^{-i[\omega_l t+\phi]} + e^{+i[\omega_l t+\phi]}\right\}. \tag{4.1}$$

Here $\hat{\boldsymbol{\epsilon}}$ is a unit vector representing the polarization state of the laser field, $E_0(t)$ is the field envelope, ω_l is the center frequency of the laser pulse, and ϕ is the pulse phase. The control Hamiltonian for the two-level system in the presence of the light field is given in the rotating wave approximation (RWA) by

$$H = \frac{\mathrm{Re}[\hbar\Omega_R]}{2}\hat{\sigma}_x + \frac{\mathrm{Im}[\hbar\Omega_R]}{2}\hat{\sigma}_y + \frac{\hbar\Delta}{2}\hat{\sigma}_z, \tag{4.2}$$

where $\hbar\Omega_R = (\boldsymbol{\mu}_{10}\cdot\hat{\boldsymbol{\epsilon}})\; E_0(t)e^{-i\phi}$ is the complex Rabi energy, $\Delta = \omega_{10} - \omega_l$ is the detuning of the laser from the QD transition, and $\hat{\sigma}_{x,y,z}$ are the Pauli spin matrices. The resulting equation of motion for the Bloch vector $\mathbf{s}$, where $s_j = \langle\hat{\sigma}_j\rangle$, is

$$\dot{\mathbf{s}} = \mathbf{s}\times\boldsymbol{\Lambda}, \tag{4.3}$$

which describes the rotation of the Bloch vector about a torque vector $\boldsymbol{\Lambda} = (-\mathrm{Re}[\Omega_R], -\mathrm{Im}[\Omega_R], \Delta)$ determined by the characteristics of the optical pulse.

During a Rabi rotation, for which $\Delta = 0$ and ϕ is constant in time, the direction of $\boldsymbol{\Lambda}$ does not change during the control pulse and the Bloch vector rotates about a fixed axis. Shaping the laser pulse (*e.g.* by incorporating a time-dependent phase $\phi(t)$) leads to a time-dependent control vector $\boldsymbol{\Lambda}$, thereby allowing for deterministic control over the trajectory of the Bloch vector and/or the choice of target final quantum state. We demonstrate the versatility of this approach to coherent control of multiple solid state qubits by applying general pulse engineering to the optimization of simultaneous single qubit rotations for excitons confined to two uncoupled quantum dots, referred to as QD1 and QD2. This approach was used in Ref. [125] to implement simultaneous (π, 2π) rotations, representing an experimental demonstration of independently specified occupation states. Here we extend this to the design of numerically-optimized pulses for arbitrary SU(2) control of the two quantum dot excitons.

In the general case, the amplitude, phase and frequency of the control laser pulse can be manipulated in either the time domain by using devices such as acousto-optic modulators, or in the frequency domain by placing controllable elements in the Fourier plane of a $4f$ pulse shaper. The most common approach for frequency-domain shaping, for which the optimum pulse shapes obtained here are intended, is to use a programmable liquid crystal spatial light modulator (SLM) containing an array of nematic liquid crystal elements each with an electrically tunable index of refraction [112]. The effect of the SLM in the Fourier plane on the laser pulse can be described by a mask function $M(\omega)$ that alters the input pulse spectrum $\tilde{E}_{\rm in}(\omega)$ to produce an output spectrum, $\tilde{E}_{\rm out}(\omega)$, given by

$$\tilde{E}_{\rm out}(\omega) = M(\omega)\tilde{E}_{\rm in}(\omega). \tag{4.4}$$

The input pulse spectrum $\tilde{E}_{\rm in}(\omega)$ is the Fourier transform of a Gaussian pulse with constant phase ϕ and a field envelope $E_0(t) = |E_0| \exp\left[-2\ln(2)t^2/\tau^2\right]$, with $\tau = 120\,\mathrm{fs}$. A dual-mask SLM can provide independent control over the amplitude and phase of the frequency components, such that the mask function can be defined in terms of an amplitude mask $A_M(\omega)$ and phase mask $\phi_M(\omega)$, where

$$M(\omega) = A_M(\omega) \exp\left[i\phi_M(\omega)\right]. \tag{4.5}$$

The desired form of $A_M(\omega)$ and $\phi_M(\omega)$ can be determined using numerical techniques that optimize any desired attribute of the quantum control process. In this work, we apply OQC to optimize the fidelity of parallel single qubit rotations involving multiple uncoupled semiconductor QDs.

We apply a phase-only mask ($A_M(\omega) = 1$), which has the advantage of reducing light losses in the system [173]. Any convenient function may be used to parametrize $\phi_M(\omega)$. Here we adopt a sinusoidal phase mask, given by

$$\phi_M(\omega) = \alpha \cos\left[\gamma(\omega - \omega_l) - \delta\right]. \tag{4.6}$$

The parameters α, γ, δ, and the pulse area $\Theta = (\boldsymbol{\mu}\cdot\hat{\boldsymbol{\epsilon}}/\hbar)\int_{-\infty}^{+\infty} E_0(t)\,\mathrm{d}t$ are optimized

numerically subject to the following constraints:

$$\begin{aligned} 0 \leq &\alpha \leq \pi, \\ 0 \leq &\gamma \leq 325\,\mathrm{fs}, \\ -\pi \leq &\delta \leq \pi, \\ 0 \leq &\Theta \leq 8\pi. \end{aligned} \tag{4.7}$$

The limits on α and γ are chosen to restrict the gradient in the phase $|\mathrm{d}\phi_M(\omega)/\mathrm{d}\omega|_{\max}$ to $\pi/10$ radians per pixel assuming the resulting optimized pulses are implemented on a pulse shaping system containing a 128-pixel SLM. This is a conservative requirement as commercial pulse shapers with a pixel count of 640 are readily available. (The implications of the resolution of the phase mask are discussed in more detail below.) The constraints on Θ are intended to simplify the experimental implementation, although Rabi rotations of up to 14π have been achieved in similar QDs [69].

For a given choice of the parameters in Eqn. 4.6, the fidelity of the operation is defined as $F = \mathrm{Tr}[\rho_{\mathrm{P}}\rho_{\mathrm{I}}] = f(\alpha, \gamma, \delta, \Theta)$, where ρ_{P} is the physical density matrix at the end of the control process, calculated by integrating Eqn. 4.3, and ρ_{I} is the ideal density matrix for the intended parallel single qubit rotation. We search for local optima in fidelity $F_{\mathrm{opt}} = f(\alpha_{\mathrm{opt}}, \gamma_{\mathrm{opt}}, \delta_{\mathrm{opt}}, \Theta_{\mathrm{opt}})$ by choosing initial vectors containing the free parameters α, γ, δ, and Θ, denoted by $q_i = (\alpha_i, \gamma_i, \delta_i, \Theta_i)$, and using the constrained optimization by linear approximations algorithm. We choose 500 initial vectors using a Sobol' sequence [177] to provide sufficient coverage of the four-dimensional space defined by Eqn. 4.7. The parameters corresponding to local optima with the highest fidelity determine the optimal pulse shape. In the RWA, the phase of the qubit oscillates at a frequency Δ even after the end of the pulse. Therefore, we determine the fidelity of the control process by reading the state of the qubits at a fixed time $t = 3\,\mathrm{ps}$ after the arrival of the laser pulse ($t = 0$ in Eqn. 4.1). In experimental implementations of quantum algorithms, flexibility in the timing of multiple control pulses would likely be exploited. The stringent requirement of a fixed read time allows us to explore the quality of arbitrary final state control under the most conservative conditions.

4.4 Results and Discussion

4.4.1 Arbitrary Rotations of QD Excitons

Figure 4.1 presents exemplary results of parallel control of excitons in two different QDs. For all results in this work, the laser pulse has a fixed tuning with $\hbar\omega_l = 1.0\,\mathrm{eV}$. For the calculation in Fig. 4.1, the transition energies of the two QDs are $\hbar\omega_{\mathrm{QD1}} = 1.00125\,\mathrm{eV}$ and $\hbar\omega_{\mathrm{QD2}} = 0.99875\,\mathrm{eV}$, chosen to be within the bandwidth of the controlling laser pulses, and the dipole moments are taken as $\mu_{\mathrm{QD1}} = 25\,\mathrm{Debye}$ and $\mu_{\mathrm{QD2}} = 28\,\mathrm{Debye}$, reflecting typical values for self-assembled QDs [57]. For these results, the pulse is optimized assuming that the qubits are initialized in their respective ground states ($|\psi_{\mathrm{QD1}}\rangle_{\mathrm{i}} = |0\rangle$, $|\psi_{\mathrm{QD2}}\rangle_{\mathrm{i}} = |0\rangle$) with a target set of final states for the two QDs given by

$$\begin{aligned} |\psi_{\mathrm{QD1}}\rangle_{\mathrm{f}} &= \frac{1}{2}\left(|0\rangle + e^{-i\pi/2}\sqrt{3}\,|1\rangle\right), \text{ and} \\ |\psi_{\mathrm{QD2}}\rangle_{\mathrm{f}} &= \frac{1}{2}\left(\sqrt{3}\,|0\rangle + e^{-i3\pi/2}\,|1\rangle\right). \end{aligned} \tag{4.8}$$

The final quantum states in Eqn. 4.8 contain different state inversions and phases for the two QDs, providing a useful test to illustrate the OQC approach. Figure 4.1(a) shows the trajectory of the Bloch vector of QD1 (QD2) when driven by the optimized laser field, represented by the black solid (red dashed) curves, with the final quantum state of the two-dot system at the chosen read time of 3 ps indicated by the black (red) dot. The target final states in Eqn. 4.8 for QD1 (QD2) are indicated on the Bloch sphere by a black (red) cross. The optimal pulse, characterized by parameters $q_{\mathrm{opt}} = (0.312\pi, 235\,\mathrm{fs}, 0.373\pi, 3.25\pi)$, implements the simultaneous qubit rotation with a fidelity of 0.996. This high fidelity is evident on the Bloch spheres by the close proximity of the final states for each QD and the respective target final states. Figure 4.1(b) shows the spectral intensity (black solid curve) and phase (blue dashed curve) of the corresponding optimal pulse, and Fig. 4.1(c) shows the resulting temporal field intensity. The temporal evolution of the three components of the optical torque vector, $\mathbf{\Lambda}$, that drives the qubit dynamics of QD1 (QD2) are shown in Fig. 4.1(d) as solid (dashed) curves. The high-fidelity control process depicted in Fig. 4.1(a), with a target final state that differs for the two quantum dots in both inversion and phase, illustrates the efficacy of pulse shape

control for independently tailoring the quantum state dynamics of the excitons in the two quantum dots.

We explore the flexibility of this scheme for achieving a range of final states by optimizing the fidelity as a function of the difference in inversion, denoted by $\delta s_z = s_{z,QD2} - s_{z,QD1}$, taking $s_{z,QD2} = -s_{z,QD1}$, and the difference in phase of the two qubits, denoted by $\delta\phi = \phi_{QD2} - \phi_{QD1}$, taking $\phi_{QD2} = -\phi_{QD1}$. The resulting final state space spans all representative states on the Bloch spheres for the two QDs. The input laser characteristics, QD initial states, transition frequencies, and dipole moments are identical to those used for the calculated results in Fig. 4.1. The featureless contour plot in Fig. 4.2(a) demonstrates that optimized pulses producing high fidelity can be found for any choice of δs_z and $\delta\phi$ within the defined parameter space of Eqn. 4.7. This result indicates that arbitrary independent high-fidelity control of the two quantum dot excitons is feasible using the OQC approach and general pulse shape engineering.

4.4.2 Dependence on QD Optoelectronic Properties

Next we implement the control process in Eqn. 4.8 and allow the optoelectronic properties of QD2 to vary while holding the properties of QD1 constant. The results of these calculations are presented in Fig. 4.2(b). If the QDs have nearly identical optoelectronic properties, it is impossible to find any pulse shape that drives the qubits from the same initial state to two different final states with high fidelity, leading to the dip in fidelity in Fig. 4.2(b) where the properties of QD1 and QD2 coincide. Nevertheless, for QDs with sufficiently different properties, optimized pulses can be engineered to implement the parallel single qubit rotation with high fidelity. In particular, it is not necessary to have a difference in both the dipole moment and transition energy for the two QDs: a difference in *either* property will suffice. This is evident from calculations that optimize the same control process as in Fig. 4.1 as a function of the dipole moments while holding the transition frequencies constant (Fig. 4.2(c)), and as a function of the transition frequencies while holding the dipole moments constant (Fig. 4.2(d)). In all cases, we find that control pulse shapes realizing high fidelity gates may be found within the accessible parameter space of the pulse shaping system.

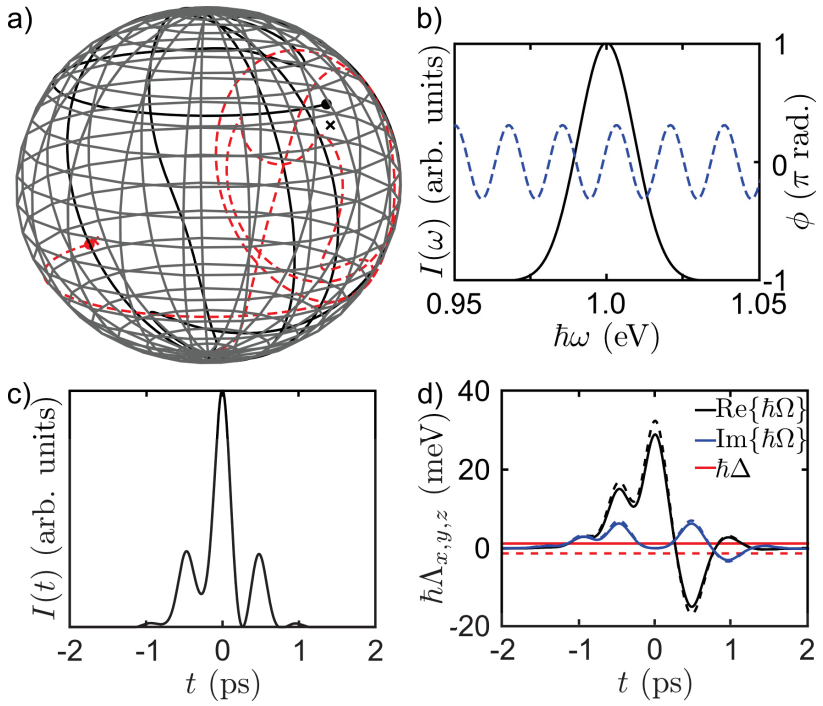

Figure 4.1: Application of OQC to quantum control transferring the excitons in QD1 and QD2 from their respective ground states to the final states in Eqn. 4.8. (a) Bloch sphere dynamics for QD1 (QD2) are indicated by a black solid (red dashed) curve. (b) The spectral amplitude (phase) of the pulse are indicated by a black solid (blue dashed) curve. (c) Temporal intensity of the shaped pulse. (d) The x, y, and z components of $\mathbf{\Lambda}$ are indicated by black, blue, and red curves, respectively, with solid curves corresponding to QD1 and the dashed curves corresponding to QD2.

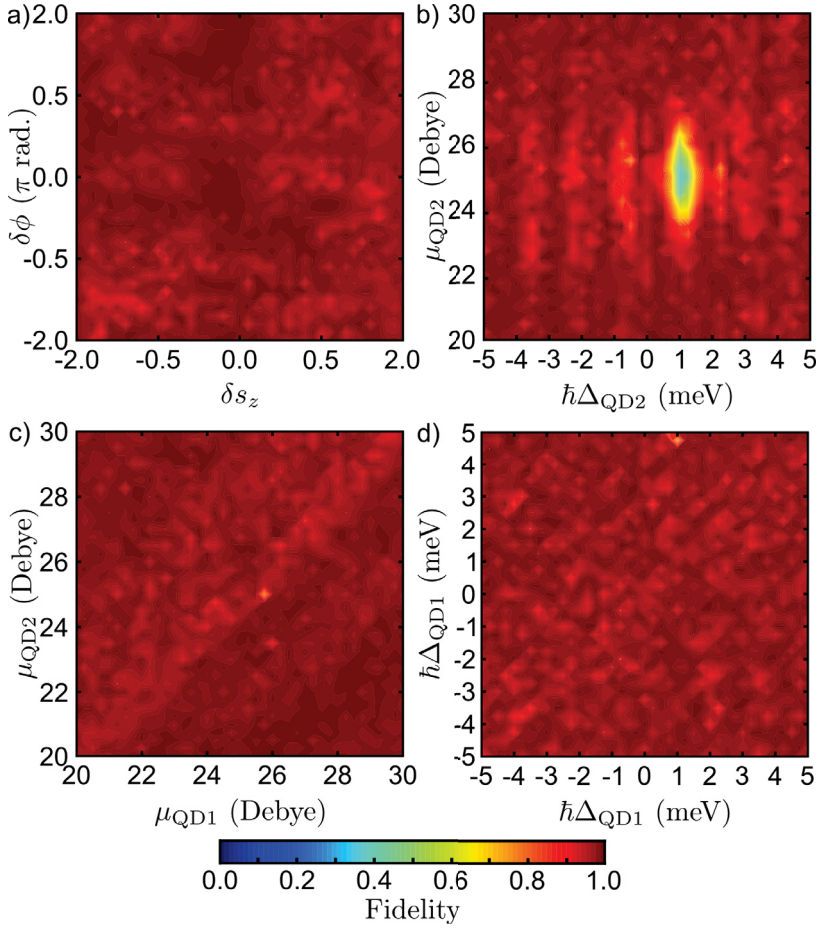

Figure 4.2: (a) Optimized fidelity as a function of the difference in phase and inversion of the two qubits for the optoelectronic properties used in Fig. 4.1. (b), (c), (d) Optimized fidelity of the quantum control process shown in Fig. 4.1 as a function of (b) the detuning of QD2 from the laser frequency ($\hbar\Delta_{\mathrm{QD2}} = \hbar(\omega_{\mathrm{QD2}} - \omega_l)$) and its dipole moment, while holding the properties of QD1 constant ($\hbar\omega_{\mathrm{QD1}} = 1.00125\,\mathrm{eV}$ and $\mu_{\mathrm{QD1}} = 25\,\mathrm{Debye}$), (c) the dipole moment of the two quantum dots while holding the transition frequencies constant ($\hbar\omega_{\mathrm{QD1}} = 1.00125\,\mathrm{eV}$ and $\hbar\omega_{\mathrm{QD1}} = 0.99875\,\mathrm{eV}$), and (d) the detuning of the QD transitions from the laser frequency while holding the dipole moments constant ($\mu_{\mathrm{QD1}} = 25\,\mathrm{Debye}$ and $\mu_{\mathrm{QD2}} = 28\,\mathrm{Debye}$).

4.4.3 Parallel Quantum Control: Scaling the Approach

The optimization scheme described here may be extended to independent simultaneous control of excitons in more than two quantum dots. The results in Fig. 4.2(b) show that independently addressing distinct QDs is possible provided that their optoelectronic properties are sufficiently different. Since the dipole moment and transition energy have been found to be systematically linked for self-assembled QDs [178, 176], we will focus here on differences in the transition energy. The width of the dip in fidelity in Fig. 4.2(b) versus transition energy is limited by the resolution of the SLM, which was assumed to contain 128 pixels. The calculation of Fig. 4.2(b) was repeated assuming a higher-resolution pulse shaping system incorporating a 640 pixel SLM. The results of these calculations are shown in Fig. 4.3. A larger SLM resolution expands the available parameter space for α and γ in Eqn. 4.7 while keeping the maximum phase change per pixel constant. In Fig. 4.3, the width of the low-fidelity feature is below the resolution of the calculation mesh ($0.25\,\mathrm{meV}$). For typical self-assembled QD ensembles, the transition energy spread is in the range $30\,\mathrm{meV}$ to $70\,\mathrm{meV}$ depending on the growth conditions and type of barrier material [54, 21]. Assuming a threshold distinguishability of $0.25\,\mathrm{meV}$ in the transition energy, this indicates that simultaneous control of several ($>$10) QDs should be readily achievable. If combined with controllable entanglement between distant quantum dots via microcavity modes [42], this approach may enable the realization of complex instruction set quantum computing in a solid state system of QDs. This would build upon recent progress involving molecular qubit systems, in which a multiple-input AND gate was realized using six qubits encoded in the rovibrational eigenstates of a lithium molecule [7]. One could foresee engineering the QD ensemble size distribution to have a spread of transition energies that matches the bandwidth of convenient commercial laser systems, in line with successful efforts to obtain narrow energy distributions coinciding with telecommunications wavelengths for QD laser applications [21]. Numerically-optimized quantum control involving three QDs is shown in Fig. 4.4, illustrating the flexibility of the OQC approach as the number of QDs is increased. The use of a more sophisticated phase mask function rather than the simple sinusoidal mask used here, as well as the freedom to employ combined amplitude and phase control, would aid in optimizing the

performance of parallel quantum control of multiple quantum dots.

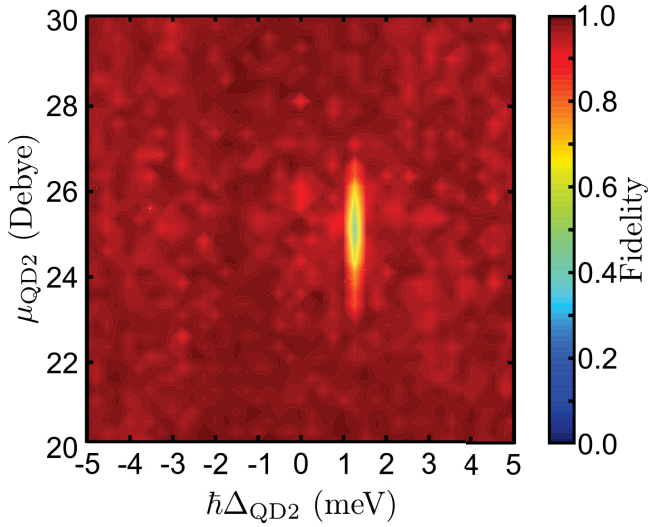

Figure 4.3: Same calculation as in Fig. 4.2(b) taking the assumption of a higher resolution pulse shaping system, incorporating a 640 pixel SLM.

4.4.4 Tolerance to Experimental Uncertainties

In the presence of uncertainties in experimental parameters, the fidelity of the control process will be reduced. The primary limitation on the sensitivity of the fidelity to such non-ideal conditions is the choice here to impose a fixed read time ($3\,\mathrm{ps}$ after $t = 0$ in Eqn. 4.1) due to the rapid evolution of the phase of the exciton qubit in any particular QD outside the pulse envelope. For instance, a laser tuning error of $0.05\,\mathrm{nm}$ produces a drop in fidelity of 0.01 averaged over the parameter space in Fig. 4.2(a). For comparison, the fidelity is much less sensitive to deviations in laser intensity: A typical specification for mode-locked laser systems of $0.5\,\%$ gives a fidelity drop of only 0.001. In the implementation of circuit-model quantum computing with multiple control pulses, one could minimize such errors experimentally by incorporating active feedback on the relative time delays for different control pulses. Small deviations in qubit phase could also be compensated for by implementing empirical feedback to the pulse shaping system, so that the optimum mask parameters may be adjusted via a genetic algorithm. Such an approach would also benefit complex instruction set implementations. Quantum state readout via differential transmission [62] or photocurrent [53] are only sensitive to the state

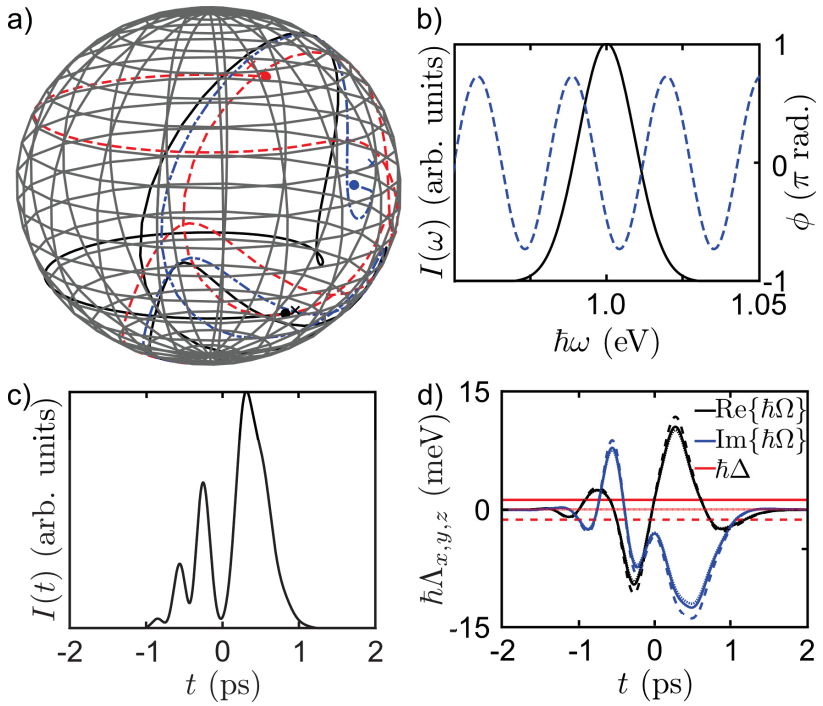

Figure 4.4: Application of OQC to the simultaneous manipulation of excitons in three QDs. For this calculation, the final state of the third quantum dot, QD3, with $\hbar\omega_{\mathrm{QD3}} = 1.00005\,\mathrm{eV}$ and $\mu_{\mathrm{QD3}} = 24\,\mathrm{Debye}$, is $|\psi_{\mathrm{QD3}}\rangle_{\mathrm{f}} = (|0\rangle + e^{-i3\pi/4}\,|1\rangle)/\sqrt{2}$, while for QD1 and QD2, the final states are given by Eqn. 4.8. (a) Bloch sphere dynamics for QD1, QD2, and QD3 are indicated by the black solid curve, the red dashed curve, and the blue dot-dashed curve, respectively. The optimal pulse in this case is defined by $q_{\mathrm{opt}} = (0.730\pi, 134\,\mathrm{fs}, -0.726\pi, 2.12\pi)$ and when implemented results in a quantum gate fidelity of 0.985. (b) The spectral amplitude (phase) of the pulse is indicated by a black solid (blue dashed) curve. (c) Temporal intensity of the shaped pulse. (d) The x, y, and z components of $\mathbf{\Lambda}$ are indicated by black, blue, and red curves, respectively, with solid curves corresponding to QD1, dashed curves corresponding to QD2, and dot-dashed curves corresponding to QD3.

occupations and so phase uncertainty would have no impact on the final quantum state detection. We also note that, while biexciton dynamics are not included in the present calculations, in full simulations of the coupled exciton-biexciton system it is possible to build into the OQC optimization the need to have the occupation of the biexciton state vanish at the end of the control pulse, as shown for the case of the C-ROT gate in Ref. [174].

4.4.5 Influence of Dephasing

It is instructive to examine the influence of sources of dephasing of the exciton qubit on the fidelity of the quantum control process. Calculations within the relaxation time approximation incorporating typical measured dephasing and recombination times in InAs self-assembled QDs [86] indicate only a minor reduction in fidelity (*e.g.* a drop from 0.996 to 0.991 for the test gate in Fig. 4.1), reflecting the short time scale of the optical pulse relative to these decay times. We also examine the effects of a power-dependent dephasing process, often referred to as *excitation-induced* dephasing (EID), in which deformation potential coupling with longitudinal acoustic phonons causes transitions between the dressed states of the optically-driven quantum dot system [90, 69, 25, 137, 138]. Such a process leads to damping of Rabi oscillations [69, 25], and a dependence of the exciton inversion on the sign of pulse chirp in adiabatic rapid passage experiments [91, 179]. The strength of the EID process is dictated by the real part of the exciton-phonon response function, $K(\omega)$, which is evaluated at the instantaneous value of $|\mathbf{\Lambda}|$. Taking a linear dispersion relation for the bulk phonon modes of the barrier material (chosen here as GaAs, appropriate for InAs/GaAs self-assembled quantum dots), and assuming a spherical quantum dot for simplicity with a carrier wave function of the form $\psi(x) \propto \exp\left[-2\ln(2)x^2/d^2\right]$, the exciton-phonon response function is given by [137],

$$\mathrm{Re}[K(\omega)] = \frac{\pi}{2}\alpha\omega^3 e^{-\omega^2/\omega_c^2}\coth\left(\omega/2k_BT\right), \tag{4.9}$$

where α is a coupling constant that depends on the deformation-potential constants of the barrier material, T is the temperature, and k_B is the Boltzmann constant. The exciton-phonon response function is characterized by a cut-off frequency, ω_c, that is inversely proportional to the spatial extent of the wave function, d [90]. This

implies that the impact of EID on the fidelity of the quantum control process depends on both the size of the quantum dot and the magnitude of the instantaneous Rabi energy. Figure 4.5 shows the fidelity for the calculation shown in Fig. 4.1 as a function of $\hbar\omega_c$ and d for $T = 10\,\mathrm{K}$. For cut-off energies less than $\sim 1.38\,\mathrm{meV}$ ($d > 5.76\,\mathrm{nm}$), the reduction in fidelity is less than $2\,\%$. This error is quite modest, but nevertheless would be reduced by incorporating EID into the OQC numerical optimization due to the dependence of this process on the pulse shape. In addition, the exploration of alternate mask parameterizations may be beneficial. The use of engineered quantum dot distributions with a larger mean size would also reduce the influence of EID and increase the fidelity of quantum control.

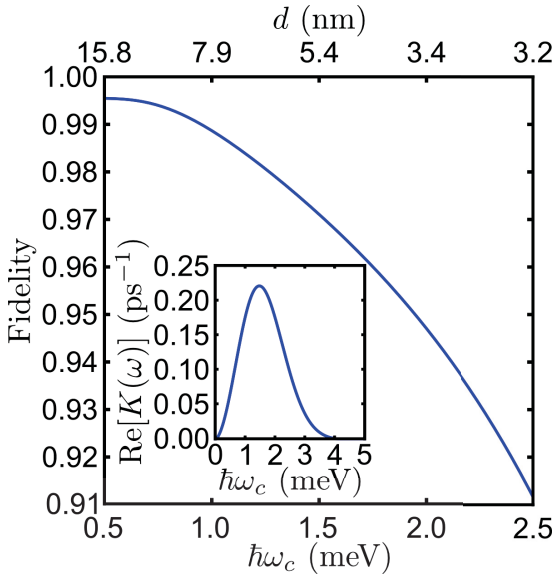

Figure 4.5: Fidelity for the calculation shown in Fig. 4.1 incorporating excitation-induced dephasing caused by coupling to longitudinal acoustic phonons as a function of the cut-off energy, $\hbar\omega_c$, of the exciton-phonon response. The phonon modes of bulk GaAs are assumed, for which $\alpha = 0.027\,\mathrm{ps}^2$. The top x-axis shows the corresponding width of the norm squared of the carrier wave function. Inset: The calculated phonon response function taking $\hbar\omega_c = 1.38\,\mathrm{meV}$, corresponding to $d = 5.76\,\mathrm{nm}$.

4.5 Conclusions

In conclusion, we have applied optimal quantum control in numerical simulations of laser-driven dynamics of excitons in semiconductor quantum dots. Our findings

demonstrate the feasibility of independent, simultaneous SU(2) control of qubits in two or more quantum dots using a single shaped laser pulse. Our results show that pulse engineering with a simple sinusoidal phase mask leads to high-fidelity parallel single qubit rotations over a wide range of optoelectronic properties and final states, indicating that this is a versatile approach to multi-qubit control. Quantum control processes optimized using this scheme could either be implemented directly in experiments, as demonstrated in Ref. [125], or provide seeding candidates for the initial population of a genetic feedback algorithm, which would aid in the compensation for experimental uncertainties. The use of arbitrary pulse shaping of broad-bandwidth control pulses builds upon the recent experimental demonstration of simultaneous (π, 2π) rotations [125] and a subpicosecond adiabatic rapid passage gate [91]. The results presented here enhance the potential scalability of QD-based platforms for quantum information applications.

4.6 Acknowledgements

The authors thank Natural Sciences and Engineering Council of Canada, Lockheed Martin Corporation, and the Canada Research Chairs program for financial support.

Chapter 5

Optimal quantum control for conditional rotation of exciton qubits in semiconductor quantum dots

Authors: Reuble Mathew[1], Craig E. Pryor[2], Michael E. Flatté[2], and Kimberley C. Hall[1]

[1]Department of Physics and Atmospheric Science, Dalhousie University, Halifax, Nova Scotia B3H4R2, Canada
[2]Department of Physics and Astronomy and Optical Science and Technology Center, University of Iowa, Iowa City, Iowa 52242, USA

Reprinted with permission from Physical Review B **84**, 205322 (2011). Reuble Mathew used the $\mathbf{k}\cdot\mathbf{p}$ computer code developed by Craig E. Pryor and Michael E. Flatté to carry out the electronic structure calculations. Craig E. Pryor and Michael E. Flatté also provided guidance and detailed feedback regarding the use of the $\mathbf{k}\cdot\mathbf{p}$ computer code. Reuble Mathew developed the pulse shaping computer code and used it to carry out the theoretical simulations and the data analysis. Reuble Mathew and Kimberley C. Hall conceived the direction for research. Reuble Mathew and Kimberley C. Hall wrote the manuscript with input from all authors.

5.1 Abstract

Pulse-shaping protocols for subpicosecond optically-controlled quantum gates in semiconductor quantum dots are reported. Our emphasis is the development of shaping schemes for either amplitude or phase control of the pulse that are easily implemented using commercial pulse shapers and femtosecond laser systems. We illustrate the efficacy of our approach through simulations of a controlled-rotation

gate in a realistic In(Ga)As quantum dot with electronic structure calculated using eight-band, strain-dependent $\mathbf{k}\cdot\mathbf{p}$ theory. Our results show that amplitude- and phase-shaping protocols both lead to substantial improvements in fidelity when compared with transform-limited pulses with equivalent gate times. Dephasing was found to have a minimal effect on the gate fidelities due to the ultrafast time scale of the quantum operations.

5.2 Introduction

The pursuit of quantum control in semiconductor quantum dots (QDs) has been the focus of a considerable body of research over the past decade [25]. In addition to enabling fundamental research into light-matter interactions, in which the three dimensional quantum confinement provides atomic-like properties in a solid state environment [180], semiconductor QDs may become the future building blocks of a quantum computing architecture. Fundamental qubits in individual quantum dots may be realized using the quantum states of an exciton or individual carrier spin [41, 181, 38, 39, 182, 183, 42, 40, 184, 44, 45]. Proposals in which optical excitation may be used for both single-qubit rotations and two-qubit gates [181, 38, 39, 182, 183, 42, 40, 184, 44, 45] are especially attractive as the exploitation of established semiconductor and photonic device fabrication capabilities enhances the potential for scaling the architecture to a large number of qubits as well as integrating it with existing computing technology. Furthermore, the use of short optical pulses may lead to operating speeds in the THz range. Seminal demonstrations of coherent optical control in QDs in recent years include single qubit rotations involving excitons [15, 53, 50, 52, 57], biexcitons [168, 82], and single carrier spins [99, 104], as well as quantum state tomography [20], the coherent manipulation of an exciton spin superposition state [169], and the introduction of controllable entanglement between excitons [16, 81, 171]. (For a recent review, see Ref [54].) These advancements represent a powerful toolkit for implementations of quantum hardware based on semiconductor QDs.

All of the above demonstrations of coherent optical control utilized transform-limited (TL) optical pulses, for which the phase of the pulse is constant [165]. By harnessing the power of femtosecond pulse-shaping techniques [112], which

allow full control over the temporal dependence of the amplitude and phase of the pulse, one may achieve a much greater degree of flexibility in the manipulation of the quantum state. In recent years, pulse shaping has been applied to quantum control in atomic and molecular systems [185, 186, 187, 188, 189, 135], in the control of chemical reactions [190, 191], and in various areas of nonlinear optics, including electromagnetically-induced transparency [192, 193] and the generation of high harmonics [194, 195, 119]. The potential utility of pulse shaping in quantum computing is clearly illustrated by various proposals for quantum gates based on adiabatic passage [183, 184, 134, 131], in which a linear chirp (quadratic time-dependent phase) results in state evolution through an anticrossing, something that was very recently demonstrated involving exciton qubits in self-assembled QDs [74, 73]. The implementation of a more general phase profile may greatly benefit the efficiency, fidelity and speed of quantum state control because the control Hamiltonian itself can be tailored to optimize the physical process involved [39, 40, 196, 197]. For example, in order to avoid unintended dynamics associated with nearby states, optical control has been limited in experiments to pulses with a duration of a few picoseconds or longer (e.g. in Ref. [73], 40 ps pulses were used). The achievement of faster operation speeds using pulse-shaping techniques would allow the full potential of optical control methods for quantum operations to be exploited.

Here we develop general pulse-shaping protocols for optimizing the speed and fidelity of optically-controlled quantum gates in self-assembled semiconductor QDs. We focus here on the controlled-rotation (C-ROT) operation involving two exciton qubits in a single QD [38]. The possibility of scaling such a system to qubits within different QDs has been addressed in several recent proposals [181, 42, 45, 85, 84]. Exciton qubits are attractive due to the ease and efficiency of quantum state control using optical techniques, and have recently been shown to benefit from dynamical decoupling schemes as a means of reducing the effective decoherence rate [92, 46, 35]. The C-ROT gate provides a test case that illustrates the effectiveness of the pulse-shaping approach in a physical scenario that is readily accessible using current optical techniques [16]. In a recent work by Chen *et al.* [39], the fidelity of the C-ROT operation was optimized through the use of two phase-locked,

transform-limited pulses with independent bandwidth control of each pulse. The implementation of this approach is complicated by the need for two separately optimized, synchronous laser sources, as well as a stabilized Michelson arrangement [40]. Our emphasis here is to develop general amplitude- and phase-shaping protocols that could be easily implemented with a single mode-locked femtosecond oscillator and a standard commercially available pulse shaper [198].[1] We optimize amplitude-shaping protocols and phase-shaping protocols separately and find that either leads to a substantial enhancement in fidelity in comparison to transform-limited pulses with an equivalent gate time. Dephasing is found to have a minimal effect on the gate fidelity, even for T_2 times as low as $10\,\mathrm{ps}$, reflecting the benefits of a subpicosecond gate time. Our findings may be easily extended to other optical operations in QDs, including two-photon Rabi rotations of biexcitons [126], adiabatic passage involving excitons [74, 73] or biexcitons [134], and schemes for dynamical decoupling [92, 46, 35]. Further improvement is likely to be possible when the amplitude and phase shape of the pulse are optimized together.

5.3 Conditional Exciton Dynamics

The C-ROT operation, originally proposed by Troiani *et al.* [38], is achieved using the four-level system created by the vacuum ground state ($|00\rangle$), two oppositely polarized exciton states ($|10\rangle$ and $|01\rangle$) and the bound biexciton state ($|11\rangle$), as shown in Fig. 5.1(a). The single exciton states $|10\rangle$ and $|01\rangle$ represent two qubits in each quantum dot. In self-assembled In(Ga)As QDs, the anisotropic exchange interaction together with a slight elongation of the dot lifts the degeneracy between the single exciton states and leads to linearly-polarized optical selection rules, in which $|10\rangle$ and $|01\rangle$ correspond to symmetric and antisymmetric combinations of spin-up and spin-down excitons [180, 56]. In Fig. 5.1(a), Π_x (Π_y) indicates linearly polarized excitation, with the polarization direction along $[110]$ ($[1\bar{1}0]$), corresponding to the long (short) axes of the QD. The exchange splitting (δ) is greatly exaggerated in Fig. 5.1(a) for clarity: it is typically found to be $\lesssim 0.2\,\mathrm{meV}$ in experiments [199, 200], much smaller than the $12\,\mathrm{meV}$ bandwidth of the optical control pulses considered here. The biexciton state $|11\rangle$ corresponds to the bound state of two

[1] See e.g. the Silhouette ultrafast pulse shaper manufactured by Coherent Inc.

excitons with opposite spin, and occurs at an energy lower than that required to create two single excitons by an amount Δ_b, the biexciton binding energy.

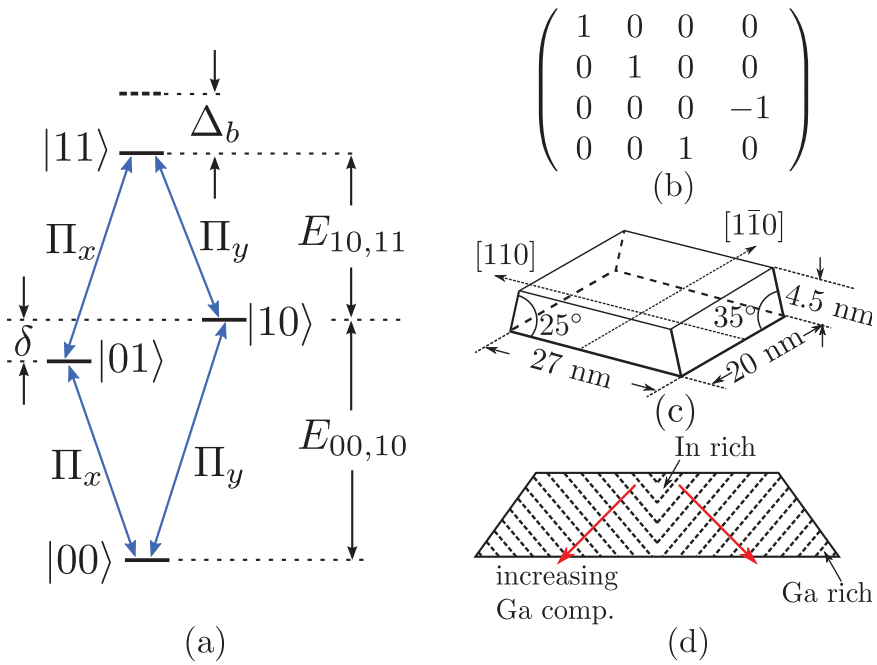

Figure 5.1: (a) Energy level diagram for the exciton and biexciton system in a QD - the vacuum ground state ($|00\rangle$), two single excitons ($|01\rangle, |10\rangle$), and a biexciton ($|11\rangle$) with a binding energy of Δ_b. The arrows indicate optically allowed, linearly polarized (Π_x or Π_y) transitions. (b) Unitary transformation matrix for the C-ROT gate. (c) Truncated pyramid quantum dot structure and (d) $\mathrm{In}_x\mathrm{Ga}_{1-x}\mathrm{As}$ composition profile within the dot. The composition is graded from high indium concentration in the shape of an inverted triangle at the center of the dot to low indium concentration at the base.

Conditional dynamics are realized in this system by exploiting the polarization selection rules in Fig. 5.1(a), in conjunction with the energy separation between the transitions associated with the excitation of a single exciton ($|00\rangle \rightarrow |01\rangle$ or $|10\rangle$) and the excitation of a second exciton in the presence of the first exciton ($|01\rangle$ or $|10\rangle \rightarrow |11\rangle$). These transitions are separated in energy by the biexciton binding energy. Using laser excitation pulses with a spectral bandwidth that is narrow compared to Δ_b, one can achieve both single qubit rotations and a C-ROT gate for suitable choice of the carrier frequency of the laser pulse. For example, for a Π_y-polarized laser pulse tuned to the $|10\rangle$ to $|11\rangle$ transition, the state of the second (target) bit will be rotated if and only if the first (control) bit is in state 1. Single

qubit rotations (in which a bit is rotated regardless of the state of the other bit) are achieved using bichromatic laser pulses with orthogonally-polarized components. The transformation matrix for the C-ROT gate is shown in Fig. 5.1(b). The restriction to narrow bandwidth excitation pulses ensures a high fidelity operation, but at the expense of a large operation time. As we show in Sec. 5.6, this trade-off between operation time and fidelity may be alleviated through the implementation of pulse shaping.

5.4 Electronic Structure of Self-Assembled QDs

We model the QD as a truncated pyramid of $\mathrm{In}_x\mathrm{Ga}_{1-x}\mathrm{As}$ embedded in GaAs, with its base in the (001) plane, and with its edges aligned along the $[110]$ and $[1\bar{1}0]$ directions, as shown in Fig. 5.1(c). The dot has a height of $4.5\,\mathrm{nm}$, length of $27\,\mathrm{nm}$, and width of $20\,\mathrm{nm}$, with the long axis along $[110]$. The facet angles for projections onto the (110) and $(1\bar{1}0)$ planes are $35\,\mathrm{degrees}$ and $25\,\mathrm{degrees}$, respectively (corresponding to facets with indices of $\{(1,-1,2.020)$,$(-1,1,2.020)\}$ and $\{(1,1,3.033)$,$(-1,-1,3.033)\}$). We use a graded indium composition within the dot in the shape of an inverted pyramid. The contours in Fig. 5.1(d) mark nested, constant-alloy composition layers with an angle of $45\,\mathrm{degrees}$ to the growth direction. The composition of the dot is graded in 16 increments from the innermost layer at the top face where it is In-rich ($x = 0.6$) to the outermost layer at the base where it is Ga-rich ($x = 0.225$) (i.e. a change in composition of $\Delta x = 0.025$ between layers). The dot shape and compositional profile is typical of In(Ga)As/GaAs self-assembled QDs [201, 47, 202].

The confined single-particle states of the QD were calculated using an eight-band, strain-dependent $\mathbf{k}\cdot\mathbf{p}$ Hamiltonian in the envelope approximation [152, 153, 154, 203], where the residual strain is found by minimizing the elastic energy in the structure. The explicit form of the kinetic and strain Hamiltonians are given in Ref. [153]. Multi-particle states are calculated within the Hartree approximation, in which the wave functions are found by iteratively solving the Schrödinger equation for a particle in the potential of the other carriers in the QD until the energy eigenvalues converge. The Hartree approach accounts for the direct Coulomb interaction between the carriers, but does not capture the exchange interaction or the effects

of correlation. The fine-structure splitting is therefore introduced by hand. We take a value of $150\,\mu\mathrm{eV}$, which is typical of values found in experiment [199]. We find that the exact value of δ is inconsequential due to the fast time scale of the optical control process relative to $1/\delta$. The matrix elements of the electric dipole operator are directly evaluated using the calculated multi-particle states. The biexciton binding energy is evaluated using the difference between the transition energies calculated using the multi-particle and single-particle wave functions. The results of our electronic structure calculations are summarized in Table 5.1.

Table 5.1: Transition energies and electric dipole moments calculated using eight-band, strain-dependent $\mathbf{k}\cdot\mathbf{p}$ theory. An empirical value was used for the fine-structure splitting [199].

Parameter	Value
Exciton transition energy ($E_{00,10}$)	$1.2723\,\mathrm{eV}$
Biexciton transition energy ($E_{10,11}$)	$1.2739\,\mathrm{eV}$
Binding energy (Δ_b)	$-1.6\,\mathrm{meV}$
Fine-structure splitting (δ)	$150\,\mu\mathrm{eV}$
Dipole moment ($d_{00,10}$)	$22.76\,\mathrm{Debye}$
Dipole moment ($d_{01,11}$)	$22.98\,\mathrm{Debye}$

The biexciton binding energy is a crucial parameter for the design of optical control pulses for both the single qubit and C-ROT gates as it determines the relative spacing of the optical transitions involved. A small value of Δ_b will require fine spectral control of the pulse phase and amplitude. Experiments have shown that it is possible to get both negative (anti-binding) and positive (binding) biexciton binding energies, with values of Δ_b ranging from $4.8\,\mathrm{meV}$ to $-6.3\,\mathrm{meV}$ in self-assembled In(Ga)As QDs [149]. This wide range of experimental values illustrates the strong sensitivity of this parameter to the details of the QD structure and composition. This sensitivity is further illustrated by the results in Fig. 5.2, which show electronic structure calculations for a range of dot compositions and heights. Variations in the biexciton binding energy in Fig. 5.2 reflect changes in the overlap of the electron and hole wavefunctions. The average indium composition in Fig. 5.2(a) is varied by changing the maximum indium concentration at the top face of the dot while maintaining an identical graded structure and compositional gradient Δx as

in Fig. 5.1(d). There is a nonmonotonic dependence on average indium composition, reflecting relative shifts in the electron and hole wavefunctions due to the nonuniform dot composition as the average indium content varies. The height of the dot in Fig. 5.2(b) is varied by adding horizontal layers to the top of the dot with a starting height of $2.5\,\mathrm{nm}$ while maintaining the same internal and external facet angles, and spacing between layers. With this approach, material added to the top simultaneously increases the height and the average indium composition because the top face of the dot contains the indium-rich layers. (For a dot height of $4.5\,\mathrm{nm}$, the average indium composition is 0.5.) The results in Fig. 5.2(b) reflect a tendency for the biexciton to become more tightly bound (smaller negative binding energies) with increasing dot height. As our calculations neglect correlation effects, we can only obtain qualitative information regarding the trends in Δ_b with QD structure (e.g. the value we extract for the biexciton binding energy is consistently negative due to the overestimation of the effects of electron-electron repulsion [204]). Nevertheless, these results suggest that Δ_b may be engineered through appropriate choice of growth conditions. This is consistent with recent experiments, in which Δ_b was tuned through control of the height of site-selected QDs [205]. The trends observed in Fig. 5.2 for the exciton transition energy are determined by competition between changes in the dot compositional profile and the degree of quantum confinement. In the numerical simulations of the C-ROT gate, we have allowed the biexciton binding energy to vary, spanning the range of accessible experimental values [149]. This will allow us to obtain flexible pulse-shaping protocols that may be adapted to a particular QD during experimental implementation of the C-ROT gate.

5.5 Optimization of the C-ROT gate

The interaction of a laser pulse with the QD is treated using the Liouville equation for the density matrix $\rho(t)$,

$$\frac{\partial \rho}{\partial t} = \frac{i}{\hbar}[\rho, H], \tag{5.1}$$

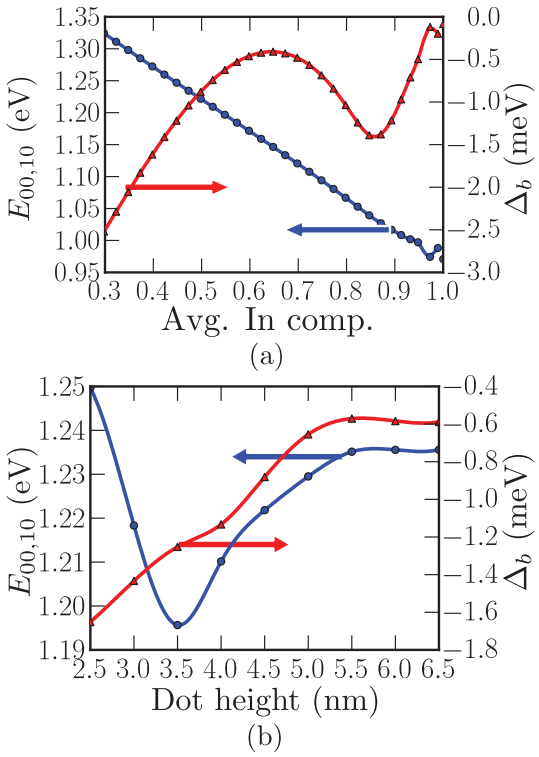

Figure 5.2: Exciton transition energy (circles) and biexciton binding energy (triangles) for variations in (a) average indium composition; and (b) quantum dot height. In varying the dot height, material was added to the top of the dot (see Fig. 5.1(d)), while maintaining the same graded structure, until a complete pyramid was formed ($h = 6.5\,\mathrm{nm}$).

where H is the total Hamiltonian, given by

$$H = \sum_i \hbar\omega_i P_{i,i} - \frac{1}{2}\sum_{i\neq j} \boldsymbol{\mu}_{i,j}\cdot\hat{\boldsymbol{\epsilon}} E_0(t) \times \{\exp\left[-i\omega t - i\Phi(t)\right] + \exp\left[i\omega t + i\Phi(t)\right]\} P_{i,j}. \tag{5.2}$$

The first term in Eqn. 5.2 describes the electronic structure for the unperturbed system, consisting of the multiparticle eigenstates obtained using our $\mathbf{k}\cdot\mathbf{p}$ formalism, where $P_{i,j}$ is the associated projection operator $|i\rangle\langle j|$. The second term is the control Hamiltonian associated with the laser field. We employ the rotating-wave approximation to remove the non-resonant term in the interaction Hamiltonian and make the change of variables $\rho_{i,j}(t) \rightarrow \tilde{\rho}_{i,j}(t)$ to remove the fast variations in the

coherences. Decay and decoherence are incorporated in the relaxation-time approximation. The resulting Bloch equations of the four-level system are given by

$$\dot{\tilde{\rho}}_{01,01} = -\frac{i}{2}(\chi_{01,00}\tilde{\rho}_{00,01} - \chi_{00,01}\tilde{\rho}_{01,00} + \chi_{01,11}\tilde{\rho}_{11,01} - \chi_{11,01}\tilde{\rho}_{01,11}) - \gamma_{01,01}\tilde{\rho}_{01,01}, \tag{5.3}$$

$$\dot{\tilde{\rho}}_{10,10} = -\frac{i}{2}(\chi_{10,00}\tilde{\rho}_{00,10} - \chi_{00,10}\tilde{\rho}_{10,00} + \chi_{10,11}\tilde{\rho}_{11,10} - \chi_{11,10}\tilde{\rho}_{10,11}) - \gamma_{10,10}\tilde{\rho}_{10,10}, \tag{5.4}$$

$$\dot{\tilde{\rho}}_{11,11} = -\frac{i}{2}(\chi_{11,01}\tilde{\rho}_{01,11} - \chi_{01,11}\tilde{\rho}_{11,01} + \chi_{11,10}\tilde{\rho}_{10,11} - \chi_{10,11}\tilde{\rho}_{11,10}) - \gamma_{11,11}\tilde{\rho}_{11,11}, \tag{5.5}$$

$$\tilde{\rho}_{00,00} = 1 - \tilde{\rho}_{01,01} - \tilde{\rho}_{10,10} - \tilde{\rho}_{11,11}, \tag{5.6}$$

$$\dot{\tilde{\rho}}_{01,00} = -\frac{i}{2}[2(\omega_{01,00} - \omega)\tilde{\rho}_{01,00} + \chi_{01,11}\tilde{\rho}_{11,00} - \chi_{10,00}\tilde{\rho}_{01,10} + \chi_{01,00}(\tilde{\rho}_{00,00} - \tilde{\rho}_{01,01})] - \gamma_{01,00}\tilde{\rho}_{01,00}, \tag{5.7}$$

$$\dot{\tilde{\rho}}_{10,00} = -\frac{i}{2}[2(\omega_{10,00} - \omega)\tilde{\rho}_{10,00} + \chi_{10,11}\tilde{\rho}_{11,00} - \chi_{01,00}\tilde{\rho}_{10,01} + \chi_{10,00}(\tilde{\rho}_{00,00} - \tilde{\rho}_{10,10})] - \gamma_{10,00}\tilde{\rho}_{10,00}, \tag{5.8}$$

$$\dot{\tilde{\rho}}_{10,01} = -\frac{i}{2}[2\omega_{10,01}\tilde{\rho}_{10,01} + \chi_{10,00}\tilde{\rho}_{00,01} - \chi_{00,01}\tilde{\rho}_{10,00} + \chi_{10,11}\tilde{\rho}_{11,01} - \chi_{11,01}\tilde{\rho}_{10,11}] - \gamma_{10,01}\tilde{\rho}_{10,01}, \tag{5.9}$$

$$\dot{\tilde{\rho}}_{11,00} = -\frac{i}{2}[2(\omega_{11,00} - 2\omega)\tilde{\rho}_{11,00} + \chi_{11,01}\tilde{\rho}_{01,00} - \chi_{01,00}\tilde{\rho}_{11,01} + \chi_{11,10}\tilde{\rho}_{10,00} - \chi_{10,00}\tilde{\rho}_{11,10}] - \gamma_{11,00}\tilde{\rho}_{11,00}, \tag{5.10}$$

$$\dot{\tilde{\rho}}_{11,01} = -\frac{i}{2}[2(\omega_{11,01} - \omega)\tilde{\rho}_{11,01} + \chi_{11,10}\tilde{\rho}_{10,01} - \chi_{00,01}\tilde{\rho}_{11,00} + \chi_{11,01}(\tilde{\rho}_{01,01} - \tilde{\rho}_{11,11})] - \gamma_{11,01}\tilde{\rho}_{11,01}, \tag{5.11}$$

$$\dot{\tilde{\rho}}_{11,10} = -\frac{i}{2}[2(\omega_{11,10} - \omega)\tilde{\rho}_{11,10} + \chi_{11,01}\tilde{\rho}_{01,10} - \chi_{00,10}\tilde{\rho}_{11,00} + \chi_{11,10}(\tilde{\rho}_{10,10} - \tilde{\rho}_{11,11})] - \gamma_{11,10}\tilde{\rho}_{11,10}, \tag{5.12}$$

where $\rho_{i,i}$ is the population in state $|i\rangle$, $\rho_{i,j}$ is the coherence between states $|i\rangle$ and $|j\rangle$, $\chi_{i,j} = \boldsymbol{\mu}_{i,j} \cdot \hat{\boldsymbol{\epsilon}} E_0(t)/\hbar$ is the Rabi frequency, and $\gamma_{i,j}$ are the constant decay rates.

The objective of quantum control is to tailor the control Hamiltonian to achieve the desired multiparticle state of the system at the end of the laser pulse. This can

be achieved experimentally, for example, using a $4f$ pulse shaper [112], as shown in Fig. 5.3. The manipulation of the pulse shape is carried out in the Fourier plane by a spatial light modulator (SLM), which may be equipped with one or two voltage-controlled liquid-crystal retarders. When two liquid-crystal retarders are used in conjunction with polarizers on the input and output of the SLM, full control of the amplitude and phase of the pulse is possible. The action of the SLM in this case may be described as the product of frequency-dependent amplitude ($A_M(\omega)$) and phase ($\Phi_M(\omega)$) masks:

$$M(\omega) = A_M(\omega) \exp\left[i\Phi_M(\omega)\right]. \tag{5.13}$$

The effect of this mask on the pulse at the Fourier plane is given by

$$\tilde{E}_{\rm out}(\omega) = \tilde{E}_{\rm in}(\omega) M(\omega) \tag{5.14}$$

where $\tilde{E}_{\rm in}(\omega)$ is the Fourier transform of the input pulse, taken to be transform-limited:

$$\mathbf{E}_{\rm in}(t) = \frac{1}{2}\hat{\boldsymbol{\epsilon}} E_0(t) \exp\left(-i\omega_0 t\right). \tag{5.15}$$

The pulse envelope is chosen to have the form: $E_0(t) = |E_0|\mathrm{sech}(1.76t/\tau)$, with $\tau = 150\,\mathrm{fs}$, which is consistent with the typical output from commercially available femtosecond laser systems operating in the wavelength range of interest. $\tilde{E}_{\rm out}(\omega)$ is the Fourier transform of the output (shaped) pulse used for quantum control. Phase-only SLM configurations minimize light losses, and for this reason we develop pulse-shaping protocols involving phase-only control as well as amplitude-only control. This will provide the greatest degree of flexibility in the experimental implementation of the phase masks presented in Sec. 5.5.1.

We optimize the phase and amplitude masks using the constrained optimization by linear approximations (COBYLA) algorithm [206]. The objective function to be maximized by the optimization routine is the fidelity of the quantum gate, given by

$$F = \mathrm{Tr}[\rho_{\rm P}\rho_{\rm I}], \tag{5.16}$$

where, $\rho_{\rm P}$ is the physical density matrix at the end of the laser pulse and $\rho_{\rm I}$ is the ideal density matrix [16]. Equation 5.16 is applied to the C-ROT operation by averaging the fidelity over four initial states, corresponding to an occupation of unity for each of the four levels in the system, with all other density matrix elements

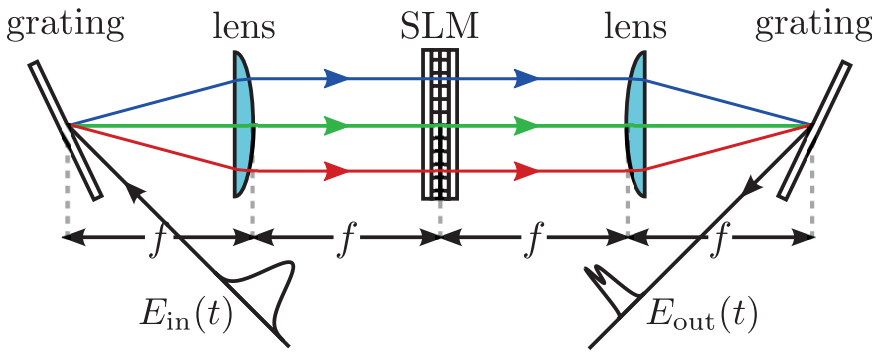

Figure 5.3: $4f$ pulse shaper consisting of two diffraction gratings, two lenses, and an optical mask shown as a spatial light modulator (SLM). The distance f is the focal length of the lenses. Manipulation of the pulse shape is carried out in the Fourier plane.

equal to zero. In this case, a pure initial system state is assumed; i.e. we do not model the quantum state initialization, assuming it to have been carried out with a fidelity of unity. The time dynamics of the system are calculated by integrating Eqns. 5.3–5.12 over the duration of the pulse. We define the fidelity, F, as a function of a vector $\mathbf{q}$, the components of which describe the mask function $M(\omega)$, such that

$$F = f(q_1, ..., q_i, ..., q_n). \tag{5.17}$$

The components of the vector $\mathbf{q}$ are subject to constraints dictated by experimental limitations, as described below for each shaping scheme. We use a Sobol' sequence [177, 207] to populate the n-dimensional parameter space with initial vectors $\{\mathbf{q}_{\text{init}}\}$, each describing different forms of the masking function, $M(\omega)$. For each vector, Eqns. 5.3–5.12 are integrated to determine the density matrix at the end of the laser pulse, and this density matrix is inserted into Eqn. 5.16 to calculate the fidelity. The optimization routine drives the system to a local optimum in fidelity by varying the components of $\mathbf{q}$. We find that the optimal solution is found uniquely for a population of 500 (or more) initial vectors, indicating that the parameter space is adequately spanned for each shaping scheme.

5.5.1 Phase Control Scheme

A scheme for quantum control in which the only degree of freedom is the phase of the pulse offers some advantages: (i) light losses in the shaping system will be

minimized; and (ii) such a system avoids deleterious effects associated with rejected light in the shaping system. The phase mask we utilize here has the following dependence on the individual frequencies ω within the pulse:

$$\Phi_M(\omega) = \alpha \cos[\gamma(\omega - \omega_{10,11}) - \delta]. \tag{5.18}$$

Here $\omega_{10,11}$ is the transition frequency resonant with the $|10\rangle$ to $|11\rangle$ transition, and α, γ, δ, and the total pulse area ($\Theta = (\boldsymbol{\mu} \cdot \hat{\boldsymbol{\epsilon}}/\hbar) \int_{-\infty}^{+\infty} E_0(t)\,\mathrm{d}t$) are taken as free parameters, so that the fidelity is a function of four variables:

$$F = f(\alpha, \gamma, \delta, \Theta). \tag{5.19}$$

The following constraints are imposed:

$$\begin{aligned} 0 \leq &\alpha \leq \pi, \\ 0 \leq &\gamma \leq 315\,\mathrm{fs}, \\ -\pi \leq &\delta \leq \pi, \\ \pi/2 \leq &\Theta \leq 6\pi. \end{aligned} \tag{5.20}$$

The limits on α and γ were chosen to restrict $|\mathrm{d}\Phi_M(\omega)/\mathrm{d}\omega|_{\max}$ to approximately $\pi/10$ radians per pixel for a 128-pixel SLM, representing a readily accessible phase gradient for typical pulse-shaping systems. Θ was allowed to vary up to 6π radians as it was found that multiple Rabi oscillation cycles provided access to higher fidelities, as discussed in Sec. 5.6. 6π radians is considered to be a good compromise for achieving high fidelities with experimentally accessible pulse fluences [14].

5.5.2 Amplitude Control Scheme

The amplitude mask function we employ here has the following form:

$$A_M(\omega) = \left| \exp\left[-\left(\frac{\omega - \omega_{10,11}}{\Delta\omega_1/(2\ln 2)^{1/2}} \right)^2 \right] - A_0 \exp\left[-\left(\frac{\omega - \omega_{00,10}}{\Delta\omega_2/(2\ln 2)^{1/2}} \right)^2 \right] \right|. \tag{5.21}$$

Equation 5.21 represents the destructive interference of simultaneous bichromatic Gaussian pulses centered at photon energies $E_{10,11} = \hbar\omega_{10,11}$, and $E_{00,01} = \hbar\omega_{00,01}$, with full-width at half maximum frequency bandwidths $\Delta\omega_i$, and a relative amplitude factor A_0. For simplicity, we set $\Phi_M(\omega)$ in Eqn. 5.13 equal to zero.

The analytical form in Eqn. 5.21 was inspired by the results in Ref. [39], in which a similar four-level system was considered, and the C-ROT gate was optimized by separately controlling the pulse durations of two phase-locked Gaussian pulses. The amplitude mask in Eqn. 5.21 is a more general form and is easily implemented using a single mode-locked oscillator and a commercial pulse shaper.

The fidelity is maximized in a four-dimensional parameter space:

$$F = f(\Delta\omega_1, \Delta\omega_2, A_0, \Theta). \tag{5.22}$$

The free parameters $\Delta\omega_i$, A_0 and Θ are subject to the following constraints:

$$\begin{aligned} 6.08 \leq &\hbar\Delta\omega_i \leq 12.2\,\mathrm{meV}, \\ 0.0 \leq &A_0 \leq 1.0, \\ \pi/2 \leq &\Theta \leq 6\pi. \end{aligned} \tag{5.23}$$

The maximum limit on the bandwidths $\Delta\omega_i$ is determined by the spectral content of the initial transform-limited optical pulse, while the minimum limit restricts the total pulse operation time. The restrictions on Θ were kept the same as for the phase control scheme, so that the effectiveness of the two schemes could be compared. It should be noted that it is not possible to enforce a constant maximum rate of change, $|\mathrm{d}A_M(\omega)/\mathrm{d}\omega|_{\max}$, for all binding energies. We nevertheless verified that the spectral amplitude features obtained for the optimal pulse shapes are sufficiently slowly varying to be well reproduced by a standard 128-pixel SLM.

5.6 Results and Discussion

5.6.1 Optimized Quantum Control Pulses

Figure 5.4 shows the results for the optimum pulse shape using the phase-only control scheme for a biexciton binding energy of $2.5\,\mathrm{meV}$. In order to quantify the efficacy of the pulse-shaping protocols presented in this work, we compare the gate performance for the shaped pulse to that for a TL pulse with an equivalent gate time.[2] The optimized parameters for the shaped pulse are: $\alpha = 0.511\pi\,\mathrm{rad}$,

[2]The gate time for a given excitation pulse was determined by normalizing the intensity profile and determining the width of a square pulse with the same total area.

$\gamma = 325\,\mathrm{fs}$, $\delta = 0.243\pi\,\mathrm{rad}$, and $\Theta = 5.780\pi\,\mathrm{rad}$. These data correspond to a gate time of $555\,\mathrm{fs}$ for the TL and shaped pulses. The population dynamics are shown in the two upper panels in Fig. 5.4 for two initial conditions: (i) $\rho_{10,10}(t=0)=1$, and (ii) $\rho_{00,00}(t=0)=1$. As discussed in Sec. 5.3, the objective of the C-ROT gate is to flip the state of the target (second) bit if and only if the control (first) bit is 1. This implies that the optical pulse should effect a π Rabi rotation between $|10\rangle$ and $|11\rangle$ if the system is initially in either $|10\rangle$ or $|11\rangle$ and have no effect if the system is in $|00\rangle$ or $|01\rangle$ at $t=0$.

For $\rho_{10,10}(t=0)=1$ (top row of panels in Fig. 5.4) the first bit is 1 at time $t=0$. In this case, the C-ROT gate must flip the second bit so that the occupation $\rho_{11,11}=1$ at the end of the pulse. As seen in Fig. 5.4(a), the shaped pulse carries out this operation with a high fidelity. The occupations $\rho_{11,11}$ and $\rho_{10,10}$ are flipped such that $\rho_{11,11}$ starts at 0 and ends at approximately 1 while $\rho_{10,10}$ starts at 1 and ends at approximately 0. The occupation for the non-target state ($\rho_{00,00}$) starts at 0 and after some transient occupation is returned to approximately 0. For the TL pulse in Fig. 5.4(b), an incomplete transfer of occupation between $\rho_{10,10}$ and $\rho_{11,11}$ occurs and the residual occupation in $\rho_{00,00}$ is non-zero, resulting in lower fidelity.

For the second initial condition, $\rho_{00,00}(t=0)=1$ (second row of panels in Fig. 5.4), the first bit is 0 at $t=0$, so an ideal pulse would return the system to its initial state. The shaped pulse is also able to perform this operation with high fidelity as seen in Fig. 5.4(a). The occupations $\rho_{11,11}$ and $\rho_{10,10}$ start at 0 at time $t=0$ and both are returned to approximately 0 after some transient dynamics. Additionally, the occupation in $\rho_{00,00}$ starts at 1 and is returned to 1. The TL pulse is ineffective for this operation as it permanently reduces the occupation $\rho_{00,00}$, resulting in residual values of the occupations $\rho_{11,11}$ and $\rho_{10,10}$ at the end of the pulse. The state evolution for the initial condition $\rho_{11,11}(t=0)=1$ is linked to the evolution for $\rho_{10,10}(t=0)=1$ as these state occupations are exchanged in the C-ROT and so only the dynamics for $\rho_{10,10}(t=0)=1$ are shown for clarity. The optical selection rules for a Π_y-polarized pulse preclude laser-induced dynamics for the fourth initial condition $\rho_{01,01}(t=0)=1$ (see Fig. 5.1(a)).

The temporal and spectral properties of the shaped and TL control laser pulses are shown in the two lower panels of Fig. 5.4. The TL pulse with an equivalent

gate time has a narrower frequency spectrum than the shaped pulse and a constant phase. The sinusoidal phase modulation for the shaped pulse results in a structured intensity profile and concomitant intermediate state dynamics. The improvement in fidelity afforded by the shaping protocol is nevertheless considerable, reaching a value of 0.964 in comparison to 0.866 for the TL pulse.

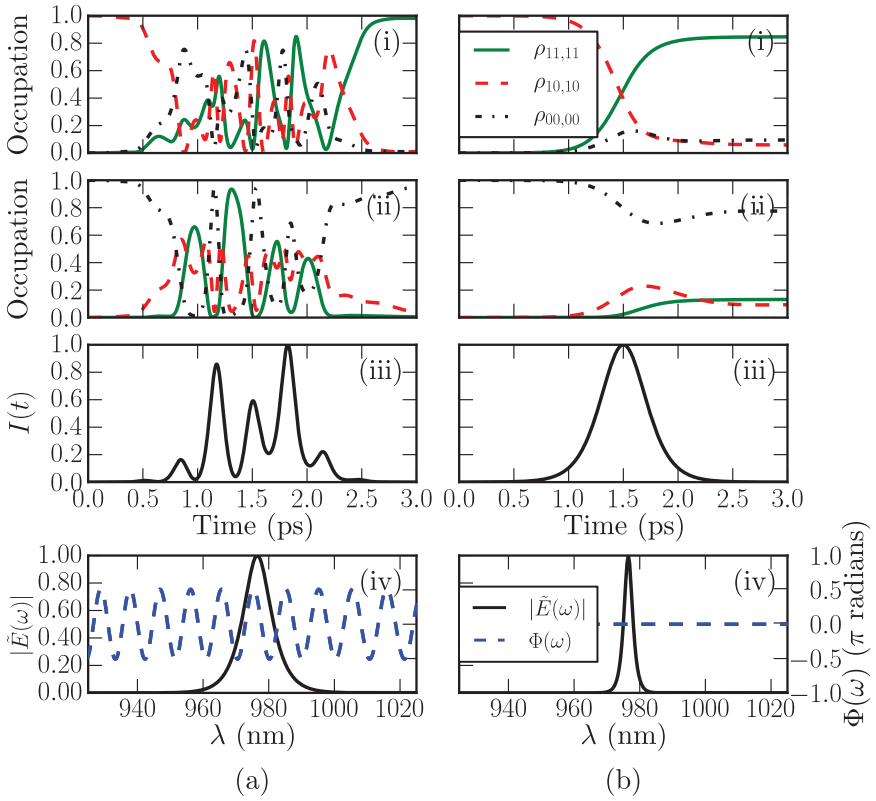

Figure 5.4: Population dynamics and control pulse characteristics for (a) the optimal phase-shaped pulse, and (b) the TL pulse. Panels (i) and (ii) show the population dynamics for the initial conditions $\rho_{10,10}(t=0)=1$ and $\rho_{00,00}(t=0)=1$, respectively. The third panel shows the temporal envelope of the electric field intensity of the control pulse. The bottom panel shows the amplitude (solid curves) and phase (dashed curves) profiles for the control pulse.

An alternative view of the state dynamics is provided by the Bloch vector representation, shown in Fig. 5.5(a) and Fig. 5.5(b) for the phase-shaped and TL pulses, respectively. The solid line indicates the Bloch vector corresponding to the first qubit for $\rho_{00,00}(t=0)=1$, while the dashed curve corresponds to the second qubit for $\rho_{10,10}(t=0)=1$. The complex trajectories in Fig. 5.5(a) reflect the intermediate state dynamics in Fig. 5.4(a). The increased efficacy of the C-ROT operation

for the phase-shaped pulse is evident in Fig. 5.5(a) as the second qubit undergoes a half-cycle rotation for $\rho_{10,10}(t = 0) = 1$ (dashed curves) while the first qubit is returned to the initial state for $\rho_{00,00}(t = 0) = 1$ (solid curves). The higher fidelity obtained with the phase-shaping protocol relative to the TL pulse is also illustrated by the truth tables in Fig. 5.5(c) and Fig. 5.5(d). The TL pulse leads to inferior control of the conditional dynamics because the wide spectral bandwidth relative to Δ_b prevents discrimination between the target and non-target states in the optical excitation process.

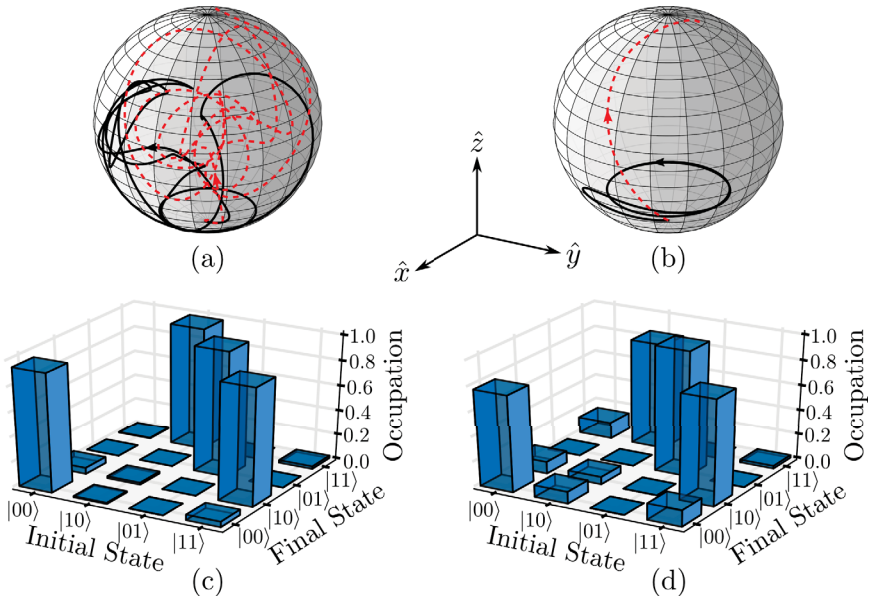

Figure 5.5: Bloch vector representations of the first qubit for $\rho_{00,00}(t = 0) = 1$ (solid curve) and the second qubit for $\rho_{10,10}(t = 0) = 1$ (dashed curve) for the (a) phase-shaped pulses, and (b) TL pulse. Truth table of the gate operation for the (c) optimal phase-shaped pulse, and (d) TL pulse.

Figure 5.6 shows the results for the optimal amplitude-shaped pulse for the same binding energy of $2.5\,\mathrm{meV}$. The optimized parameters for the shaped pulse are: $\hbar\Delta\omega_1 = 6.083\,\mathrm{meV}$, $\hbar\Delta\omega_2 = 12.166\,\mathrm{meV}$, $A_0 = 0.772$, and $\Theta = 3.6\pi\,\mathrm{rad}$. The gate time for the data in Fig. 5.6 is $335.5\,\mathrm{fs}$ for both shaped and TL pulses. The Bloch vector and truth table results corresponding to the state dynamics in Fig. 5.6 are shown in Fig. 5.7. The fidelity of the C-ROT gate for the amplitude-shaped pulse is 0.967, in comparison with a value of 0.689 for the TL pulse, illustrating a dramatic improvement with pulse shaping.

The amplitude mask in Eqn. 5.21 is a superposition of two Gaussians that are

π out of phase with each other. From the bottom panel in Fig. 5.6, it is clear that the optimum condition for high fidelity corresponds to the generation of a node in the pulse spectrum resonant with the $|00\rangle \rightarrow |10\rangle$ transition (occurring at $974.5\,\mathrm{nm}$). The optimum pulse parameters therefore result in perfect destructive interference between the two terms in Eqn. 5.21 at $\omega = \omega_{00,10}$. Such a cancellation effect was also found in Ref. [39] for a similar 4-level scheme involving pure exciton spin states in cylindrically-symmetric quantum dots. Our results for the level scheme in Fig. 5.1(a), for which the ground state is coupled to the biexciton via the intermediate state $|01\rangle$, and for which our more general amplitude mask in Eqn. 5.21 permits relative amplitude control between the two terms, indicates that the cancellation effect is a general consequence of the use of this bichromatic control scheme. As described in the next section, our findings also verify that the spectral node tracks the $|00\rangle \rightarrow |10\rangle$ transition as Δ_b is varied. (In Ref. [39] Δ_b was fixed). Unlike the amplitude shaping scheme, for which there exists a simple interpretation of the improvement in fidelity introduced by pulse shaping in terms of destructive light interference at $\omega_{00,10}$, for the phase-only shaping protocol the pulse spectrum is unaffected by the shaping mask and consequently no such simple interpretation exists. In contrast to the case of a TL pulse, in which the Rabi rotation on the Bloch sphere occurs about a fixed axis in the x-y plane, the introduction of a time- (and frequency-) dependent phase in the control pulse will lead to the motion of the Rabi control vector during the operation. In conjunction with the freedom to perform more than one full Rabi cycle in our shaping protocol, this leads to a complex motion of the Bloch vector, as evident in Fig. 5.5(a). Optimization of the fidelity only requires that the system reach the target state *at the end of the control pulse*. The phase-only shaping scheme used in Eqn. 5.18 was chosen for its simplicity of implementation and for the ease of monitoring the control pulses using common pulse measurement techniques.[3] We expect that another choice of phase mask function would lead to similar improvements in fidelity provided sufficiently rapid phase variations may be generated within the experimental constraints of conventional SLMs. The ability to tailor the coherent state dynamics using only control over the pulse phase, illustrated here for exciton qubits in self-assembled

[3] In a follow-up paper (A. Gamouras, R. Mathew and K. C. Hall, unpublished) we describe the experimental characterization of pulse shapes using multiphoton intrapulse interference phase scan.

quantum dots, highlights the power and flexibility of pulse shaping in tailoring the light-matter interaction.

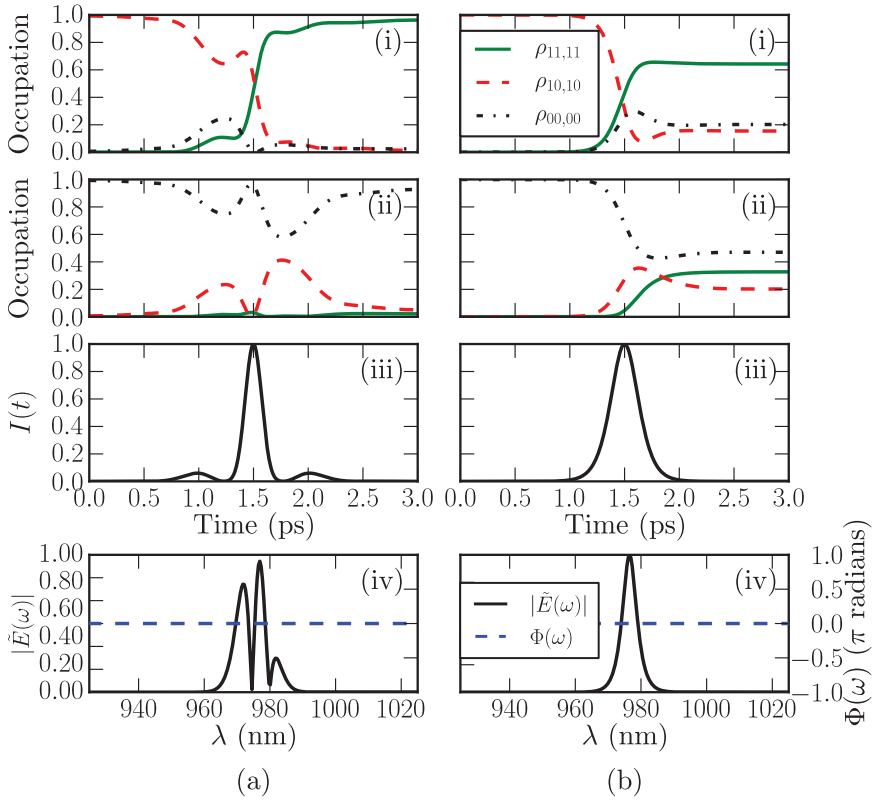

Figure 5.6: Population dynamics and control pulse characteristics for (a) the optimal amplitude-shaped pulse, and (b) the TL pulse. Panels (i) and (ii) show the population dynamics for the initial conditions $\rho_{10,10}(t=0)=1$ and $\rho_{00,00}(t=0)=1$, respectively. The third panel shows the temporal envelope of the electric field intensity of the control pulse. The bottom panel shows the amplitude (solid curves) and phase (dashed curves) profiles for the control pulse.

5.6.2 Dependence on Biexciton Binding Energy

The variation of the fidelity and gate time with the size of the binding energy of the biexciton is shown in Fig. 5.8 for the optimum shaped and TL pulses. The gate fidelity is independent of the sign of Δ_b, indicating that only the magnitude of the energy separation between the $|00\rangle \rightarrow |10\rangle$ and $|10\rangle \rightarrow |11\rangle$ transitions is important. The phase- and amplitude-shaped pulses outperform the TL pulses for the full range of binding energies investigated. The pulse parameters corresponding to the data in Fig. 5.8 are shown in Table 5.2 and Table 5.3 for the phase- and amplitude-shaping

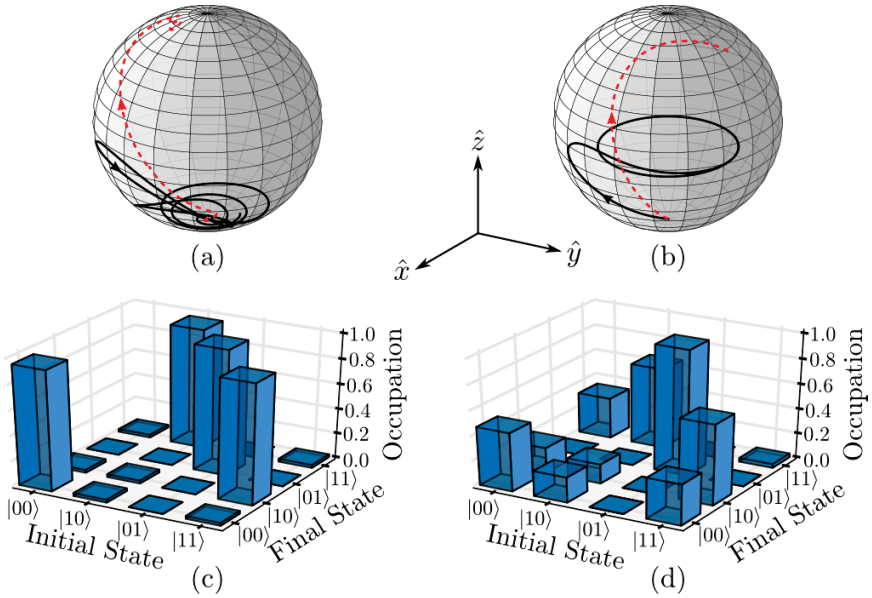

Figure 5.7: Bloch vector representations of the first qubit for $\rho_{00,00}(t = 0) = 1$ (solid curve) and the second qubit for $\rho_{10,10}(t = 0) = 1$ (dashed curve) for the (a) amplitude-shaped pulses, and (b) TL pulse. Truth table of the gate operation for the (c) optimal amplitude-shaped pulse, and (d) TL pulse.

protocols, respectively. The pulse parameters for positive and negative binding energies were found to be similar, and so only the trends for positive binding energies are provided. For the phase-shaped pulses, the decrease in the sinusoidal amplitude α and frequency γ with increasing Δ_b in Table 5.2 occurs because less rapid changes in the phase are required for a high fidelity operation between increasingly distant transitions. The phase δ, while having a critical influence on the temporal pulse profile and the resulting dynamics, does not have a discernible trend. We observe that $\Theta > \pi$ in all cases, indicating that the target quantum state is reached after multiple cycles of the Bloch vector. As Δ_b increases, the pulse center-frequency tracks the $|10\rangle \rightarrow |11\rangle$ transition, and therefore the pulse energy at the $|00\rangle \rightarrow |10\rangle$ transition decreases. A greater overall pulse energy is then needed to reach the desired final state for all initial conditions simultaneously, leading to the increase in Θ with Δ_b in Table 5.2. Our calculations indicate that further increasing the binding energy to values that are larger than the pulse bandwidth causes the optimum value of the pulse area to decrease towards π radians (e.g. $\Theta = 4.44\pi$ for $\Delta_b = 12\,\mathrm{meV}$ and $\Theta = \pi$ for $\Delta_b = 24\,\mathrm{meV}$), as expected because in this trivial limit the undesired

transition is not coupled to the laser field. We note that the meaning of the optimized pulse parameters are questionable for $\Delta_b \approx 0$, likely accounting for the two anomalous points around $\Delta_b = 0$ in the results for the amplitude mask in Fig. 5.8.

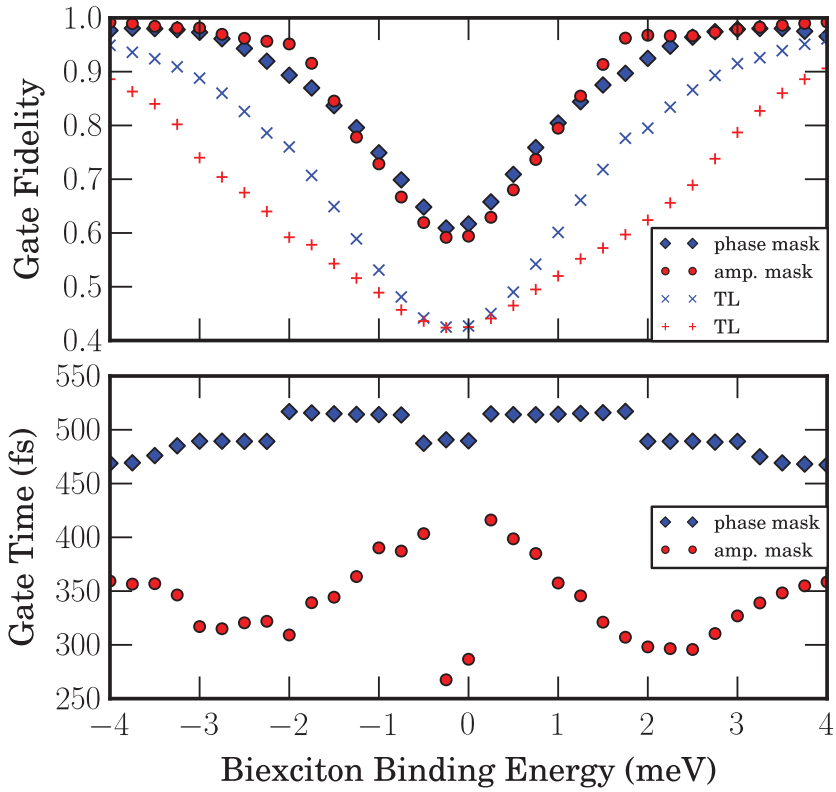

Figure 5.8: (Top) Fidelity for the optimal phase-shaped pulses (diamonds), and optimal amplitude-shaped pulses (circles) is shown as a function of the biexciton binding energy. The fidelities of the corresponding TL pulses with equivalent gate times are also shown for the phase-shaped pulses ($\times$), and amplitude-shaped pulses ($+$). (Bottom) Gate time of optimal phase-shaped (diamonds) and amplitude-shaped (circles) pulses as a function of binding energy.

As seen in Table 5.3, the amplitude-shaping protocol is ineffective for small Δ_b. The fidelity nevertheless increases rapidly as the separation between the transitions increases: A fidelity near unity is already achieved for $\Delta_b > 1.5\,\mathrm{meV}$. The bandwidth of the first Gaussian function is nearly constant at the lower limit of the imposed constraint because a narrow function maximizes the fraction of light contributing to the $|10\rangle \rightarrow |11\rangle$ Rabi rotation. In contrast, the bandwidth of the second term increases to its maximum value as Δ_b increases. A large value for $\hbar\Delta\omega_2$ maximizes the overlap of the pulse bandwidth of the second pulse with that of the

first pulse. However, it is not clear why this overlap is advantageous for increasing the fidelity. The optimum values for A_0 in Table 5.3 ensure that destructive interference at the $|10\rangle \rightarrow |11\rangle$ transition is complete. The pulse area, Θ, decreases monotonically with Δ_b in Table 5.3, reflecting the relaxed requirements for high fidelity operation. This reduction in Θ also leads to a decrease in the fraction of light reflected by the pulse shaper in imposing the amplitude-shaping scheme.

Table 5.2: The optimum pulse parameters obtained for the phase-shaping protocol for a range of values of the biexciton binding energy. The resulting C-ROT gate time (GT) is also shown.

$\Delta_b\,(\mathrm{meV})$	F	$\alpha\,(\pi\,\mathrm{rad})$	$\gamma\,(\mathrm{fs})$	$\delta\,(\pi\,\mathrm{rad})$	$\Theta\,(\pi\,\mathrm{rad})$	GT (fs)
0.00	0.617	0.460	325.0	-0.770	3.617	555.7
0.25	0.658	0.600	325.0	0.854	5.841	584.1
0.50	0.709	0.602	325.0	0.841	5.769	583.3
0.75	0.759	0.603	325.0	-0.165	5.759	583.2
1.00	0.805	0.606	325.0	0.832	5.758	583.8
1.25	0.844	0.608	325.0	-0.168	5.765	584.5
1.50	0.875	0.610	325.0	0.832	5.759	585.3
1.75	0.897	0.613	325.0	-0.165	5.771	586.7
2.00	0.925	0.507	325.0	-0.758	5.775	555.0
2.25	0.947	0.509	325.0	-0.757	5.779	555.2
2.50	0.964	0.511	325.0	0.243	5.780	555.3
2.75	0.974	0.513	323.3	-0.758	5.790	554.2
3.00	0.979	0.514	324.5	0.245	5.782	489.2
3.25	0.980	0.522	301.6	0.218	5.945	555.0
3.50	0.980	0.525	293.1	-0.791	6.000	532.4
3.75	0.975	0.526	291.2	-0.794	6.000	531.1
4.00	0.966	0.527	289.9	-0.796	6.000	530.3

It should be noted that the amplitude-shaping protocol provides shorter gate times (by $\sim 30\,\%$ on average) than the phase-shaping protocol, while the phase-shaping scheme avoids the deleterious effects associated with the rejected light in the pulse shaper. As only two shaping schemes are investigated here, it is reasonable to expect a further improvement in the overall gate characteristics with the generalization of the shaping protocol to include simultaneous control over the amplitude and phase of the pulse. Improvements in gate performance may also be achieved using phase-only control schemes with a more complex choice for the phase mask function than that used here. The simple shaping schemes we have implemented

Table 5.3: The optimum pulse parameters obtained for the amplitude-shaping protocol for a range of values of the biexciton binding energy. The resulting C-ROT gate time (GT) is also shown.

$\Delta_b\,(\mathrm{meV})$	F	$\hbar\Delta\omega_1\,(\mathrm{meV})$	$\hbar\Delta\omega_2\,(\mathrm{meV})$	A_0	$\Theta\,(\pi\,\mathrm{rad})$	GT (fs)
0.00	0.594	6.967	9.428	0.902	5.843	325.2
0.25	0.629	6.099	6.458	0.898	5.889	472.1
0.50	0.680	6.083	6.744	0.899	6.000	452.3
0.75	0.737	6.083	7.085	0.900	6.000	436.7
1.00	0.795	6.083	7.572	0.902	6.000	405.7
1.25	0.855	6.083	8.340	0.900	6.000	392.1
1.50	0.913	6.083	9.780	0.897	6.000	364.4
1.75	0.962	6.190	11.121	0.885	6.000	348.5
2.00	0.968	6.083	11.991	0.850	5.029	338.2
2.25	0.966	6.083	12.166	0.815	4.318	336.4
2.50	0.967	6.083	12.166	0.772	3.600	335.5
2.75	0.973	6.083	12.166	0.728	3.048	352.3
3.00	0.979	6.083	12.166	0.685	2.683	370.9
3.25	0.983	6.083	12.166	0.643	2.400	384.7
3.50	0.986	6.083	12.166	0.603	2.175	395.2
3.75	0.990	6.083	12.166	0.566	1.998	402.7
4.00	0.992	6.083	12.166	0.530	1.857	406.7

serve to illustrate the power and flexibility of the pulse-shaping approach in achieving rapid, high-fidelity quantum operations on qubits in semiconductor quantum dots.

5.6.3 Inclusion of Relaxation Effects

The effects of dephasing were examined by introducing relaxation to the model, as discussed in Sec. 5.5. The population decay constants are set to values that are typical of $\mathrm{In}_x\mathrm{Ga}_{1-x}\mathrm{As}$ dots [208]: $T_1 = 480\,\mathrm{ps}$ for the exciton states $|01\rangle$ and $|10\rangle$, and $T_1 = 320\,\mathrm{ps}$ for the biexciton state $|11\rangle$ (i.e. $\gamma_{01,01} = \gamma_{10,10} = T_1^{-1}$ for the single excitons and $\gamma_{11,11} = T_1^{-1}$ for the biexciton). As described in Sec. 5.5, these effects are incorporated in the relaxation-time approximation. The longitudinal decay times are held fixed while the T_2 times (γ_{ij}^{-1} for $i \neq j$) are taken to be the same for both exciton and biexciton states and are varied over a wide range up to the radiatively-limited case. The fidelity was calculated by integrating Eqns. 5.3–5.12

over $8\,\mathrm{ps}$, with the pulse arriving at the center of the temporal window. The results of these calculations are shown in Fig. 5.9. We find that dephasing has only a small impact on the fidelity in all cases, even down to the shortest decoherence time considered ($10\,\mathrm{ps}$). This reflects the rapid nature of the C-ROT gate when ultrafast optical pulses are used. The impact of dephasing depends only on the gate time, giving a reduction of $6\,\%$ for the phase-shaping scheme and $3\,\%$ for the amplitude-shaping scheme with a dephasing time of $10\,\mathrm{ps}$. Dephasing times for exciton qubits in semiconductor quantum dots in the range of several hundred picoseconds have been measured experimentally at low temperature [86]. In conjunction with the implementation of dynamical decoupling schemes for mitigating decoherence between gate operations [92, 46, 35], these results indicate the feasibility of high fidelity quantum computing using subpicosecond optical gates and semiconductor quantum dots.

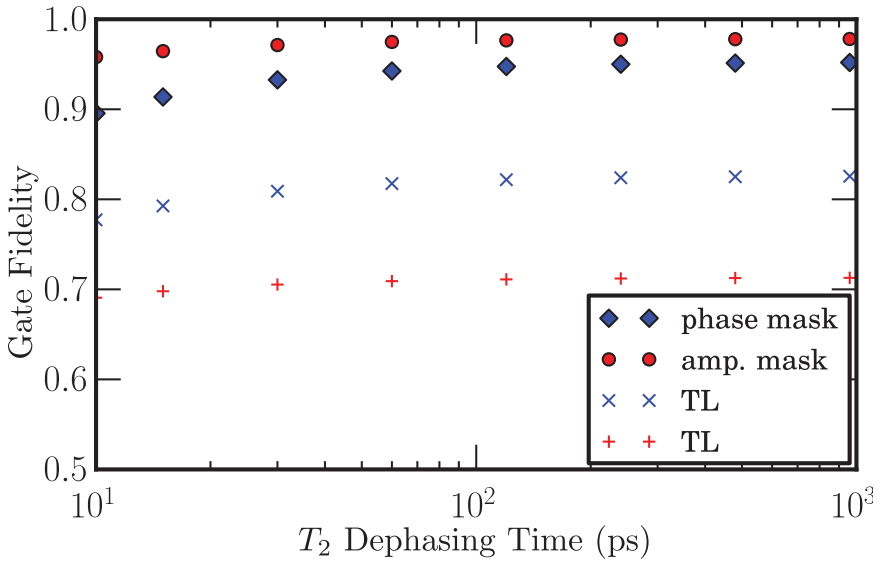

Figure 5.9: Fidelity versus dephasing time T_2 for the optimal phase-shaped pulses (diamonds), and optimal amplitude-shaped pulses (circles), and the TL sech pulses with gate time equivalent to that of the phase-shaped pulses ($\times$), and amplitude-shaped pulses ($+$).

5.7 Conclusions

In conclusion, we have studied the use of pulse-shaping protocols that can be easily implemented using commercially available femtosecond laser systems and pulse

shapers. We demonstrated the use of these protocols for the C-ROT gate in a realistic In(Ga)As quantum dot with electronic structure obtained using eight-band, strain-dependent $\mathbf{k}\cdot\mathbf{p}$ theory. Our results show that engineering the pulse using simple amplitude-only and phase-only shaping schemes provides considerable improvements in fidelity over a transform-limited pulse with the same operation time. The power and flexibility of pulse-shaping systems, which provide independent control of the pulse amplitude and phase, may be exploited to obtain further improvements in gate performance through generalization to more complex shaping schemes. The introduction of relaxation to the model was found to have a minimal effect on the gate fidelity for experimentally relevant dephasing times, reflecting the advantages of femtosecond optical pulses for quantum operations. Our results lay the ground work for implementing pulse shaping in other quantum control processes, including two-photon Rabi rotations, adiabatic passage, and schemes for dynamical decoupling.

Chapter 6

Subpicosecond Adiabatic Rapid Passage on a Single Semiconductor Quantum Dot: Phonon-Mediated Dephasing in the Strong Driving Regime

Authors: Reuble Mathew[1], Eric Dilcher[1], Angela Gamouras[1], Ajan Ramachandran[1], Hong Yi Shi Yang[1], Sabine Freisem[2], Dennis Deppe[2], and Kimberley C. Hall[1]

[1]Department of Physics and Atmospheric Science, Dalhousie University, Halifax, Nova Scotia B3H4R2, Canada
[2]The College of Optics and Photonics, University of Central Florida, Orlando, Florida 32816-2700, USA

Reprinted with permission from Physical Review B **90**, 035316 (2014). Copyrighted 2011 by the American Physical Society. Reuble Mathew developed the techniques, performed the experiments and the data analysis. Eric Dilcher, Ajan Ramachandran, and Hong Yi Shi Yang assisted with data collection. Angela Gamouras designed and built part of the apparatus. Sabine Freisem and Dennis Deppe developed and grew the sample. Kimberley C. Hall and Reuble Mathew conceived and designed the experiments. Reuble Mathew and Kimberley C. Hall wrote the manuscript with input from all authors.

6.1 Abstract

We demonstrate adiabatic rapid passage on a subpicosecond timescale in a single semiconductor quantum dot, enabling the exploration of a regime of strong (and rapidly-varying) Rabi energies for optical control of excitons. An observed dependence of exciton inversion efficiency on the sign of pulse chirp demonstrates the dominance of phonon-mediated dephasing, which is suppressed for positive chirp

at low temperature. Our findings will support the realization of dynamical decoupling strategies, and suggest that multi-phonon emission and/or non-Markovian effects should be taken into account.

6.2 Introduction

Semiconductor quantum dots (QDs) are attractive for a variety of applications in quantum information science as they offer atom-like properties in a solid state environment, coupled with the ease and efficiency of quantum state manipulation using coherent optical pulses [15, 50, 52, 100, 106, 209]. Adiabatic rapid passage (ARP) provides a particularly effective strategy for achieving quantum state inversion in these systems because, unlike optical control via Rabi oscillations [15, 50, 52], ARP is insensitive to variations in the QD parameters (dipole moment, transition energy) that are inherent to the natural size variations present in such systems. The robustness of quantum state inversion via ARP is due to the use of frequency-swept optical pulses, which results in a transfer of the system through an anticrossing for which the final state is uniquely identified with the exciton after the laser pulse is over [136, 135, 129, 138, 130, 128]. Building upon demonstrations in atomic systems [135, 136], ARP was recently achieved experimentally in single semiconductor quantum dots [74, 73], paving the way for application to efficient single and entangled photon sources [48, 127], quantum gates [130, 131, 132, 133, 134], all-optical switches [128, 129] and the realization of a Bose-Einstein condensate in a QD ensemble [210].

Despite this promise, quantum state control in QDs is impeded by coupling to phonons, representing an intrinsic source of decoherence within the solid state environment. The need to both elucidate and mitigate phonon-mediated decoherence processes in optical control experiments on semiconductor QDs has stimulated a comprehensive research effort in recent years [69, 25, 137, 138, 139, 140, 141, 130, 89, 142, 143, 144, 145, 129, 146]. For ARP, the impact of phonons has recently been predicted to depend on the magnitude of the peak Rabi energy during the control pulse as well as the direction of the sweep of the instantaneous pulse frequency (*i.e.*, the sign of the pulse chirp) [138, 139, 140]. The former prediction is consistent with the observation of a drop in the final exciton occupation with increasing

pulse area above the threshold for ARP [73, 74]. A dependence on pulse chirp, however, provides a more transparent means of distinguishing phonon-induced dephasing from other sources of decoherence. In particular, in previous studies of damping of Rabi oscillations, coupling of the optically excited exciton with phonons [69, 25] or unintended carriers excited into the wetting layer [64, 211] have been identified as potential sources of decoherence. For control via ARP, only the phonon-related process depends on the sign of pulse chirp, allowing for the experimental isolation of phonon-related decoherence effects in optical control.

In the experiments reported here, we show that phonons represent the primary source of dephasing in optical control experiments on excitons in single semiconductor QDs by revealing a dependence of the exciton inversion efficiency on the sign of the control pulse chirp: For positively-chirped pulses, the system traverses the lower-energy adiabatic branch, resulting in greater exciton inversion, consistent with suppression of phonon emission processes. Our experiments also represent a demonstration of ARP in a new experimental regime of large Rabi energy through the use of shorter optical pulses (representing a factor of $\gtrsim 20$ reduction in comparison to previous work [74, 73]). In addition to enabling a larger number of quantum operations within the decoherence time, the ultrafast control pulses used in the experiments reported here lay the groundwork for realizing decoherence protection via dynamical decoupling [33, 35, 46, 92]. Comparison of our experimental results with a theoretical model including phonon-mediated decoherence [69, 25, 137] suggests the importance of multi-phonon emission processes and non-Markovian effects, with implications for the theoretical design of optimal control pulses that minimize decoherence. The use of short pulses also reduces the magnitude of the spectral chirp required for ARP, facilitates the accurate application of chirp via readily available commercial pulse shaping systems, and provides a means to further optimize the quantum state evolution and to realize parallel quantum gates on multiple quantum dots through the use of general pulse shaping techniques [134, 141, 173, 174, 125].

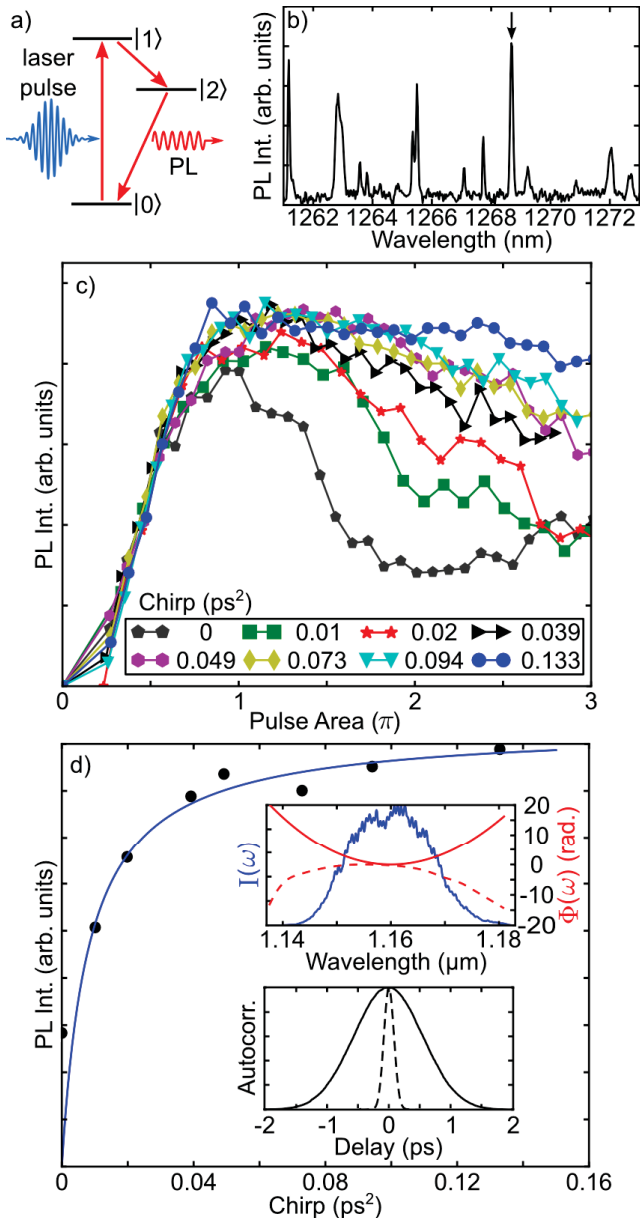

Figure 6.1: (a) Quantum state control and read-out scheme with ground state ($|0\rangle$), p-shell exciton ($|1\rangle$), and s-shell exciton ($|2\rangle$). (b) Spectrally-resolved PL from the s-shell. The arrow marks the s-shell emission for the QD studied here. (c) PL intensity as a function of pulse area for increasing positive chirp. (d) PL intensity at $\Theta = 2\pi$ as a function of the magnitude of the chirp (black circles) and a fit to a saturation function ($I = I_0\phi''/(\phi'' + \phi''_{\rm sat})$), with $\phi''_{\rm sat} = 0.0083\,{\rm ps}^2$ (blue curve). Inset: (top) Laser pulse spectrum (solid blue curve), dispersion compensation mask (dashed red curve) and the chirp mask applied to the dispersion-compensated pulse for $\phi'' = 0.039\,{\rm ps}^2$ (solid red curve). (bottom) Measured pulse autocorrelation for the transform-limited pulse with $\tau_0 = 120\,{\rm fs}$ (dashed curve) and a chirped $910\,{\rm fs}$ pulse with $\phi'' = 0.039\,{\rm ps}^2$ (solid curve).

6.3 Experimental Details

The sample under study is an InAs/GaAs quantum dot structure grown using molecular beam epitaxy. We spectrally isolate single QDs from the ensemble using a metallic mask with a $0.4\,\mu\mathrm{m}$ aperture. The sample is held on a nanopositioning stage in a continuous-flow cryostat at $10\,\mathrm{K}$. The optical source is a $76\,\mathrm{MHz}$ optical parametric oscillator (OPO) generating 1.16 μm pulses with a dispersion-compensated pulse width of $120\,\mathrm{fs}$. Dispersion compensation [162] and the introduction of chirp is achieved by passing the pulses through a $4f$ pulse shaper, with a dual mask, 128-pixel spatial light modulator at the Fourier plane. The laser pulses, resonant with the crystal ground state ($|0\rangle$) to p-shell exciton ($|1\rangle$) transition in the QD (see Fig. 6.1(a)), are focused onto the sample using a high-resolution objective lens (numerical aperture 0.7). Relaxation to the s-shell exciton ($|2\rangle$) occurs non-radiatively and the photoluminescence (PL) emitted from the s-shell is collected through the same objective lens and detected using a $0.75\,\mathrm{m}$ monochromator and InGaAs array detector with a resolution of $30\,\mu\mathrm{eV}$. For the QD under study, the p-shell and s-shell transitions are at $1.0688\,\mathrm{eV}$ and $0.9772\,\mathrm{eV}$, respectively, determined using micro-PL and PL excitation techniques. For further details on the sample structure and experimental techniques, see Ref. [125].

6.4 Results

6.4.1 Ultrafast ARP

We demonstrate ARP by measuring the PL intensity as a function of the pulse area (Θ) for increasing positive spectral chirp (ϕ''), which is applied to a transform-limited pulse using the pulse shaper [1]. Here the linearly chirped laser pulse is given by $E(t) = \frac{1}{2}E_p(t)\exp\left[-i(\omega_l t + \alpha t^2)\right]$ where ω_l is the center frequency of the laser pulse and the frequency is swept at rate α, where $\alpha = 2\phi''/[\tau_0^4/(2\ln(2))^2 + (2\phi'')^2]$, τ_0 is the transform-limited pulse width, and $\tau_p = \tau_0[1+(4\ln 2\phi'')^2/\tau_0^4]^{1/2}$ is the width of the chirped pulse. The results of these experiments are shown in Fig. 6.1(c). A strongly-damped Rabi oscillation is observed for zero pulse chirp, a signature

[1] The average power required to reach a given pulse area is proportional to the laser pulse bandwidth, limiting the maximum pulse area that avoids sample heating effects.

of coherent manipulation of the exciton, as seen in previous work [15, 50, 52, 69, 211]. As the magnitude of the chirp is increased, the PL intensity for $\Theta > \pi$ increases and a plateau in the emission emerges, corresponding to high inversion efficiency over a wider range of Θ as ϕ'' is increased. For the largest value of chirp ($\phi'' = 0.133\,\mathrm{ps}^2$), the PL intensity is nearly independent of pulse area above the threshold for ARP. This trend was observed for both linearly and circularly-polarized control pulses indicating that biexciton dynamics do not play a significant role, consistent with previous studies of Rabi oscillations on the p-shell transition [211]. Figure 6.1(d) shows the PL intensity for a pulse area of 2π as a function of the magnitude of the chirp (black circles), indicating a saturation behaviour.

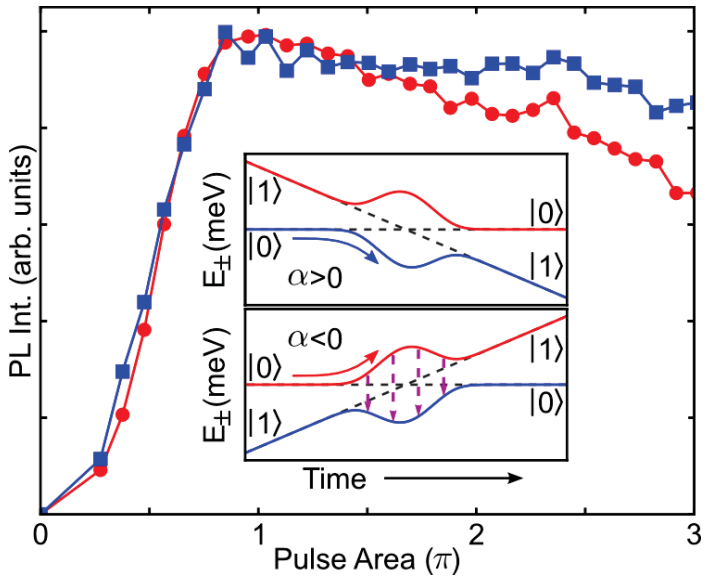

Figure 6.2: PL intensity as a function of pulse area for $\phi'' = +0.133\,\mathrm{ps}^2$ (blue squares) and $\phi'' = -0.133\,\mathrm{ps}^2$ (red circles). Inset: Illustration of the temporal evolution of the energies of the dressed states for positively-chirped and negatively-chirped pulses. The vertical dashed arrows represent diabatic transitions caused by phonon emission.

The insensitivity of the exciton PL intensity to changes in pulse area for a sufficiently large pulse chirp is a signature of adiabatic rapid passage and robust state inversion [136, 135, 129, 138, 130, 128]. For ARP, coupling of a two-level system with a light field may be understood in terms of the instantaneous eigenstates of the system, the so-called dressed states $|\psi_+\rangle$ and $|\psi_-\rangle$. In the adiabatic regime, the system remains in one of the dressed states while the admixture of the bare

QD states ($|0\rangle$ and $|1\rangle$) is evolved to invert the two-level system. The energy splitting of the states is given by $\sqrt{\Omega(t)^2 + \Delta(t)^2}$, where $\Omega(t) = (\sqrt{2\ln 2})(\Theta/\sqrt{\pi\tau_0\tau_p})$ $\exp\left[-2\ln(2)t^2/\tau_p^2\right]$ is the instantaneous Rabi frequency and $\Delta(t) = -2\alpha t$ is the detuning of the laser field from the transition. For the positive chirp applied in the experiments in Fig. 6.1(c), the system evolves from the ground state to the exciton through the anticrossing in state $|\psi_-\rangle$, corresponding to traversal along the lower-energy adiabatic branch (see inset to Fig. 6.2). Using the condition $\phi''_{\min} \approx \pi\tau_0^2/[2\ln(2)]$ from Ref. [138], we estimate the minimum chirp required to achieve ARP to be $0.033\,\mathrm{ps}^2$ in our experiments, corresponding to a pulse width of $\tau_p = 770\,\mathrm{fs}$. This represents a reduction in the gate time for exciton inversion using ARP by a factor of $\gtrsim 20$ relative to previous demonstrations [73, 74]. The use of broadband pulses in our experiments has also resulted in a lower threshold spectral chirp ($0.033\,\mathrm{ps}^2$ here, in comparison to $\sim 10\,\mathrm{ps}^2$ in Refs. [74, 73]). Furthermore, the requisite chirp is much easier to implement with standard commercially available frequency-domain pulse shapers when femtosecond pulses are used.

The achievement of ARP using subpicosecond pulses demonstrated here is greatly beneficial for quantum computing applications because it permits more gate operations within the decoherence time [130, 131, 132, 133, 134, 120]. While this benefit is universal, the protective effect of short pulse control is particularly evident for our experiments, in which efficient ARP is achieved for the first time on the p-shell transition in a semiconductor QD despite a short energy relaxation time to the s-shell [51, 212]. Our demonstration of a sub-picosecond gate also paves the way for strategies for decoherence protection based on dynamical decoupling [33, 35, 46, 92], for which faster gates lead to greater protection. The ease and flexibility of pulse shaping in the femtosecond regime also permits more accurate dispersion compensation [162] as well as the ability to pursue arbitrary (nonlinear) phase control that can be used to optimize gate performance (e.g. fidelity, speed) [134, 141, 173, 174, 125] and may enable parallel processing in solid state qubit systems [125]. The use of broadband pulses is aided by the strong confinement in the QDs studied here, which are characterized by a large energy separation between the s-shell and p-shell transitions and between the p-shell and the wetting layer transitions ($90\,\mathrm{meV}$ and $310\,\mathrm{meV}$, respectively). The latter separation is

expected to strongly diminish sources of decoherence associated with coupling to unwanted excitations in the wetting layer [64, 211].

6.4.2 Role of Phonons

In order to investigate the role of phonons in our experiments, measurements were made of the dependence of the PL intensity on the sign of the pulse chirp (*i.e.* the sign of α). The results of these experiments (for which $|\phi''| = 0.133$ ps^2, well above the threshold for ARP) are shown in Fig. 6.2. The PL intensity from the exciton transition for negative pulse chirp (red circles) is lower than that for positive pulse chirp (blue squares) by an amount that increases with increasing pulse area. This chirp sign dependence is observed for both linearly and circularly-polarized excitation, indicating a negligible role of biexcitons in this effect. For $\alpha < 0$, the system evolves from the ground state to the exciton through the anticrossing via the higher-energy adiabatic branch. In this case, diabatic transitions can occur in the vicinity of the anticrossing due to emission of phonons [69, 25, 137, 144, 141]. In contrast, for $\alpha > 0$, state evolution proceeds via the lower-energy adiabatic branch. Phonon mediated transitions to the upper branch would occur through phonon absorption in this case, which is suppressed at $10\,\mathrm{K}$ [138, 139, 140][2]. Phonon-mediated transitions between the adiabatic branches are a form of excitation-induced dephasing (EID), since the decoherence rate is dictated by the characteristics of the optical pulse. The results in Fig. 6.2 therefore indicate that coupling to phonons is the primary mechanism limiting the efficiency of exciton inversion via ARP and that proper choice of the sign of the pulse chirp can diminish such effects at low temperatures. The protective effect of the energy gap between the upper and lower energy adiabatic branches should exist for temperatures T for which $k_B T \lesssim \hbar\Lambda(t)$ where $\Lambda(t) = \sqrt{\Omega(t)^2 + \Delta(t)^2}$ is the instantaneous value of the effective Rabi frequency. A reduced exciton inversion for negative pulse chirp was observed within the range of accessible temperatures in our experiments ($\leq$ 25 K, limited by the noise floor of the InGaAs detector and the micro-PL technique used here for quantum state readout). This is consistent with the large Rabi energies in our experiments, as $\hbar\Lambda_p$ is

[2]The suppression of phonon absorption follows from the large value of the minimum splitting between the dressed states during the control pulse [approximately 4 meV; see Fig. 6.3, inset] relative to the thermal energy available at 10 K.

approximately 7 meV, representing an enhancement of several orders of magnitude compared to previous work [74, 73]. The strong driving conditions achieved in our experiments through the use of subpicosecond control pulses is therefore beneficial for the potential operation of devices that exploit ARP at elevated temperatures.

The identification of the physical process limiting the quality of quantum control is possible here because the sign of pulse chirp in ARP provides a means to isolate phonon-related decoherence, as contributions to EID tied to wetting layer excitations exhibit no such chirp sign dependence. The general conclusion of the dominance of phonon coupling also translates to other control processes such as Rabi rotations, for which the system is in a superposition of the upper- and lower-energy dressed states during optical control. In the case of Rabi oscillations, distinguishing between the wetting layer and phonon contributions to EID represents a more formidable challenge [69, 25, 64, 211, 146] as both mechanisms lead to similar trends in the dependence of the dephasing rate on pulse bandwidth and Θ (for small Θ). Recent measurements of Rabi oscillation damping over a broad range of experimental conditions [69, 25] point to the dominance of phonon-mediated EID, in agreement with the findings we report here. For ARP, the sensitivity of exciton inversion efficiency on the sign of pulse chirp demonstrated here provides a clear isolation of phonon-mediated EID. A weak decay at the highest pulse areas for $\alpha > 0$ in the results in Fig. 6.2 may indicate a weak contribution from the wetting layer mechanism, which increases in strength with increasing Θ [64, 211], although the broad range of pulse area with a relatively constant PL intensity in Fig. 6.2 is promising for applications utilizing ARP for exciton inversion.

While the above results clearly indicate the dominant role of phonons in dephasing for optical control on single semiconductor QDs, the relatively unexplored regime of strong (and rapid) driving of the coupled quantum dot-phonon system achieved in our experiments may also be exploited in strategies for decoherence mitigation. In particular, the influence of phonon-mediated dephasing is dictated by the instantaneous value of $\Lambda(t)$ for times during the state evolution in the vicinity of the anticrossing, together with the frequency dependence of the phonon response function ($K(\omega)$) [144, 69, 25, 139, 138, 140]. The exciton-phonon coupling is strongest when $K(\Lambda)$ is significant since in this case the phonon modes can respond

resonantly to laser-induced driving of the exciton at the effective Rabi frequency, resulting in phonon-mediated transitions between the adiabatic branches. The finite size of the exciton wave function within the quantum dot leads to a nonmonotonic frequency dependence of $K(\omega)$ that translates into a nonmonotonic dependence of the dephasing rate on the effective Rabi frequency: For small Λ, the phonon coupling increases with Λ, while for sufficiently large Λ, the phonon coupling may be reduced considerably due to the finite response time of the phonon bath. The latter result favours the execution of optical control on very short time scales since the peak value of Ω (and therefore of Λ) is given by $\Omega_p = (\sqrt{2\ln 2})(\Theta/\sqrt{\pi\tau_0\tau_p})$, which is strongly enhanced for a given pulse area in the experiments reported here due to the small values of τ_p and τ_0.

In order to gain insight into the transition between the regime of Rabi frequencies considered in past demonstrations of ARP [73, 74] and the experiments in Fig. 6.2, numerical simulations of the quantum state evolution were carried out using a density matrix approach [174] in which deformation coupling to acoustic phonons was included taking into account pure dephasing via the real part of the complex phonon response function, following the model presented in Ref. [137]. The dependence of the exciton inversion efficiency on the sign of the pulse chirp was calculated for four different values of τ_0, taking $\phi'' = 4\pi\tau_0^2/(2\ln 2)$; *i.e.* four times the threshold chirp for ARP discussed above. For $\tau_0 = 120\,\mathrm{fs}$, this corresponds to $\phi'' = 0.131\,\mathrm{ps}^2$, reflecting the experimental conditions for the results in Fig. 6.2. The results of these calculations are shown in Fig. 6.3(a)-(d). The general trends are in line with the expected dependence on Ω_p discussed above. For the largest value of τ_0 (825 fs, Fig. 6.3(a)), phonon-mediated dephasing results in a difference between the exciton occupation for positive and negative chirp that increases with increasing pulse area, similar to the trend observed experimentally (Fig. 6.2). As τ_0 decreases, the coupling to phonons becomes most prominent for lower values of pulse area until τ_0 = 120 fs, where the model indicates negligible coupling to phonons, in contrast to the experimental results.

The quantitative deviations between the experimental results and the model considered here (*i.e.* the pulse bandwidth at which good agreement is obtained) provides new insight into coherent control in the strong field regime. In particular,

the persistence of phonon-mediated dephasing in our experiments despite the large instantaneous Rabi frequencies suggests that other physical processes not included in the model of exciton-phonon coupling considered here may play a role and must be considered in the design of control pulses to minimize exciton-phonon coupling. While coupling to LO phonons [213, 129, 145] may contribute to the strong damping of the Rabi oscillation in the zero chirp results of Fig. 6.1(c), for the pulse characteristics used in the experiments of Fig. 6.2, coupling to LO phonons may be neglected since the peak Rabi energy remains below 7 meV (see inset to Fig. 6.3(d)). While the addition of piezoelectric coupling would enhance the phonon mediated dephasing somewhat [213], for the conditions of our experiments in which the Rabi energy exceeds 4 meV during the control pulse it may also be necessary to include multi-phonon emission processes, which are absent in the model due to the perturbative treatment of exciton-phonon coupling [137, 142]. In addition, the rapid variation of the laser pulse parameters in our experiments may necessitate a more accurate treatment of non-Markovian (memory) effects in the dynamics of the phonon bath than in the model considered here [89, 142, 143, 139, 141]. Our findings suggest that simply increasing the Rabi frequency may not be enough for decoherence mitigation when considering quantum state control at elevated temperatures. Alternate techniques such as the so-called 'bang bang' protocol of dynamic decoupling with engineered pulse trains may provide a more effective strategy [33, 35, 46, 92], for which the short time scale of ARP demonstrated here would be an important asset.

6.5 Conclusions

In summary, we have demonstrated adiabatic rapid passage in a new experimental regime by using control pulses that are more than an order of magnitude shorter than those used in previous ARP experiments. The combination of a subpicosecond control time with the robustness of ARP achieved in this work will support the application of QDs in quantum information science by enabling more quantum manipulations within the decoherence time. Our results demonstrate the dominant role played by coupling to phonons in optical control experiments in single QDs by isolating such effects from other sources of decoherence through a dependence of

the exciton inversion efficiency on the sign of the control pulse chirp. The importance of phonon-mediated dephasing is confirmed despite the large instantaneous Rabi frequencies in our experiments, which explore the limit of strong (and rapid) driving of the coupled exciton-phonon system.

6.6 Acknowledgements

The authors thank the Natural Sciences and Engineering Research Council of Canada and Lockheed Martin Corporation for financial support.

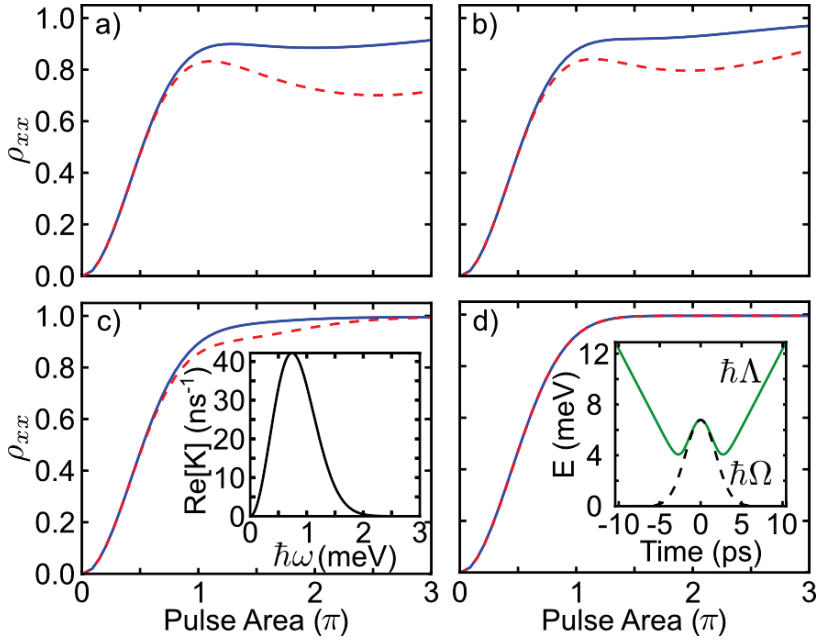

Figure 6.3: Calculated occupation of the exciton for positively-chirped (solid blue curve) and negatively-chirped (dashed red curve) pulses as a function of pulse area for increasing pulse bandwidth (*i.e.* decreasing τ_0). The chirp applied to each pulse (dictating the chirped pulse duration τ_p) is four times the threshold value, as described in the main text. (a) $\tau_0 = 825\,\mathrm{fs}$; (b) $\tau_0 = 650\,\mathrm{fs}$; (c) $\tau_0 = 410\,\mathrm{fs}$, Inset: Spectral dependence of the real part of the phonon response function. (d) $\tau_0 = 120\,\mathrm{fs}$, Inset: Temporal evolution of the Rabi energy $\hbar\Omega$ (dashed black curve) and the effective Rabi energy $\hbar\Lambda$ (solid green curve) for a chirp of $\phi'' = 0.133\,\mathrm{ps}^2$. Values of material parameters governing the strength of phonon coupling were taken from Ref. [138].

Chapter 7

Conclusion

Semiconductor quantum dots are a promising platform for the development of quantum information processing systems. The advantages afforded by this system include the scalability that is inherent to a solid-state architecture, the ability to leverage existing semiconductor-processing facilities, the ease of integration with classical semiconductor-based hardware, the tunability that permits operation at telecommunication wavelengths, and the ability to interface with photon qubits. Previous demonstrations of quantum state control in quantum dots, with the exception of demonstrations of adiabatic rapid passage, have employed transform-limited pulses to manipulate the qubit. This thesis has advanced the field of quantum state manipulation of exciton qubits confined to self-assembled InAs quantum dots through numerical and experimental demonstrations of pulse engineering to improve the speed and fidelity of quantum operations. Pulse shaping schemes that are routinely employed in atomic and molecular systems are extended here to a solid state qubit. The relatively simple electronic structure of QDs compared to the often intractable systems for atoms and molecules, allows for numerical optimization of engineered pulses to optimize fidelity. This thesis work has also used pulse shaping to improve our understanding of exciton-phonon coupling in confined systems in the strong-driving regime.

Optimal quantum control theory is the science of manipulating the system Hamiltonian to drive the quantum system to a desired final state at the end of the laser pulse. The first component of this thesis work showed that optimal quantum control theory can be used to devise pulse shapes to implement simultaneous high-fidelity operations for multiple exciton qubits confined to quantum dots. The pulse shapes were numerically optimized for fidelity subject to constraints that ensured that they can be accurately implemented on commercially available pulse shaping system. The numerical simulations used a cosine, phase-only shaping mask and

demonstrated that it is possible to implement high fidelity operations on two QDs provided the two exciton qubits in those QDs have sufficiently different optoelectronic properties. Pulses generated using this approach can either be implemented directly or may be used to seed an initial population for a genetic algorithm that maximizes the fidelity experimentally. The findings of thesis also indicated that parallel control of > 10 QDs using this approach is feasible, limited only by the resolution of the shaping system and the complexity of the phase function used in the pulse shaping system. This demonstration should enhance the scalability of the quantum-dot based architecture by reducing the laser resources required to control multiple qubits.

In addition to single-qubit operations, this thesis also demonstrated that optimal quantum control can be used to optimize the two-qubit C-ROT gate. This gate has recently been demonstrated for the exciton-biexciton system in a single quantum dot using long picosecond pulses and is an important test case to illustrate the effectiveness of pulse shaping. The theoretical work shows that pulse shaping enables subpicosecond C-ROT operations using a single laser pulse. This removes the complexity required for an implementation with transform-limited femtosecond pulses, such as multiple laser sources and stabilized beam paths. The optoelectronic properties used to define the quantum dot were determined using $\mathbf{k}\cdot\mathbf{p}$ theory. The results demonstrate that both amplitude- and phase-shaped pulses can be employed to provide improvements in gate fidelity compared to a transform-limited laser pulses with comparable gate times. The advantages afforded by the use of short pulses include a reduced sensitivity of the fidelity to dephasing. The presented results lay the groundwork for the implementation of pulse shaping for other control processes in quantum dot systems.

This thesis work also encompassed the demonstration of adiabatic rapid passage used linearly-chirped ultrafast laser pulses to implement robust state inversion of the exciton state in a single quantum dot. The use of broadband pulses allowed for π gates that were $\sim 20\times$ faster than those in previous experimental demonstrations of this quantum control process in single QDs. Faster π gates will permit more operations within the decoherence time and will be particularly useful for applications

such as all-optical switches and single- and entangled-photon sources. The experiments also confirmed the dominance of phonon-mediated dephasing by observing for the first time, the predicted chirp-sign dependence of the inversion efficiency. The persistence of phonon-mediated dephasing in the regime of strong and rapid driving of the exciton-phonon system suggests that multi-phonon effects, piezoelectric coupling, and non-Markovian effects may play a role in the dynamics. The findings of this work further the implementation of dynamical decoupling schemes as a means for mitigating the effects of decoherence of excitons in semiconductor QDs by realizing the demonstration of ultrafast π gates in this system.

The advances presented in this thesis have built upon an existing body of work and the impressive experimental demonstrations of recent years. The contributions made by this thesis work to the field of state manipulation in quantum dots using pulse engineering should promote the scalability of the quantum dot based computing platform. It has also provided an improved understanding of the nature of the interactions of qubits with their solid state environment and laid the foundations for demonstrations of experimental techniques to mitigate the resulting deleterious effects.

Bibliography

[1] P. Shor, "Algorithms for quantum computation: discrete logarithms and factoring," in *Proceedings 35th Annual Symposium on Foundations of Computer Science*, pp. 124–134, IEEE Comput. Soc. Press, 1994.

[2] L. Grover, "Quantum Mechanics Helps in Searching for a Needle in a Haystack," *Physical Review Letters*, vol. 79, pp. 325–328, July 1997.

[3] K. L. Pudenz and D. a. Lidar, "Quantum adiabatic machine learning," *Quantum Information Processing*, vol. 12, no. 5, pp. 2027–2070, 2013.

[4] R. P. Feynman, "Simulating physics with computers," *International Journal of Theoretical Physics*, vol. 21, pp. 467–488, June 1982.

[5] R. Harris, J. Johansson, A. J. Berkley, M. W. Johnson, T. Lanting, S. Han, P. Bunyk, E. Ladizinsky, T. Oh, I. Perminov, E. Tolkacheva, S. Uchaikin, E. M. Chapple, C. Enderud, C. Rich, M. Thom, J. Wang, B. Wilson, and G. Rose, "Experimental demonstration of a robust and scalable flux qubit," *Phys. Rev. B*, vol. 81, p. 134510, Apr 2010.

[6] G. Sanders, K. Kim, and W. Holton, "Quantum computing with complex instruction sets," *Physical Review A*, vol. 59, no. 2, pp. 1098–1101, 1999.

[7] Z. Amitay, R. Kosloff, and S. R. Leone, "Experimental coherent computation of a multiple-input AND gate using pure molecular superpositions," *Chemical Physics Letters*, vol. 359, no. 1-2, pp. 8–14, 2002.

[8] R. Raussendorf and H. J. Briegel, "A one-way quantum computer," *Phys. Rev. Lett.*, vol. 86, pp. 5188–5191, May 2001.

[9] D. P. DiVincenzo, "The Physical Implementation of Quantum Computation," *Fortschritte der Physik*, vol. 48, pp. 771–783, Sept. 2000.

[10] M. W. Doherty, N. B. Manson, P. Delaney, F. Jelezko, J. Wrachtrup, and L. C. Hollenberg, "The nitrogen-vacancy colour centre in diamond," *Physics Reports*, vol. 528, pp. 1–45, July 2013.

[11] R. Blatt and D. Wineland, "Entangled states of trapped atomic ions.," *Nature*, vol. 453, pp. 1008–15, June 2008.

[12] J. Clarke and F. K. Wilhelm, "Superconducting quantum bits.," *Nature*, vol. 453, pp. 1031–42, June 2008.

[13] F. A. Zwanenburg, A. S. Dzurak, A. Morello, M. Y. Simmons, L. C. L. Hollenberg, G. Klimeck, S. Rogge, S. N. Coppersmith, and M. A. Eriksson, "Silicon quantum electronics," *Rev. Mod. Phys.*, vol. 85, pp. 961–1019, Jul 2013.

[14] a. J. Ramsay, "A review of the coherent optical control of the exciton and spin states of semiconductor quantum dots," *Semiconductor Science and Technology*, vol. 25, p. 103001, Oct. 2010.

[15] T. Stievater, X. Li, D. Steel, D. Gammon, D. Katzer, D. Park, C. Piermarocchi, and L. Sham, "Rabi Oscillations of Excitons in Single Quantum Dots," *Physical Review Letters*, vol. 87, pp. 1–4, Sept. 2001.

[16] X. Li, Y. Wu, D. Steel, D. Gammon, T. H. Stievater, D. S. Katzer, D. Park, C. Piermarocchi, and L. J. Sham, "An all-optical quantum gate in a semiconductor quantum dot.," *Science (New York, N.Y.)*, vol. 301, pp. 809–11, Aug. 2003.

[17] T. Unold, K. Mueller, C. Lienau, T. Elsaesser, and A. Wieck, "Optical Stark Effect in a Quantum Dot: Ultrafast Control of Single Exciton Polarizations," *Physical Review Letters*, vol. 92, p. 157401, Apr. 2004.

[18] T. Unold, K. Mueller, C. Lienau, T. Elsaesser, and A. D. Wieck, "Optical control of excitons in a pair of quantum dots coupled by the Dipole-Dipole interaction," *Physical Review Letters*, vol. 94, no. 13, pp. 1–4, 2005.

[19] B. Patton, U. Woggon, and W. Langbein, "Coherent Control and Polarization Readout of Individual Excitonic States," *Physical Review Letters*, vol. 95, pp. 1–4, Dec. 2005.

[20] Y. Wu, X. Li, L. Duan, D. Steel, and D. Gammon, "Density Matrix Tomography through Sequential Coherent Optical Rotations of an Exciton Qubit in a Single Quantum Dot," *Physical Review Letters*, vol. 96, pp. 1–4, Feb. 2006.

[21] D. L. Huffaker, G. Park, Z. Zhengzhong, O. B. Shchekin, and D. G. Deppe, "Continuous-wave low-threshold performance of 1.3-um InGaAs-GaAs quantum-dot lasers," *IEEE Journal on Selected Topics in Quantum Electronics*, vol. 6, no. 3, pp. 452–461, 2000.

[22] D. Chithrani, R. L. Williams, J. Lefebvre, P. J. Poole, and G. C. Aers, "Optical spectroscopy of single, site-selected, InAs/InP self-assembled quantum dots," *Applied Physics Letters*, vol. 84, no. 6, pp. 978–980, 2004.

[23] A. Rastelli, A. Ulhaq, S. Kiravittaya, L. Wang, A. Zrenner, and O. G. Schmidt, "In situ laser microprocessing of single self-assembled quantum dots and optical microcavities," *Applied Physics Letters*, vol. 90, no. 7, pp. 16–19, 2007.

[24] D. J. P. Ellis, R. M. Stevenson, R. J. Young, a. J. Shields, P. Atkinson, and D. a. Ritchie, "Control of fine-structure splitting of individual InAs quantum dots by rapid thermal annealing," *Applied Physics Letters*, vol. 90, no. 1, pp. 16–19, 2007.

[25] A. J. Ramsay, "A review of the coherent optical control of the exciton and spin states of semiconductor quantum dots," *Semiconductor Science and Technology*, vol. 25, p. 103001, Oct. 2010.

[26] Z. Yuan, B. E. Kardynal, R. M. Stevenson, A. J. Shields, C. J. Lobo, K. Cooper, N. S. Beattie, D. a. Ritchie, and M. Pepper, "Electrically driven single-photon source.," *Science*, vol. 295, pp. 102–5, Jan. 2002.

[27] X. Gao, L. Yang, J. a. Petros, F. F. Marshall, J. W. Simons, and S. Nie, "In vivo molecular and cellular imaging with quantum dots.," *Current opinion in biotechnology*, vol. 16, pp. 63–72, Feb. 2005.

[28] Y. Masumoto and T. Takagahara, *Semiconductor Quantum Dots*. Berlin: Springer-Verlag, 2002.

[29] P. Bhattacharya, D. Klotzkin, and O. Qasaimeh, "High-Speed Modulation and Switching Characteristics of In(Ga)As-Al(Ga)As self-organized quantum-dot lasers," *IEEE Journal of Selected Topics in Quantum Electronics*, vol. 6, no. 3, pp. 426–438, 2000.

[30] R. M. Stevenson, R. J. Young, P. Atkinson, K. Cooper, D. a. Ritchie, and a. J. Shields, "A semiconductor source of triggered entangled photon pairs.," *Nature*, vol. 439, pp. 179–82, Jan. 2006.

[31] E. H. Sargent, "Colloidal quantum dot solar cells," *Nature Photonics*, vol. 6, no. 3, pp. 133–135, 2012.

[32] D. Sridharan and E. Waks, "All-Optical Switch Using Quantum-Dot Saturable Absorbers in a DBR Microcavity," *IEEE Journal of Quantum Electronics*, vol. 47, no. 1, pp. 31–39, 2011.

[33] L. Viola and S. Lloyd, "Dynamical suppression of decoherence in two-state quantum systems," *Physical Review A*, vol. 58, pp. 2733–2744, Oct. 1998.

[34] L. Viola, E. Knill, and S. Lloyd, "Dynamical Decoupling of Open Quantum Systems," *Physical Review Letters*, vol. 82, no. 12, pp. 2417–2421, 1999.

[35] V. Axt, P. Machnikowski, and T. Kuhn, "Reducing decoherence of the confined exciton state in a quantum dot by pulse-sequence control," *Physical Review B*, vol. 71, pp. 1–9, Apr. 2005.

[36] G. Uhrig, "Keeping a Quantum Bit Alive by Optimized π-Pulse Sequences," *Physical Review Letters*, vol. 98, p. 100504, Mar. 2007.

[37] T. E. Hodgson, L. Viola, and I. D'Amico, "Effect of quantum dot shape on dynamical dephasing suppression in exciton qubits under applied electric field," *Microelectronics Journal*, vol. 40, pp. 502–504, Mar. 2009.

[38] F. Troiani, U. Hohenester, and E. Molinari, "Exploiting exciton-exciton interactions in semiconductor quantum dots for quantum-information processing," *Physical Review B*, vol. 62, no. 4, pp. 2263–2266, 2000.

[39] P. Chen, C. Piermarocchi, and L. Sham, "Control of Exciton Dynamics in Nanodots for Quantum Operations," *Physical Review Letters*, vol. 87, pp. 1–4, July 2001.

[40] C. Piermarocchi, P. Chen, L. Sham, and D. Steel, "Optical RKKY Interaction between Charged Semiconductor Quantum Dots," *Physical Review Letters*, vol. 89, pp. 14–17, Sept. 2002.

[41] D. Loss and D. P. Divincenzo, "Quantum computation with quantum dots," *Physical Review A*, vol. 57, no. 1, pp. 120–126, 1998.

[42] A. Imamoglu, D. D. Awschalom, G. Burkard, D. P. DiVincenzo, D. Loss, M. Sherwin, and A. Small, "Quantum Information Processing Using Quantum Dot Spins and Cavity QED," *Physical Review Letters*, vol. 83, pp. 4204–4207, Nov. 1999.

[43] P. Chen, C. Piermarocchi, L. J. Sham, D. Gammon, and D. G. Steel, "Theory of Quantum Optical Control of Single Spin in a Quantum Dot," *Physical Review B*, vol. 69, p. 075320, 2003.

[44] S. Economou, L. Sham, Y. Wu, and D. Steel, "Proposal for optical U(1) rotations of electron spin trapped in a quantum dot," *Physical Review B*, vol. 74, Nov. 2006.

[45] S. M. Clark, K.-M. C. Fu, T. D. Ladd, and Y. Yamamoto, "Quantum Computers Based on Electron Spins Controlled by Ultrafast Off-Resonant Single Optical Pulses," *Physical Review Letters*, vol. 99, pp. 2–5, July 2007.

[46] T. Hodgson, L. Viola, and I. D'Amico, "Decoherence-protected storage of exciton qubits through ultrafast multipulse control," *Physical Review B*, vol. 78, Oct. 2008.

[47] D. M. Bruls, J. W. A. M. Vugs, P. M. Koenraad, H. W. M. Salemink, J. H. Wolter, M. Hopkinson, M. S. Skolnick, F. Long, and S. P. a. Gill, "Determination of the shape and indium distribution of low-growth-rate InAs quantum dots by cross-sectional scanning tunneling microscopy," *Applied Physics Letters*, vol. 81, no. 9, p. 1708, 2002.

[48] P. Michler, A. Kiraz, C. Becher, W. V. Schoenfeld, P. M. Petroff, L. Zhang, E. Hu, and A. Imamoglu, "A quantum dot single-photon turnstile device.," *Science*, vol. 290, pp. 2282–5, Dec. 2000.

[49] N. Bonadeo, J. Erland, D. Gammon, D. Park, D. Katzer, and D. Steel, "Coherent optical control of the quantum state of a single quantum Dot," *Science (New York, N.Y.)*, vol. 282, pp. 1473–6, Nov. 1998.

[50] H. Kamada, H. Gotoh, J. Temmyo, T. Takagahara, and H. Ando, "Exciton Rabi Oscillation in a Single Quantum Dot," *Physical Review Letters*, vol. 87, pp. 10–13, Nov. 2001.

[51] H. Htoon, D. Kulik, O. Baklenov, A. Holmes, T. Takagahara, and C. Shih, "Carrier relaxation and quantum decoherence of excited states in self-assembled quantum dots," *Physical Review B*, vol. 63, pp. 3–6, June 2001.

[52] H. Htoon, T. Takagahara, D. Kulik, O. Baklenov, A. Holmes, and C. Shih, "Interplay of Rabi Oscillations and Quantum Interference in Semiconductor Quantum Dots," *Physical Review Letters*, vol. 88, Feb. 2002.

[53] A. Zrenner, E. Beham, S. Stufler, F. Findeis, M. Bichler, and G. Abstreiter, "Coherent properties of a two-level system based on a quantum-dot photodiode.," *Nature*, vol. 418, pp. 612–4, Aug. 2002.

[54] A. J. Ramsay, A. V. Gopal, E. M. Gauger, A. Nazir, B. W. Lovett, a. M. Fox, and M. S. Skolnick, "Damping of Exciton Rabi Rotations by Acoustic Phonons in Optically Excited InGaAs/GaAs Quantum Dots," *Physical Review Letters*, vol. 104, pp. 20–23, Jan. 2010.

[55] K. Kuroda, T. Kuroda, K. Watanabe, T. Mano, K. Sakoda, G. Kido, and N. Koguchi, "Final-state readout of exciton qubits by observing resonantly excited photoluminescence in quantum dots," *Applied Physics Letters*, vol. 90, no. 5, p. 051909, 2007.

[56] A. Muller, Q. Q. Wang, P. Bianucci, C. K. Shih, and Q. K. Xue, "Determination of anisotropic dipole moments in self-assembled quantum dots using Rabi oscillations," *Applied Physics Letters*, vol. 84, no. 6, p. 981, 2004.

[57] P. Borri, W. Langbein, S. Schneider, U. Woggon, R. Sellin, D. Ouyang, and D. Bimberg, "Rabi oscillations in the excitonic ground-state transition of InGaAs quantum dots," *Physical Review B*, vol. 66, pp. 2–5, Aug. 2002.

[58] A. Greilich, D. R. Yakovlev, A. Shabaev, A. L. Efros, I. a. Yugova, R. Oulton, V. Stavarache, D. Reuter, A. Wieck, and M. Bayer, "Mode locking of electron spin coherences in singly charged quantum dots.," *Science (New York, N.Y.)*, vol. 313, no. 5785, pp. 341–345, 2006.

[59] A. Greilich, R. Oulton, E. A. Zhukov, I. A. Yugova, D. R. Yakovlev, M. Bayer, A. Shabaev, A. L. Efros, I. A. Merkulov, V. Stavarache, D. Reuter, and A. Wieck, "Optical control of spin coherence in singly charged $(\mathrm{In,Ga})\mathrm{As}/\mathrm{GaAs}$ quantum dots," *Phys. Rev. Lett.*, vol. 96, p. 227401, Jun 2006.

[60] M. V. Gurudev Dutt, J. Cheng, Y. Wu, X. Xu, D. G. Steel, A. S. Bracker, D. Gammon, S. E. Economou, R.-B. Liu, and L. J. Sham, "Ultrafast optical control of electron spin coherence in charged GaAs quantum dots," *Phys. Rev. B*, vol. 74, p. 125306, Sep 2006.

[61] M. M. Glazov, I. A. Yugova, S. Spatzek, A. Schwan, S. Varwig, D. R. Yakovlev, D. Reuter, A. D. Wieck, and M. Bayer, "Effect of pump-probe detuning on the faraday rotation and ellipticity signals of mode-locked spins in (in,ga)as/gaas quantum dots," *Phys. Rev. B*, vol. 82, p. 155325, Oct 2010.

[62] E. D. Kim, K. Truex, Y. Wu, a. Amo, X. Xu, D. G. Steel, a. S. Bracker, D. Gammon, and L. J. Sham, "Picosecond optical spectroscopy of a single negatively charged self-assembled InAs quantum dot," *Applied Physics Letters*, vol. 97, no. 11, p. 113110, 2010.

[63] E. B. Flagg, A. Muller, J. W. Robertson, S. Founta, D. G. Deppe, M. Xiao, W. Ma, G. J. Salamo, and C. K. Shih, "Resonantly driven coherent oscillations in a solid-state quantum emitter," *Nature Physics*, vol. 5, no. 3, pp. 203–207, 2009.

[64] A. Vasanelli, R. Ferreira, and G. Bastard, "Continuous Absorption Background and Decoherence in Quantum Dots," *Physical Review Letters*, vol. 89, pp. 1–4, Nov. 2002.

[65] Q. Wang, A. Muller, P. Bianucci, E. Rossi, Q. Xue, T. Takagahara, C. Piermarocchi, A. MacDonald, and C. Shih, "Decoherence processes during optical manipulation of excitonic qubits in semiconductor quantum dots," *Physical Review B*, vol. 72, pp. 1–5, July 2005.

[66] A. J. Ramsay, R. S. Kolodka, F. Bello, P. W. Fry, W. K. Ng, A. Tahraoui, H. Y. Liu, M. Hopkinson, D. M. Whittaker, a. M. Fox, and M. S. Skolnick, "Coherent response of a quantum dot exciton driven by a rectangular spectrum optical pulse," *Physical Review B - Condensed Matter and Materials Physics*, vol. 75, no. 11, pp. 1–4, 2007.

[67] H. Takagi, T. Nakaoka, K. Watanabe, N. Kumagai, and Y. Arakawa, "Coherently driven semiconductor quantum dot at a telecommunication wavelength.," *Optics express*, vol. 16, no. 18, pp. 13949–13954, 2008.

[68] R. Melet, V. Voliotis, A. Enderlin, D. Roditchev, X. L. Wang, T. Guillet, and R. Grousson, "Resonant excitonic emission of a single quantum dot in the

Rabi regime," *Physical Review B - Condensed Matter and Materials Physics*, vol. 78, no. 7, pp. 3–6, 2008.

[69] A. Ramsay, T. Godden, S. Boyle, E. Gauger, A. Nazir, B. Lovett, A. Fox, and M. Skolnick, "Phonon-Induced Rabi-Frequency Renormalization of Optically Driven Single InGaAs/GaAs Quantum Dots," *Physical Review Letters*, vol. 105, pp. 1–4, Oct. 2010.

[70] L. Besombes, J. J. Baumberg, and J. Motohisa, "Coherent spectroscopy of optically gated charged single InGaAs quantum dots.," *Physical review letters*, vol. 90, no. 25 Pt 1, p. 257402, 2003.

[71] S. Stufler, P. Ester, a. Zrenner, and M. Bichler, "Quantum optical properties of a single InxGa1−xAs-GaAs quantum dot two-level system," *Physical Review B*, vol. 72, no. 12, pp. 1–4, 2005.

[72] R. S. Kolodka, a. J. Ramsay, J. Skiba-Szymanska, P. W. Fry, H. Y. Liu, a. M. Fox, and M. S. Skolnick, "Inversion recovery of single quantum-dot exciton based qubit," *Physical Review B - Condensed Matter and Materials Physics*, vol. 75, no. 19, pp. 2–5, 2007.

[73] C.-M. Simon, T. Belhadj, B. Chatel, T. Amand, P. Renucci, a. Lemaitre, O. Krebs, P. Dalgarno, R. Warburton, X. Marie, and B. Urbaszek, "Robust Quantum Dot Exciton Generation via Adiabatic Passage with Frequency-Swept Optical Pulses," *Physical Review Letters*, vol. 106, pp. 1–4, Apr. 2011.

[74] Y. Wu, I. Piper, M. Ediger, P. Brereton, E. Schmidgall, P. Eastham, M. Hugues, M. Hopkinson, and R. Phillips, "Population Inversion in a Single InGaAs Quantum Dot Using the Method of Adiabatic Rapid Passage," *Physical Review Letters*, vol. 106, pp. 1–4, Feb. 2011.

[75] L. J. Xu, Xiaodong and Sun, Bo and Berman, Paul R. and Steel, Duncan G. and Bracker, Allan S. and Gammon, Dan and Sham, "Coherent Optical Spectroscopy of a Strongly Driven Quantum Dot," *Science*, vol. 317, no. 5840, p. 929, 2007.

[76] S. J. Boyle, A. J. Ramsay, A. M. Fox, M. S. Skolnick, A. P. Heberle, and M. Hopkinson, "Beating of exciton-dressed states in a single semiconductor InGaAs/GaAs quantum dot," *Physical Review Letters*, vol. 102, no. 20, pp. 1–4, 2009.

[77] A. Muller, W. Fang, J. Lawall, and G. S. Solomon, "Creating polarization-entangled photon pairs from a semiconductor quantum dot using the optical stark effect," *Physical Review Letters*, vol. 103, no. 21, pp. 2–5, 2009.

[78] B. D. Gerardot, D. Brunner, P. A. Dalgarno, K. Karrai, A. Badolato, P. M. Petroff, and R. J. Warburton, "Dressed excitonic states and quantum interference in a three-level quantum dot ladder system," *New Journal of Physics*, vol. 11, 2009.

[79] G. Jundt, L. Robledo, A. Högele, S. Fält, and A. Imamoğlu, "Observation of dressed excitonic states in a single quantum dot," *Physical Review Letters*, vol. 100, no. 17, pp. 1–4, 2008.

[80] A. Nick Vamivakas, Y. Zhao, C.-Y. Lu, and M. Atatüre, "Spin-resolved quantum-dot resonance fluorescence," *Nature Physics*, vol. 5, no. 3, pp. 198–202, 2009.

[81] S. Boyle, A. Ramsay, F. Bello, H. Liu, M. Hopkinson, A. Fox, and M. Skolnick, "Two-qubit conditional quantum-logic operation in a single self-assembled quantum dot," *Physical Review B*, vol. 78, pp. 1–6, Aug. 2008.

[82] S. Stufler, P. Machnikowski, P. Ester, M. Bichler, V. Axt, T. Kuhn, and A. Zrenner, "Two photon rabi oscillations in a single InxGa1xAsGaAs quantum dot," *Physical Review B*, vol. 73, pp. 1–7, Mar. 2006.

[83] A. Barenco, D. Deutsch, A. Ekert, and R. Jozsa, "Conditional quantum dynamics and logic gates," *Phys. Rev. Lett.*, vol. 74, pp. 4083–4086, May 1995.

[84] L. Quiroga and N. F. Johnson, "Entangled bell and greenberger-horne-zeilinger states of excitons in coupled quantum dots," *Phys. Rev. Lett.*, vol. 83, pp. 2270–2273, Sep 1999.

[85] T. A. Brun and H. Wang, "Coupling nanocrystals to a high-q silica microsphere: Entanglement in quantum dots via photon exchange," *Phys. Rev. A*, vol. 61, p. 032307, Feb 2000.

[86] P. Borri, W. Langbein, S. Schneider, U. Woggon, R. Sellin, D. Ouyang, and D. Bimberg, "Ultralong Dephasing Time in InGaAs Quantum Dots," *Physical Review Letters*, vol. 87, pp. 1–4, Sept. 2001.

[87] P. Borri, W. Langbein, U. Woggon, V. Stavarache, D. Reuter, and A. Wieck, "Exciton dephasing via phonon interactions in InAs quantum dots: Dependence on quantum confinement," *Physical Review B*, vol. 71, pp. 1–8, Mar. 2005.

[88] J. Johansen, S. r. Stobbe, I. S. Nikolaev, T. Lund-Hansen, P. T. Kristensen, J. r. M. Hvam, W. L. Vos, and P. Lodahl, "Size dependence of the wavefunction of self-assembled InAs quantum dots from time-resolved optical measurements," *Physical Review B - Condensed Matter and Materials Physics*, vol. 77, no. 7, pp. 1–4, 2008.

[89] A. Vagov, M. Croitoru, V. Axt, T. Kuhn, and F. Peeters, "Nonmonotonic Field Dependence of Damping and Reappearance of Rabi Oscillations in Quantum Dots," *Physical Review Letters*, vol. 98, pp. 1–4, June 2007.

[90] A. Nazir, "Photon statistics from a resonantly driven quantum dot," *Physical Review B*, vol. 78, pp. 18–21, Oct. 2008.

[91] R. Mathew, E. Dilcher, A. Gamouras, A. Ramachandran, H. Y. S. Yang, S. Freisem, D. Deppe, and K. C. Hall, "Subpicosecond adiabatic rapid passage on a single semiconductor quantum dot: Phonon-mediated dephasing in the strong-driving regime," *Physical Review B - Condensed Matter and Materials Physics*, vol. 90, no. 3, pp. 1–6, 2014.

[92] P. Karbach, S. Pasini, and G. Uhrig, "Numerical analysis of optimized coherent control pulses," *Physical Review A*, vol. 78, pp. 1–9, Aug. 2008.

[93] J. M. Elzerman, R. Hanson, L. H. van Beveren, B. Witkamp, L. M. K. Vandersypen, and L. P. Kouwenhoven, "Single-shot read-out of an individual electron spin in a quantum dot," *Nature*, vol. 430, pp. 431–435, July 2004.

[94] F. H. L. Koppens, J. a. Folk, J. M. Elzerman, R. Hanson, L. H. W. van Beveren, I. T. Vink, H. P. Tranitz, W. Wegscheider, L. P. Kouwenhoven, and L. M. K. Vandersypen, "Control and detection of singlet-triplet mixing in a random nuclear field.," *Science (New York, N.Y.)*, vol. 309, no. 5739, pp. 1346–1350, 2005.

[95] F. H. L. Koppens, C. Buizert, K. J. Tielrooij, I. T. Vink, K. C. Nowack, T. Meunier, L. P. Kouwenhoven, and L. M. K. Vandersypen, "Driven coherent oscillations of a single electron spin in a quantum dot.," *Nature*, vol. 442, no. 7104, pp. 766–771, 2006.

[96] K. C. Nowack, F. H. L. Koppens, Y. V. Nazarov, and L. M. K. Vandersypen, "Coherent control of a single electron spin with electric fields.," *Science*, vol. 318, no. 5855, pp. 1430–3, 2007.

[97] K. C. Nowack, M. Shafiei, M. Laforest, G. E. D. K. Prawiroatmodjo, L. R. Schreiber, C. Reichl, W. Wegscheider, and L. M. K. Vandersypen, "Single-Shot Correlations and Two-Qubit Gate of Solid-State Spins," *Science*, vol. 333, no. 6047, pp. 1269–1272, 2011.

[98] M. D. Shulman, O. E. Dial, S. P. Harvey, H. Bluhm, V. Umansky, and a. Yacoby, "Demonstration of Entanglement of Electrostatically Coupled Singlet-Triplet Qubits," *Science*, vol. 336, no. 6078, pp. 202–205, 2012.

[99] D. Press, T. D. Ladd, B. Zhang, and Y. Yamamoto, "Complete quantum control of a single quantum dot spin using ultrafast optical pulses.," *Nature*, vol. 456, pp. 218–21, Nov. 2008.

[100] D. Press, K. D. Greve, P. L. Mcmahon, T. D. Ladd, B. Friess, A. Forchel, Y. Yamamoto, C. Schneider, M. Kamp, and S. Ho, "Ultrafast optical spin echo in a single quantum dot," *Nature Photonics*, vol. 4, no. April, pp. 367–370, 2010.

[101] A. Greilich, S. E. Economou, S. Spatzek, D. R. Yakovlev, D. Reuter, A. D. Wieck, T. L. Reinecke, and M. Bayer, "Ultrafast optical rotations of electron spins in quantum dots," *Nature Physics*, vol. 5, no. 4, p. 10, 2009.

[102] E. D. Kim, K. Truex, X. Xu, B. Sun, D. G. Steel, a. S. Bracker, D. Gammon, and L. J. Sham, "Fast Spin Rotations by Optically Controlled Geometric Phases in a Charge-Tunable InAs Quantum Dot," *Physical Review Letters*, vol. 104, pp. 1–4, Apr. 2010.

[103] K. De Greve, P. L. McMahon, D. Press, T. D. Ladd, D. Bisping, C. Schneider, M. Kamp, L. Worschech, S. Höfling, A. Forchel, and Y. Yamamoto, "Ultrafast coherent control and suppressed nuclear feedback of a single quantum dot hole qubit," *Nature Physics*, vol. 7, pp. 872–878, Aug. 2011.

[104] B. D. Gerardot, D. Brunner, P. a. Dalgarno, P. Ohberg, S. Seidl, M. Kroner, K. Karrai, N. G. Stoltz, P. M. Petroff, and R. J. Warburton, "Optical pumping of a single hole spin in a quantum dot.," *Nature*, vol. 451, pp. 441–4, Jan. 2008.

[105] T. M. Godden, J. H. Quilter, a. J. Ramsay, Y. Wu, P. Brereton, S. J. Boyle, I. J. Luxmoore, J. Puebla-Nunez, a. M. Fox, and M. S. Skolnick, "Coherent optical control of the spin of a single hole in an InAs/GaAs quantum dot," *Physical Review Letters*, vol. 108, no. 1, pp. 1–5, 2012.

[106] D. Kim, S. G. Carter, A. Greilich, A. S. Bracker, and D. Gammon, "Ultrafast optical control of entanglement between two quantum-dot spins," *Nature Physics*, vol. 7, pp. 223–229, Dec. 2010.

[107] A. Greilich, S. G. Carter, D. Kim, A. S. Bracker, and D. Gammon, "Optical control of one and two hole spins in interacting quantum dots," *Nature Photonics*, vol. 5, no. September, 2011.

[108] E. A. Chekhovich, M. N. Makhonin, a. I. Tartakovskii, A. Yacoby, H. Bluhm, K. C. Nowack, and L. M. K. Vandersypen, "Nuclear spin effects in semiconductor quantum dots.," *Nature materials*, vol. 12, no. 6, pp. 494–504, 2013.

[109] J. J. Kroutvar, Miro and Ducommun, Yann and Heiss, Dominik and Bichler, Max and Schuh, Dieter and Abstreiter, Gerhard and Finley, "Letters To Nature," *Nature*, vol. 432, no. November, pp. 81–84, 2004.

[110] D. Heiss, S. Schaeck, H. Huebl, M. Bichler, G. Abstreiter, J. J. Finley, D. V. Bulaev, and D. Loss, "Observation of extremely slow hole spin relaxation in self-assembled quantum dots," *Physical Review B - Condensed Matter and Materials Physics*, vol. 76, no. 24, pp. 1–4, 2007.

[111] K. Muller, T. Kaldewey, R. Ripszam, J. S. Wildmann, A. Bechtold, M. Bichler, G. Koblmuller, G. Abstreiter, and J. J. Finley, "All optical quantum control of a spin-quantum state and ultrafast transduction into an electric current," *Sci. Rep.*, vol. 3, p. 1906, May 2013.

[112] A. M. Weiner, "Femtosecond pulse shaping using spatial light modulators," *Review of Scientific Instruments*, vol. 71, no. 5, p. 1929, 2000.

[113] A. P. Peirce, M. a. Dahleh, and H. Rabitz, "Optimal control of quantum-mechanical systems: Existence, numerical approximation, and applications," *Physical Review A*, vol. 37, no. 12, pp. 4950–4964, 1988.

[114] R. Kosloff, S. A. Rice, P. Gaspard, and S. Tersigni, "Wavepackets dancing: Achieving chemical selectivity by shaping light pulses," *Chemical Physics*, vol. 139, pp. 201–220, 1989.

[115] R. J. Levis, G. M. Menkir, and H. Rabitz, "Selective bond dissociation and rearrangement with optimally tailored, strong-field laser pulses.," *Science (New York, N.Y.)*, vol. 292, no. 5517, pp. 709–713, 2001.

[116] G. Assion, A. and Baumert, T. and Bergt, M. and Brixner, T. and Kiefer, B. and Seyfried, V. and Strehle, M. and Gerber, "Control of Chemical Reactions by Feedback-Optimized Phase-Shaped Femtosecond Laser Pulses," 1998.

[117] D. Pestov, R. K. Murawski, G. O. Ariunbold, X. Wang, M. Zhi, A. V. Sokolov, V. A. Sautenkov, Y. V. Rostovtsev, A. Dogariu, Y. Huang, and M. O. Scully, "Optimizing the Laser-Pulse Raman Spectroscopy," *Science*, vol. 316, no. April, pp. 265–268, 2007.

[118] R. Bartels, S. Backus, E. Zeek, L. Misoguti, G. Vdovin, I. Christov, M. Murnane, and H. Kapteyn, "Shaped-pulse optimization of coherent emission of high-harmonic soft X-rays," *Nature*, vol. 406, no. 6792, pp. 164–6, 2000.

[119] T. Rickes, "Enhancement of third-harmonic generation by Stark-chirped rapid adiabatic passage," *Optics Communications*, vol. 227, pp. 133–142, Nov. 2003.

[120] W. C. Campbell, J. Mizrahi, Q. Quraishi, C. Senko, D. Hayes, D. Hucul, D. N. Matsukevich, P. Maunz, and C. Monroe, "Ultrafast Gates for Single Atomic Qubits," *Physical Review Letters*, vol. 105, p. 090502, Aug. 2010.

[121] G. Kirchmair, J. Benhelm, F. Zähringer, R. Gerritsma, C. F. Roos, and R. Blatt, "Deterministic entanglement of ions in thermal states of motion," *New Journal of Physics*, vol. 11, 2009.

[122] T. Choi, S. Debnath, T. a. Manning, C. Figgatt, Z. X. Gong, L. M. Duan, and C. Monroe, "Optimal quantum control of multimode couplings between trapped ion qubits for scalable entanglement," *Physical Review Letters*, vol. 112, no. 19, pp. 1–5, 2014.

[123] J. Kelly, R. Barends, B. Campbell, Y. Chen, Z. Chen, B. Chiaro, A. Dunsworth, a. G. Fowler, I. C. Hoi, E. Jeffrey, A. Megrant, J. Mutus, C. Neill, P. J. J. O'Malley, C. Quintana, P. Roushan, D. Sank, A. Vainsencher, J. Wenner, T. C. White, A. N. Cleland, and J. M. Martinis, "Optimal quantum control using randomized benchmarking," *Physical Review Letters*, vol. 112, no. 24, pp. 1–5, 2014.

[124] F. Dolde, V. Bergholm, Y. Wang, I. Jakobi, B. Naydenov, S. Pezzagna, J. Meijer, F. Jelezko, P. Neumann, T. Schulte-Herbrüggen, J. Biamonte, and J. Wrachtrup, "High-fidelity spin entanglement using optimal control.," *Nature communications*, vol. 5, p. 3371, 2014.

[125] A. Gamouras, R. Mathew, S. Freisem, D. G. Deppe, and K. C. Hall, "Simultaneous deterministic control of distant qubits in two semiconductor quantum dots.," *Nano letters*, vol. 13, pp. 4666–70, Oct. 2013.

[126] G. Chen, T. Stievater, E. Batteh, X. Li, D. Steel, D. Gammon, D. Katzer, D. Park, and L. Sham, "Biexciton Quantum Coherence in a Single Quantum Dot," *Physical Review Letters*, vol. 88, pp. 1–4, Mar. 2002.

[127] A. Dousse, J. Suffczyński, A. Beveratos, O. Krebs, A. Lemaître, I. Sagnes, J. Bloch, P. Voisin, and P. Senellart, "Ultrabright source of entangled photon pairs.," *Nature*, vol. 466, pp. 217–20, July 2010.

[128] E. R. Schmidgall, P. R. Eastham, and R. T. Phillips, "Population inversion in quantum dot ensembles via adiabatic rapid passage," *Physical Review B*, vol. 81, pp. 1–5, May 2010.

[129] K. Schuh, F. Jahnke, and M. Lorke, "Rapid adiabatic passage in quantum dots: Influence of scattering and dephasing," *Applied Physics Letters*, vol. 99, no. 1, p. 011105, 2011.

[130] E. Gauger, S. Benjamin, A. Nazir, and B. Lovett, "High-fidelity all-optical control of quantum dot spins: Detailed study of the adiabatic approach," *Physical Review B*, vol. 77, pp. 1–6, Mar. 2008.

[131] T. Calarco, a. Datta, P. Fedichev, E. Pazy, and P. Zoller, "Spin-based all-optical quantum computation with quantum dots: Understanding and suppressing decoherence," *Physical Review A*, vol. 68, pp. 1–21, July 2003.

[132] B. Lovett, A. Nazir, E. Pazy, S. Barrett, T. Spiller, and G. Briggs, "Quantum computing with spin qubits interacting through delocalized excitons: Overcoming hole mixing," *Physical Review B*, vol. 72, p. 115324, Sept. 2005.

[133] C. Creatore, R. T. Brierley, R. T. Phillips, P. B. Littlewood, and P. R. Eastham, "Creation of entangled states in coupled quantum dots via adiabatic rapid passage," *Physical Review B*, vol. 86, p. 155442, Oct. 2012.

[134] H. Hui and R. Liu, "Proposal for geometric generation of a biexciton in a quantum dot using a chirped pulse," *Physical Review B*, vol. 78, pp. 1–5, Oct. 2008.

[135] J. S. Melinger, S. R. Gandhi, A. Hariharan, D. Goswami, and W. S. Warren, "Adiabatic population transfer with frequency-swept laser pulses," *The Journal of Chemical Physics*, vol. 101, no. 8, p. 6439, 1994.

[136] N. V. Vitanov, T. Halfmann, B. W. Shore, and K. Bergmann, "Laser-induced population transfer by adiabatic rapid passage," *Annu. Rev. Chem.*, vol. 52, pp. 763–809, 2001.

[137] A. J. Ramsay, T. M. Godden, S. J. Boyle, E. M. Gauger, A. Nazir, B. W. Lovett, A. V. Gopal, a. M. Fox, and M. S. Skolnick, "Effect of detuning on the phonon induced dephasing of optically driven InGaAs/GaAs quantum dots," *Journal of Applied Physics*, vol. 109, no. 10, p. 102415, 2011.

[138] A. Debnath, C. Meier, B. Chatel, and T. Amand, "Chirped laser excitation of quantum dot excitons coupled to a phonon bath," *Physical Review B*, vol. 86, p. 161304, Oct. 2012.

[139] S. Lüker, K. Gawarecki, D. E. Reiter, A. Grodecka-Grad, V. M. Axt, P. Machnikowski, and T. Kuhn, "Influence of acoustic phonons on the optical control of quantum dots driven by adiabatic rapid passage," *Physical Review B*, vol. 85, p. 121302, Mar. 2012.

[140] D. E. Reiter, S. Lüker, K. Gawarecki, and P. Machnikowski, "Phonon E ects on Population Inversion in Quantum Dots : Resonant , Detuned and Frequency-Swept Excitations," *Acta Physica Polonica A*, vol. 122, no. 6, 2012.

[141] P. R. Eastham, a. O. Spracklen, and J. Keeling, "Lindblad theory of dynamical decoherence of quantum-dot excitons," *Physical Review B*, vol. 87, p. 195306, May 2013.

[142] D. P. S. McCutcheon and A. Nazir, "Quantum dot Rabi rotations beyond the weak exciton–phonon coupling regime," *New Journal of Physics*, vol. 12, p. 113042, Nov. 2010.

[143] J. Förstner, C. Weber, J. Danckwerts, and A. Knorr, "Phonon-Assisted Damping of Rabi Oscillations in Semiconductor Quantum Dots," *Physical Review Letters*, vol. 91, pp. 1–4, Sept. 2003.

[144] P. Machnikowski and L. Jacak, "Resonant nature of phonon-induced damping of Rabi oscillations in quantum dots," *Physical Review B*, vol. 69, pp. 1–4, May 2004.

[145] V. M. Axt, M. Herbst, and T. Kuhn, "Coherent control of phonon quantum beats," *Superlattices and Microstructures*, vol. 26, no. 2, pp. 117–128, 1999.

[146] L. Monniello, C. Tonin, R. Hostein, A. Lemaitre, A. Martinez, V. Voliotis, and R. Grousson, "Excitation-Induced Dephasing in a Resonantly Driven InAs/GaAs Quantum Dot," *Physical Review Letters*, vol. 111, p. 026403, July 2013.

[147] B. L. Liang, Z. M. Wang, K. a. Sablon, Y. I. Mazur, and G. J. Salamo, "Influence of GaAs Substrate Orientation on InAs Quantum Dots: Surface Morphology, Critical Thickness, and Optical Properties," *Nanoscale Research Letters*, vol. 2, pp. 609–613, Nov. 2007.

[148] M. Bayer, G. Ortner, O. Stern, a. Kuther, a. Gorbunov, a. Forchel, P. Hawrylak, S. Fafard, K. Hinzer, T. Reinecke, S. Walck, J. Reithmaier, F. Klopf, and F. Schäfer, "Fine structure of neutral and charged excitons in self-assembled In(Ga)As/(Al)GaAs quantum dots," *Physical Review B*, vol. 65, no. 19, pp. 1–23, 2002.

[149] C. Dal Savio, K. Pierz, G. Ade, H.-U. Danzebrink, E. Göbel, and a. Hangleiter, "Optical study of single InAs on In0.12Ga0.88As self-assembled quantum dots: biexciton binding energy dependence on the dots size," *Applied Physics B*, vol. 84, pp. 317–322, June 2006.

[150] E. Poem, Y. Kodriano, C. Tradonsky, N. H. Lindner, B. D. Gerardot, P. M. Petroff, and D. Gershoni, "Accessing the dark exciton with light," *Nature Physics*, vol. 6, no. 12, pp. 993–997, 2010.

[151] W. Langbein, P. Borri, and U. Woggon, "Control of fine-structure splitting and biexciton binding in InxGa1-xAs quantum dots by annealing," *Physical Review B*, vol. 69, p. 161301, Apr. 2004.

[152] T. Bahder, "Eight-band k.p model of strained zinc-blende crystals," *Physical Review B*, vol. 41, pp. 11992–12001, June 1990.

[153] C. Pryor, "Eight-band calculations of strained InAs/GaAs quantum dots compared with one-, four-, and six-band approximations," *Physical Review B*, vol. 57, no. 12, pp. 7190–7195, 1998.

[154] M. Holm, M.-E. Pistol, and C. Pryor, "Calculations of the electronic structure of strained InAs quantum dots in InP," *Journal of Applied Physics*, vol. 92, no. 2, p. 932, 2002.

[155] L. A. Eberly and J. H., *Optical Resonance and Two-Level Systems*. New York: Wiley, 1987.

[156] V. S. Malinovsky and J. L. Krause, "General theory of population transfer by adiabatic rapid passage with intense , chirped laser pulses," *The European Physical Journal D - Atomic, Molecular, Optical and Plasma Physics*, vol. 155, pp. 147–155, 2001.

[157] C. C. G. Knight and P. L., *Introductory Quantum Mechanics*. Cambridge: Cambridge, 2005.

[158] J. Villas-Bôas, S. Ulloa, and a. Govorov, "Decoherence of Rabi Oscillations in a Single Quantum Dot," *Physical Review Letters*, vol. 94, pp. 1–4, Feb. 2005.

[159] V. Axt, P. Machnikowski, and T. Kuhn, "Reducing decoherence of the confined exciton state in a quantum dot by pulse-sequence control," *Physical Review B*, vol. 71, pp. 1–9, Apr. 2005.

[160] R. Trebino, K. W. DeLong, D. N. Fittinghoff, J. N. Sweetser, M. A. Krumbügel, B. A. Richman, and D. J. Kane, "Measuring ultrashort laser pulses in the time-frequency domain using frequency-resolved optical gating," *Review of Scientific Instruments*, vol. 68, no. 9, pp. 3277–3295, 1997.

[161] M. Takeda, H. Ina, and S. Kobayashi, "Fourier-transform method of fringe-pattern analysis for computer-based topography and interferometry," *J. Opt. Soc. Am.*, vol. 72, pp. 156–160, Jan 1982.

[162] V. V. Lozovoy, I. Pastirk, and M. Dantus, "Multiphoton intrapulse interference. IV. Ultrashort laser pulse spectral phase characterization and compensation.," *Optics letters*, vol. 29, pp. 775–7, Apr. 2004.

[163] B. Xu, J. M. Gunn, J. M. D. Cruz, V. V. Lozovoy, and M. Dantus, "Quantitative investigation of the multiphoton intrapulse interference phase scan method for simultaneous phase measurement and compensation of femtosecond laser pulses," *Journal of the Optical Society of America B*, vol. 23, no. 4, p. 750, 2006.

[164] M. Kujiraoka, J. Ishi-Hayase, K. Akahane, N. Yamamoto, K. Ema, and M. Sasaki, "Optical Rabi Oscillations in a Quantum Dot Ensemble," *Applied Physics Express*, vol. 3, p. 092801, Aug. 2010.

[165] A. E. Siegman, *Lasers*. University Science Books, 1986.

[166] J. Werschnik and E. K. U. Gross, "Quantum optimal control theory," *Journal of Physics B: Atomic, Molecular and Optical Physics*, vol. 40, no. 18, p. R175, 2007.

[167] D. J. Egger and F. K. Wilhelm, "Adaptive hybrid optimal quantum control for imprecisely characterized systems," *Physical Review Letters*, vol. 112, no. 24, pp. 1–5, 2014.

[168] T. Flissikowski, a. Betke, I. Akimov, and F. Henneberger, "Two-Photon Coherent Control of a Single Quantum Dot," *Physical Review Letters*, vol. 92, pp. 1–4, June 2004.

[169] E. Poem, O. Kenneth, Y. Kodriano, Y. Benny, S. Khatsevich, J. Avron, and D. Gershoni, "Optically Induced Rotation of an Exciton Spin in a Semiconductor Quantum Dot," *Physical Review Letters*, vol. 107, pp. 1–5, Aug. 2011.

[170] Y. Kodriano, I. Schwartz, E. Poem, Y. Benny, R. Presman, T. A. Truong, P. M. Petroff, and D. Gershoni, "Complete control of a matter qubit using a single picosecond laser pulse," *Physical Review B - Condensed Matter and Materials Physics*, vol. 85, no. 24, pp. 1–5, 2012.

[171] G. Chen, "Optically Induced Entanglement of Excitons in a Single Quantum Dot," *Science*, vol. 289, pp. 1906–1909, Sept. 2000.

[172] a. Gamouras, M. Britton, M. M. Khairy, R. Mathew, D. Dalacu, P. Poole, D. Poitras, R. L. Williams, and K. C. Hall, "Energy-selective optical excitation and detection in InAs/InP quantum dot ensembles using a one-dimensional optical microcavity," *Applied Physics Letters*, vol. 103, no. 25, 2013.

[173] A. Gamouras, R. Mathew, and K. C. Hall, "Optically engineered ultrafast pulses for controlled rotations of exciton qubits in semiconductor quantum dots," *Journal of Applied Physics*, vol. 112, no. 1, p. 014313, 2012.

[174] R. Mathew, C. Pryor, M. Flatté, and K. Hall, "Optimal quantum control for conditional rotation of exciton qubits in semiconductor quantum dots," *Physical Review B*, vol. 84, p. 205322, Nov. 2011.

[175] H. Y. Liu, I. R. Sellers, T. J. Badcock, D. J. Mowbray, M. S. Skolnick, K. M. Groom, M. Gutiérrez, M. Hopkinson, J. S. Ng, J. P. R. David, and R. Beanland, "Improved performance of 1.3 μm multilayer InAs quantum-dot lasers using a high-growth-temperature GaAs spacer layer," *Applied Physics Letters*, vol. 85, no. 5, pp. 704–706, 2004.

[176] C. Zhang, V. W. Scarola, S. Tewari, and S. Das Sarma, "Anyonic braiding in optical lattices.," *Proceedings of the National Academy of Sciences of the United States of America*, vol. 104, pp. 18415–20, Nov. 2007.

[177] I. M. Sobol', "On the distribution of points in a cube and the approximate evaluation of integrals," {*USSR*} *Computational Mathematics and Mathematical Physics*, vol. 7, no. 4, pp. 86–112, 1967.

[178] C. E. Pryor and M. E. Flattá, "Predicted ultrafast single-qubit operations in semiconductor quantum dots," *Applied Physics Letters*, vol. 88, no. 23, pp. 2004–2007, 2006.

[179] Y.-J. Wei, Y.-M. He, M.-C. Chen, Y.-N. Hu, Y. He, D. Wu, C. Schneider, M. Kamp, S. Höfling, C.-Y. Lu, and J.-W. Pan, "Deterministic and robust generation of single photons from a single quantum dot with 99.5% indistinguishability using adiabatic rapid passage," *Nano Letters*, vol. 14, no. 11, pp. 6515–6519, 2014. PMID: 25357153.

[180] D. Gammon, E. S. Snow, B. V. Shanabrook, D. S. Katzer, and D. Park, "Homogeneous Linewidths in the Optical Spectrum of a Single Gallium Arsenide Quantum Dot," *Science*, vol. 273, pp. 87–90, July 1996.

[181] E. Biolatti, R. C. Iotti, P. Zanardi, and F. Rossi, "Quantum information processing with semiconductor macroatoms.," *Physical review letters*, vol. 85, pp. 5647–50, Dec. 2000.

[182] J. H. Reina, L. Quiroga, and N. F. Johnson, "Quantum entanglement and information processing via excitons in optically driven quantum dots," *Physical Review*, vol. 62, pp. 1–8, 2000.

[183] C. Piermarocchi, P. Chen, Y. Dale, and L. Sham, "Theory of fast quantum control of exciton dynamics in semiconductor quantum dots," *Physical Review B*, vol. 65, pp. 1–10, Jan. 2002.

[184] F. Troiani, E. Molinari, and U. Hohenester, "High-Finesse Optical Quantum Gates for Electron Spins in Artificial Molecules," *Physical Review Letters*, vol. 90, pp. 1–4, May 2003.

[185] D. Meshulach and Y. Silberberg, "Coherent quantum control of two-photon transitions by a femtosecond laser pulse," *Nature*, vol. 396, no. November, pp. 239–242, 1998.

[186] S. Zhdanovich, E. Shapiro, M. Shapiro, J. Hepburn, and V. Milner, "Population Transfer between Two Quantum States by Piecewise Chirping of Femtosecond Pulses: Theory and Experiment," *Physical Review Letters*, vol. 100, pp. 1–4, Mar. 2008.

[187] B. Broers, H. van Linden van den Heuvell, and L. Noordam, "Efficient population transfer in a three-level ladder system by frequency-swept ultrashort laser pulses," *Physical Review Letters*, vol. 69, pp. 2062–2065, Oct. 1992.

[188] B. Chatel, J. Degert, S. Stock, and B. Girard, "Competition between sequential and direct paths in a two-photon transition," *Physical Review A*, vol. 68, pp. 1–4, Oct. 2003.

[189] S. Chelkowski, A. Bandrauk, and P. Corkum, "Efficient molecular dissociation by a chirped ultrashort infrared laser pulse," *Physical Review Letters*, vol. 65, pp. 2355–2358, Nov. 1990.

[190] P. Brumer and M. Shapiro, "Laser control of molecular processes.," *Annual review of physical chemistry*, vol. 43, pp. 257–82, Jan. 1992.

[191] H. Rabitz, "Whither the Future of Controlling Quantum Phenomena?," *Science*, vol. 288, pp. 824–828, May 2000.

[192] K.-J. Boller, A. Imamolu, and S. Harris, "Observation of electromagnetically induced transparency," *Physical Review Letters*, vol. 66, pp. 2593–2596, May 1991.

[193] J. Field, K. Hahn, and S. Harris, "Observation of electromagnetically induced transparency in collisionally broadened lead vapor," *Physical Review Letters*, vol. 67, pp. 3062–3065, Nov. 1991.

[194] J. Watson, a. Sanpera, X. Chen, and K. Burnett, "Harmonic generation from a coherent superposition of states.," *Physical review. A*, vol. 53, pp. R1962–R1965, Apr. 1996.

[195] M. Jain, H. Xia, G. Yin, A. Merriam, and S. Harris, "Efficient Nonlinear Frequency Conversion with Maximal Atomic Coherence.," *Physical review letters*, vol. 77, pp. 4326–4329, Nov. 1996.

[196] A. Borzì, G. Stadler, and U. Hohenester, "Optimal quantum control in nanostructures: Theory and application to a generic three-level system," *Physical Review A*, vol. 66, pp. 1–6, Nov. 2002.

[197] R.-B. Liu, W. Yao, and L. Sham, "Coherent control of cavity quantum electrodynamics for quantum nondemolition measurements and ultrafast cooling," *Physical Review B*, vol. 72, pp. 1–4, Aug. 2005.

[198] T. M. Sweeney, C. Phelps, and H. Wang, "Quantum control of electron spins in the two-dimensional electron gas of a CdTe quantum well with a pair of Raman-resonant phase-locked laser pulses," *Physical Review B*, vol. 84, p. 075321, Aug. 2011.

[199] M. Bayer, A. Kuther, A. Forchel, A. Gorbunov, V. B. Timofeev, F. Schäfer, and J. P. Reithmaier, "Electron and Hole g Factors and Exchange Interaction from Studies of the Exciton Fine Structure in In 0 . 60 Ga 0 . 40 As Quantum Dots B = 8T," *Physical Review Letters*, pp. 22–25, 1999.

[200] R. Seguin, a. Schliwa, S. Rodt, K. Pötschke, U. Pohl, and D. Bimberg, "Size-Dependent Fine-Structure Splitting in Self-Organized InAs/GaAs Quantum Dots," *Physical Review Letters*, vol. 95, pp. 10–13, Dec. 2005.

[201] N. Liu, J. Tersoff, O. Baklenov, A. Holmes, and C. Shih, "Nonuniform composition profile in In0.5Ga0.5As alloy quantum dots," *Physical review letters*, vol. 84, pp. 334–7, Jan. 2000.

[202] P. W. Fry, I. E. Itskevich, D. J. Mowbray, M. S. Skolnick, J. J. Finley, J. a. Barker, E. P. O'Reilly, L. R. Wilson, I. a. Larkin, P. a. Maksym, M. Hopkinson, M. Al-Khafaji, J. P. David, a. G. Cullis, G. Hill, and J. C. Clark, "Inverted electron-hole alignment in InAs-GaAs self-assembled quantum dots.," *Physical review letters*, vol. 84, pp. 733–6, Jan. 2000.

[203] C. Pryor and M. Flatté, "Accuracy of Circular Polarization as a Measure of Spin Polarization in Quantum Dot Qubits," *Physical Review Letters*, vol. 91, pp. 3–6, Dec. 2003.

[204] D. Bimberg, *Semiconductor Nanostructures*. NanoScience and Technology, Springer, 2008.

[205] M. E. Reimer, D. Dalacu, P. J. Poole, and R. L. Williams, "Biexciton binding energy control in site-selected quantum dots," *Journal of Physics: Conference Series*, vol. 210, p. 012019, Feb. 2010.

[206] S. Johnson, "The NLopt Nonlinear Optimization Package."

[207] W. H. Press, B. P. Flannery, S. A. Teukolsky, and W. T. Vetterling, *Numerical Recipes in C: The Art of Scientific Computing, Second Edition*. Cambridge University Press, 2 ed., Oct. 1992.

[208] C. Santori, G. Solomon, M. Pelton, and Y. Yamamoto, "Time-resolved spectroscopy of multiexcitonic decay in an InAs quantum dot," *Physical Review B*, vol. 65, p. 073310, Feb. 2002.

[209] K. De Greve, L. Yu, P. L. McMahon, J. S. Pelc, C. M. Natarajan, N. Y. Kim, E. Abe, S. Maier, C. Schneider, M. Kamp, S. Höfling, R. H. Hadfield, A. Forchel, M. M. Fejer, and Y. Yamamoto, "Quantum-dot spin-photon entanglement via frequency downconversion to telecom wavelength.," *Nature*, vol. 491, pp. 421–5, Nov. 2012.

[210] P. Eastham and R. Phillips, "Quantum condensation from a tailored exciton population in a microcavity," *Physical Review B*, vol. 79, p. 165303, Apr. 2009.

[211] Q. Wang, A. Muller, M. Cheng, H. Zhou, P. Bianucci, and C. Shih, "Coherent Control of a V-Type Three-Level System in a Single Quantum Dot," *Physical Review Letters*, vol. 95, pp. 1–4, Oct. 2005.

[212] T. F. Boggess, L. Zhang, D. G. Deppe, D. L. Huffaker, and C. Cao, "Spectral engineering of carrier dynamics in In(Ga)As self-assembled quantum dots," *Applied Physics Letters*, vol. 78, no. 3, p. 276, 2001.

[213] B. Krummheuer, V. Axt, and T. Kuhn, "Theory of pure dephasing and the resulting absorption line shape in semiconductor quantum dots," *Physical Review B*, vol. 65, pp. 1–12, May 2002.

[214] J. Preskill, "Fault tolerant quantum computation," *arXiv*, 1997.

[215] M. H. Devoret and R. J. Schoelkopf, "Superconducting circuits for quantum information: An outlook," *Science*, vol. 339, no. 6124, pp. 1169–1174, 2013.

[216] W. K. Wootters and W. H. Zurek, "A single quantum cannot be cloned," *Nature*, vol. 299, pp. 802–803, Oct 1982.

[217] P. W. Shor, "Scheme for reducing decoherence in quantum computer memory," *Phys. Rev. A*, vol. 52, pp. R2493–R2496, Oct 1995.

[218] A. M. Steane, "Simple quantum error-correcting codes," *Phys. Rev. A*, vol. 54, pp. 4741–4751, Dec 1996.

[219] E. Knill, R. Laflamme, and W. H. Zurek, "Resilient quantum computation.," *Science*, vol. 279, no. 5349, pp. 342 – 345, 1998.

[220] S. J. Devitt, W. J. Munro, and K. Nemoto, "Quantum error correction for beginners," *Reports on Progress in Physics*, vol. 76, no. 7, p. 076001, 2013.

[221] K. Saeedi, S. Simmons, J. Z. Salvail, P. Dluhy, H. Riemann, N. V. Abrosimov, P. Becker, H.-J. Pohl, J. J. L. Morton, and M. L. W. Thewalt, "Room-temperature quantum bit storage exceeding 39 minutes using ionized donors in silicon-28," *Science*, vol. 342, no. 6160, pp. 830–833, 2013.

[222] X. Rong, Y. Wang, J. Yang, J. Zhu, W. Xu, P. Feng, X. Wen, J. Su, and J. Du, "Dynamical decoupling of electron spins in phosphorus-doped silicon," *Chinese Science Bulletin*, vol. 56, no. 7, pp. 591–597, 2011.

[223] J. Chiaverini, D. Leibfried, T. Schaetz, M. D. Barrett, R. B. Blakestad, J. Britton, W. M. Itano, J. D. Jost, E. Knill, C. Langer, R. Ozeri, and D. J. Wineland, "Realization of quantum error correction," *Nature*, vol. 432, pp. 602–605, Dec 2004.

[224] P. Schindler, J. T. Barreiro, T. Monz, V. Nebendahl, D. Nigg, M. Chwalla, M. Hennrich, and R. Blatt, "Experimental repetitive quantum error correction," *Science*, vol. 332, no. 6033, pp. 1059–1061, 2011.

[225] M. D. Reed, L. DiCarlo, S. E. Nigg, L. Sun, L. Frunzio, S. M. Girvin, and R. J. Schoelkopf, "Realization of three-qubit quantum error correction with superconducting circuits," *Nature*, vol. 482, pp. 382–385, Feb 2012.

[226] D. Ristè, C. C. Bultink, K. W. Lehnert, and L. DiCarlo, "Feedback control of a solid-state qubit using high-fidelity projective measurement," *Phys. Rev. Lett.*, vol. 109, p. 240502, Dec 2012.

[227] P. Campagne-Ibarcq, E. Flurin, N. Roch, D. Darson, P. Morfin, M. Mirrahimi, M. H. Devoret, F. Mallet, and B. Huard, "Persistent control of a superconducting qubit by stroboscopic measurement feedback," *Phys. Rev. X*, vol. 3, p. 021008, May 2013.

[228] A. D. Corcoles, E. Magesan, S. J. Srinivasan, A. W. Cross, M. Steffen, J. M. Gambetta, and J. M. Chow, "Demonstration of a quantum error detection code using a square lattice of four superconducting qubits," *Nat Commun*, vol. 6, Apr 2015.

[229] G. Waldherr, Y. Wang, S. Zaiser, M. Jamali, T. Schulte-Herbruggen, H. Abe, T. Ohshima, J. Isoya, J. F. Du, P. Neumann, and J. Wrachtrup, "Quantum error correction in a solid-state hybrid spin register," *Nature*, vol. 506, pp. 204–207, Feb 2014. Letter.

[230] D. Nigg, M. Müller, E. A. Martinez, P. Schindler, M. Hennrich, T. Monz, M. A. Martin-Delgado, and R. Blatt, "Quantum computations on a topologically encoded qubit," *Science*, vol. 345, no. 6194, pp. 302–305, 2014.

[231] A. V. Kuhlmann, J. Houel, A. Ludwig, L. Greuter, D. Reuter, A. D. Wieck, M. Poggio, and R. J. Warburton, "Charge noise and spin noise in a semiconductor quantum device," *Nature Physics*, vol. 9, no. 9, pp. 570–575, 2013.

Appendix A

A Comparison of Progress Inovling Quantum Computing Platforms

A fault-tolerant quantum computer [214] capable of solving important scientific problems using the gate model of quantum computing may be more than a decade away. Overcoming the engineering hurdles required to assemble the quantum processor and supporting classical infrastructure will likely require progress across a range of disciplines (physics, chemistry, engineering, computer science) as well as a coordinated effort involving academic institutions and industry. Figure A.1 shows one possible representation of the various stages of development of a quantum information processing device (adapted from Ref. [215]). The first stage involves demonstrations of coherent control involving a single physical qubit, with the ability to implement high fidelity arbitrary qubit rotations within the decoherence time. In the next stage, it must be shown that multiple physical qubits can be entangled and manipulated using a set of universal gates. The third stage involves building the toolkit for quantum error correction (QEC). Classical bits can be protected against errors by introducing redundancy. In quantum systems on the other hand, the no-cloning theory precludes copying of qubit states [216]. Instead, in QEC schemes, multiple physical qubits are entangled to create a single *logical qubit* [217, 218, 219, 220]. Errors are detected via quantum non-demolition measurements that, for example, measure the parity of pairs of physical qubits. The number of physical qubits required per logical qubit is determined in part by the desired error threshold [219]. The demonstration of QEC allows for the implementation of quantum memory elements that can be maintained for an arbitrarily long quantum computation, provided the error rate remains below the prescribed threshold. Having implemented quantum memory, one must demonstrate single- and multiple-qubit operations on logical qubits. The last step involves the assembly of a large array of logical qubits with the required interconnects and architecture for

the implementation of quantum algorithms on a fault-tolerant quantum computer.

Chapter 1 provided a detailed review of the field of coherent control of spin and exciton based qubits confined to quantum dots. It also briefly introduced alternate qubit platforms that are under active development for quantum information processing applications, including ion-traps qubits, superconducting qubits, nitrogen vacancy (NV) center qubits, and silicon-dopant based qubits. Table A.1 shows an overview of the progress made for the different platforms based on the stages of development shown in Fig. A.1. For single- and multiple-qubit gates on physical qubits, the references provided are review articles for the field. For demonstrations of QEC, the table lists some of the most recent demonstrations. Currently, the most advanced platforms are those based on trapped ion qubits where operations have been performed on a single logical qubit protected by quantum error correction.

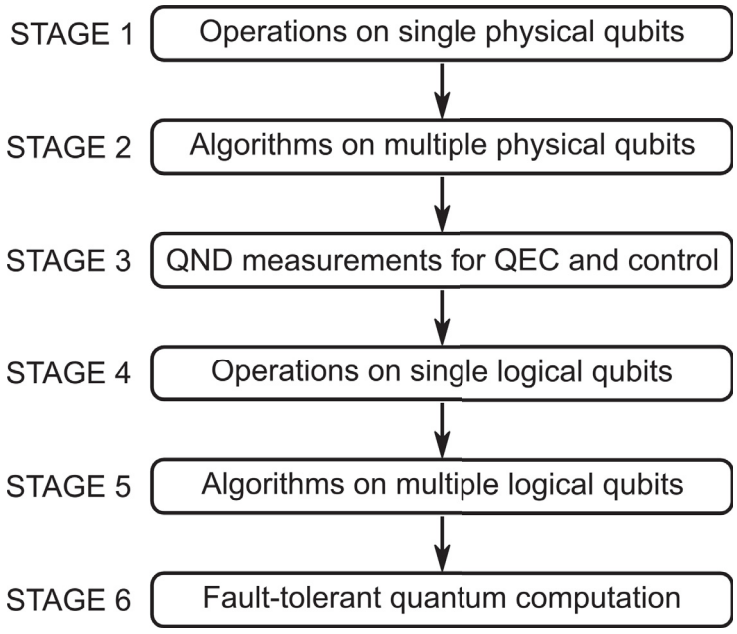

Figure A.1: Six stages of development of a quantum computer. (Adapted from Ref. [215].)

For qubits based on phosphorous dopants in silicon (Si:P) and quantum dots, quantum error correction schemes have not yet been implemented. Nevertheless, there are reasons to be optimistic. The effects of decoherence for the qubit are a result of coupling to the environment. In the case of Si:P qubits, the primary source of

dephasing is the fluctuating magnetic field created by Si-29 isotopes. Recent experiments have shown that in enriched Si-28 systems, the dephasing time of the qubit can be extended to $39\,\mathrm{mins}$ at room temperature and up to $3\,\mathrm{hrs}$ at $4.2\,\mathrm{K}$ [221]. Additionally, dynamical decoupling, an open-loop control scheme for limiting errors, has been demonstrated in this system [222]. In quantum dot based systems, decoherence is primarily due to coupling to LA phonons. It was shown numerically, that dynamical decoupling schemes using just a few π pulses can serve to protect an exciton qubit against decoherence between quantum gates [46]. The demonstration in this thesis of fast, robust π gates should enable demonstrations of dynamical decoupling in the quantum dot platform, providing a method of long-term storage of information.

Table A.1: Stages of development for qubit platforms (See Fig. A.1 and text for a description of the various stages.)

Platform:	Trapped ions	Superconductors	NV center	Si dopants	SAQDs
Stage 1	[11]	[12]	[10]	[13]	[14]
Stage 2	[11]	[12]	[10]	[13]	[14]
Stage 3	[223], [224]	[225], [226], [227], [228]	[229]	X	X
Stage 4	[230]	X	X	X	X
Stage 5	X	X	X	X	X
Stage 6	X	X	X	X	X

Appendix B

Discussion of Experimental Uncertainties

There are a variety of sources of experimental uncertainties in the measured micro-PL signal from the quantum dots. These uncertainties are discussed in this appendix, together with their implications for the experimental results reported in Ch. 6, in which adiabatic rapid passage was demonstrated using subpicosecond control pulses.

For the experiments described in this thesis, the upper limit for the photons flux from the quantum dot is set by the repetition rate of the laser to $76\,\mathrm{MHz}$. However, due to inefficiencies in collection, only a small number of photons are detected at the CCD. The largest losses occur because the majority of photons emitted from the QD are not coupled into the collection optics. Half of the photons are lost because only those emitted in the "forward" direction, toward the objective lens, can be collected. Further, for light traversing the GaAs/vacuum boundary, the 16.7° critical angle means that only $1\,\%$ of the emitted photons leave the sample. These photons are collected by an objective lens, that despite being optimized for operation at near-infrared wavelengths, transmits only $60\,\%$ of the light at the emission wavelengths of $1.3\,\mu\mathrm{m}$. The collected PL is then expanded (using anti-reflection coated lenses) to match the f-number of the monochromator. The light focused into the monochromator is incident on a grating with an efficiency of $\sim 90\,\%$. The spectrally-resolved frequency components are detected using a liquid-nitrogen cooled InGaAs CCD with a quantum efficiency of $85\,\%$ and a gain of $58\,\mathrm{electrons/count}$. Taking into account all of the discussed losses, an estimate of the upper limit for the collection efficiency is $0.008\,\%$, indicating the challenging nature of experiments in this work.

The low light level as well as the need to work at $1.3\,\mu\mathrm{m}$ for quantum state detection makes the experiments in this thesis work more difficult than many previous quantum control experiments, where it was more typical to work on either IFQDs

(with large optical dipole moments and emission wavelengths matching more efficient and less noisy silicon CCD or single-photon detectors) or SAQDs for which the sample has been annealed to shift the ground state transition energies within the range of silicon detectors. In our experiments, quantum dots with an emission close to the telecommunication band at $1.3\,\mu\mathrm{m}$ were chosen, despite the increased complexity, since the use of such QDs would ease the eventual integration of quantum chips with classical hardware. The QD emission around $1.3\,\mu\mathrm{m}$ makes it necessary to use an InGaAs CCD array. The sources of noise in a CCD detector include read noise, dark noise, and fixed pattern noise. Read noise originates from the on-chip amplifier and is inherent to the conversion of charge to a measured voltage. The dark noise signal is due to thermally excited carriers and follows a Poissonian distribution. Small band-gap semiconductors such as InGaAs are particularly prone to dark noise but its effect can be dramatically reduced by cooling the detector. The CCD that was used in this work was cooled to $170\,\mathrm{K}$ using liquid nitrogen. The presence of dark noise can also accentuate any non-uniformities in CCD pixels during long exposures. Differences in the offset voltage or gain for each pixel can manifest as a non-uniform, but fixed pattern across the detector. Table B.1 provides the magnitude of these noise sources, measured by the manufacturer for the CCD used in this work.

In the experiments, the DC offset of the background signal was removed by measuring the pixel counts from the CCD while the laser source was blocked, using the same integration time as that used for data collection ($30\,\mathrm{seconds}$). Five replicate measurements of the background were taken and averaged to reduce the noise. This averaged, pixel-dependent background was subtracted from all data collected during experiments. The presence of stray light in the monochromator, from either ambient light sources or reflected laser light, can also result in noise at the detector. We reduce the reflected laser light intensity by using an optical filter in the beam path prior to coupling into the monochromator. We reduce leakage of ambient light through the housing by working in a low-light environment and by covering the monochromator and detector with black cloth.

In addition to sources of noise inherent to the detector, fluctuations in the laser intensity ($\Delta I \approx 0.5\,\%$) and wavelength ($\Delta\lambda \approx 0.01\,\mathrm{nm}$) can also introduce noise

Table B.1: Noise sources for the CCD detector.

Parameter	Value	Units
Read Noise	532.7	$\mathrm{e^{-}rms}$
Dark Signal	6.72	$\mathrm{ke^{-}/sec}$
Fixed Pattern Noise	169.1	$\mathrm{e^{-}/sec}$

in the emitted PL intensity by virtue of unintended variations in the final quantum state at the end of the laser pulse. Another source of noise is charge noise, resulting from fluctuations in the quantum dot environment or occupancy that in turn lead to fluctuations in the local electric field. This will manifest itself by a shift in the transition frequency via the d.c. Stark effect [231]. The noise introduced by these fluctuations in the PL intensity are reduced by measuring the PL signal three times and averaging the result (after subtraction of the background).

Despite such uncertainties, a clear trend in the variation of the PL intensity from the exciton in a given QD may be observed with respect to some varied experimental parameter. For example, consider the Rabi oscillation from Fig. 6.1(c) and the data showing the chirp sign dependence from Fig. 6.2 that are reproduced here in Fig. B.1. As previously mentioned, the measurements representing a data set collected on a particular day are reported with an average of three points. This allows for an estimate of the error in the measured values to be determined by taking the standard deviation (σ) of the three data sets. The curves in each plot indicate the average value, while the shaded regions indicate an estimate of the uncertainty ($\pm\sigma$). Data that is collected on different days cannot be averaged because of variations in collection efficiency, spot size, and pulse width characteristics. However, the observation of the same trend was verified on several experimental measurement days for all results reported in this thesis. For example, for the trend with respect to chirp sign for adiabatic rapid passage, reported in Fig. 6.2, the ratio of PL intensity for positively- and negatively-chirped pulses at a pulse area of 3π radians was found to be 1.13. Similar measurement made on two other experimental days confirmed the chirp-sign dependent asymmetry, with ratios of 1.17 and 1.33.

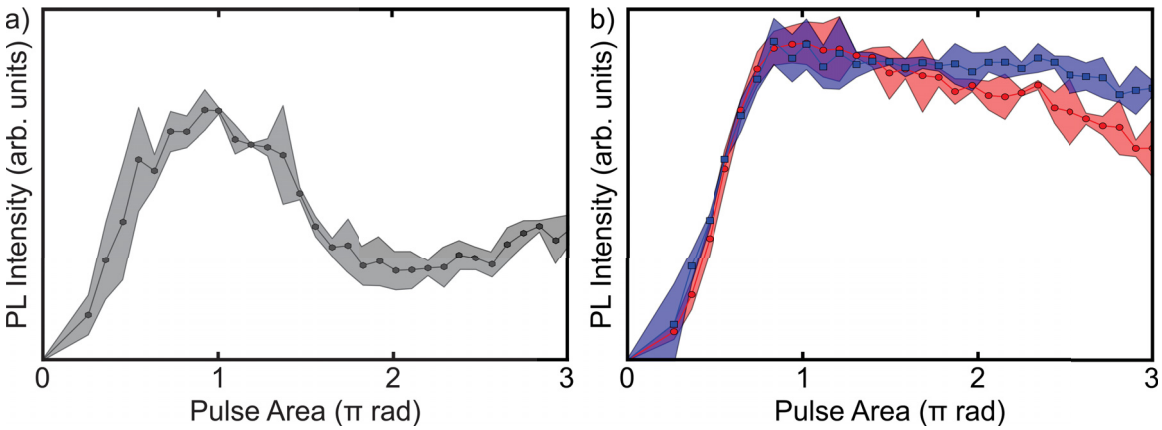

Figure B.1: PL intensity as a function of pulse area for (a) a Rabi rotation using TL pulses, and (b) for positively- (blue) and negatively-chirped (red) pulses with $|\phi''| = 0.133\,\mathrm{ps}^2$ reported in Ch. 6 (see Fig. 6.1(c) and Fig. 6.2). The shaded regions represent the uncertainty ($\pm\sigma$) in the PL intensity for the three averaged data sets collected during the experiment.

Appendix C

Copyright Permission

NATURE PUBLISHING GROUP LICENSE TERMS AND CONDITIONS

May 04, 2015

This is a License Agreement between Reuble Mathew ("You") and Nature Publishing Group ("Nature Publishing Group") provided by Copyright Clearance Center ("CCC"). The license consists of your order details, the terms and conditions provided by Nature Publishing Group, and the payment terms and conditions.

All payments must be made in full to CCC. For payment instructions, please see information listed at the bottom of this form.

License Number	3621941216745
License date	May 04, 2015
Order Content Publisher	Nature Publishing Group
Order Content Publication	Nature Physics
Order Content Title	Resonantly driven coherent oscillations in a solid-state quantum emitter
Order Content Author	E. B. Flagg, A. Muller, J. W. Robertson, S. Founta, D. G. Deppe et al.
Order Content Date	Jan 25, 2009
Volume number	5
Issue number	3
Type of Use	reuse in a dissertation / thesis
Requestor type	non-commercial (non-profit)
Format	print and electronic
Portion	figures/tables/illustrations
Number of figures/tables /illustrations	1
High-res required	no
Figures	Figure 2
Author of this NPG article	no
Your reference number	None
Title of your thesis / dissertation	Optical Control of Exciton Qubits in Semiconductor Quantum Dots Using Pulse Shaping Techniques
Expected completion date	Aug 2015
Estimated size (number of pages)	150
Total	**0.00 CAD**
Terms and Conditions	

Terms and Conditions for Permissions

Nature Publishing Group hereby grants you a non-exclusive license to reproduce this material for this purpose, and for no other use,subject to the conditions below:

1. NPG warrants that it has, to the best of its knowledge, the rights to license reuse of this material. However, you

should ensure that the material you are requesting is original to Nature Publishing Group and does not carry the copyright of another entity (as credited in the published version). If the credit line on any part of the material you have requested indicates that it was reprinted or adapted by NPG with permission from another source, then you should also seek permission from that source to reuse the material.

2. Permission granted free of charge for material in print is also usually granted for any electronic version of that work, provided that the material is incidental to the work as a whole and that the electronic version is essentially equivalent to, or substitutes for, the print version.Where print permission has been granted for a fee, separate permission must be obtained for any additional, electronic re-use (unless, as in the case of a full paper, this has already been accounted for during your initial request in the calculation of a print run).NB: In all cases, web-based use of full-text articles must be authorized separately through the 'Use on a Web Site' option when requesting permission.

3. Permission granted for a first edition does not apply to second and subsequent editions and for editions in other languages (except for signatories to the STM Permissions Guidelines, or where the first edition permission was granted for free).

4. Nature Publishing Group's permission must be acknowledged next to the figure, table or abstract in print. In electronic form, this acknowledgement must be visible at the same time as the figure/table/abstract, and must be hyperlinked to the journal's homepage.

5. The credit line should read:
   Reprinted by permission from Macmillan Publishers Ltd: [JOURNAL NAME] (reference citation), copyright (year of publication)
   For AOP papers, the credit line should read:
   Reprinted by permission from Macmillan Publishers Ltd: [JOURNAL NAME], advance online publication, day month year (doi: 10.1038/sj.[JOURNAL ACRONYM].XXXXX)

   Note: For republication from the *British Journal of Cancer,* the following credit lines apply.
   Reprinted by permission from Macmillan Publishers Ltd on behalf of Cancer Research UK: [JOURNAL NAME] (reference citation), copyright (year of publication)For AOP papers, the credit line should read:
   Reprinted by permission from Macmillan Publishers Ltd on behalf of Cancer Research UK: [JOURNAL NAME], advance online publication, day month year (doi: 10.1038/sj.[JOURNAL ACRONYM].XXXXX)

6. Adaptations of single figures do not require NPG approval. However, the adaptation should be credited as follows:

   Adapted by permission from Macmillan Publishers Ltd: [JOURNAL NAME] (reference citation), copyright (year of publication)

   Note: For adaptation from the *British Journal of Cancer,* the following credit line applies.
   Adapted by permission from Macmillan Publishers Ltd on behalf of Cancer Research UK: [JOURNAL NAME] (reference citation), copyright (year of publication)

7. Translations of 401 words up to a whole article require NPG approval. Please visit http://www.macmillanmedicalcommunications.com for more information.Translations of up to a 400 words do not require NPG approval. The translation should be credited as follows:

   Translated by permission from Macmillan Publishers Ltd: [JOURNAL NAME] (reference citation), copyright (year of publication).

   Note: For translation from the *British Journal of Cancer,* the following credit line applies.

Translated by permission from Macmillan Publishers Ltd on behalf of Cancer Research UK: [JOURNAL NAME] (reference citation), copyright (year of publication)

We are certain that all parties will benefit from this agreement and wish you the best in the use of this material. Thank you.
Special Terms:
v1.1

Questions? customercare@copyright.com or +1-855-239-3415 (toll free in the US) or +1-978-646-2777.

Gratis licenses (referencing $0 in the Total field) are free. Please retain this printable license for your reference. No payment is required.

American Physical Society
License Details

May 04, 2015

This is an Agreement between Reuble Mathew ("You") and American Physical Society ("Publisher"). It consists of your order details, the terms and conditions provided by American Physical Society, and the payment instructions.

License Number	3622001146169
License date	May 04, 2015
Order Content Publisher	American Physical Society
Order Content Publication	Physical Review Letters
Order Content Title	Phonon-Induced Rabi-Frequency Renormalization of Optically Driven Single $\mathrm{InGaAs}/\mathrm{GaAs}$ Quantum Dots
Licensed copyright line	© 2010 The American Physical Society
Order Content Author	A. J. Ramsay et al.
Order Content Date	Oct 20, 2010
Volume number	105
I would like to...	Thesis/Dissertation
Requestor type	Student
Format	Print, Electronic
Portion	image/photo
Number of images/photos requested	1
Portion description	Figure 2
Rights for	Main product
Duration of use	Life of current edition
Creation of copies for the disabled	no
With minor editing privileges	no
For distribution to	Worldwide
In the following language(s)	Original language of publication
With incidental promotional use	no
The lifetime unit quantity of new product	0 to 499
The requesting person/organization is:	Reuble Mathew
Order reference number	None
Title of your thesis / dissertation	Optical Control of Exciton Qubits in Semiconductor Quantum Dots Using Pulse Shaping Techniques
Expected completion date	Aug 2015

Expected size (number of pages)	150
Total	**0.00 CAD**

Terms and Conditions

Terms and Conditions

The American Physical Society (APS) is pleased to grant the Requestor of this license a non-exclusive, non-transferable permission, limited to [**print** and/or **electronic** format, depending on what they chose], provided all criteria outlined below are followed.

1. For electronic format permissions, Requestor agrees to provide a hyperlink from the reprinted APS material using the source material's DOI on the web page where the work appears. The hyperlink should use the standard DOI resolution URL, http://dx.doi.org/{DOI}. The hyperlink may be embedded in the copyright credit line.
2. For print format permissions, Requestor agrees to print the required copyright credit line on the first page where the material appears: "Reprinted (abstract/excerpt/figure) with permission from [(FULL REFERENCE CITATION) as follows: Author's Names, APS Journal Title, Volume Number, Page Number and Year of Publication.] Copyright (YEAR) by the American Physical Society."
3. Permission granted in this license is for a one-time use and does not include permission for any future editions, updates, databases, formats or other matters. Permission must be sought for any additional use.
4. Use of the material does not and must not imply any endorsement by APS.
5. Under no circumstance does APS purport or intend to grant permission to reuse materials to which it does not hold copyright. It is the requestors sole responsibility to ensure the licensed material is original to APS and does not contain the copyright of another entity, and that the copyright notice of the figure, photograph, cover or table does not indicate that it was reprinted by APS, with permission from another source.
6. The permission granted herein is personal to the Requestor for the use specified and is not transferable or assignable without express written permission of APS. This license may not be amended except in writing by APS.
7. You may not alter, edit or modify the material in any manner.
8. You may translate the materials only when translation rights have been granted.
9. You may not use the material for promotional, sales, advertising or marketing purposes.
10. The foregoing license shall not take effect unless and until APS or its agent, Copyright Clearance Center (CCC), receives payment in full in accordance with CCC Billing and Payment Terms and Conditions, which are incorporated herein by reference.
11. Should the terms of this license be violated at any time, APS or CCC may revoke the license with no refund to you and seek relief to the fullest extent of the laws of the USA. Official written notice will be made using the contact information provided with the permission request. Failure to receive such notice will not nullify revocation of the permission.
12. APS reserves all rights not specifically granted herein.
13. This document, including the CCC Billing and Payment Terms and Conditions, shall be the entire agreement between the parties relating to the subject matter hereof.

Other Terms and Conditions

None

Questions? customercare@copyright.com or +1-855-239-3415 (toll free in the US) or +1-978-646-2777.

Gratis licenses (referencing $0 in the Total field) are free. Please retain this printable license for your reference. No payment is required.

THE AMERICAN ASSOCIATION FOR THE ADVANCEMENT OF SCIENCE LICENSE TERMS AND CONDITIONS

May 04, 2015

This is a License Agreement between Reuble Mathew ("You") and The American Association for the Advancement of Science ("The American Association for the Advancement of Science") provided by Copyright Clearance Center ("CCC"). The license consists of your order details, the terms and conditions provided by The American Association for the Advancement of Science, and the payment terms and conditions.

All payments must be made in full to CCC. For payment instructions, please see information listed at the bottom of this form.

License Number	3621950249445
License date	May 04, 2015
Order Content Publisher	The American Association for the Advancement of Science
Order Content Publication	Science
Order Content Title	Coherent Optical Control of the Quantum State of a Single Quantum Dot
Order Content Author	N. H. Bonadeo, J. Erland, D. Gammon, D. Park, D. S. Katzer, D. G. Steel
Order Content Date	Nov 20, 1998
Volume number	282
Issue number	5393
Type of Use	Thesis / Dissertation
Requestor type	Scientist/individual at a research institution
Format	Print and electronic
Portion	Figure
Number of figures/tables	1
Order reference number	None
Title of your thesis / dissertation	Optical Control of Exciton Qubits in Semiconductor Quantum Dots Using Pulse Shaping Techniques
Expected completion date	Aug 2015
Estimated size(pages)	150
Total	**0.00 CAD**

Terms and Conditions

American Association for the Advancement of Science TERMS AND CONDITIONS
Regarding your request, we are pleased to grant you non-exclusive, non-transferable permission, to republish the AAAS material identified above in your work identified above, subject to the terms and conditions herein. We must be contacted for permission for any uses other than those specifically identified in your request above.
The following credit line must be printed along with the AAAS material: "From [Full Reference Citation]. Reprinted with permission from AAAS."
All required credit lines and notices must be visible any time a user accesses any part of the AAAS material and must appear on any printed copies and authorized user might make.
This permission does not apply to figures / photos / artwork or any other content or materials included in your work that

are credited to non-AAAS sources. If the requested material is sourced to or references non-AAAS sources, you must obtain authorization from that source as well before using that material. You agree to hold harmless and indemnify AAAS against any claims arising from your use of any content in your work that is credited to non-AAAS sources.
If the AAAS material covered by this permission was published in Science during the years 1974 - 1994, you must also obtain permission from the author, who may grant or withhold permission, and who may or may not charge a fee if permission is granted. See original article for author's address. This condition does not apply to news articles.
The AAAS material may not be modified or altered except that figures and tables may be modified with permission from the author. Author permission for any such changes must be secured prior to your use.
Whenever possible, we ask that electronic uses of the AAAS material permitted herein include a hyperlink to the original work on AAAS's website (hyperlink may be embedded in the reference citation).
AAAS material reproduced in your work identified herein must not account for more than 30% of the total contents of that work.
AAAS must publish the full paper prior to use of any text.
AAAS material must not imply any endorsement by the American Association for the Advancement of Science.
This permission is not valid for the use of the AAAS and/or Science logos.
AAAS makes no representations or warranties as to the accuracy of any information contained in the AAAS material covered by this permission, including any warranties of
merchantability or fitness for a particular purpose.
If permission fees for this use are waived, please note that AAAS reserves the right to charge for reproduction of this material in the future.
Permission is not valid unless payment is received within sixty (60) days of the issuance of this permission. If payment is not received within this time period then all rights granted herein shall be revoked and this permission will be considered null and void.
In the event of breach of any of the terms and conditions herein or any of CCC's Billing and Payment terms and conditions, all rights granted herein shall be revoked and this permission will be considered null and void.
AAAS reserves the right to terminate this permission and all rights granted herein at its discretion, for any purpose, at any time. In the event that AAAS elects to terminate this permission, you will have no further right to publish, publicly perform, publicly display, distribute or otherwise use any matter in which the AAAS content had been included, and all fees paid hereunder shall be fully refunded to you. Notification of termination will be sent to the contact information as supplied by you during the request process and termination shall be immediate upon sending the notice. Neither AAAS nor CCC shall be liable for any costs, expenses, or damages you may incur as a result of the termination of this permission, beyond the refund noted above.
This Permission may not be amended except by written document signed by both parties.
The terms above are applicable to all permissions granted for the use of AAAS material. Below you will find additional conditions that apply to your particular type of use.

FOR A THESIS OR DISSERTATION

If you are using figure(s)/table(s), permission is granted for use in print and electronic versions of your dissertation or thesis. A full text article may be used in print versions only of a dissertation or thesis.
Permission covers the distribution of your dissertation or thesis on demand by ProQuest / UMI, provided the AAAS material covered by this permission remains in situ.
If you are an Original Author on the AAAS article being reproduced, please refer to your License to Publish for rules on reproducing your paper in a dissertation or thesis.

FOR JOURNALS:

Permission covers both print and electronic versions of your journal article, however the AAAS material may not be used in any manner other than within the context of your article.

FOR BOOKS/TEXTBOOKS:

If this license is to reuse figures/tables, then permission is granted for non-exclusive world rights in all languages in both print and electronic formats (electronic formats are defined below).
If this license is to reuse a text excerpt or a full text article, then permission is granted for non-exclusive world rights in English only. You have the option of securing either print or electronic rights or both, but electronic rights are not automatically granted and do garner additional fees. Permission for translations of text excerpts or full text articles into other languages must be obtained separately.
Licenses granted for use of AAAS material in electronic format books/textbooks are valid only in cases where the electronic version is equivalent to or substitutes for the print version of the book/textbook. The AAAS material

reproduced as permitted herein must remain in situ and must not be exploited separately (for example, if permission covers the use of a full text article, the article may not be offered for access or for purchase as a stand-alone unit), except in the case of permitted textbook companions as noted below.
You must include the following notice in any electronic versions, either adjacent to the reprinted AAAS material or in the terms and conditions for use of your electronic products: "Readers may view, browse, and/or download material for temporary copying purposes only, provided these uses are for noncommercial personal purposes. Except as provided by law, this material may not be further reproduced, distributed, transmitted, modified, adapted, performed, displayed, published, or sold in whole or in part, without prior written permission from the publisher."
If your book is an academic textbook, permission covers the following companions to your textbook, provided such companions are distributed only in conjunction with your textbook at no additional cost to the user:

- Password-protected website
- Instructor's image CD/DVD and/or PowerPoint resource
- Student CD/DVD

All companions must contain instructions to users that the AAAS material may be used for non-commercial, classroom purposes only. Any other uses require the prior written permission from AAAS.
If your license is for the use of AAAS Figures/Tables, then the electronic rights granted herein permit use of the Licensed Material in any Custom Databases that you distribute the electronic versions of your textbook through, so long as the Licensed Material remains within the context of a chapter of the title identified in your request and cannot be downloaded by a user as an independent image file.
Rights also extend to copies/files of your Work (as described above) that you are required to provide for use by the visually and/or print disabled in compliance with state and federal laws.
This permission only covers a single edition of your work as identified in your request.

FOR NEWSLETTERS:

Permission covers print and/or electronic versions, provided the AAAS material reproduced as permitted herein remains in situ and is not exploited separately (for example, if permission covers the use of a full text article, the article may not be offered for access or for purchase as a stand-alone unit)

FOR ANNUAL REPORTS:

Permission covers print and electronic versions provided the AAAS material reproduced as permitted herein remains in situ and is not exploited separately (for example, if permission covers the use of a full text article, the article may not be offered for access or for purchase as a stand-alone unit)

FOR PROMOTIONAL/MARKETING USES:

Permission covers the use of AAAS material in promotional or marketing pieces such as information packets, media kits, product slide kits, brochures, or flyers limited to a single print run. The AAAS Material may not be used in any manner which implies endorsement or promotion by the American Association for the Advancement of Science (AAAS) or Science of any product or service. AAAS does not permit the reproduction of its name, logo or text on promotional literature.
If permission to use a full text article is permitted, The Science article covered by this permission must not be altered in any way. No additional printing may be set onto an article copy other than the copyright credit line required above. Any alterations must be approved in advance and in writing by AAAS. This includes, but is not limited to, the placement of sponsorship identifiers, trademarks, logos, rubber stamping or self-adhesive stickers onto the article copies.
Additionally, article copies must be a freestanding part of any information package (i.e. media kit) into which they are inserted. They may not be physically attached to anything, such as an advertising insert, or have anything attached to them, such as a sample product. Article copies must be easily removable from any kits or informational packages in which they are used. The only exception is that article copies may be inserted into three-ring binders.

FOR CORPORATE INTERNAL USE:

The AAAS material covered by this permission may not be altered in any way. No additional printing may be set onto an article copy other than the required credit line. Any alterations must be approved in advance and in writing by AAAS. This includes, but is not limited to the placement of sponsorship identifiers, trademarks, logos, rubber stamping or self-adhesive stickers onto article copies.
If you are making article copies, copies are restricted to the number indicated in your request and must be distributed only to internal employees for internal use.
If you are using AAAS Material in Presentation Slides, the required credit line must be visible on the slide where the AAAS material will be reprinted

If you are using AAAS Material on a CD, DVD, Flash Drive, or the World Wide Web, you must include the following notice in any electronic versions, either adjacent to the reprinted AAAS material or in the terms and conditions for use of your electronic products: "Readers may view, browse, and/or download material for temporary copying purposes only, provided these uses are for noncommercial personal purposes. Except as provided by law, this material may not be further reproduced, distributed, transmitted, modified, adapted, performed, displayed, published, or sold in whole or in part, without prior written permission from the publisher." Access to any such CD, DVD, Flash Drive or Web page must be restricted to your organization's employees only.

FOR CME COURSE and SCIENTIFIC SOCIETY MEETINGS:

Permission is restricted to the particular Course, Seminar, Conference, or Meeting indicated in your request. If this license covers a text excerpt or a Full Text Article, access to the reprinted AAAS material must be restricted to attendees of your event only (if you have been granted electronic rights for use of a full text article on your website, your website must be password protected, or access restricted so that only attendees can access the content on your site).

If you are using AAAS Material on a CD, DVD, Flash Drive, or the World Wide Web, you must include the following notice in any electronic versions, either adjacent to the reprinted AAAS material or in the terms and conditions for use of your electronic products: "Readers may view, browse, and/or download material for temporary copying purposes only, provided these uses are for noncommercial personal purposes. Except as provided by law, this material may not be further reproduced, distributed, transmitted, modified, adapted, performed, displayed, published, or sold in whole or in part, without prior written permission from the publisher."

FOR POLICY REPORTS:

These rights are granted only to non-profit organizations and/or government agencies. Permission covers print and electronic versions of a report, provided the required credit line appears in both versions and provided the AAAS material reproduced as permitted herein remains in situ and is not exploited separately.

FOR CLASSROOM PHOTOCOPIES:

Permission covers distribution in print copy format only. Article copies must be freestanding and not part of a course pack. They may not be physically attached to anything or have anything attached to them.

FOR COURSEPACKS OR COURSE WEBSITES:

These rights cover use of the AAAS material in one class at one institution. Permission is valid only for a single semester after which the AAAS material must be removed from the Electronic Course website, unless new permission is obtained for an additional semester. If the material is to be distributed online, access must be restricted to students and instructors enrolled in that particular course by some means of password or access control.

FOR WEBSITES:

You must include the following notice in any electronic versions, either adjacent to the reprinted AAAS material or in the terms and conditions for use of your electronic products: "Readers may view, browse, and/or download material for temporary copying purposes only, provided these uses are for noncommercial personal purposes. Except as provided by law, this material may not be further reproduced, distributed, transmitted, modified, adapted, performed, displayed, published, or sold in whole or in part, without prior written permission from the publisher."

Permissions for the use of Full Text articles on third party websites are granted on a case by case basis and only in cases where access to the AAAS Material is restricted by some means of password or access control. Alternately, an E-Print may be purchased through our reprints department (brocheleau@rockwaterinc.com).

REGARDING FULL TEXT ARTICLE USE ON THE WORLD WIDE WEB IF YOU ARE AN ‘ORIGINAL AUTHOR’ OF A SCIENCE PAPER

If you chose "Original Author" as the Requestor Type, you are warranting that you are one of authors listed on the License Agreement as a "Licensed content author" or that you are acting on that author's behalf to use the Licensed content in a new work that one of the authors listed on the License Agreement as a "Licensed content author" has written.

Original Authors may post the ‘Accepted Version’ of their full text article on their personal or on their University website and not on any other website. The ‘Accepted Version’ is the version of the paper accepted for publication by AAAS including changes resulting from peer review but prior to AAAS’s copy editing and production (in other words not the AAAS published version).

FOR MOVIES / FILM / TELEVISION:

Permission is granted to use, record, film, photograph, and/or tape the AAAS material in connection with your program/film and in any medium your program/film may be shown or heard, including but not limited to broadcast and cable television, radio, print, world wide web, and videocassette.

The required credit line should run in the program/film's end credits.

FOR MUSEUM EXHIBITIONS:
Permission is granted to use the AAAS material as part of a single exhibition for the duration of that exhibit. Permission for use of the material in promotional materials for the exhibit must be cleared separately with AAAS (please contact us at permissions@aaas.org).
FOR TRANSLATIONS:
Translation rights apply only to the language identified in your request summary above.
The following disclaimer must appear with your translation, on the first page of the article, after the credit line: "This translation is not an official translation by AAAS staff, nor is it endorsed by AAAS as accurate. In crucial matters, please refer to the official English-language version originally published by AAAS."
FOR USE ON A COVER:
Permission is granted to use the AAAS material on the cover of a journal issue, newsletter issue, book, textbook, or annual report in print and electronic formats provided the AAAS material reproduced as permitted herein remains in situ and is not exploited separately
By using the AAAS Material identified in your request, you agree to abide by all the terms and conditions herein.
Questions about these terms can be directed to the AAAS Permissions department permissions@aaas.org.
Other Terms and Conditions:
v 2

Questions? customercare@copyright.com or +1-855-239-3415 (toll free in the US) or +1-978-646-2777.

Gratis licenses (referencing $0 in the Total field) are free. Please retain this printable license for your reference. No payment is required.

American Physical Society
License Details

May 04, 2015

This is an Agreement between Reuble Mathew ("You") and American Physical Society ("Publisher"). It consists of your order details, the terms and conditions provided by American Physical Society, and the payment instructions.

License Number	3621961420195
License date	May 04, 2015
Order Content Publisher	American Physical Society
Order Content Publication	Physical Review Letters
Order Content Title	Density Matrix Tomography through Sequential Coherent Optical Rotations of an Exciton Qubit in a Single Quantum Dot
Licensed copyright line	Copyright © 2006, American Physical Society
Order Content Author	Yanwen Wu et al.
Order Content Date	Feb 28, 2006
Volume number	96
I would like to...	Thesis/Dissertation
Requestor type	Student
Format	Print, Electronic
Portion	image/photo
Number of images/photos requested	1
Portion description	Figure 3
Rights for	Main product
Duration of use	Life of current edition
Creation of copies for the disabled	no
With minor editing privileges	no
For distribution to	Worldwide
In the following language(s)	Original language of publication
With incidental promotional use	no
The lifetime unit quantity of new product	0 to 499
The requesting person/organization is:	Reuble Mathew
Order reference number	None
Title of your thesis / dissertation	Optical Control of Exciton Qubits in Semiconductor Quantum Dots Using Pulse Shaping Techniques
Expected completion date	Aug 2015

Expected size (number of pages)	150
Total	**0.00 CAD**

Terms and Conditions

Terms and Conditions

The American Physical Society (APS) is pleased to grant the Requestor of this license a non-exclusive, non-transferable permission, limited to [**print** and/or **electronic** format, depending on what they chose], provided all criteria outlined below are followed.

1. For electronic format permissions, Requestor agrees to provide a hyperlink from the reprinted APS material using the source material's DOI on the web page where the work appears. The hyperlink should use the standard DOI resolution URL, http://dx.doi.org/{DOI}. The hyperlink may be embedded in the copyright credit line.
2. For print format permissions, Requestor agrees to print the required copyright credit line on the first page where the material appears: "Reprinted (abstract/excerpt/figure) with permission from [(FULL REFERENCE CITATION) as follows: Author's Names, APS Journal Title, Volume Number, Page Number and Year of Publication.] Copyright (YEAR) by the American Physical Society."
3. Permission granted in this license is for a one-time use and does not include permission for any future editions, updates, databases, formats or other matters. Permission must be sought for any additional use.
4. Use of the material does not and must not imply any endorsement by APS.
5. Under no circumstance does APS purport or intend to grant permission to reuse materials to which it does not hold copyright. It is the requestors sole responsibility to ensure the licensed material is original to APS and does not contain the copyright of another entity, and that the copyright notice of the figure, photograph, cover or table does not indicate that it was reprinted by APS, with permission from another source.
6. The permission granted herein is personal to the Requestor for the use specified and is not transferable or assignable without express written permission of APS. This license may not be amended except in writing by APS.
7. You may not alter, edit or modify the material in any manner.
8. You may translate the materials only when translation rights have been granted.
9. You may not use the material for promotional, sales, advertising or marketing purposes.
10. The foregoing license shall not take effect unless and until APS or its agent, Copyright Clearance Center (CCC), receives payment in full in accordance with CCC Billing and Payment Terms and Conditions, which are incorporated herein by reference.
11. Should the terms of this license be violated at any time, APS or CCC may revoke the license with no refund to you and seek relief to the fullest extent of the laws of the USA. Official written notice will be made using the contact information provided with the permission request. Failure to receive such notice will not nullify revocation of the permission.
12. APS reserves all rights not specifically granted herein.
13. This document, including the CCC Billing and Payment Terms and Conditions, shall be the entire agreement between the parties relating to the subject matter hereof.

Other Terms and Conditions

None

Questions? customercare@copyright.com or +1-855-239-3415 (toll free in the US) or +1-978-646-2777.

Gratis licenses (referencing $0 in the Total field) are free. Please retain this printable license for your reference. No payment is required.

American Physical Society
License Details

May 04, 2015

This is an Agreement between Reuble Mathew ("You") and American Physical Society ("Publisher"). It consists of your order details, the terms and conditions provided by American Physical Society, and the payment instructions.

License Number	3622001282106
License date	May 04, 2015
Order Content Publisher	American Physical Society
Order Content Publication	Physical Review Letters
Order Content Title	Population Inversion in a Single InGaAs Quantum Dot Using the Method of Adiabatic Rapid Passage
Licensed copyright line	© 2011 American Physical Society
Order Content Author	Yanwen Wu et al.
Order Content Date	Feb 8, 2011
Volume number	106
I would like to...	Thesis/Dissertation
Requestor type	Student
Format	Print, Electronic
Portion	image/photo
Number of images/photos requested	2
Portion description	Figure 2 Figure 4
Rights for	Main product
Duration of use	Life of current edition
Creation of copies for the disabled	no
With minor editing privileges	no
For distribution to	Worldwide
In the following language(s)	Original language of publication
With incidental promotional use	no
The lifetime unit quantity of new product	0 to 499
The requesting person/organization is:	Reuble Mathew
Order reference number	None
Title of your thesis / dissertation	Optical Control of Exciton Qubits in Semiconductor Quantum Dots Using Pulse Shaping Techniques
Expected completion date	Aug 2015

Expected size (number of pages)	150
Total	**0.00 CAD**

Terms and Conditions

Terms and Conditions

The American Physical Society (APS) is pleased to grant the Requestor of this license a non-exclusive, non-transferable permission, limited to [**print** and/or **electronic** format, depending on what they chose], provided all criteria outlined below are followed.

1. For electronic format permissions, Requestor agrees to provide a hyperlink from the reprinted APS material using the source material's DOI on the web page where the work appears. The hyperlink should use the standard DOI resolution URL, http://dx.doi.org/{DOI}. The hyperlink may be embedded in the copyright credit line.
2. For print format permissions, Requestor agrees to print the required copyright credit line on the first page where the material appears: "Reprinted (abstract/excerpt/figure) with permission from [(FULL REFERENCE CITATION) as follows: Author's Names, APS Journal Title, Volume Number, Page Number and Year of Publication.] Copyright (YEAR) by the American Physical Society."
3. Permission granted in this license is for a one-time use and does not include permission for any future editions, updates, databases, formats or other matters. Permission must be sought for any additional use.
4. Use of the material does not and must not imply any endorsement by APS.
5. Under no circumstance does APS purport or intend to grant permission to reuse materials to which it does not hold copyright. It is the requestors sole responsibility to ensure the licensed material is original to APS and does not contain the copyright of another entity, and that the copyright notice of the figure, photograph, cover or table does not indicate that it was reprinted by APS, with permission from another source.
6. The permission granted herein is personal to the Requestor for the use specified and is not transferable or assignable without express written permission of APS. This license may not be amended except in writing by APS.
7. You may not alter, edit or modify the material in any manner.
8. You may translate the materials only when translation rights have been granted.
9. You may not use the material for promotional, sales, advertising or marketing purposes.
10. The foregoing license shall not take effect unless and until APS or its agent, Copyright Clearance Center (CCC), receives payment in full in accordance with CCC Billing and Payment Terms and Conditions, which are incorporated herein by reference.
11. Should the terms of this license be violated at any time, APS or CCC may revoke the license with no refund to you and seek relief to the fullest extent of the laws of the USA. Official written notice will be made using the contact information provided with the permission request. Failure to receive such notice will not nullify revocation of the permission.
12. APS reserves all rights not specifically granted herein.
13. This document, including the CCC Billing and Payment Terms and Conditions, shall be the entire agreement between the parties relating to the subject matter hereof.

Other Terms and Conditions

None

Questions? customercare@copyright.com or +1-855-239-3415 (toll free in the US) or +1-978-646-2777.

Gratis licenses (referencing $0 in the Total field) are free. Please retain this printable license for your reference. No payment is required.

THE AMERICAN ASSOCIATION FOR THE ADVANCEMENT OF SCIENCE LICENSE TERMS AND CONDITIONS

May 04, 2015

This is a License Agreement between Reuble Mathew ("You") and The American Association for the Advancement of Science ("The American Association for the Advancement of Science") provided by Copyright Clearance Center ("CCC"). The license consists of your order details, the terms and conditions provided by The American Association for the Advancement of Science, and the payment terms and conditions.

All payments must be made in full to CCC. For payment instructions, please see information listed at the bottom of this form.

License Number	3622011347831
License date	May 04, 2015
Order Content Publisher	The American Association for the Advancement of Science
Order Content Publication	Science
Order Content Title	Coherent Optical Spectroscopy of a Strongly Driven Quantum Dot
Order Content Author	Xiaodong Xu, Bo Sun, Paul R. Berman, Duncan G. Steel, Allan S. Bracker, Dan Gammon, L. J. Sham
Order Content Date	Aug 17, 2007
Volume number	317
Issue number	5840
Type of Use	Thesis / Dissertation
Requestor type	Scientist/individual at a research institution
Format	Print and electronic
Portion	Figure
Number of figures/tables	2
Order reference number	None
Title of your thesis / dissertation	Optical Control of Exciton Qubits in Semiconductor Quantum Dots Using Pulse Shaping Techniques
Expected completion date	Aug 2015
Estimated size(pages)	150
Total	**0.00 CAD**

Terms and Conditions

American Association for the Advancement of Science TERMS AND CONDITIONS
Regarding your request, we are pleased to grant you non-exclusive, non-transferable permission, to republish the AAAS material identified above in your work identified above, subject to the terms and conditions herein. We must be contacted for permission for any uses other than those specifically identified in your request above.
The following credit line must be printed along with the AAAS material: "From [Full Reference Citation]. Reprinted with permission from AAAS."
All required credit lines and notices must be visible any time a user accesses any part of the AAAS material and must appear on any printed copies and authorized user might make.

This permission does not apply to figures / photos / artwork or any other content or materials included in your work that are credited to non-AAAS sources. If the requested material is sourced to or references non-AAAS sources, you must obtain authorization from that source as well before using that material. You agree to hold harmless and indemnify AAAS against any claims arising from your use of any content in your work that is credited to non-AAAS sources.
If the AAAS material covered by this permission was published in Science during the years 1974 - 1994, you must also obtain permission from the author, who may grant or withhold permission, and who may or may not charge a fee if permission is granted. See original article for author's address. This condition does not apply to news articles.
The AAAS material may not be modified or altered except that figures and tables may be modified with permission from the author. Author permission for any such changes must be secured prior to your use.
Whenever possible, we ask that electronic uses of the AAAS material permitted herein include a hyperlink to the original work on AAAS's website (hyperlink may be embedded in the reference citation).
AAAS material reproduced in your work identified herein must not account for more than 30% of the total contents of that work.
AAAS must publish the full paper prior to use of any text.
AAAS material must not imply any endorsement by the American Association for the Advancement of Science.
This permission is not valid for the use of the AAAS and/or Science logos.
AAAS makes no representations or warranties as to the accuracy of any information contained in the AAAS material covered by this permission, including any warranties of
merchantability or fitness for a particular purpose.
If permission fees for this use are waived, please note that AAAS reserves the right to charge for reproduction of this material in the future.
Permission is not valid unless payment is received within sixty (60) days of the issuance of this permission. If payment is not received within this time period then all rights granted herein shall be revoked and this permission will be considered null and void.
In the event of breach of any of the terms and conditions herein or any of CCC's Billing and Payment terms and conditions, all rights granted herein shall be revoked and this permission will be considered null and void.
AAAS reserves the right to terminate this permission and all rights granted herein at its discretion, for any purpose, at any time. In the event that AAAS elects to terminate this permission, you will have no further right to publish, publicly perform, publicly display, distribute or otherwise use any matter in which the AAAS content had been included, and all fees paid hereunder shall be fully refunded to you. Notification of termination will be sent to the contact information as supplied by you during the request process and termination shall be immediate upon sending the notice. Neither AAAS nor CCC shall be liable for any costs, expenses, or damages you may incur as a result of the termination of this permission, beyond the refund noted above.
This Permission may not be amended except by written document signed by both parties.
The terms above are applicable to all permissions granted for the use of AAAS material. Below you will find additional conditions that apply to your particular type of use.

FOR A THESIS OR DISSERTATION

If you are using figure(s)/table(s), permission is granted for use in print and electronic versions of your dissertation or thesis. A full text article may be used in print versions only of a dissertation or thesis.
Permission covers the distribution of your dissertation or thesis on demand by ProQuest / UMI, provided the AAAS material covered by this permission remains in situ.
If you are an Original Author on the AAAS article being reproduced, please refer to your License to Publish for rules on reproducing your paper in a dissertation or thesis.

FOR JOURNALS:

Permission covers both print and electronic versions of your journal article, however the AAAS material may not be used in any manner other than within the context of your article.

FOR BOOKS/TEXTBOOKS:

If this license is to reuse figures/tables, then permission is granted for non-exclusive world rights in all languages in both print and electronic formats (electronic formats are defined below).
If this license is to reuse a text excerpt or a full text article, then permission is granted for non-exclusive world rights in English only. You have the option of securing either print or electronic rights or both, but electronic rights are not automatically granted and do garner additional fees. Permission for translations of text excerpts or full text articles into other languages must be obtained separately.
Licenses granted for use of AAAS material in electronic format books/textbooks are valid only in cases where the

electronic version is equivalent to or substitutes for the print version of the book/textbook. The AAAS material reproduced as permitted herein must remain in situ and must not be exploited separately (for example, if permission covers the use of a full text article, the article may not be offered for access or for purchase as a stand-alone unit), except in the case of permitted textbook companions as noted below.
You must include the following notice in any electronic versions, either adjacent to the reprinted AAAS material or in the terms and conditions for use of your electronic products: "Readers may view, browse, and/or download material for temporary copying purposes only, provided these uses are for noncommercial personal purposes. Except as provided by law, this material may not be further reproduced, distributed, transmitted, modified, adapted, performed, displayed, published, or sold in whole or in part, without prior written permission from the publisher."
If your book is an academic textbook, permission covers the following companions to your textbook, provided such companions are distributed only in conjunction with your textbook at no additional cost to the user:

- Password-protected website
- Instructor's image CD/DVD and/or PowerPoint resource
- Student CD/DVD

All companions must contain instructions to users that the AAAS material may be used for non-commercial, classroom purposes only. Any other uses require the prior written permission from AAAS.
If your license is for the use of AAAS Figures/Tables, then the electronic rights granted herein permit use of the Licensed Material in any Custom Databases that you distribute the electronic versions of your textbook through, so long as the Licensed Material remains within the context of a chapter of the title identified in your request and cannot be downloaded by a user as an independent image file.
Rights also extend to copies/files of your Work (as described above) that you are required to provide for use by the visually and/or print disabled in compliance with state and federal laws.
This permission only covers a single edition of your work as identified in your request.

FOR NEWSLETTERS:

Permission covers print and/or electronic versions, provided the AAAS material reproduced as permitted herein remains in situ and is not exploited separately (for example, if permission covers the use of a full text article, the article may not be offered for access or for purchase as a stand-alone unit)

FOR ANNUAL REPORTS:

Permission covers print and electronic versions provided the AAAS material reproduced as permitted herein remains in situ and is not exploited separately (for example, if permission covers the use of a full text article, the article may not be offered for access or for purchase as a stand-alone unit)

FOR PROMOTIONAL/MARKETING USES:

Permission covers the use of AAAS material in promotional or marketing pieces such as information packets, media kits, product slide kits, brochures, or flyers limited to a single print run. The AAAS Material may not be used in any manner which implies endorsement or promotion by the American Association for the Advancement of Science (AAAS) or Science of any product or service. AAAS does not permit the reproduction of its name, logo or text on promotional literature.
If permission to use a full text article is permitted, The Science article covered by this permission must not be altered in any way. No additional printing may be set onto an article copy other than the copyright credit line required above. Any alterations must be approved in advance and in writing by AAAS. This includes, but is not limited to, the placement of sponsorship identifiers, trademarks, logos, rubber stamping or self-adhesive stickers onto the article copies.
Additionally, article copies must be a freestanding part of any information package (i.e. media kit) into which they are inserted. They may not be physically attached to anything, such as an advertising insert, or have anything attached to them, such as a sample product. Article copies must be easily removable from any kits or informational packages in which they are used. The only exception is that article copies may be inserted into three-ring binders.

FOR CORPORATE INTERNAL USE:

The AAAS material covered by this permission may not be altered in any way. No additional printing may be set onto an article copy other than the required credit line. Any alterations must be approved in advance and in writing by AAAS. This includes, but is not limited to the placement of sponsorship identifiers, trademarks, logos, rubber stamping or self-adhesive stickers onto article copies.
If you are making article copies, copies are restricted to the number indicated in your request and must be distributed only to internal employees for internal use.
If you are using AAAS Material in Presentation Slides, the required credit line must be visible on the slide where the

AAAS material will be reprinted
If you are using AAAS Material on a CD, DVD, Flash Drive, or the World Wide Web, you must include the following notice in any electronic versions, either adjacent to the reprinted AAAS material or in the terms and conditions for use of your electronic products: "Readers may view, browse, and/or download material for temporary copying purposes only, provided these uses are for noncommercial personal purposes. Except as provided by law, this material may not be further reproduced, distributed, transmitted, modified, adapted, performed, displayed, published, or sold in whole or in part, without prior written permission from the publisher." Access to any such CD, DVD, Flash Drive or Web page must be restricted to your organization's employees only.

FOR CME COURSE and SCIENTIFIC SOCIETY MEETINGS:

Permission is restricted to the particular Course, Seminar, Conference, or Meeting indicated in your request. If this license covers a text excerpt or a Full Text Article, access to the reprinted AAAS material must be restricted to attendees of your event only (if you have been granted electronic rights for use of a full text article on your website, your website must be password protected, or access restricted so that only attendees can access the content on your site).
If you are using AAAS Material on a CD, DVD, Flash Drive, or the World Wide Web, you must include the following notice in any electronic versions, either adjacent to the reprinted AAAS material or in the terms and conditions for use of your electronic products: "Readers may view, browse, and/or download material for temporary copying purposes only, provided these uses are for noncommercial personal purposes. Except as provided by law, this material may not be further reproduced, distributed, transmitted, modified, adapted, performed, displayed, published, or sold in whole or in part, without prior written permission from the publisher."

FOR POLICY REPORTS:

These rights are granted only to non-profit organizations and/or government agencies. Permission covers print and electronic versions of a report, provided the required credit line appears in both versions and provided the AAAS material reproduced as permitted herein remains in situ and is not exploited separately.

FOR CLASSROOM PHOTOCOPIES:

Permission covers distribution in print copy format only. Article copies must be freestanding and not part of a course pack. They may not be physically attached to anything or have anything attached to them.

FOR COURSEPACKS OR COURSE WEBSITES:

These rights cover use of the AAAS material in one class at one institution. Permission is valid only for a single semester after which the AAAS material must be removed from the Electronic Course website, unless new permission is obtained for an additional semester. If the material is to be distributed online, access must be restricted to students and instructors enrolled in that particular course by some means of password or access control.

FOR WEBSITES:

You must include the following notice in any electronic versions, either adjacent to the reprinted AAAS material or in the terms and conditions for use of your electronic products: "Readers may view, browse, and/or download material for temporary copying purposes only, provided these uses are for noncommercial personal purposes. Except as provided by law, this material may not be further reproduced, distributed, transmitted, modified, adapted, performed, displayed, published, or sold in whole or in part, without prior written permission from the publisher."
Permissions for the use of Full Text articles on third party websites are granted on a case by case basis and only in cases where access to the AAAS Material is restricted by some means of password or access control. Alternately, an E-Print may be purchased through our reprints department (brocheleau@rockwaterinc.com).
REGARDING FULL TEXT ARTICLE USE ON THE WORLD WIDE WEB IF YOU ARE AN 'ORIGINAL AUTHOR' OF A SCIENCE PAPER
If you chose "Original Author" as the Requestor Type, you are warranting that you are one of authors listed on the License Agreement as a "Licensed content author" or that you are acting on that author's behalf to use the Licensed content in a new work that one of the authors listed on the License Agreement as a "Licensed content author" has written.
Original Authors may post the 'Accepted Version' of their full text article on their personal or on their University website and not on any other website. The 'Accepted Version' is the version of the paper accepted for publication by AAAS including changes resulting from peer review but prior to AAAS's copy editing and production (in other words not the AAAS published version).

FOR MOVIES / FILM / TELEVISION:

Permission is granted to use, record, film, photograph, and/or tape the AAAS material in connection with your program/film and in any medium your program/film may be shown or heard, including but not limited to broadcast and cable television, radio, print, world wide web, and videocassette.

The required credit line should run in the program/film's end credits.

FOR MUSEUM EXHIBITIONS:

Permission is granted to use the AAAS material as part of a single exhibition for the duration of that exhibit. Permission for use of the material in promotional materials for the exhibit must be cleared separately with AAAS (please contact us at permissions@aaas.org).

FOR TRANSLATIONS:

Translation rights apply only to the language identified in your request summary above.

The following disclaimer must appear with your translation, on the first page of the article, after the credit line: "This translation is not an official translation by AAAS staff, nor is it endorsed by AAAS as accurate. In crucial matters, please refer to the official English-language version originally published by AAAS."

FOR USE ON A COVER:

Permission is granted to use the AAAS material on the cover of a journal issue, newsletter issue, book, textbook, or annual report in print and electronic formats provided the AAAS material reproduced as permitted herein remains in situ and is not exploited separately

By using the AAAS Material identified in your request, you agree to abide by all the terms and conditions herein.

Questions about these terms can be directed to the AAAS Permissions department permissions@aaas.org.

Other Terms and Conditions:

v 2

Questions? customercare@copyright.com or +1-855-239-3415 (toll free in the US) or +1-978-646-2777.

Gratis licenses (referencing $0 in the Total field) are free. Please retain this printable license for your reference. No payment is required.

American Physical Society
License Details

May 04, 2015

This is an Agreement between Reuble Mathew ("You") and American Physical Society ("Publisher"). It consists of your order details, the terms and conditions provided by American Physical Society, and the payment instructions.

License Number	3622020240915
License date	May 04, 2015
Order Content Publisher	American Physical Society
Order Content Publication	Physical Review D
Order Content Title	Twoxqubit conditional quantumxlogic operation in a single selfxassembled quantum dot
Licensed copyright line	Copyright E 200Q American Physical Society
Order Content Author	S. © Doyle et al.
Order Content Wate	Aug 1, 200Q
Folume number	8Q
I would liVe to...	ThesiskWssertation
Requestor type	Student
/ ormat	Print, z lectronic
Portion	chartkgraphktablekfigure
Number of chartskgraphsktables kfigures	2
Portion description	/ igure 2, / igure 3
Rights for	Main product
Wuration of use	Life of current edition
Creation of copies for the disabled	no
: ith minor editing privileges	no
/ or distribution to	: orldwide
In the following language(s)	Original language of publication
: ith incidental promotional use	no
The lifetime unit quantity of new product	0 to 499
The requesting personkorganiUation is-	Reuble Mathew
Order reference number	None
Title of your thesis k dissertation	Optical Control of z [citon] ubits in Semiconductor] uantum Wots ' sing Pulse Shaping Techniques
z [pected completion date	Aug 2015
z [pected siUe (number of pages)	150

Total **0.00 CAD**

Terms and Conditions

Terms and Conditions

The American Physical Society (APS) is pleased to grant the Requestor of this license a nonxe[clusive, nonxtransferable permission, limited to {**print** andkor **electronic** format, depending on what they chose}, provided all criteria outlined below are followed.

1. / or electronic format permissions, Requestor agrees to provide a hyperlinV from the reprinted APS material using the source material's WOI on the web page where the worV appears. The hyperlinV should use the standard WOI resolution ' RL, http-kkd[.doi.orgkWOI7. The hyperlinV may be embedded in the copyright credit line.

2. / or print format permissions, Requestor agrees to print the required copyright credit line on the first page where the material appears- "Reprinted (abstractke[cerptkfigure) with permission from {(/ ' LL Rz / z Rz NCz CITATION) as follows- AuthorB Names, APS @ournal Title, Folume Number, Page Number and Year of Publication.} Copyright (Yz AR) by the American Physical Society."

3. Permission granted in this license is for a onextime use and does not include permission for any future editions, updates, databases, formats or other matters. Permission must be sought for any additional use.

4. ' se of the material does not and must not imply any endorsement by APS.

5. ' nder no circumstance does APS purport or intend to grant permission to reuse materials to which it does not hold copyright. It is the requestors sole responsibility to ensure the licensed material is original to APS and does not contain the copyright of another entity, and that the copyright notice of the figure, photograph, cover or table does not indicate that it was reprinted by APS, with permission from another source.

6. The permission granted herein is personal to the Requestor for the use specified and is not transferable or assignable without e[press written permission of APS. This license may not be amended e[cept in writing by APS.

8. You may not alter, edit or modify the material in any manner.

Q. You may translate the materials only when translation rights have been granted.

9. You may not use the material for promotional, sales, advertising or marVeting purposes.

10. The foregoing license shall not taVe effect unless and until APS or its agent, Copyright Clearance Center (CCC), receives payment in full in accordance with CCC Dilling and Payment Terms and Conditions, which are incorporated herein by reference.

11. Should the terms of this license be violated at any time, APS or CCC may revoVe the license with no refund to you and seeV relief to the fullest e[tent of the laws of the ' SA. Official written notice will be made using the contact information provided with the permission request. / ailure to receive such notice will not nullify revocation of the permission.

12. APS reserves all rights not specifically granted herein.

13. This document, including the CCC Dilling and Payment Terms and Conditions, shall be the entire agreement between the parties relating to the subject matter hereof.

Other Terms and Conditions

None

Questions? customercare@copyright.com or +1-855-239-3415 (toll free in the US) or +1-978-646-2777.

Gratis licenses (referencing $0 in the Total field) are free. Please retain this printable license for your reference. No payment is required.

American Physical Society
License Details

May 04, 2015

This is an Agreement between Reuble Mathew ("You") and American Physical Society ("Publisher"). It consists of your order details, the terms and conditions provided by American Physical Society, and the payment instructions.

License Number	3622020346030
License date	May 04, 2015
Order Content Publisher	American Physical Society
Order Content Publication	Physical Review B
Order Content Title	Two-photon Rabi oscillations in a single ${\mathrm{In}}_{x}{\mathrm{Ga}}_{1$-${}x} \mathrm{As}/\mathrm{Ga}\mathrm{As}$ quantum dot
Licensed copyright line	Copyright © 2006, American Physical Society
Order Content Author	S. Stufler et al.
Order Content Date	Mar 7, 2006
Volume number	73
I would like to...	Thesis/Dissertation
Requestor type	Student
Format	Print, Electronic
Portion	chart/graph/table/figure
Number of charts/graphs/tables /figures	1
Portion description	Figure 4
Rights for	Main product
Duration of use	Life of current edition
Creation of copies for the disabled	no
With minor editing privileges	no
For distribution to	Worldwide
In the following language(s)	Original language of publication
With incidental promotional use	no
The lifetime unit quantity of new product	0 to 499
The requesting person/organization is:	Reuble Mathew
Order reference number	None
Title of your thesis / dissertation	Optical Control of Exciton Qubits in Semiconductor Quantum Dots Using Pulse Shaping Techniques
Expected completion date	Aug 2015

Expected size (number of pages)	150
Total	**0.00 CAD**

Terms and Conditions

Terms and Conditions

The American Physical Society (APS) is pleased to grant the Requestor of this license a non-exclusive, non-transferable permission, limited to [**print** and/or **electronic** format, depending on what they chose], provided all criteria outlined below are followed.

1. For electronic format permissions, Requestor agrees to provide a hyperlink from the reprinted APS material using the source material's DOI on the web page where the work appears. The hyperlink should use the standard DOI resolution URL, http://dx.doi.org/{DOI}. The hyperlink may be embedded in the copyright credit line.
2. For print format permissions, Requestor agrees to print the required copyright credit line on the first page where the material appears: "Reprinted (abstract/excerpt/figure) with permission from [(FULL REFERENCE CITATION) as follows: Author's Names, APS Journal Title, Volume Number, Page Number and Year of Publication.] Copyright (YEAR) by the American Physical Society."
3. Permission granted in this license is for a one-time use and does not include permission for any future editions, updates, databases, formats or other matters. Permission must be sought for any additional use.
4. Use of the material does not and must not imply any endorsement by APS.
5. Under no circumstance does APS purport or intend to grant permission to reuse materials to which it does not hold copyright. It is the requestors sole responsibility to ensure the licensed material is original to APS and does not contain the copyright of another entity, and that the copyright notice of the figure, photograph, cover or table does not indicate that it was reprinted by APS, with permission from another source.
6. The permission granted herein is personal to the Requestor for the use specified and is not transferable or assignable without express written permission of APS. This license may not be amended except in writing by APS.
7. You may not alter, edit or modify the material in any manner.
8. You may translate the materials only when translation rights have been granted.
9. You may not use the material for promotional, sales, advertising or marketing purposes.
10. The foregoing license shall not take effect unless and until APS or its agent, Copyright Clearance Center (CCC), receives payment in full in accordance with CCC Billing and Payment Terms and Conditions, which are incorporated herein by reference.
11. Should the terms of this license be violated at any time, APS or CCC may revoke the license with no refund to you and seek relief to the fullest extent of the laws of the USA. Official written notice will be made using the contact information provided with the permission request. Failure to receive such notice will not nullify revocation of the permission.
12. APS reserves all rights not specifically granted herein.
13. This document, including the CCC Billing and Payment Terms and Conditions, shall be the entire agreement between the parties relating to the subject matter hereof.

Other Terms and Conditions

None

Questions? customercare@copyright.com or +1-855-239-3415 (toll free in the US) or +1-978-646-2777.

Gratis licenses (referencing $0 in the Total field) are free. Please retain this printable license for your reference. No payment is required.

NATURE PUBLISHING GROUP LICENSE TERMS AND CONDITIONS

May 04, 2015

This is a License Agreement between Reuble Mathew ("You") and Nature Publishing Group ("Nature Publishing Group") provided by Copyright Clearance Center ("CCC"). The license consists of your order details, the terms and conditions provided by Nature Publishing Group, and the payment terms and conditions.

All payments must be made in full to CCC. For payment instructions, please see information listed at the bottom of this form.

License Number	3622020465837
License date	May 04, 2015
Order Content Publisher	Nature Publishing Group
Order Content Publication	Nature
Order Content Title	Complete quantum control of a single quantum dot spin using ultrafast optical pulses
Order Content Author	David Press, Thaddeus D. Ladd, Bingyang Zhang and Yoshihisa Yamamoto
Order Content Date	Nov 13, 2008
Volume number	456
Issue number	7219
Type of Use	reuse in a dissertation / thesis
Requestor type	non-commercial (non-profit)
Format	print and electronic
Portion	figures/tables/illustrations
Number of figures/tables /illustrations	2
High-res required	no
Figures	Figure 3, Figure 5
Author of this NPG article	no
Your reference number	None
Title of your thesis / dissertation	Optical Control of Exciton Qubits in Semiconductor Quantum Dots Using Pulse Shaping Techniques
Expected completion date	Aug 2015
Estimated size (number of pages)	150
Total	**0.00 CAD**
Terms and Conditions	

Terms and Conditions for Permissions

Nature Publishing Group hereby grants you a non-exclusive license to reproduce this material for this purpose, and for no other use,subject to the conditions below:

1. NPG warrants that it has, to the best of its knowledge, the rights to license reuse of this material. However, you

should ensure that the material you are requesting is original to Nature Publishing Group and does not carry the copyright of another entity (as credited in the published version). If the credit line on any part of the material you have requested indicates that it was reprinted or adapted by NPG with permission from another source, then you should also seek permission from that source to reuse the material.

2. Permission granted free of charge for material in print is also usually granted for any electronic version of that work, provided that the material is incidental to the work as a whole and that the electronic version is essentially equivalent to, or substitutes for, the print version.Where print permission has been granted for a fee, separate permission must be obtained for any additional, electronic re-use (unless, as in the case of a full paper, this has already been accounted for during your initial request in the calculation of a print run).NB: In all cases, web-based use of full-text articles must be authorized separately through the 'Use on a Web Site' option when requesting permission.

3. Permission granted for a first edition does not apply to second and subsequent editions and for editions in other languages (except for signatories to the STM Permissions Guidelines, or where the first edition permission was granted for free).

4. Nature Publishing Group's permission must be acknowledged next to the figure, table or abstract in print. In electronic form, this acknowledgement must be visible at the same time as the figure/table/abstract, and must be hyperlinked to the journal's homepage.

5. The credit line should read:
   Reprinted by permission from Macmillan Publishers Ltd: [JOURNAL NAME] (reference citation), copyright (year of publication)
   For AOP papers, the credit line should read:
   Reprinted by permission from Macmillan Publishers Ltd: [JOURNAL NAME], advance online publication, day month year (doi: 10.1038/sj.[JOURNAL ACRONYM].XXXXX)

   Note: For republication from the *British Journal of Cancer,* the following credit lines apply.
   Reprinted by permission from Macmillan Publishers Ltd on behalf of Cancer Research UK: [JOURNAL NAME] (reference citation), copyright (year of publication)For AOP papers, the credit line should read:
   Reprinted by permission from Macmillan Publishers Ltd on behalf of Cancer Research UK: [JOURNAL NAME], advance online publication, day month year (doi: 10.1038/sj.[JOURNAL ACRONYM].XXXXX)

6. Adaptations of single figures do not require NPG approval. However, the adaptation should be credited as follows:

   Adapted by permission from Macmillan Publishers Ltd: [JOURNAL NAME] (reference citation), copyright (year of publication)

   Note: For adaptation from the *British Journal of Cancer,* the following credit line applies.
   Adapted by permission from Macmillan Publishers Ltd on behalf of Cancer Research UK: [JOURNAL NAME] (reference citation), copyright (year of publication)

7. Translations of 401 words up to a whole article require NPG approval. Please visit http://www.macmillanmedicalcommunications.com for more information.Translations of up to a 400 words do not require NPG approval. The translation should be credited as follows:

   Translated by permission from Macmillan Publishers Ltd: [JOURNAL NAME] (reference citation), copyright (year of publication).

   Note: For translation from the *British Journal of Cancer,* the following credit line applies.

Translated by permission from Macmillan Publishers Ltd on behalf of Cancer Research UK: [JOURNAL NAME] (reference citation), copyright (year of publication)

We are certain that all parties will benefit from this agreement and wish you the best in the use of this material. Thank you.
Special Terms:
v1.1

Questions? customercare@copyright.com or +1-855-239-3415 (toll free in the US) or +1-978-646-2777.

Gratis licenses (referencing $0 in the Total field) are free. Please retain this printable license for your reference. No payment is required.

American Physical Society
License Details

May 04, 2015

This is an Agreement between Reuble Mathew ("You") and American Physical Society ("Publisher"). It consists of your order details, the terms and conditions provided by American Physical Society, and the payment instructions.

License Number	36219C0045094
License date	May 04, 2015
Crder Dontent Publisher	American Physical Society
Crder Dontent Publication	Physical Review x
Crder Dontent Title	Cptimal quantum control for conditional rotation of eEciton qubits in semiconductor quantum dots
Licensed copyright line	Q2011 American Physical Society
Crder Dontent Author	Reuble Mathew et al.
Crder Dontent ©ate	Nov 1Q 2011
W̊olume number	F4
I would li8e to...	ThesisV©issertation
Requestor type	Student
kormat	Print, / lectronic
Portion	chapterV́rticle
Rights for	Main product
©uration of use	Life of current edition
Dreation of copies for the disabled	no
z ith minor editing privileges	no
kor distribution to	z orldwide
In the following language(s)	Criginal language of publication
z ith incidental promotional use	no
The lifetime unit quantity of new product	0 to 499
The requesting personV́rgani: ation isU	Reuble Mathew
Crder reference number	None
Title of your thesis V dissertation	Cptical Dontrol of / Eciton - ubits in Semiconductor - uantum ©ots [sing Pulse Shaping Techniques
/ Epected completion date	Aug 2015
/ Epected si: e (number of pages)	150
Total	**0.00 CAD**
Terms and Donditions	

Terms and Conditions

The American Physical Society (APS) is pleased to grant the Requestor of this license a non]eEclusive, non]transferable permission, limited to '**print** andVor **electronic** format, depending on what they chose{, provided all criteria outlined below are followed.

1. kor electronic format permissions, Requestor agrees to provide a hyperlin8 from the reprinted APS material using the source material}s ©CI on the web page where the wor8 appears. The hyperlin8 should use the standard ©CI resolution [RL, httpUWdE doi.orgV©CIJ. The hyperlin8 may be embedded in the copyright credit line.

2. kor print format permissions, Requestor agrees to print the required copyright credit line on the first page where the material appearsU"Reprinted (abstractVeEcerptVfigure) with permission from '(k[LL R/ k/ R/ ND/ DITATICN) as followsU Author7s Names, APS Bournal Title, Wolume Number, Page Number and Year of Publication.{ Dopyright (Y/ AR) by the American Physical Society."

3. Permission granted in this license is for a one]time use and does not include permission for any future editions, updates, databases, formats or other matters. Permission must be sought for any additional use.

4. [se of the material does not and must not imply any endorsement by APS.

5. [nder no circumstance does APS purport or intend to grant permission to reuse materials to which it does not hold copyright. It is the requestors sole responsibility to ensure the licensed material is original to APS and does not contain the copyright of another entity, and that the copyright notice of the figure, photograph, cover or table does not indicate that it was reprinted by APS, with permission from another source.

6. The permission granted herein is personal to the Requestor for the use specified and is not transferable or assignable without eEpress written permission of APS. This license may not be amended eEcept in writing by APS.

O. You may not alter, edit or modify the material in any manner.

F. You may translate the materials only when translation rights have been granted.

9. You may not use the material for promotional, sales, advertising or mar8eting purposes.

10. The foregoing license shall not ta8e effect unless and until APS or its agent, Dopyright Dlearance Denter (DDD), receives payment in full in accordance with DDD x illing and Payment Terms and Donditions, which are incorporated herein by reference.

11. Should the terms of this license be violated at any time, APS or DDD may revo8e the license with no refund to you and see8 relief to the fullest eEtent of the laws of the [SA. Cfficial written notice will be made using the contact information provided with the permission request. kailure to receive such notice will not nullify revocation of the permission.

12. APS reserves all rights not specifically granted herein.

13. This document, including the DDD x illing and Payment Terms and Donditions, shall be the entire agreement between the parties relating to the subject matter hereof.

Other Terms and Conditions

None

Questions? customercare@copyright.com or +1-855-239-3415 (toll free in the US) or +1-978-646-2777.

Gratis licenses (referencing $0 in the Total field) are free. Please retain this printable license for your reference. No payment is required.

American Physical Society
License Details

May 04, 2015

This is an Agreement between Reuble Mathew ("You") and American Physical Society ("Publisher"). It consists of your order details, the terms and conditions provided by American Physical Society, and the payment instructions.

License Number	362196149O444
License date	May 04, 2015
Crder Dontent Publisher	American Physical Society
Crder Dontent Publication	Physical Review x
Crder Dontent Title	Subpicosecond adiabatic rapid passage on a single semiconductor quantum dotEPhononQ mediated dephasing in the strongQdriving regime
Licensed copyright line	©2014 American Physical Society
Crder Dontent Author	Reuble Mathew et al.
Crder Dontent Wate	Ful 25, 2014
8olume number	90
I would liVe to...	ThesiskWssertation
Requestor type	Student
/ ormat	Print, z lectronic
Portion	chapterkarticle
Rights for	Main product
Wuration of use	Life of current edition
Dreation of copies for the disabled	no
: ith minor editing privileges	no
/ or distribution to	: orldwide
In the following language(s)	Criginal language of publication
: ith incidental promotional use	no
The lifetime unit quantity of new product	0 to 499
The requesting personkorganiUation isE	Reuble Mathew
Crder reference number	None
Title of your thesis k dissertation	Cptical Dontrol of z-citon [ubits in Semiconductor [uantum Wbts] sing Pulse Shaping Techniques
z-pected completion date	Aug 2015
z-pected siUe (number of pages)	150
Total	**0.00 CAD**
Terms and Donditions	

Terms and Conditions

The American Physical Society (APS) is pleased to grant the Requestor of this license a non-exclusive, non-transferable permission, limited to **print** and/or **electronic** format, depending on what they chose, provided all criteria outlined below are followed.

1. For electronic format permissions, Requestor agrees to provide a hyperlink from the reprinted APS material using the source material's DOI on the web page where the work appears. The hyperlink should use the standard DOI resolution URL, http://dx.doi.org/DOI. The hyperlink may be embedded in the copyright credit line.
2. For print format permissions, Requestor agrees to print the required copyright credit line on the first page where the material appears: "Reprinted (abstract/excerpt/figure) with permission from [Author/s Names, APS Journal Title, Volume Number, Page Number and Year of Publication.] Copyright (Year) by the American Physical Society."
3. Permission granted in this license is for a one-time use and does not include permission for any future editions, updates, databases, formats or other matters. Permission must be sought for any additional use.
4. Use of the material does not and must not imply any endorsement by APS.
5. Under no circumstance does APS purport or intend to grant permission to reuse materials to which it does not hold copyright. It is the requestors sole responsibility to ensure the licensed material is original to APS and does not contain the copyright of another entity, and that the copyright notice of the figure, photograph, cover or table does not indicate that it was reprinted by APS, with permission from another source.
6. The permission granted herein is personal to the Requestor for the use specified and is not transferable or assignable without express written permission of APS. This license may not be amended except in writing by APS.
7. You may not alter, edit or modify the material in any manner.
8. You may translate the materials only when translation rights have been granted.
9. You may not use the material for promotional, sales, advertising or marketing purposes.
10. The foregoing license shall not take effect unless and until APS or its agent, Copyright Clearance Center (CCC), receives payment in full in accordance with CCC Billing and Payment Terms and Conditions, which are incorporated herein by reference.
11. Should the terms of this license be violated at any time, APS or CCC may revoke the license with no refund to you and seek relief to the fullest extent of the laws of the USA. Official written notice will be made using the contact information provided with the permission request. Failure to receive such notice will not nullify revocation of the permission.
12. APS reserves all rights not specifically granted herein.
13. This document, including the CCC Billing and Payment Terms and Conditions, shall be the entire agreement between the parties relating to the subject matter hereof.

Other Terms and Conditions

None

Questions? customercare@copyright.com or +1-855-239-3415 (toll free in the US) or +1-978-646-2777.

Gratis licenses (referencing $0 in the Total field) are free. Please retain this printable license for your reference. No payment is required.